UNIVERSITY OF NAPLES "PARTHENOPE"

DEPARTMENT OF ENGINEERING

Ph.D. Program in Energy Science and Engineering

SYNTHESIS AND CHARACTERIZATION OF NON-FLUORINATED MEMBRANES FOR FUEL CELL APPLICATIONS

Emmanuel De Gregorio

Supervisor

Prof. Giuseppina Roviello

Co-Supervisor

Dr. Valentina Naticchioni (ENEA)

XXXVIII Cycle

Coordinator: Prof. Laura Vanoli

Academic Years: 2022-2025

ENERGY SCIENCE AND ENGINEERING (ESE)
PhD PROGRAM

ITALIAN NATIONAL AGENCY FOR NEW TECHNOLOGIES, ENERGY AND SUSTAINABLE ECONOMIC DEVELOPMENT

*"*Socrate*: Su dunque, Teeteto, prova ancora una volta dall'inizio:*

che cos'è, in realtà, la conoscenza? Non stancarti, perché forse ne hai ancora la forza

Teeteto*: Sì, per Zeus, Socrate, ci proverò.*

Socrates*: Avanti allora, con coraggio: nulla di bello nasce senza fatica."*

*"*Socrates*: Come now, Theaetetus, try once more from the beginning:*

What truly is knowledge? You may still have the strength within you.

Theaetetus*: By Zeus, Socrates, I will try again.*

Socrates*: Then forward with courage, for nothing truly worthwhile is ever born without effort"*

(Plato, Theaetetus, 150c-151a)

ACKNOWLEDGEMENT

It is not easy to find the right words to describe all that this journey has given me. It was something unexpected, yet from the very first moment, it completely captivated me. I dedicate this work to the difficult times, to the deepest despair, and to the awareness that, in my own small way, I managed to carry out a project that I consider a great achievement, one of the main reasons that drives me, every day, to give the best of myself.

A special thanks goes to my family, the true engine behind everything. Thank you for your constant support and for your often vain attempts to understand what I was actually doing in the lab each day. Thank you for always being there, for being the backbone of my life and for giving me, through your example and courage, the strength to face every challenge. I dedicate this small but meaningful milestone to you, along with all the beautiful things that are yet to come.

To my parents-in-law, for your warmth, affection, and closeness, which you have never let me lack. A second family, in every sense of the word.

My heartfelt gratitude goes to Professor Giuseppina Roviello, much more than a tutor, a loyal friend, always ready to listen and to offer advice in every situation. Thank you for believing in me and for giving me the opportunity to live this wonderful experience of personal and professional growth. Thank you for the countless conversations, for your kindness, your determination, and your remarkable ability to always find something good in everything. Thank you, quite simply, for being who you are: strong-willed, tenacious, and deeply sensitive.

To Professor Oreste Tarallo, who knew how to embrace and enhance every one of my “extravagant” and “exotic” ideas. I vividly remember each of our exchanges, from which I learned that perseverance and the ability to think outside the box often lead to the best results.

My sincere thanks also go to Professor Claudio Ferone and Professor Raffaele Cioffi, always available and remarkably open to any kind of discussion, from science to beer, which, after all, is still chemistry.

None of this would have been possible without Professor Elio Jannelli. Thank you for believing in my work and, above all, for teaching me that believing does not mean accepting, but questioning,

exploring, and testing every idea. Your genuine curiosity and attention to detail showed me what it truly means to do research: never being satisfied with easy answers.

My heartfelt thanks to the entire ENEA team, Dr. Viviana Cigolotti, Dr. Valentina Naticchioni, and Dr. Alfonso Pozio. You made me feel truly at home, and that has meant the world to me. I am proud to have shared this journey with you.

Of course, this achievement would not have been the same without Michele, Alessio, Carlo, Ciro, Peppe, Luigi, Luca, Domenico, and all those I was lucky enough to meet along the way. You are much more than colleagues or friends, I consider you true brothers. Thank you for the countless laughs, the shared coffees, and simply for always being there. You have made my life better, perhaps without even realizing it, making each day lighter and filled with joy.

Special thanks go to someone special: Grandpa Gigi, the Gunslinger of Sant'Antonio Abate. More than a grandfather, he was a father and a true friend. I will never forget your first words when I was trying, somewhat awkwardly, to explain the beginning of this journey to you:

"*You must do whatever feels right for you. If you're happy, then take that path*."

I took that path, I followed it, and today I have arrived here. I thank you, not only for that advice, but for the example you set for me: even in the difficulties of life, you always faced everything with a smile. You left me so suddenly that I will never come to terms with your absence. A piece of my heart went away with you, but the memory of your smile, your jokes, and your way of being humble, funny, and loving, remains vivid. You and I still have unfinished business... a nice plate of spaghetti that you loved so much and that I was supposed to cook for you. What I would give to relive those moments. I dedicate this achievement to you in the hope that one day I will be able to hear your jokes and your fantastic motto again: Amabile? Sempre!

And now that you've all followed me to this point, we come to the most beautiful part. Maria, light of my eyes, you have no idea how much good you bring into my life. Thank you for always being there, day and night, through the darkest and most difficult moments.

Plato once said: "*Love is the desire to possess the good forever*."

And I have found that good in you. If today I stand here with a smile, with the strength not to give up, and with the serenity of someone who knows where he is going, it is because of you. You believed in me even when I couldn't, you picked up the pieces of my bad days and put them back together, with your patience, your wit, and your disarming sweetness.

You gave meaning to every effort, turning chaos into calm, fatigue into relief, and fear into courage. Every time I thought I couldn't make it, all it took was looking at you to remember why it was worth continuing. You are home. If this work is a milestone, you are the reason I was able to reach it. I don't know what the future holds, but I know that whatever comes, I want to face it with you, because with you everything is truer, simpler, more mine, more ours. Thank you for loving me even on the days when I didn't deserve it.

Thank you for waiting, supporting, encouraging, and softening me.

And thank you, above all, for being you: my constant, my balance, my love forever.

A warm embrace also to those of you up there.

I hope you are proud of me.

ABSTRACT

In the challenging path toward the energy transition, the World is facing the urgent need to reduce greenhouse gas emissions and gradually move away from fossil fuels. In this context, fuel cells are emerging as one of the most promising technologies for producing clean and sustainable energy, as they can directly convert the chemical energy of fuels, such as hydrogen, into electricity.

The versatility of fuel cells enables a wide range of applications, from hydrogen-powered vehicles to the generation of electricity and heat for residential, commercial, and industrial uses. In a global energy scenario increasingly focused on sustainability, efficiency, and security of supply, fuel cells represent not only an advanced technological solution but also a key element in the future energy mix.

In line with the sustainability goals defined by European and international standards, this Thesis focuses on the development of new polymeric membranes to be used as solid electrolytes in proton-exchange membrane fuel cells (PEMFC) that are more environmentally friendly, cost-effective, and, at the same time, high-performing and durable compared to those currently used.

This ambitious objective was pursued through a comprehensive research plan including the design and synthesis of new non-fluorinated polymers, followed by their detailed thermal, mechanical, and morphological characterization, and finally by their electrochemical testing—carried out, in some cases, directly on electrochemical devices assembled with the newly developed membranes.

Specifically, this work focuses on the development of polymer membranes obtained through chemical (Chapters I and V) and morphological-structural (Chapter IV) modifications of commercial, widely available polymers such as poly(2,6-dimethyl-1,4-phenylene)oxide (PPO) and poly[2,2′-*m*-(phenylene)-5,5′-bibenzimidazole] (*m*-PBI), suitable for low and high-temperature fuel cell applications, respectively.

Chapter I provides an overview of the global energy context and the fundamentals of fuel cell technology, emphasizing the need for non-fluorinated polymer membranes that meet modern environmental and performance standards.

Chapter II and III describes in detail the chemical, physical, mechanical, and electrochemical characterization techniques used throughout the work.

Chapter IV presents the synthesis and characterization of sulfonated poly(2,6-dimethyl-1,4-phenylene)oxide (sPPO) membranes, obtained by sulfonating PPO to impart key properties such as hydrophilicity, water uptake, and proton conductivity. Structural analyses, including FTIR spectroscopy, wide-angle X-ray diffraction (WAXD), as well as thermal, mechanical, and electrochemical tests, allowed the evaluation of proton conductivity as a function of temperature and humidity. The results are discussed in comparison with commercial benchmarks such as Nafion® and Pemion®, highlighting the main strengths and weaknesses of these different materials.

Chapter V focuses on PBI-based membranes designed for high-temperature PEM applications. In particular, it explores innovative production techniques such as electrospinning and examines in detail the influence of fibrous morphology on the chemical, physical, and electrochemical properties of the membranes.

Finally, Chapter VI focuses on the synthesis and characterization of a new aminated derivative of PPO to be used in high temperature PEM applications.

Overall, this Thesis contributes to the challenging goal of developing fuel cell components that combine high performance with environmental and economic sustainability. The results obtained, though preliminary, are very promising and are intended to serve as a foundation for future studies and as a stimulus for the scientific community to continue exploring innovative polymer materials through chemical and structural modifications.

SINOSSI

Nel difficile percorso verso la transizione energetica, il mondo si trova oggi ad affrontare l'urgente necessità di ridurre le emissioni di gas serra e di abbandonare progressivamente l'utilizzo dei combustibili fossili. In questo contesto, le celle a combustibile stanno emergendo come una delle tecnologie più promettenti per la produzione di energia pulita e sostenibile, poiché sono in grado di convertire direttamente l'energia chimica dei combustibili, come l'idrogeno, in energia elettrica.

La versatilità delle celle a combustibile consente un'ampia gamma di applicazioni, che spaziano dai veicoli alimentati a idrogeno alla produzione combinata di elettricità e calore per usi residenziali, commerciali e industriali. In uno scenario energetico globale sempre più orientato alla sostenibilità, all'efficienza e alla sicurezza dell'approvvigionamento, le celle a combustibile rappresentano non solo una soluzione tecnologica avanzata, ma anche un elemento chiave nel futuro mix energetico mondiale.

In linea con gli obiettivi di sostenibilità definiti dagli standard europei e internazionali, la presente Tesi è incentrata sullo sviluppo di nuove membrane polimeriche da impiegare come elettroliti solidi nelle celle a combustibile a membrana a scambio protonico (PEMFC), con l'obiettivo di renderle più ecosostenibili, economicamente vantaggiose e, al tempo stesso, performanti e durevoli rispetto a quelle attualmente in uso.

Questo ambizioso obiettivo è stato perseguito attraverso un piano di ricerca articolato, comprendente la progettazione e la sintesi di nuovi polimeri non fluorurati, seguite da un'approfondita caratterizzazione termica, meccanica e morfologica, e infine da una valutazione elettrochimica, condotta in alcuni casi direttamente su dispositivi elettrochimici assemblati con le membrane sviluppate nel corso del lavoro.

In particolare, la ricerca si concentra sullo sviluppo di membrane polimeriche ottenute mediante modifiche chimiche (Capitoli I e V) e morfologico-strutturali (Capitolo IV) di polimeri commerciali ampiamente disponibili, quali il poli(2,6-dimetil-1,4-fenilene ossido) (PPO) e il poli[2,2′-*m*-(fenilene)-5,5′-bibenzimidazolo] (*m*-PBI), idonei rispettivamente per applicazioni in celle a combustibile a bassa e alta temperatura.

Il Capitolo I fornisce una panoramica del contesto energetico globale e dei principi fondamentali delle celle a combustibile, evidenziando la necessità di membrane polimeriche non fluorurate in grado di soddisfare gli attuali requisiti ambientali e prestazionali.

I Capitoli II e III descrivono nel dettaglio le tecniche di caratterizzazione chimico-fisica, meccanica ed elettrochimica impiegate nel corso del lavoro sperimentale.

Il Capitolo IV presenta la sintesi e la caratterizzazione delle membrane di poli(2,6-dimetil-1,4-fenilene ossido) solfonato (sPPO), ottenute mediante solfonazione del PPO, finalizzata a conferire al materiale proprietà chiave quali idrofilicità, capacità di assorbimento d'acqua e conducibilità protonica. Le analisi strutturali — comprendenti spettroscopia FTIR, diffrazione a raggi X ad alto angolo (WAXD), oltre a test termici, meccanici ed elettrochimici, hanno permesso di valutare la conducibilità protonica in funzione della temperatura e dell'umidità. I risultati ottenuti sono stati confrontati con quelli di membrane commerciali di riferimento, quali Nafion® e Pemion®, mettendo in evidenza i principali punti di forza e le criticità dei diversi materiali analizzati.

Il Capitolo V è dedicato alle membrane a base di PBI, destinate ad applicazioni in celle a combustibile a membrana a scambio protonico operanti ad alta temperatura (HT-PEM). In particolare, esso esplora tecniche di produzione innovative, come l'elettrofilatura (electrospinning), analizzando in dettaglio l'influenza della morfologia fibrosa sulle proprietà chimiche, fisiche ed elettrochimiche delle membrane ottenute.

Infine, il Capitolo VI si concentra sulla sintesi e caratterizzazione di un nuovo derivato amminato del PPO, progettato per essere impiegato in applicazioni HT-PEM, con l'obiettivo di estendere ulteriormente la versatilità funzionale di questo backbone polimerico.

Nel complesso, la presente Tesi contribuisce al difficile ma necessario obiettivo di sviluppare componenti per celle a combustibile che coniughino elevate prestazioni, sostenibilità ambientale ed economicità. I risultati ottenuti, seppur preliminari, si sono rivelati estremamente promettenti e costituiscono una base solida per futuri approfondimenti, oltre a rappresentare uno stimolo per la comunità scientifica a proseguire l'esplorazione di materiali polimerici innovativi attraverso modifiche chimiche e strutturali mirate.

LIST OF PUBLICATIONS

SCIENTIFIC PUBLICATIONS

I. ***Emmanuel De Gregorio**, Giuseppina Roviello, Valentina Naticchioni, Viviana Cigolotti, Alfonso Pozio, Luis Alexander Hein, Carlo De Luca, Claudio Ferone, Antonio Rinaldi, Oreste Tarallo,* "Electrospun Polybenzimidazole Membranes: Fabrication and Fine-tuning through physical and statistical approaches". *Polymers,* 2025, 17(12), 1594. **10.3390/polym17121594.**

II. ***Emmanuel De Gregorio**, Tommaso Cogliano, Giuseppina Roviello, Valentina Naticchioni, Claudio Ferone, Giulia Monteleone, Oreste Tarallo,* "Adsorption of Phosphoric Acid on Electrospun PBI Membranes: A Thermodynamic and Kinetic Insight". *ACS Applied Energy Materials, 2026.* **https://doi.org/10.1021/acsaem.5c03104**

PATENT

I. ***Emmanuel De Gregorio,** Carlo De Luca, Elio Jannelli, Alessio Occhicone, Giuseppina Roviello, Oreste Tarallo, "*Assemblato Membrana-Elettrodo a base di componenti non fluorurati per applicazioni in celle a combustibile ed elettrolizzatori a scambio protonico", 102025000011018, ***Pending*** (2025).

OTHER PUBLICATIONS

I. ***Emmanuel De Gregorio**, Alessio Occhicone, Fabio Montagnaro, Giuseppina Roviello, Laura Ricciotti, Claudio Ferone*, "A novel method of iron oxalate production through the valorization of red mud", *Chemical Engineering Research and Design*, 194, 95-104, 2023. **https://doi.org/10.1016/j.cherd.2023.04.036.**

II. *Alessio Occhicone, Stanislao G. Graziuso, **Emmanuel De Gregorio**, Fabio Montagnaro, Laura Ricciotti, Oreste Tarallo, Giuseppina Roviello, Claudio Ferone.* "Synthesis and characterization of new acid-activated red mud-metakaolin geopolymers and comparison with their alkaline counterparts". *Journal of Cleaner Production*, 435, 140492, 2024. **https://doi.org/10.1016/j.jclepro.2023.140492**.

III. *Alessio Occhicone, **Emmanuel De Gregorio**, Fabio Montagnaro, Giovanni Ausanio, Valentina Gargiulo, Michela Alfè, Giuseppina Roviello, Claudio Ferone*, "Production and characterization of nano-magnetic material through different red mud reduction processes". *Materials Chemistry and Physics*, 2024, 129950. **https://doi.org/10.1016/j.matchemphys.2024.129950.**

IV. *Giuseppina Roviello, Alessio Occhicone, **Emmanuel De Gregorio***, Laura Ricciotti, Claudio Ferone, Raffaele Cioffi, Oreste Tarallo*, "Geopolymer-based composite and hybrid materials: The synergistic interaction between components". *Sustainable Materials and Technologies*, 2025, e01404. **https://doi.org/10.1016/j.susmat.2025.e01404**.

V. *Alessio Occhicone, **Emmanuel De Gregorio***, Gianmarco Di Rienzo, Gabor Mucsi, Giovanni Battista Salzano, Giuseppina Roviello, Claudio Ferone*, "Alkali-activated porous materials from biomass bottom ash for the production of insulation panels". *Waste and biomass valorization*, 2025. **https://doi.org/10.1007/s12649-025-03245-9.**

***Corresponding author**

CONFERENCE CONTRIBUTIONS

Conferences with Oral Contribution of the PhD candidate.

I. ***Emmanuel De Gregorio***, Carlo De Luca, Alessio Occhicone, Giuseppina Roviello, Claudio Ferone, Oreste Tarallo, Viviana Cigolotti, Elio Jannelli, Luis Alexander Hein, Alfonso Pozio. "Electrospinning of polybenzimidazole: a new approach for the obtainment of non-fluorinated membranes for Fuel Cells applications", European Ph.D Hydrogen Conference – EPHyC 2024, Ghent (Belgium), 20-22 March 2024.

II. ***Emmanuel De Gregorio***, Luca Riccio, Carlo De Luca, Giuseppina Roviello, Viviana Cigolotti, Elio Jannelli, Antonio Rinaldi, Luis Alexander Hein, Claudio Ferone, Oreste Tarallo. "Impregnation of PBI-based electrospun membranes in phosphoric acid solutions for fuel cell applications", IX Symposium on Hydrogen, Fuel Cells and Advanced Batteries, Milazzo (Italy), from 30 June to 03 July 2024.

III. ***Emmanuel De Gregorio***, Carlo De Luca, Claudio Ferone, Alfonso Pozio, Oreste Tarallo, Giuseppina Roviello. "Polybenzimidazole-based electrospun membranes for fuel cell application", Il contributo dei Giovani Chimici in Campania – Edizione 2024, Caserta (Italy), 19 July 2024.

IV. ***Emmanuel De Gregorio***, Tommaso Cogliano, Claudio Ferone, Viviana Cigolotti, Valentina Naticchioni, Elio Jannelli, Luis Alexander Hein, Alfonso Pozio, Oreste Tarallo, Giuseppina Roviello. "Adsorption kinetic of phosphoric acid on Polybenzimidazole Electrospun membranes for HTPEMs", European Ph.D Hydrogen Conference – EPHyC 2025, Trieste (Italy), 09-11 April 2025.

V. ***Emmanuel De Gregorio***, Tommaso Cogliano, Carlo De Luca, Claudio Ferone, Viviana Cigolotti, Valentina Naticchioni, Elio Jannelli, Oreste Tarallo, Giuseppina Roviello. "Phosphoric Acid Adsorption on PBI electrospun Membranes: a kinetic overview", International Congress on Sustainable Energy and related Technologies – ICSET, Lipari (Italy), 22-26 June 2025.

VI. ***Emmanuel De Gregorio***, Tommaso Cogliano, Oreste Tarallo, Giuseppina Roviello. "Acid Adsorption on PBI Electrospun Membrane: A kinetic and thermodynamic evaluation", Il Contributo dei giovani chimici in Campania, Salerno (Italy), 03-04 July 2025.

VII. ***Emmanuel De Gregorio***, Claudio Ferone, Oreste Tarallo, Giuseppina Roviello. "Innovation in fuel cells: towards sustainable membranes", III Convegno Nazione della Divisione di Chimica per le Tecnologie della SCI – AICIng, Milazzo (Italy), 01-04 September 2025.

Conferences with Poster Contribution of the PhD candidate.

I. ***Emmanuel De Gregorio***, Carlo De Luca, Alessio Occhicone, Giuseppina Roviello, Claudio Ferone, Oreste Tarallo, Viviana Cigolotti, Elio Jannelli, Luis Alexander Hein, Alfonso Pozio. "New PBI Electrospun membranes for HTPEM-FCs applications", European Hydrogen Conference – EFC 2023, Capri (Italy), 13-15 September 2023.

II. ***Emmanuel De Gregorio***, Carlo De Luca, Claudio Ferone, Viviana Cigolotti, Valentina Naticchioni, Elio Jannelli, Oreste Tarallo, Giuseppina Roviello. "Development and characterization of Electrospun PBI Membranes for Enhanced Acid Uptake in HTPEMFC Applications" and "Innovative supported Pd@CeO_2-ZrO_2 catalysts for fuel cells applications", European Fuel Cell and Hydrogen Conference 2025, Capri (Italy), 17-19 September 2025.

Other Conferences:

I. ***Emmanuel De Gregorio***, Alessio Occhicone, Claudio Ferone, Fabio Montagnaro, Giuseppina Roviello, Oreste Tarallo. "Leaching of red mud: from iron recovery to fine chemicals", Il contributo dei giovani chimici in Campania – Edizione 2023, Napoli (Italy), 20 June 2023.

LIST OF CONTENT

CHAPTER I – INTRODUCTION

1.1 Fuel Cells technology: an overview

The growing population and increasing global energy demand, coupled with the need to mitigate climate change, has stimulated the search for alternative energy sources and technologies to fossil fuels [1], [2]. In this global context, hydrogen (H_2) has emerged as one of the most promising energy carriers [3], [4] and fuel cells represent one of the key technologies for its electrochemical conversion into electricity [5]. Fuel cells are electrochemical devices that enable electricity to be obtained from hydrogen in a direct and highly efficient manner, producing water as the only "waste" product [6]. This is of major importance as it eliminates the emission of pollutants and greenhouse gases, typical of combustion, making fuel cells particularly attractive for applications in transport, renewable energy generation and storage [7], [8]. From an operational point of view, a fuel cell is an electrochemical device that converts the chemical energy of a redox reaction into electrical energy [9]. In these devices, the main components are the electrolyte and the two porous electrodes [10], [11], in which the electrochemical reaction takes place: at the anode, hydrogen (H_2) is oxidized into protons and electrons (HOR, Hydrogen Oxidation Reaction, Eq. 1.1) and is generally the fast stage of the reaction with negligible overpotentials [12]. The protons pass through the electrolyte, the electrons recombine with the protons through a circuit outside the cathode, where the oxygen reduction reaction (ORR, Oxygen Reduction Reaction, Eq. 1.2) takes place, allowing the formation of water [13], [14] (Eq. 1.3). Given the two different reaction contributions, the anode is traditionally regarded as the reference and counter electrode (RCE) while the cathode is regarded as the working electrode (WE).

HOR, anode : $H_2 = 2H^+ + 2e^-$ Eq. 1.1

ORR, cathode : $\frac{1}{2} O_2 + 2H^+ + 2e^- = H_2O$ Eq. 1.2

Overall : $\frac{1}{2} O_2 + H_2 = H_2O$ Eq. 1.3

There are different types of fuel cells, which differ according to the nature of the electrolyte, i.e. the component capable of exchanging ions [15], the operating temperature and the purity and type of gas entering the system [16]. The most widespread type is that of polymer electrolyte fuel cells (also addressed to as "Polymer Exchange Membrane" fuel cells, PEMFC), which can be subdivided into two macro categories: low-temperature polymer electrolyte fuel cells (LT-PEMFC) capable of operating below 100 °C and in high-humidity conditions [17], and high-temperature PEM cells (HT-

PEMFC), which instead operate in a temperature range between 120-180 °C under anhydrous conditions [18]. In PEMFC, the polymer membranes function both as a solid proton-conducting electrolyte and as a physical barrier separating the reactant gases between anode and cathode [19], [20]. Since the 1960s, the technological standard in this field has been represented by membranes based on perfluoroalkylated substances (PFAS), in particular Nafion™ (DuPont/Chemours), which have been joined more recently by short side-chain analogues such as Aquivion™ (Solvay) and 3M polymers [21], [22] (Figure 1.1).

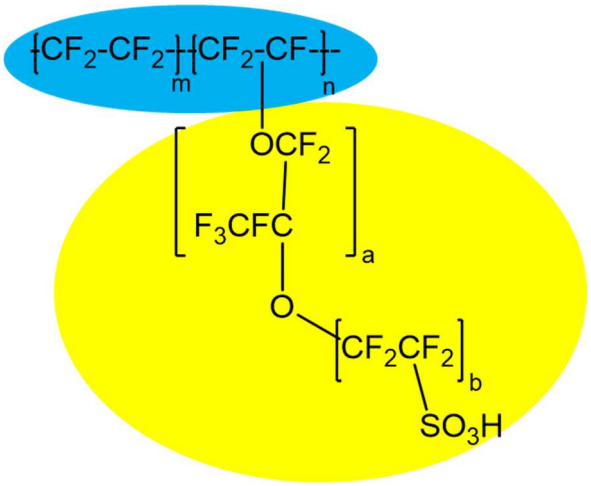

Figure 1.1 - Chemical structure of the main PFAS polymers used in fuel cell applications: Nafion® (Equivalent Weight, EW=1100, m/n=6.6, a=1, b=1), Aquivion® (EW=830, m/n=5.5, a=0, b=1), 3M® (EW=850, m/n 4.7, a=0, b=2). The blue circle highlight the polymer backbone, while the yellow one the side chain.

These fluorinated materials combine high proton conductivity with good chemical and mechanical stability under typical operating conditions of 60-80 °C and high relative humidity (70-90 %) [23], [24]. The key to their performance lies in their unique phase-separated nanostructure consisting of a hydrophobic polytetrafluoroethylene (PTFE)-based backbone that provides mechanical support and hydrophobic properties [25], while perfluorinated side chains terminated with acidic sulfonic groups (SO_3^- H^+) form hydrophilic domains [26] that interact with the absorbed water to create continuous channels for proton transport (Figure 1.2), which are essential for the proper functioning of these materials [24].

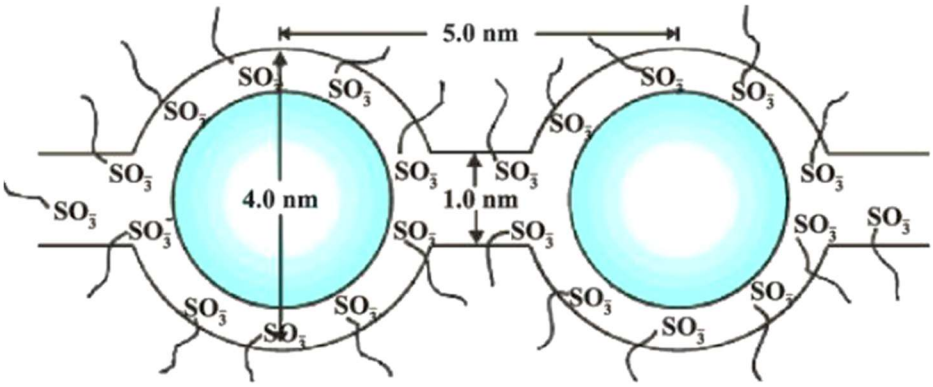

Figure 1.2 – Schematic representation of the biphasic nanostructure of Nafion. The sulfonic acid groups ($–SO_3^-$) decorate the interfaces between these two phases, forming interconnected ionic channels (≈1.0 nm in width) that link spherical water clusters (≈4.0 nm in diameter, spaced ≈5.0 nm apart). This morphology enables efficient proton transport while maintaining mechanical stability, making Nafion a key ionomer for polymer electrolyte fuel cell applications. Picture taken from reference [26].

Due to this bicontinuous morphology, membranes such as Nafion exhibit proton conductivities on the order of 0.1 S cm^{-1} at 80 °C under high hydration conditions [27] and allow high current densities in cells > 3 A cm^{-2} [28], In addition, PFAS membranes tend to be chemically inert (the $-CF_2-$ polymer chain is very stable) due to the strong C-F bond (characterized by a typical average bond energy ~485 kJ mol^{-1}, significantly higher than ~350 kJ mol^{-1} in the case of C-C single bond) and show good electrochemical durability up to several thousand hours of operation (> 10000 h) [29]. To further enhance the mechanical strength and durability of these membranes, they are typically reinforced with expanded PTFE (ePTFE) fabrics [30] or porous films and/or composite materials [31] that similarly improve their resistance to thermal and mechanical stresses without sacrificing proton conduction [32]. Thanks to all these features, PFAS membranes such as Nafion have been the benchmark for PEMFCs for decades, spanning applications from automotive to power generation in stationary or dynamic systems, due to their properties of high conductivity, chemical stability and operational flexibility in the presence of water. Despite their industrial success, PFAS membranes have important intrinsic limitations that are now well documented [33], [34]:

(a) environmental and health impact. The use of the aforementioned fluoropolymers entails potential ecological and public health risks [35] linked to the persistence and bioaccumulability of these molecules [36]. For this reason they are often referred to as “forever chemicals” [37];

(b) high cost. These materials are derived from complex chemical processes [38] such as radical polymerization in the presence of fluorinated monomers in multiple steps, and their production is

geographically limited to a few global suppliers [39]. This results in very high costs per unit area estimated in the order of €500-1000/m² (depending on membrane thickness and type) for Nafion, making the membrane one of the most expensive components of the fuel cell stack [38] thus affecting the cost of the overall PEMFC system, especially in automotive applications where to maintain high performance and good durability, a large membrane area per cell (> 50 cm^2) is required [40];

(c) limited temperature range. PFAS membranes work optimally in the range ~80-90 °C, as beyond this threshold they begin to lose water and dehydrate, causing a rapid degradation process of the sulfonic group (SO_3^- H^+) followed by a drastic drop in proton conductivity and overall cell performance [41]. Hence, one of the key points for the proper functioning of such materials is the need to keep the perfluorinated backbone and the sulfonic group hydrated, as this is the only way to guarantee an optimal proton jump on each acid site: at high temperatures (>100 °C), water evaporates rapidly and the PFSA membrane undergoes, as described above, dehydration, resulting in an increase in proton resistivity [42], an increase in the hydrogen/oxygen crossover gas and an acceleration of the chemical degradation processes[43] due, generally, to the formation and attack of radical species that compromise its function [44]. This makes conventional Nafion-based PEMs unsuitable for operation in high-temperature cells [45] (HT-PEMFC) without adequate humidification or structural modifications (e.g. using organic and/or inorganic hygroscopic additives) [31]. Furthermore, it must be considered that thin PFAS membranes tend to lose mechanical integrity at temperatures close to 100 °C [46] due to a thermal softening phenomenon in the absence of sufficient hydration (T_g of Nafion hydrate is ~110 °C) [47]. This thermal constraint limits the efficiency of the cell as higher temperatures would in fact be desirable to improve electrochemical kinetics (lower charge transfer resistance), simplifying heat and water management and increasing tolerance to impurities in the feed (e.g. CO) [48].

(d) permeability to gases [49] and, more generally, to fuels. The crossover of H_2 and O_2 in PEMFCs become particularly relevant when the PFAS based PEMFCs operates above 100 °C or at high pressures [50], causes an internal short circuit and mixed potential at the electrodes. The parasitic reaction lowers the open-circuit voltage (OCV), which is the maximum voltage a fuel cell can produce. Gas crossover can also lead to the formation of hydrogen peroxide (H_2O_2) and other reactive oxygen species (ROS) such as hydroxyl ($OH\cdot$) and hydroperoxyl ($HO_2\cdot$) radicals [51]. The decomposition of hydrogen peroxide, catalyzed by trace metal ions, is a primary source of these radicals. The highly reactive radicals attack the polymer membrane's chemical structure, causing chain scission and other damage. This chemical degradation weakens the membrane, leading to the

formations of pinholes and cracks, which, in turn, increase gas crossover. This degradation loop reduces the fuel cell's efficiency [52] and shortens its lifespan.

Increasing the thickness of the PEM is the most immediate countermeasure; however, it imposes ohmic penalties. This is why multilayer approaches and architectures employing nanoscale barriers based on two-dimensional materials, such as graphene [53] and reduced/functionalized graphene oxides [54], or inorganic nanofillers like SiO_2 [55] or ZrO_2 [56], are being explored. Such layers, incorporated into the PFSA matrix, increase the tortuosity of the gas pathway [57] and can halve the hydrogen permeation while keeping the proton conductivity virtually unchanged [58]. Even so, a proportion of the $-SO_3H$ groups undergo desulfonation and the breakdown of the fluorinated backbone generates volatile species of considerable environmental concern [59]. In this regard, the insertion of radical scavengers based on CeO_2 or MnO_2, dispersed in nanometric form, intercept hydroxyl radicals [60], prolonging the cell's operational life without leaching phenomena. Finally, durability is further hampered by mechanical stresses due to wetting/drying cycles, pressure differences between the two sides of the membrane, and local and global thermal fluctuations in the cell. The continuous swelling and contraction creates micro-cracks [61] that can turn into pin-holes, opening crossover paths and triggering short circuits. To counteract these effects, the insertion of a microporous ePTFE scaffold - as in the Nafion XL® or Gore-Select® membranes [62] - redistributes the mechanical stresses and makes it possible to go down to thicknesses of 6-14 μm without losing mechanical integrity, with performance exceeding 20000 h [63]. However, the challenge related to their cost and the increasing regulatory pressure on PFAS remains open with industrial initiatives that aim at more cost-efficient production and end-of-life recycling programmes.

In conclusion, despite their established performance and long industrial experience, PFAS based membranes today show a number of structural, operational and economic limitations that call into question their long-term sustainability. These operational limitations are compounded by a growing concern over the environmental impact of the fluorinated nature of these materials [64], whose persistence and bioaccumulability have attracted the attention of regulatory authorities in Europe and the United States. It is clear that PFSAs, while remaining the industry standard for LT PEMFC cells, now find themselves under dual pressure: on the one hand, the need to improve efficiency, durability and plant simplification; on the other, the urgency of meeting new environmental directives that aim to phase out non-essential fluoropolymers. For all these reasons, the development of non-fluorinated membranes is now one of the most urgent task to overcome the environmental and regulatory limitations of PFAS in LT PEMFC cells [65].

1.2 Low Temperature Fuel Cell (LT-PEMFC)

Low-temperature proton exchange fuel cells (LT-PEMFC) generally operate in a temperature range of 60-80 °C and under varying humidity conditions. The heart of the LT-PEM cell is the proton exchange polymer membrane, typically Nafion®, which ensures proper and efficient proton conduction. Each membrane is integrated in the membrane-electrode assembly (MEA) [66] where the electrode mainly consists of a metal catalyst (e.g. Pt) supported on a conducting carbon-based material (with a high specific area) and its quantity (load) is a function of the nature of the used electrolyte, the specific size of the catalyst nanoparticles, and, in general, the architecture of the electrode and how it is distributed on the membrane [67]. To date, this technology is one of the most established due, and above all, to several key advantages:

i) low operating temperature, as in their operating range, these systems can reach an optimal operating condition in a very short time [68] without the aid of pre-heating systems;
ii) high power density, typically in the range 0.5-1 W/cm^2 [69], which makes these systems suitable for practical and compact applications such as vehicles and/or mobility [40];
iii) instantaneous dynamic response, as the system's high reactivity leads to load variations almost in real time, rapidly adapting the production of electrical power [70];
iv) high electrical efficiency, typically varying between 40-60 % but which can be further increased up to 80% with the use of combined heat and power (CHP) systems [71];
v) zero emissions, as the only by-products are water vapor and heat.

Despite the advantages mentioned above, low-temperature PEM (LT-PEM) technology still faces several technical challenges that limit its large-scale production and global deployment. One of the main issues is the high production cost, which arises from both the expensive materials required – such as Platinum and Nafion® - and the complex manufacturing processes involved in assembling the different components [72]. Another important challenge concerns the development of an effective water management system [73] and the maintenance of proper water balance within the cell. In fact, on the one hand, adequate hydration of the membrane is essential to ensure efficient ion exchange and optimal performance [74]. On the other hand, poor water management can lead to performance losses or even to flooding within the cell: excess water can block the pores of the electrodes or the flow channels, preventing gases (mainly oxygen) from reaching the catalytic sites and thus reducing the overall efficiency of the cell [75]. Degradation is another critical issue that strongly affects the durability of LT-PEM cells: microstructural changes in the electrodes due to cyclic flooding, carbon corrosion, and degradation of both the catalyst and the polymer membrane due to chemical reactions can result in a progressive loss of conductivity [76]. As a consequence, the operational lifetime of the

cell may drop below 1000 hours. Finally, safety and environmental aspects must also be considered. Although fuel cells are regarded as a clean energy technology, their full life cycle and the potential risks associated with the materials and reagents used cannot be ignored. Hydrogen, for instance, is a highly flammable and requires careful handling, with appropriate sensors to detect leaks and prevent fires [77]. Moreover, the use of precious metals such as platinum or palladium, and of fluorinated polymer membranes, has a notable environmental impact that should be minimized in future developments.

1.2.1 Environmental Constraints on LT-PEMFCs

As already discussed in previous sections, low-temperature PEM fuel cells (LT-PEMFCs) currently heavily on high-molecular-weight fluoropolymers (for example, Nafion®, Aquivion® and Flemion®). This polymers fall under the broad regulatory definitions of PFAS (per- and polyfluoroalkyl substances) as adopted by European Chemicals Agency (ECHA) [78] and the Organization for Economic Co-operation and Development (OECD) [79]. Because of growing environmental concerns over PFAS, pressure is mounting to restrict or eliminate their use in many applications – including in energy systems.

Under EU's Chemicals Strategy for Sustainability (2020), the aims is to "*phase out the use of all PFAS, allowing it only where essential for society*" [80]. In January 2023, five European Countries (Germany, Netherlands, Sweden, Norway and Denmark) submitted a restriction dossier to ECHA that included fluoropolymers among the PFAS to be reviewed. In January 2025, ECHA announced the start of the final phase of this evaluation: the scientific committees (Risk Assessment Committee, RAC and Socio-Economic Analysis Committee, SEAC) are now evaluating the dossier sector by sector [81], with decision expected by 2026 and possible transitional periods of 5-12 years. If PFAS are restricted or banned without exemptions, the cost and supply risks for LT-PEMFC deployment would rise sharply. Stakeholders (e.g. Hydrogen Europe) warn that indiscriminate bans could jeopardize billions in investment [82] and hinder decarbonization targets [83].

In the United States, regulatory actions on PFAS are also intensifying. For example, the Environmental Protection Agency (EPA) recently proposed stringent limits on certain PFAS in drinking water and extended reporting requirements under Toxic Substances Control Act (TSCA) for PFAS producers [84]. State-level regulations vary, with some measures exempting solid fluoropolymers for their use in critical applications, whereas others apply broader restrictions without these specific allowances.

In response to this regulatory uncertainty, major membrane and fluoropolymer producers (such as Chemours, Solvay, and Tokuyama) are already developing closed-loop recycling, recovery and end-of-life programs to mitigate environmental impact and regulatory risk. Simultaneously, the research community is pushing hard toward PFAS-free membranes. Promising results have emerged: for example aromatic hydrocarbon ionomers reinforced with nanofibers have shown stability comparable to Nafion at 120 °C and 30 % relative humidity in laboratory settings [85]. However, to date no fluorine-free material has demonstrated the combination of high conductivity, durability, chemical resistance, and scale-up viability required for full automotive or industrial stacks [86]. Therefore, PFSA membranes may become constrained – or even disallowed – materials in the medium term, depending on how "essential use" is defined by regulators and how different jurisdictions align their policies. In this transitional period, the fuel cell industry faces two parallel strategies:

1. Intensify recovery, recycling, and closed-loop design of fluoropolymers to reduce their environmental footprint and exposure to regulation;
2. Accelerate development of truly high-performance, fluorine-free alternatives that can meet future regulatory constraints without compromising system performance.

These challenges should be viewed as opportunities, not simply as regulatory obstacles, to rethink the entire fuel cell materials chain. In particular, the success of new fluorine-free membranes (for example, high-temperature PBI-based polymers doped with phosphoric acid) can open a new path toward sustainable, scalable PEM technologies.

1.2.2 Recent trends and Perspective of LT-PEMFCs

Low-temperature proton exchange membrane fuel cells (LT-PEMFCs) are undergoing a significant transformation as research and industry seek alternatives to perfluorinated ionomers such as Nafion®. While these materials have long been considered the benchmark for high proton conductivity and durability, increasing regulatory restrictions on PFAS and the growing emphasis on life-cycle sustainability are driving a shift toward fluorine-free electrolytes. This transition is not merely a response to policy pressure but represents a broader scientific and technological evolution toward cleaner, circular, and more resilient hydrogen energy systems.

In recent years, cross-disciplinary research programmes involving macromolecular chemistry, materials science, process engineering and life cycle analysis (LCA) have been developed [87]. Recent developments in molecular design have been central to this progress. The availability of *ab initio* and multiscale simulation tools allows accurate prediction of polymer behavior [88], bridging

the gap between molecular structure and macroscopic performance. Computational screening now enables the selection of suitable monomers and polymer architectures based on proton transport mechanisms, mechanical stability, and processability, greatly reducing the need for iterative experimental synthesis. Studies have demonstrated that optimized sulfonated aromatic poly(ether)s, polyimides, and block copolymers can achieve conductivities exceeding 100 mS cm^{-1} at 80 °C and 40% relative humidity—values comparable to or surpassing Nafion®. Moreover, the fine-tuning of side-chain length, sulfonation degree, and backbone rigidity enables materials with lower swelling and higher dimensional stability under variable humidity conditions. Parallel to molecular optimization, advances in fabrication technologies are enabling the production of high-performance membranes at reduced cost. Processes such as double-jet electrospinning [89] and reactive extrusion have emerged as scalable and environmentally friendly routes to produce ultrathin membranes (typically below 30 μm) with controlled porosity and nanophase separation. These methods allow for the incorporation of cross-linked domains or secondary networks that enhance mechanical resilience without compromising conductivity. The integration of functional fillers—such as sulfonated graphene oxide, phosphonated silica, or zirconium phosphate—has proven particularly effective in promoting microhydration [54] and stabilizing ionic domains. Such hybrid structures maintain high conductivity even under low-humidity conditions (<40% RH), which are critical for efficient automotive and portable applications. Durability remains a key challenge for LT-PEMFCs operating with hydrocarbon-based membranes, as hydrocarbon backbones are generally more susceptible to oxidative degradation than PFSA materials. However, recent advances in crosslinking chemistry, antioxidant additives, and radical-scavenging fillers have significantly improved membrane longevity. Several studies have reported continuous operation exceeding 10,000 hours under automotive-relevant cycling conditions, with minimal loss of conductivity and mechanical strength [54]. This durability, combined with improved processability, makes hydrocarbon membranes increasingly competitive with fluorinated analogues. Furthermore, these materials exhibit lower environmental persistence and are easier to recycle, contributing to a marked improvement in the overall sustainability profile of the technology.

Life Cycle Assessment (LCA) analyses have quantitatively confirmed these environmental advantages. Replacing PFSA membranes with hydrocarbon analogues results in an estimated 80% reduction in acidification potential, a 15–20% decrease in cumulative energy demand [90], and a reduction of two orders of magnitude in human toxicity indicators. Additionally, many hydrocarbon polymers can be synthesized from widely available aromatic precursors, avoiding the use of specialty fluorinated monomers with complex supply chains and high embedded energy. These benefits make LT-PEMFCs more compatible with circular-economy strategies [91] and align with global

sustainability frameworks such as the EU Green Deal and the U.S. DOE Hydrogen Shot Initiative. A promising direction is the integration of hydrocarbon membranes across both fuel cell and electrolyzer technologies. Using the same polymer platform for hydrogen generation and utilization simplifies logistics, reduces material qualification costs, and opens the path toward reversible "fuel-cell-to-grid" architectures. Such systems can dynamically switch between power generation and hydrogen production modes depending on energy demand and renewable availability, thereby improving grid flexibility and storage efficiency. This integration also accelerates knowledge transfer between the two technologies, as insights from electrolyzer durability under oxidative conditions can inform fuel cell membrane stabilization strategies. Industrial interest in fluorine-free materials is growing rapidly. Several major chemical companies, including Solvay, Toray, and Asahi Kasei, along with research consortia and start-ups, are investing in pre-commercial production of hydrocarbon ionomers. Pilot lines for continuous casting and extrusion are being developed using low-toxicity solvents and solvent-recovery systems to minimize environmental impact. Techno-economic assessments indicate that large-scale adoption of hydrocarbon-based membranes could lower stack material costs by 25–40%, depending on production scale and configuration. The elimination of PFAS-related supply risks, combined with easier end-of-life management and domestic raw material availability, further strengthens the economic case for these materials. At the system level, LT-PEMFCs are benefiting from advances in component integration and modeling. Modern stack designs leverage improved bipolar plate coatings, corrosion-resistant alloys, and optimized gas diffusion layers to ensure compatibility with the new electrolyte chemistries. Multiphysics simulations now provide detailed insights into coupled water transport, proton conduction, and heat management within non-fluorinated membranes, guiding cell and stack optimization. These approaches are essential to maintaining high efficiency under transient and low-humidity conditions, which remain among the most demanding operational scenarios for LT-PEMFCs.

Despite remarkable progress, several challenges persist before hydrocarbon-based LT-PEMFCs can reach full commercial maturity. Long-term chemical stability under start-stop cycling, compatibility between the ionomer and catalyst layers, and standardized accelerated stress test (AST) protocols remain open research areas. The interfacial behavior between new ionomers and platinum-based or non-platinum catalysts requires further study, as local hydration and acid–base interactions strongly influence electrode performance. Additionally, upscaling membrane fabrication from laboratory casting to industrial-scale continuous production must address issues of defect control, uniform thickness, and cost consistency.

Nevertheless, the overall trajectory of LT-PEMFC development is increasingly aligned with the global shift toward sustainable energy technologies. The combination of predictive molecular design, green processing, and integrated system engineering is producing a new generation of membranes that are both high-performing and regulation-ready. These advances indicate that the historical dependence on PFSA materials is no longer an inevitable constraint. Instead, the ongoing transformation represents an opportunity to redefine the performance and sustainability benchmarks of proton exchange membrane technologies.

1.3 High Temperature Fuel Cell (HT-PEMFC)

High-temperature PEM fuel cells (HT-PEM) have been developed to try to overcome the limitations of low-temperature cells in terms of ionic strength, moisture management and tolerance to impurities [18] (e.g. CO, H_2S). These systems operate in a temperature range typically between 150-180 °C, and so under anhydrous conditions [45]. The main electrolyte used today is polybenzimidazole (PBI) doped with phosphoric acid (H_3PO_4), which maintains excellent proton conductivity in the absence of water [92]. As mentioned above, the use of these devices brings considerable advantages from an operational point of view:

a) high tolerance to fuel impurities: at high temperatures, HT-PEM cells can also operate with “high” concentrations of impurities such as carbon monoxide (CO, up to 10 ppm), without irreversibly poisoning the catalyst in the electrode;

b) simplified temperature and humidity management: operating at temperatures above 100 °C, the water produced at the cathode is in the vapor phase. Thus, no humidification system for the incoming gases is needed and, consequently, no cell flooding problems are experienced. This is a great strength compared to the LT-PEM technology, which instead requires extremely efficient water management, which has a significant impact on system costs. In addition, the presence of a single vapor phase simplifies the design of gas diffusion systems [93] (bipolar plate), making the entire cell less sensitive to the morphology of the electrodes and gas flow;

c) development of polymeric materials with high mechanical and thermal resistance [94]: the polymers used for HT-PEM applications have an intrinsic thermomechanical stability that allows them to work at high temperatures (unlike PFAS membranes, which undergo degradation already after 100 °C). Important is also the fact that the use of polymer electrolytes capable of exchanging ions at high temperatures without degrading has renewed interest in the development of new fuel cell technologies operating at 120 °C, as set by the US DoE and the NEDO agency [95] (located in Japan).

Operating at higher temperatures allows for enhanced electrode kinetics, improved tolerance to CO and other fuel impurities, and simplified water and thermal management, since product water remains in the vapor phase;

d) high electrochemical reaction speed: charge transfer reactions in the electrode (especially ORR) and in the polymer electrolyte benefit from the high temperature by accelerating reaction kinetics and overpotential losses [96]. Cells operating in the 150-180 °C range can achieve high efficiencies by working at much higher loads and avoiding diffusive phenomena.

Furthermore, the total absence of PFAS in HT-PEM membranes makes them compatible with future European and US restrictions and regulations, which are now increasingly stringent for fluorinated materials, as extensively described above.

From a materials point of view, the polybenzimidazole-based membranes used on the market to date have demonstrated good thermal and chemical stability, with service lives in excess of 20000 operating hours [97]. Recent developments include the production of cross-linked membranes with a double network or different morphology [98] (e.g. fibrous) and new aromatic ionomers with phosphonic or sulfonic groups [99], capable of maintaining conductivity above 160 °C even at low relative humidities. Although the power density remains slightly lower than LT PEMs (0.6-0.8 A cm^{-2} at 0.6 V) [94], the simplification of the system (no humidifiers, compact cooling system) and greater operational robustness make HT PEMs particularly suitable for sectors such as heavy transport, marine, aviation and cogeneration. From a commercial point of view, HT-PEM technology is carried out by only a few players internationally. Specifically, one of the first membranes available on the market was the Celtec developed by BASF [97], which over the years has represented and still represents the state of the art for this type of material. There are other components available for these applications, such as the TPS membrane [100], developed by Advent Technologies (owned by BASF).

In conclusion, HT-PEMs offer a concrete alternative to overcome the environmental and regulatory constraints on fluorinated membranes, with materials and architectures that combine high performance, durability and sustainability. They therefore represent not only a technical answer to the PFAS problem, but also a strategic trajectory to ensure the continuity of the energy transition in compliance with new regulations.

1.3.1 Limitations and challenges of HT-PEMFCs

Despite HT-PEMFC technology is a promising alternative to LT PEMFC, it presents a complex set of technical and material challenges that slow down its current industrial-scale deployment. The core of the system consists of polybenzimidazole (PBI)-based membranes impregnated with phosphoric (H_3PO_4) or polyphosphoric acid (PPA) [101], which acts as an electrolyte for proton exchange. In this context, the ionic conduction takes place according to a mixed carrier/Grotthuss mechanism [102], in which the acid forms hydrogen bonds with the imidazole groups of the polymer, allowing the transport of protons even in the absence of water, and whose mobility is further conveyed by the presence of free acid in the polymer matrix. However, acid management represents one of the main structural problems of the cell: H_3PO_4 tends to migrate from the membrane towards the electrode or to escape completely (acid leaching), especially in the presence of local concentration gradients [103], thermal cycling or low acid retention capacity on the part of the membrane itself. This phenomenon leads to a progressive loss of ionic conductivity, reduced performance, corrosion of the bipolar plates, damage to the seals, and, consequently, a deterioration of the cell's main components. In order to mitigate this criticality, studies are underway on polymer blends and membranes cross-linked or reinforced with organic/inorganic fillers [104] (e.g. SiO_2, TiO_2, graphene oxide, ZrP) that can better retain acid molecules in the polymer matrix, increasing their durability under prohibitive operating conditions [105].

A second relevant limitation is related to the kinetics of the oxygen reduction reaction (ORR) at the cathode. Although high temperatures generally favor electrochemical reactions, the presence of phosphoric acid around the crystalline domains of the catalyst (typically Pt/C or Pt-Ni/C) hinders the diffusion of O_2 towards the active sites, forming a viscous and poorly permeable film [106]. Added to this is the low solubility and diffusivity of oxygen in H_3PO_4 compared to water, which makes HT PEMs inherently slower on the cathode side than LT-PEMs. As a result, higher activation surges are observed, especially concerning the cathodic reduction reaction (ORR), with lower current densities at the same catalyst loading (0.3-0.5 W cm^{-2}).

To counter these effects, approaches such as optimizing cathode porosity, developing new ionomers capable of working under anhydrous and acidic conditions, formulating polymer blends [107] and using biphasic catalysts are being explored [108]. From the point of view of cell materials, the acidic operating environment and high operating temperatures require components that are highly resistant to corrosion and deformation. Bipolar plates must maintain good dimensional stability while guaranteeing efficient electrical conductivity under acidic conditions [109], so special alloy coated steels, specially treated graphite or composite materials are used. Gaskets must be chemically

compatible with H_3PO_4 and resistant to cyclic thermal stress. Any degradation or contamination poses the risk of leaks, short circuits or electrochemical pollution of the interface. From a performance point of view, HT PEMFCs have, as mentioned earlier, a typical power density of between 0.3 and 0.5 W cm^{-2}, which is lower than Nafion-based LT-PEM cells, which can exceed 1 W cm^{-2} under optimal conditions. However, recent developments on filler-modified and cross-linked PBI-based membranes [110] have shown electrochemical results comparable to those obtained for LT-PEM systems, with a stability above 15000 h in continuous thermal cycling tests [111]. However, a further challenge is the lack of standardization in testing and Accelerated Stress Test (AST) protocols for HT PEMs: unlike LT-PEMs, which have standardized protocols (e.g. by DOE or EU-JRC), high-temperature cells still lack shared guidelines for assessing activation, degradation and boundary conditions [112]. This hampers comparability between electrochemical tests, even on a laboratory scale, and slows down industrial engineering. In conclusion, we can say that HT-PEMFCs offer numerous advantages such as high tolerance to impurities, absence of humidification systems, higher thermal recoverability and independence from fluorinated materials. However, they still require extensive optimization efforts in terms of materials, system design, electrolyte chemistry and regulatory validation. Only through a multidisciplinary approach that integrates polymer science with the development of new catalysts and advanced components can this technology be brought to the industrial maturity required to meet the challenges of decarbonization.

1.3.2 Future perspective of HT-PEMFCs

For fuel cells stably operating between 120 and 200 °C, the fragilities lie not so much in the basic chemistry of polybenzimidazole (PBI) as in the difficulty of retaining the proton carrier (phosphoric acid, H_3PO_4), dissipating cyclic thermal stresses and containing radical-induced degradation phenomena. The abandonment of fluorine has opened up scope for innovation in this area, but the urgency today is to perfect the technologies for the manufacture and internal handling of phosphoric acid without disrupting the existing polymer matrix. The most promising strategy in terms of the development and production of materials for HT-PEM has two converging avenues, which aim to make the membrane a hierarchical system capable of self-repairing and adapting to load variations. The first proposed avenue may be the multiscale confinement of phosphate by in situ growth of inorganic lattices [113] that imprison small portions of phosphoric acid without impeding proton transport. It has been shown that the use of these lattices improves mass losses even after a thousand hours at 200 °C, compared to untreated samples [114]. The second strategy concerns the production of nanofibers employing a coaxial electrospinning technique: by electrospinning an external dopant-

poor solution and a high acid core, hollow fibers are obtained that, once coupled together by hot pressing, generate preferential proton conduction channels. The orientation of the fibers during deposition aligns the ion transport pathways with the current gradient, significantly decreasing ohmic resistance by more than 15 % compared to homogeneous films [115]. These two lines of action, combined in an integrated process chain, have already led in pilot plants to an increase in cell life of more than 20000 hours, converging towards objectives of superior conductivity and durability and efficient thermochemical management of the proton carrier.

1.4 Poly(2,6-dimethyl-1,4-phenylene oxide): State of art

Poly(2,6-dimethyl-1,4-phenylene oxide), better known as PPO (polyphenylene oxide), is a thermoplastic heteroaromatic polymer known for its thermal, mechanical and chemical stability [116]. The repeating unit of this material consists of a benzene ring with two methyl substituents at positions 2 and 6, which is bonded to the next unit via oxygen bridges at positions para 1,4. From a historical point of view, the synthesis of PPO was developed in 1956 [117] by the chemist Allan S. Hay, who attempted to oxidatively couple 2,6-dimethylphenol (DMP) using air and cuprous chloride in pyridine at room temperature (Figure 1.3). The reaction quickly led to the formation of the polymer, and subsequent improvements in the catalyst (cuprous-amine complexes or other ligands, Cu-L) enabled the reaction to be made more efficient, with PPO first being produced in 1961.

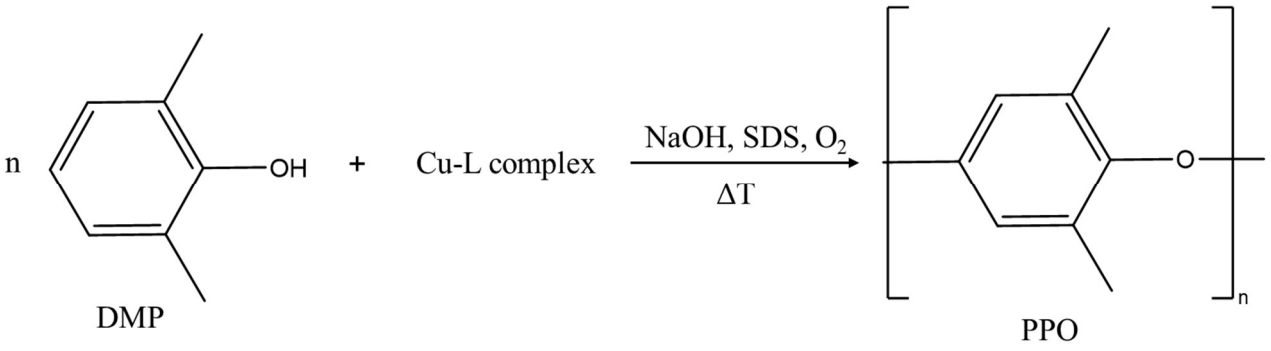

Figure 1.3 - Synthesis of PPO from the reaction between DMP (2,6-dimethylphenol) and cuprous-ligand complexes (Cu-L complexes) in a basic environment in the presence of sodium hydroxide (NaOH), sodium dodecyl sulfate (SDS) and oxygen (O_2)

Structurally, PPO is characterized by a high glass transition temperature (T_g ~ 210 °C), indicative of considerable rigidity dictated by the aromatic unit, and a high melting temperature (T_m ~ 270 °C),

which makes this polymer suitable for engineering applications [116]. In addition, it is an excellent electrical insulator with a dielectric constant D_k between 2.6-2.7 [118], which makes this material not very polarizable and stable over wide temperature and humidity ranges. In terms of chemical resistance, PPO benefits from its hydrophobic structure that makes the material inherently resistant to hydrolysis and degradation processes by acidic or basic solutions, especially when diluted [116]. Another interesting feature of PPO concerns its ability to exist not only in the amorphous phase but also in crystalline forms: this polymer can form ordered crystalline structures through co-crystallization treatments with host molecules [119]. In particular, the use of low-molecular-mass organic molecules, such as, for example, terpenes (limonene, carvone, anisole), allows the formation of helical crystalline structures [120] in which the low molecular mass "host"' molecule is included in the helical channels formed by the PPO. This class of polymeric materials is called "clathrates" [121]. In several cases, the co-crystalline phase formed can be "emptied", i.e. specially treated through extraction processes or substitution with volatile solvents, leaving the channels previously occupied by the guest empty [122]. This results in a new nanoporous crystalline (NC) phase, which, despite its lower density in respect to the starting amorphous phase (1.06 g cm^{-3} and 1.08 g cm^{-3}, respectively) is a metastable polymorph characterized by a good thermal stability.

From an application point of view, one of the most relevant features of PPO is the presence of methyl groups (CH_3) on the aromatic ring. These groups increase the solubility of the polymer, making PPO soluble in aromatic and/or chlorinated organic solvents [123], and activate the aromatic ring towards electrophilic substitution reactions [124]. Thus, despite its high chemical stability, PPO can be "easily" chemically functionalized through aromatic substitution reactions, typical of aromatic compound. In particular, PPO oxide can be subjected to sulfonation [125], nitration or halogenation reactions [126], introducing functional groups on the aromatic ring: this reactivity is of great interest, as it allows the properties of the polymer to be modified by making it hydrophilic or ionically conductive through the introduction of acid/basic groups, thus extending its field of application.

1.4.1 Electrochemical applications of Poly(2,6-dimethyl-1,4-phenyleneoxide)

The unique characteristics of PPO can be successfully exploited towards energy and electronic applications, for the production of advanced materials. In particular, the possibility of substituting various aromatic and/or benzyl positions in the polymer opens the door to the synthesis of ionically active and hydrophilic PPO-based materials [127]. For electrochemical applications, the most established strategy is the sulfonation of PPO at aromatic positions, which transforms the material into a proton exchange ionomer. Sulfonation involves the introduction of $-SO_3^-\ H^+-$ groups on the

aromatic rings of PPO in the para position to oxygen, corresponding to positions 3 and 5 of the starting ring (Figure 1.4).

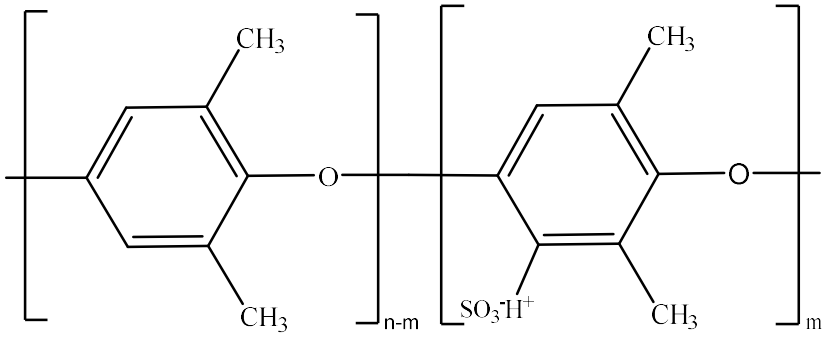

Figure 1.4 – Chemical structure of sulfonated poly(phenylene oxide) (sPPO). The polymer backbone consists of repeating aromatic ether units with variable degrees of sulfonation, where –SO_3H groups are grafted onto the phenyl rings. The sulfonic acid functionalities introduce proton-conducting sites, enabling ion exchange and hydrophilic channel formation within the otherwise hydrophobic aromatic matrix.

This electrophilic substitution can be conducted through the use of different sulfonating agents: a common method is to treat the powdered material with concentrated sulphuric acid (H_2SO_4) or chlorosulfonic acid ($ClSO_3H$) in aprotic organic solvents [124]. Depending on the reaction conditions and the concentration of the sulfonating agents, different sulfonation degrees (SD) and ion exchange capacities (IEC) can be achieved. Alternatively, solid-state approaches are possible, i.e. treatments in which an already cast PPO film is immersed in a sulfonating reagent such as, for example, acylsulphates or oleum (H_2SO_4-SO_3) at different times [125]. This last approach allows to fine tune the degree of sulfonation of the material by changing the time of immersion in the sulfonating solution while preserving the film mechanical and morphological integrity since relatively high degrees of sulfonation can be obtained while avoiding chain-scission or excessive swelling that often occur in homogeneous liquid reactions.

Preliminary studies have already demonstrated that sulfonated PPO (sPPO) exhibits good ionic conductivity, with fair proton conductivities (> 0.05 mS cm^{-1}) and low permeability to hydrogen and oxygen. However, a crucial issue concerns the management of water and the mechanical stability of the material, since excessive sulfonation degrees (SD) enhance ion exchange but also lead to higher membrane swelling and, consequently, reduced resilience under operating conditions. Despite these promising features, only a limited number of studies have addressed the full electrochemical description of sulfonated PPO. Most of the available works investigate sPPO as a component in

blends or copolymers rather than as a standalone material. As a result, a comprehensive understanding of the intrinsic electrochemical behavior of sPPO remains largely absent in the current literature.

Beside sulfonation, in this thesis PPO has been functionalized also with other chemical moieties - useful for electrochemical applications; in particular, an effective nitration and amination procedure has been developed to give the polymer basic Lewis-Bronsted properties allowing the material to interact with strong acids or to be further modified by forming ammonium sites [128]. Specifically, the range of applications would cover: HT-PEM applications, as the aminated PPO can act as a basic polymer that binds phosphoric acid in a similar way to polybenzimidazole. This would allow the formation of NH_3^+ groups counterbalanced by $H_2PO_4^-$ anions, creating an acid-containing polymeric lattice. This aspect is extremely important as it would open the door to a new field of application for this polymer, making it suitable for the reaction of conductive membranes at 150-180 °C under anhydrous conditions. Alternatively, aminated PPO can serve as a valuable component for the formulation of polymer blends with other amine- or imidazole-based polymeric materials (e.g., PBI), ensuring excellent phosphoric acid retention and good membrane durability over time. Beyond these applications, PPO amination also represents a particularly promising route for the development of ionically conductive materials in alkaline electrolysis (AEM-WE). Starting from aminated PPO, quaternization reactions can be carried out using alkylating agents such as methyl iodide (CH_3I), converting the amine groups into quaternary ammonium salts and thereby introducing fixed positive charges capable of conducting hydroxide ions. This chemical pathway provides a rational and versatile strategy for tuning both ionic conductivity and chemical stability in alkaline environments.

Despite this potential, the number of studies focusing specifically on aminated and quaternized PPO for electrochemical applications remains remarkably limited. Most of the existing works only address PPO derivatives as secondary components within polymer blends or copolymers, often without a comprehensive assessment of their intrinsic electrochemical and physicochemical behavior. As a result, the systematic investigation of PPO as a stand-alone polymer platform for both protonic and anionic conduction is still an open research field.

The present doctoral work aims to fill this gap by providing a detailed study of the synthesis, structural modification, and electrochemical characterization of functionalized PPO membranes. Through this approach, PPO is explored not merely as a passive matrix, but as an adaptable and chemically robust backbone that can be tailored to different electrochemical environments. This contributes to a broader understanding of PPO-based systems and reinforces the concept of PPO as a genuinely “multi-purpose” polymer platform for next-generation energy conversion and storage devices.

1.5 Polybenzimidazoles (PBIs): State of art

Polybenzimidazoles (PBIs) constitute a family of high-performance heterocyclic polymers whose history began in 1961, when Vogel and Marvel synthesized the first aromatic specimen, revealing an excellent thermal and oxidative stability that immediately aroused the interest of NASA and the US Department of Defence for aerospace applications. Structurally, all PBIs share the presence of a benzimidazole unit, formed by the condensation of a benzene ring and an imidazole ring sharing two atoms (nitrogen and carbon) in the backbone [101]. PBIs are therefore highly aromatic and planar polymers, characterized by strong intermolecular bonds (H-bond or π-π) that reflect their high chemical, thermal and mechanical properties.

The most industrially relevant and representative polymer of this family is poly(2,2'-(m-phenylene)-5,5' bibenzimidazole), better known as *m*-PBI, characterized by a glass transition temperature of 425-435 °C and a degradation temperature of about 600 °C [129]. Synthetically, the most general route involves the polycondensation of aromatic bis or diamines with, typically, dicarboxylic acids (DCAs). Several synthesis protocols for *m*-PBI exist to date, but the most commonly adopted is the single-stage process, which allows the reaction of 3,3′,4,4′ tetra aminobiphenyl (TAB) with isophthalic acid (IPA) at high temperatures [129]: this results in a shorter reaction cycle, with only water as a by-product, but requires a careful choice of catalyst ($SnCl_2$, phosphoric compounds or ammonium salts) to ensure high molecular weights (Fig. 1.3). The properties of PBIs reflect the stiffness of the backbone and the density of interchain hydrogen bonds: mechanically, the resin exhibits a tensile modulus of about 5.7 GPa, a compressive strength of almost 400 MPa and essentially rigid elastic behaviour with an elongation at break of about 2 %). Chemical stability is equally remarkable, a quality that makes PBI-based materials suitable for continuous operating temperatures over 200 °C under rigid humidity conditions.

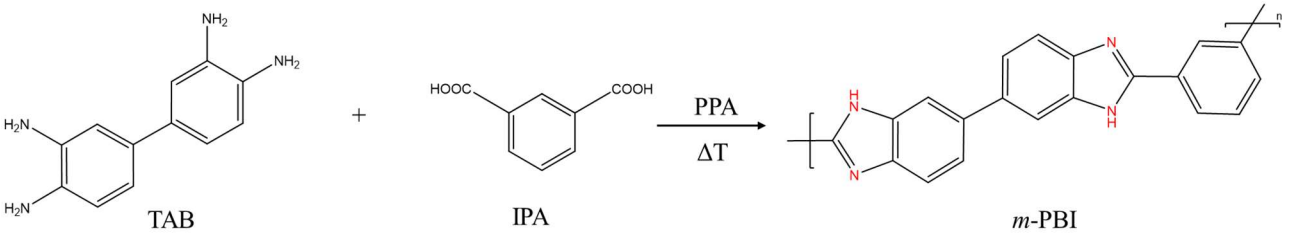

Figure 1.3 – Scheme for the synthesis of *m*-PBI: polycondensation reaction between 3,3',4,4'-tetraminobiphenyl (TAB) and isophthalic acid (IPA) in an acidic environment (PPA, polyphosphoric acid) and under controlled temperature [129].

PBIs are insoluble or poorly soluble in almost all major organic solvents, but, depending on the nature of the starting dicarboxylic acid (DCAs), it exhibits good solubility in high-boiling polar aprotic solvents such as N,N-dimethylacetamide (DMAc), dimethyl sulfoxide (DMSO) and N-methyl-2-pyrrolidone (NMP). Over the past decade, PBIs have been widely studied and used for fuel cell applications due to their ability to interact with strong acids due to the presence of the nitrogen groups present in imidazole. For this reason, PBI membranes are generally "doped", i.e. specially treated with appropriate organic and/or inorganic species to overcome all the listed problems [130]. The impregnation of PBI with phosphoric acid (PA) is, to date, the technique mainly used for HT-PEMFCs as it makes the material ductile and highly conductive [131], even at temperatures above 100°C and thus in the absence of water. In particular, it was seen that for the production of conductive proton exchange membranes, the highest conductivity values were achieved by impregnation with the following inorganic acids in order:

$H_2SO_4 > H_3PO_4 > HClO_4 > HNO_3 > HCl$.

Although sulphuric acid (H_2SO_4) is the most conductive [99], it necessarily requires a high water content for proper operation, with the need for a humidification of more than 50%, preventing its use at high temperature (it can be used for LT-PEMs). In contrast, PBI membranes impregnated with phosphoric acid can work in anhydrous conditions, showing overall better electrochemical performance than PEMs working at low temperature. For these systems, the proton conductivity can be attributed to a particular proton hopping mechanism involving the N-H sites bound to the imidazole group and the acid sites from the acid impregnation [132]. The conductive mechanism is not only limited to the acid-base interaction described so far, but also by the presence of "free" acid molecules in the form of $H_2PO_4^-$ /HPO_4^{2-} anions, which further increase the conductivity of the entire system [133]. The proton leap described is a mixed mechanism between a proton exchange that is generated between the phosphoric acid molecules and the PBI (Grotthuss mechanism), and a carrier mechanism ensured by the presence of free acid molecules on the membrane surface.

1.5.1 Electrochemical applications of PBIs

Today's cutting-edge applications mainly concern polymer electrolyte membranes (PEM) operating in the 150-200 °C range (HT-PEMs): treatment of PBI with phosphoric acid ensures stable proton conductivity in the absence of hydration with increased tolerance to pollutants [18] such as carbon monoxide, a notoriously critical problem for low-temperature fuel cells. It should be emphasized that

the amount of acid present on the membranes plays a key role in membrane performance: acid penetrates the polymer matrix and binds to the basic N-H sites of benzimidazole. Acid content is often identified through parameters such as the ADL (Acid Doping Level), which identifies the number of moles of H_3PO_4 per repetitive unit of PBI. From an electrochemical point of view, acid treatment is necessary because undoped PBI has a conductivity of less than 10^{-3} S/cm at room temperature, which can increase to 0.1 S/cm at around 150 °C with a high phosphoric acid load [18]. However, this doping treatment significantly weakens the membrane, which is why improved solutions involving new synthesis methods have been developed. In particular, a synthesis process called the "PPA Process" [101] was developed, in which it is possible to obtain PBI membranes with a high degree of doping, thanks to the reaction between PBI monomers (TAB and IPA) in polyphosphoric acid (PPA), which acts as both solvent and dehydrating agent for the polycondensation mechanism. In this case, a gel is formed, which can be cast or extruded in film form and subsequently treated in water: the water enables the hydrolysis of PPA into H_3PO_4, which is thus directly present in the polymer matrix in an amount of 40-50 % wt. This ensures high and stable doping with superior mechanical modulus when compared to the counterpart immersed in phosphoric acid. These types of membranes, which form the basis of today's commercial materials (BASF/Advent Celtec P1000), have shown conductivities of up to 0.3 S/cm at 160 °C [97], far exceeding the benchmarks on the fuel cell market to date. However, the main problem is the acid leaching of these membranes, which compromises their electrochemical performance and mechanical stability. PBI research continues to explore new compromises and new doping protocols with less volatile acids such as phosphonic acid or new ionic liquids. Another alternative may be the use of polymeric blends or mixtures between acids and bases capable of forming stable complexes, in which the acid is bound as a salt, reducing its mobility and thus the leaching phenomenon. Furthermore, recent advances in the field of materials manufacturing are enabling the production of new PBI-based membranes through innovative techniques such as electrospinning. Fibrous morphology can further improve the water retention capacity and mechanical properties of membranes by developing, in this way, composite materials for HT-PEM applications that hopefully offer high proton conductivity and good durability under operating conditions.

1.6 Outline of the thesis

The overall aim of this doctoral thesis is to develop a new generation of non-fluorinated polymer electrolytes for hydrogen-fueled fuel cells, providing a concrete contribution to the global transition away from traditional perfluoro-sulfonated membranes (PFAS). Although perfluorinated ionomers such as Nafion® have set the benchmark for proton conductivity and chemical stability, they are now under increasing regulatory and environmental scrutiny due to their persistence, bioaccumulation potential, and high manufacturing costs. Against this background, the search for sustainable and economically viable polymeric electrolytes that can combine high ionic conductivity, chemical robustness, and long-term durability has become a key scientific challenge.

The innovative approach adopted in this work is based on the chemical and morphological transformation of commercially available polymers, in particular poly(2,6-dimethyl-1,4-phenylene oxide) (PPO) and *m*-polybenzimidazole (*m*-PBI), into high-performance ion-conducting materials. Instead of relying on complex synthetic routes or exotic monomers, this research demonstrates that well-known engineering polymers, if intelligently modified and re-engineered, can rival or even outperform traditional fluorinated materials. This strategy guarantees both scalability and sustainability, while opening a new pathway in the design of functional membranes for fuel cells and related electrochemical devices.

In Chapter IV, the thesis explores the development of dense sulfonated PPO (sPPO) membranes obtained through solution/blade casting from optimized formulations in aprotic solvents. PPO was selected as a base polymer due to its high glass transition temperature, mechanical strength, and oxidative stability, all of which are crucial for durability under fuel cell operating conditions. The novelty of this study lies in the solid-state sulfonation process, where the degree of sulfonation (SD) was precisely modulated by adjusting immersion times and reagent concentrations. This systematic control made it possible to tune the ion-exchange capacity (IEC) and the water management properties of the membrane, minimizing excessive swelling while preserving excellent proton conductivity, in some cases approaching that of Nafion®. While several studies have reported on the synthesis of sPPO, the number of works providing a comprehensive electrochemical evaluation of the material remains extremely limited, especially when sPPO is used as a stand-alone polymer rather than as part of a blend or copolymer. This thesis therefore fills a significant gap in the current literature. Beyond the synthesis and chemical characterization, performed through FTIR/ATR, WAXD, NMR, and TGA, complete membrane–electrode assemblies (MEAs) were fabricated using the optimized sPPO membranes and tested in single-cell fuel cell configurations. This step represents

one of the most distinctive and innovative aspects of the work. By validating the membranes directly in operational fuel cell setups, it was possible to correlate processing parameters, chemical structure, and real electrochemical performance. This experimental approach, rarely found in PPO-based research, transforms what is often a purely materials-science study into a full device-level investigation, bridging fundamental chemistry with applied electrochemistry.

Building on these results, Chapter V focuses on the morphological engineering of polymer membranes through the fabrication of electrospun *m*-polybenzimidazole (*m*-PBI) mats. Electrospinning was selected as a powerful tool to create fibrous structures with high specific surface area, controlled fiber diameter, and tailored porosity, features that can dramatically influence ionic conductivity and acid retention in high-temperature proton exchange membranes (HT-PEM). Although *m*-PBI is a well-known polymer for phosphoric-acid-doped fuel cells, the application of electrospinning to this material has remained relatively unexplored. In this thesis, the process was optimized using Design of Experiments (DoE) and Analysis of Variance (ANOVA) methodologies, allowing a systematic correlation between operational variables (solution concentration, applied voltage, flow rate, and collector distance) and resulting morphology, mechanical stability, and electrochemical response. A custom phosphoric acid impregnation protocol was specifically developed for these electrospun structures, taking into account their open morphology and high surface area. This ad-hoc treatment enhanced acid retention capacity, proton conductivity, and mechanical resilience, demonstrating that morphological design can be as impactful as chemical functionalization in improving membrane performance. Crucially, as with sPPO, the electrospun *m*-PBI membranes were assembled into MEAs and tested in single fuel cell setups, enabling a direct evaluation of in-cell conductivity, ohmic resistance, and long-term stability. The successful operation of these electrospun membranes in a real fuel cell environment represents a major outcome of this work and provides valuable insights into how fiber morphology and processing conditions influence overall cell efficiency.

Finally, Chapter VI extends the exploration of PPO chemistry towards a different class of electrochemical systems by introducing aminated PPO (aPPO). Through controlled amination reactions, amine functionalities were grafted onto the PPO backbone, creating an amphoteric matrix capable of interacting with both acidic and basic environments. This functionalization opens two complementary pathways. On one hand, aPPO can coordinate phosphoric acid molecules, behaving as a proton-conducting ionomer suitable for high-temperature PEM applications; on the other hand, by performing quaternization reactions with alkylating agents such as methyl iodide (CH_3I), the

polymer can be converted into a quaternary ammonium salt, thereby enabling hydroxide-ion conduction for alkaline electrolysis (AEM-WE).

This dual functionality is rarely discussed in the literature and highlights the exceptional versatility of the PPO backbone. Most previous studies have considered sulfonated and aminated polymers as distinct material families, each optimized for a single purpose. In contrast, this thesis proposes a unified concept of PPO as a multi-purpose polymer platform that can be chemically tuned to meet the requirements of different electrochemical technologies. This idea not only expands the design space for membrane materials but also underscores the potential for cost-effective, scalable production of multifunctional electrolytes.

Across all systems, sulfonated PPO, electrospun *m*-PBI, and aminated PPO, the research integrates multi-scale characterization, chemical analysis, and in-cell electrochemical testing. Techniques such as FTIR/ATR, WAXRD, NMR, and TGA were combined with single-cell performance assessments to establish clear correlations between synthesis conditions (degree of sulfonation or amination, electrospinning parameters, acid loading) and key functional properties (ionic conductivity, ion-transfer resistance, cell efficiency, and stability). This comprehensive methodology ensures that every stage of the research, from molecular design to device validation, contributes to a coherent understanding of structure–property–performance relationships.

In summary, this doctoral work demonstrates that true innovation in the field of polymer electrolytes does not necessarily require entirely new materials, but rather a deep and strategic re-engineering of existing ones. By transforming common, low-cost polymers into high-performance functional membranes, this research presents an integrated and scalable approach to material development that aligns with current sustainability goals and the global drive toward decarbonization. The combination of chemical modification, morphological control, and full electrochemical validation in real MEA configurations distinguishes this thesis from much of the existing literature and establishes a solid foundation for future non-fluorinated membrane technologies in both protonic and anionic fuel cell systems.

CHAPTER II – MATERIALS AND METHODS

2.1 Sulfonated Poly(2,6-dimethyl-1,4-phenylene oxide)

2.1.1 Materials

The poly(2,6-dimethyl-1,4-phenylene oxide) (PPO) used in this thesis work is supplied by Sabic (The Netherlands , grade P6130, M_w: 350 000 g/mol). The obtainment of the PPO films is carried out from a 15 % wt. solution in chloroform ($CHCl_3$, ≥ 99.8%, Sigma Aldrich). The subsequent sulfonation process is conducted in the solid state, using a reactive system consisting of lauric acid ($C_{12}H_{24}O_2$, ≥ 98%, Sigma Aldrich), chlorosulfonic acid ($ClSO_3H$, ≥ 99%, Sigma Aldrich), and cyclohexane (C_6H_{12}, ≥ 99.5%, Honeywell) as solvent. This method achieves a well-controlled functionalization of the PPO, thereby reducing the risk of chain degradation and preserving the material's mechanical properties. After an appropriate treatment period, the sulfonated polymer (sPPO) is washed repeatedly with ethanol (C_2H_6O, ≥ 99.5 %, Sigma Aldrich) and acetone (C_3H_6O, ≥ 99.5%, VWR Chemicals) to remove acidic, organic residues and by-products.

Preliminary Ion Exchange Capacity (IEC) tests were performed using diluted solutions of hydrochloric acid (HCl, 37%, Sigma-Aldrich), sodium chloride (NaCl, ≥ 99.5%, Sigma-Aldrich), and sodium hydroxide (NaOH, ≥ 98%, VWR Chemicals) for acid–base titration, with phenolphthalein ($C_{20}H_{14}O_4$, ≥ 99%, Sigma Aldrich) used as indicator. The fabrication of the MEAs was carried out using Pt/C catalyst powder (40 wt%, Tanaka, Japan), deionized water, isopropanol (C_3H_8O, IPA, ≥ 99.7%, Sigma-Aldrich), and a Nafion® ionomer solution (5% wt. in hydroalcoholic solution, Sigma-Aldrich), according to the catalyst-coated membrane (CCM) approach. MEA assembly into the single-cell setup (Fuel Cell Technologies, US) was conducted using Sigracet 22BB gas diffusion layers (GDLs) (SGL Carbon, carbon paper, thickness ~235 µm) that were applied on both sides of the MEA to ensure uniform reactant gas distribution and mechanical support during testing. In order to compare the electrochemical performances, different Nafion® 212-based (Chemours, US) MEAs were produced following the same fabrication steps and testing protocols.

2.1.2 Preparation of PPO films

Neat PPO films were prepared from a 15 % wt. solution in chloroform after optimization trials in collaboration with the University of Naples Federico II (Department of Chemical Sciences). This solution was deposited on a glass substrate by the blade casting technique using an automated Doctor Blade film coating machine (MTI Corporation, model EQ-Se-KTQ-150). To this aim, the polymer solution is poured into a chamber terminated by a blade at a variable height in respect to a fixed flat substrate. The blade runs parallel to the substrate for a well-defined length that is a function of the amount of polymer solution introduced and, of its viscosity. A vacuum system facilitates the adhesion of the film to the substrate and reduces the formation of air bubbles or surface defects during film coating. The production of PPO films was conducted through a systematic study on the variation of blade height to optimize the final thickness of the membrane, while keeping the concentration of the polymer solution constant. Several membrane thicknesses were prepared and evaluated in terms of film uniformity, mechanical stability, and ease of handling. Based on these observations, a thickness of approximately 50 μm was chosen as a representative value for further investigation.. After deposition, the films were allowed to dry at room temperature under a fume hood and then placed in a vacuum oven at 40 °C for at least 12 hours, in order to completely remove the residual solvent and stabilize the film structure before their use in subsequent steps.

2.1.3 Solid-state sulfonation of PPO

The sulfonation of the PPO polymer films was conducted using a solid-state protocol: the dry PPO films were first immersed in cyclohexane for at least 24 hours at room temperature, in order to favor the absorption and diffusion of the sulfonating agent into the polymer matrix thank to the plasticizing effect of cyclohexane. Then, the membranes were removed from the cyclohexane bath and immediately transferred into a reactive sulfonating solution of acyl sulphate (20% by volume) in cyclohexane. The acyl sulphate was prepared by the reaction between lauric acid and chlorosulfonic acid (molar ratio 1:1.6), under magnetic stirring for 24 hours at room temperature, in an anhydrous environment and an inert atmosphere (N_2), within a closed and controlled system.

The PPO membranes were kept in the sulfonating bath maintained at 40 °C, in a closed system to avoid solvent evaporation and external contamination. The sulfonation reaction was conducted for different time (3, 4 and 5 hours) to obtain films with different sulfonation degrees (SD). At the end of each treatment, the membranes were removed from the bath, washed thoroughly with ethanol and acetone, and left to dry under a fume hood for at least 12 hours. The resulting polymeric material was

subsequently characterized through spectroscopic and thermal techniques, including ATR/FTIR, TGA and WAXD analyses, in order to verify the success of the functionalization process, and finally stored in sealed glass containers at room temperature. The solid-state sulfonation process is described in Scheme 2.1.

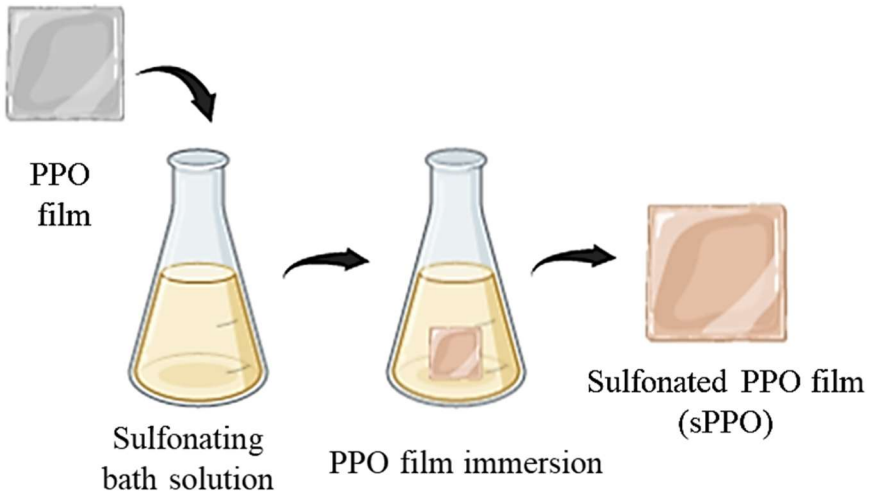

Scheme 2.1 - Schematic representation of the solid-state sulfonation process applied to PPO films. The pristine PPO film, obtained through casting from an aprotic solvent, is immersed in the sulfonation bath, leading to the formation of the sulfonated PPO (sPPO) membrane after controlled reaction and washing steps.

2.1.4 sPPO Ion Exchange Capacity and Water Uptake

Sulfonated poly(2,6-dimethyl-1,4-phenylene oxide) (sPPO) membranes were characterized in order to assess the effectiveness of the functionalization process by evaluating their *Ion Exchange Capacity* (IEC) and *Water Uptake* (WU), two parameters that are directly related to the SD of the membrane and, therefore, to the membrane's ability to absorb water and transport protons. IEC reflects the concentration of sulfonic groups ($-SO_3H$) attached to the polymer backbone, as these functional groups are responsible for the material's ability to exchange ions. In this study, the IEC was quantitatively determined through an acid-base titration procedure, in which the protons released from the sulfonic groups were neutralized by a standardized basic solution. The measured titration data were then used to calculate the IEC, expressed as milliequivalents of acid sites per gram of dry polymer. The dried membranes were carefully weighed and then were immersed in a 1M hydrochloric acid solution for 24h. Subsequently, the membranes were washed with distilled water to remove all traces of acid and then immersed in a 1 M sodium chloride solution, promoting the exchange of H^+ ions with Na^+. The acid released in solution was then titrated with 0.01 M sodium hydroxide aqueous

solution in the presence of phenolphthalein as an indicator. The IEC value (in meq/g) was calculated using the following Equation 2.1:

$$IEC = \frac{V_{NaOH} \cdot C_{NaOH}}{m_0} \quad \text{Eq. 2.1}$$

where V_{NaOH} is the volume of titrant used (in millilitres), C_{NaOH} is its concentration (mol/L) and m_0 the mass of the dry membrane (g).

The water uptake (WU) of the membranes was evaluated by comparing their hydrated and dry masses. To this end, the samples were first completely dried to obtain their dry mass (m_{Dry}) and then immersed in distilled water at room temperature for 24 hours to allow a full hydration. After immersion, the membranes were carefully removed, gently blotted with filter paper to remove excess surface water, and immediately weighed to determine the wet mass (m_{Wet}). The water uptake was then calculated using Eq. 2.2:

$$WU\ (\%) = \frac{m_{Wet} - m_{Dry}}{m_{Dry}} \quad \text{Eq. 2.2}$$

This parameter provides insight into the membrane's hydrophilicity and its ability to retain water, which are key factors influencing proton conductivity and mechanical stability under operating conditions.

2.1.5 Membrane-Electrode Assembly (MEA) Fabrication

The manufacture and electrochemical testing of the sPPO-based membrane-electrode-assemblies (MEAs) were conducted as part of a scientific collaboration with the laboratories of the KTH-Royal Institute of Technology in Stockholm, at the Department of Chemical Engineering (Applied Electrochemistry Section) under the supervision of Prof. Rakel Wreland Linström.

The overall performance of the proton exchange membrane fuel cell (PEMFC) system depends not only on the membrane's properties, but also on the quality of the electrodes and, critically, on the characteristics of the membrane-electrode interface. For this reason, MEAs incorporating the developed sPPO membranes were fabricated using the Catalyst-Coated Membrane (CCM) method. In this approach, a catalytic ink is directly applied onto the membrane surface, promoting the formation of a compact, well-adhered interface and ensuring a uniform of the catalyst across the active area.

The ink preparation procedure is shown in Scheme 2.2. A defined amount of Pt/C catalyst (40 wt% Pt) was dispersed in a water/isopropanol (1:1 w/w), to which a Nafion® solution was added as the ionomer, ensuring a ionomer-to-catalyst (I/C) weight ratio of 0.3. The resulting suspension was sonicated in an ice bath for 1 hour to promote homogeneous dispersion of the catalyst particles and prevent overheating, followed by a magnetic stirring for an additional 30 minutes. The prepared ink was then deposited onto 4 cm^2 of sPPO membrane using an automatic ultrasonic spray coater (Sonotek Exacta Coat, USA), achieving a platinum loading of 0.4 mg_{Pt} cm^{-2}. The deposition was performed under vacuum and at 80 °C to facilitate rapid solvent evaporation and enhance catalyst adhesion to the membrane surface.

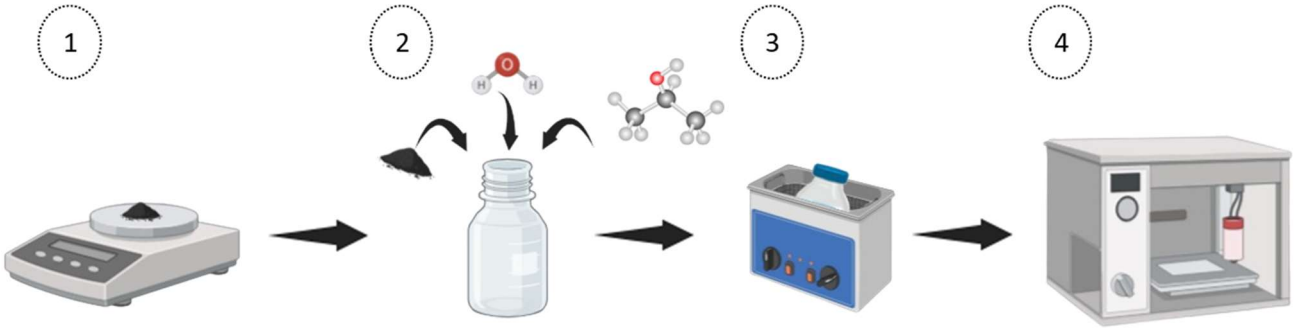

Scheme 2.2 – Steps in the preparation and deposition of the catalytic ink for MEA fabrication: (1) Weighing the required amount of Pt/C catalyst (40 wt% Pt); (2) Preparing the ink in a water/isopropanol mixture with addition of a Nafion®-based ionomer (I/C = 0.3); (3) Sonication of the electrocatalyst suspension in an ice bath; (4) Ultrasonic spray deposition of the ink directly onto the membrane surface using an automated coater.

2.1.6 Fuel Cell Setup and Testing

The MEAs obtained by spray deposition were assembled into single-cell fuel cells (Figure 2.1a), equipped with custom-designed bipolar graphite plates featuring a spiral flow-field geometry and a geometric active area of 2.55 cm^2, developed in-house at the KTH laboratories (Figure 2.1b). To ensure uniform distribution of the reactant gases across the electrode surfaces, gas diffusion layers (GDLs) were placed on both the anode and cathode sides of the MEA (Figure 2.1c). The cell assembly was completed by carefully aligning the GDLs and compressing the stack with a torque of 5 N·m. This torque value was selected to guarantee optimal electrical contact between the electrodes and the bipolar plates while preventing mechanical damage or deformation of the membrane. Electrochemical characterization was performed on the central active area (0.95 cm^2, “button cell” configuration), which is particularly suitable for prototype tests and electrochemical screening.

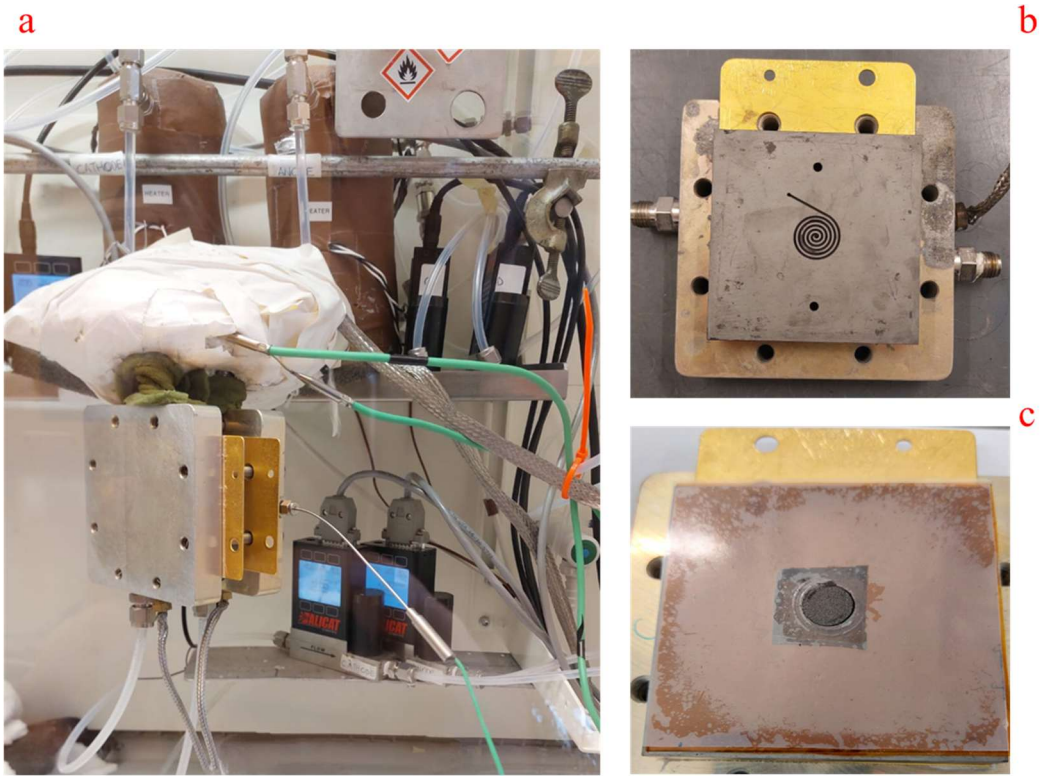

Figure 2.1 – Single-cell fuel cell setup used for electrochemical testing of sPPO-based membranes: (a) assembled single-cell configuration, (b) spiral graphite bipolar plate design, and (c) sPPO-based MEA with gasket and GDLs.

Electrochemical tests were carried out using a Gamry 5000E Potentiostat (Gamry Instruments, US), according to an in-house developed experimental protocol (Table 2.1). The protocol combined several complementary electrochemical techniques, including polarization curve (PC) measurements, Potentiostatic electrochemical impedance spectroscopy (PEIS), cyclic voltammetry (CV), linear sweep voltammetry (LSV), chronoamperometry (ChronoA), and open-circuit voltage (OCV) monitoring. Measurements were initially performed at 30 °C under fully humidified conditions to establish baseline performance, followed by tests at 80 °C under two controlled relative humidity levels (70% and 90%). This approach enabled a comprehensive assessment of the electrochemical performance, proton transport resistance, and gas crossover behavior of the membranes. For benchmarking, additional MEAs were prepared and tested using commercial Nafion® 212 membranes, following the same fabrication and testing protocols. This comparison provided a direct and objective evaluation of the performance of the sPPO-based membranes relative to an established commercial standard. Among the sPPO membranes, only those exhibiting distinct ion exchange capacity (IEC) values, correlated with significant differences in ionic conductivity, were selected for fuel cell testing.

Temperature [°C]	Relative Humidity [%]	Gases	Treatment	Characterization
80	90	H_2 (A) ; N_2 (C)	Pre-testing	CV, LSV, PEIS
80	90	H_2 (A) ; O_2 (C)	Testing	OCV, PC, PEIS
80	90	H_2 (A) ; O_2 (C)	Durability	ChronoA

Table 2.1 – Experimental protocol used for testing MEAs based on sPPO and Nafion® 212: CV, Cyclic Voltammetry; LSV, Linear Sweep Voltammetry; PEIS, Potentiostatic Electrochemical Impedance Spectroscopy; PC, Polarization Curves; ChronoA, Chrono Amperometry; OCV, Open Circuit Voltage.

2.2 *m*-Polybenzimidazole Membranes

2.2.1 Materials

A commercial *m*-polybenzimidazole (*m*-PBI) solution, designated as S26 and supplied by PBI Performance Products Inc. (Charlotte, NC, USA), was used for the fabrication of membranes via both electrospinning and solution casting techniques. The S26 formulation is a concentrated solution containing 26 % wt *m*-PBI dissolved in N,N-dimethylacetamide (DMAc), with lithium chloride (LiCl) added to enhance both solution stability and ionic conductivity. The polymer has an average molecular weight (M_w) of 27000-30000 g/mol, a polydispersity index (PDI) > 2, and a viscosity approximately 2200 Poise, making it not suitable for processing into nanofibrous or dense membrane structures. for this reason, N,N-dimethylacetamide (DMAc, ≥ 99.5 %, Sigma-Aldrich) was used to dilute the stock S26 solution to achieve the appropriate viscosity required for electrospinning.. For the subsequent acid doping , phosphoric acid (H_3PO_4, 85 %, Sigma-Aldrich) was used after being diluted to specific concentrations in deionized water. This step facilitated controlled interaction between the acid and the PBI matrix, promoting protonation without compromising the integrity of the fibrous network.. Finally, methanol (≥ 99.8%, Sigma-Aldrich) was used as the washing solvent during the evaluation of acid doping stability, enabling the removal of unbound or weakly associated phosphoric acid species from the membrane structure.

2.2.2 Membrane Production: Solution Casting

The solution casting technique is a well-established method for producing polymeric membranes with a dense morphology, based on the controlled casting of a polymer solution onto a substrate, followed by the gradual evaporation of the solvent. This approach yields films with homogeneous thicknesses and good structural cohesion and is a particularly suitable technique for comparative studies and applications requiring low porosity values.

In the present work, solution casting was applied to the production of dense membranes based on *m*-PBI, which were used as a reference concerning membranes obtained by electrospinning, in particular for the analysis of morphological, microstructural and impregnation differences in phosphoric acid. The membranes were made from a 16 % wt. solution of m PBI in N,N dimethylacetamide. The polymer solution was cast into glass Petri dishes, resulting in films with a uniform thickness of approximately 50 μm following solvent evaporation that was conducted at 60 °C and followed by drying in a vacuum oven at 100 °C for 24 h, in order to completely remove the residual DMAc and consolidate the membrane structure.

2.2.3 Membrane Production: Electrospinning

Electrospinning is a versatile and established technique for the production of continuous nanofibers with diameters ranging from a few tens of nanometers to a few micrometers. This process is based on the application of a high-voltage electric field to a polymer solution, which, as it overcomes the surface tension, forms a stable jet that is progressively stretched and thinned to generate solid fibers, once the solvent has evaporated. A typical electrospinning setup (Figure 2.2) comprises a high-voltage power supply (DC or AC), a syringe pump for controlled extrusion of the solution, a conductive needle (usually blunt) and a static or rotating metal manifold. The droplet formed at the end of the needle is electrified and deformed into a Taylor cone, from which the polymer jet starts. The jet, initially straight, undergoes bending instabilities and stretches to deposit as solid fibers on the manifold.

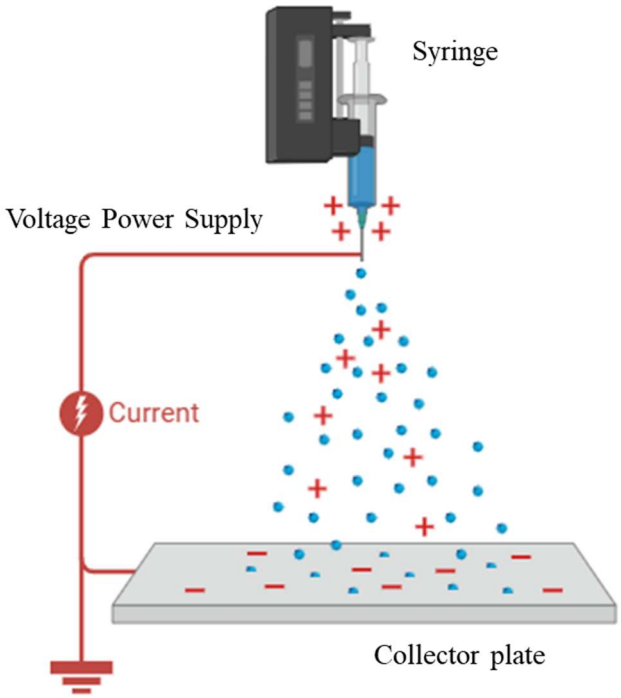

Figure 2.2 - Schematic representation of the electrospinning setup. A high-voltage power supply induces a strong electric field between the syringe needle and the grounded collector plate, causing the polymer solution to be ejected from the syringe tip as a charged jet that elongates and solidifies into nanofibers upon deposition on the collector.

The Electrospun PBI membranes were fabricated in collaboration with ENEA (Italian Agency for Energy) and Nanofaber s.r.l. laboratories (Rome, Italy), using pilot-scale electrospinning equipment (Fluidnatek LE100, Bioinicia SL, Valencia, Spain), equipped with a static collector, measuring 40 cm × 40 cm (A6 Sheet). The system is also equipped with an Environmental Control Unit (ECU) capable of controlling temperature with an accuracy of ±1 °C and relative humidity with a maximum error of 5%. Initial electrospinning tests were carried out using a 15% wt. PBI solution in order to identify the environmental and process conditions required to obtain a well-defined fibrous structure. Subsequent analyses revealed a strong dependence of the fiber structure on temperature and humidity, and showed that a stable cast is only formed when a certain threshold of electrical voltage and flow rate is exceeded. From these conditions, the optimal values of temperature, humidity and applied collector voltage were kept fixed, and a rationalization of the experimental plan was adopted using a 2^k factorial DOE (Design Of Experiments) approach with $k = 4$ to systematically investigate the influence of the main process parameters.

Design of Experiment (DOE) is a rational and systematic approach used to determine the relationship between the factors (X_i) influencing a process and the responses generated by it (Y_i). Linear regression models describe the dependence of each output variable (Y) on the process variables (X). The general form of the regression model is described by the following equation (Eq. 2.3) in the case of four regressors:

$$Y = \alpha_0 + \alpha_i x_i + \alpha_{ij} x_i x_j + \alpha_{ijk} x_i x_j x_k + \alpha_{ijkm} x_i x_j x_k x_m \rightarrow \quad (i, j, k, m = 1 \text{ to } 4) \qquad \text{Eq. 2.3}$$

The primary objective of this approach is to identify the optimal descriptive model using a limited number of parameters and experiments, which can be directly and reproducibly applied to produce materials with desired chemical-physical properties, in accordance with the employment application. In DOE analysis, regression models play a central role, as they allow the effect of different factors and the interactions of the response variable to be quantified. Each membrane was manufactured from a specific combination of X_i operating parameters, selected according to a complete factorial approach 2^4, provided for in the DOE experimental plan, to study the influence of four process parameters on the microstructural properties of the membranes. In the adopted experimental models, the process factors were treated in coded form, assuming the values +1, 0 and -1 to represent the high, middle and low values (levels) of each parameter, respectively. This coding allowed an easier statistical interpretation of the results and a normalization of the data within the regression model, the processing and analysis of which was carried out using JMP® software (SAS Institute Inc.). More details on the electrospinning parameters and statistical description of the DOE models can be found in **Paper I**.

2.2.4 Calendering treatment of electrospun membranes

Electrospun membranes are intrinsically porous, so permeable to gases. To enhance the suitability of electrospun membranes for operation in high-temperature fuel cells, a calendering post-treatment was implemented in addition to the optimization of electrospinning parameters. This process involves passing the membranes through a pair of heated rollers that compress and flatten the fibrous structure, with the goal of improving their mechanical strength, dimensional stability, and microstructural uniformity. Prior to calendering, the thickness of each electrospun *m*-PBI membrane was measured at 50 different points using a digital micrometer to determine the initial thickness (IT). The samples were then sandwiched between two rigid, non-compressible flat supports obtained from commercial Mylar sheets, to ensure uniform pressure distribution and to prevent adhesion to the rollers. The membranes were subsequently processed using a Hot Roller Press Machine (Model 200L, TOB

Machine, China). The final thickness (FT) of the membranes was defined by adjusting the gap between the rollers according to a specified Lamination Ratio (LR), defined as the ratio between the initial and nominal final thickness values (LR = IT/FT). In this study, LR values of 2 and 3 were applied to neat electrospun *m*-PBI membranes to systematically assess the influence of calendering on key physical and functional properties, including air permeability, porosity, water uptake, and acid doping level.

2.2.5 Phosphoric Acid Impregnation

Before proceeding with the phosphoric acid impregnation step, both solution-cast and electrospun *m*-PBI membranes were thoroughly washed in deionized water to remove residual lithium chloride (LiCl) and solvent traces. Although LiCl is used as a solubilizing agent during the preparation of the PBI solution, no traces of residual inorganic phases were detected by XRD, and TGA analyses (described in Chapter III) revealed no further signs attributable to salt residues. Therefore, any potential contribution of residual LiCl to the mass of PBI membranes should be below the detection limit of the techniques used and has been neglected in ADL normalization. This preliminary purification step is essential, as residual salts or solvent molecules can interfere with acid–polymer interactions, alter the membrane's porosity, and compromise the reproducibility of subsequent characterization and impregnation results. After washing, all samples were vacuum-dried at 120 °C for 24 hours and weighed to determine their dry mass (m_{dry}), which served as the reference for subsequent measurements.

The initial acid impregnation was performed by immersing the membranes in concentrated phosphoric acid (85 wt%), following procedures widely reported in the literature for PBI-based membranes. While dense membranes maintained good structural integrity under these conditions, electrospun membranes rapidly dissolved—often within less than one minute of immersion—due to their high surface area and open porosity. To overcome this instability, a modified impregnation protocol was developed using diluted phosphoric acid solutions, designed to balance membrane stability with sufficient acid uptake for functional performance in fuel cell applications.

As the first step of the protocol, the water uptake (WU) was determined. Membranes with a thickness of 50 ± 5 µm and a porosity of 80 ± 5%, previously dried at 150 °C for 24 h and weighed (m_{dry}), were immersed in deionized water. At regular time intervals, the samples were removed, gently blotted, weighed, and their WU was calculated according to Equation 5 (as defined previously).

To evaluate the acid doping level (ADL), the same procedure was repeated using phosphoric acid solutions of increasing concentrations. The ADL was calculated from the mass increase normalized to the WU and expressed as the molar ratio between acid molecules (molar mass 98 g mol^{-1}) and PBI repeating units (molar mass 308 g mol^{-1}) according to Equation 2.4:

$$ADL = \frac{\text{mol H}^+}{\text{mol PBI}} = [\frac{m_{tot} - m_{dry} \cdot (1+WU)}{m_{dry}}]/(\frac{308}{98}) \quad \text{Eq. 2.4}$$

After impregnation, the membranes were dried again at 150 °C for 24 h to reach equilibrium, and the final acid content was determined gravimetrically.

Each experiment was performed in triplicate, and the results were reported as mean values with 95% confidence intervals. To ensure consistency, the same procedure was also applied to dense *m*-PBI membranes under identical conditions, allowing direct comparison of acid uptake behavior between the two morphologies. All experiments were conducted under static conditions to eliminate the influence of forced diffusion and to isolate the intrinsic acid absorption capacity of the membranes. The acid adsorption process was dynamically monitored to obtain both kinetic and thermodynamic insights into phosphoric acid uptake. The kinetic behavior was described using models commonly applied in solid-phase adsorption studies, which effectively capture the temporal evolution of the process without explicitly accounting for mass transport phenomena. These models provide practical insight into the adsorption dynamics by quantifying the rate of solute uptake and the time required to reach equilibrium. The general kinetic expression used (Equation 2.5) relates the instantaneous adsorption rate to the difference between the equilibrium loading (q_e) and the time-dependent loading (q):

$$\frac{dq}{dt} = k\,(q_e - q)^n \quad \text{Eq. 2.5}$$

The temperature dependence of the kinetic constant k was modeled by the Arrhenius equation (Equation 2.6):

$$k = A_0 \exp(-E_a/RT) \quad \text{Eq. 2.6}$$

Three kinetic models were evaluated: the pseudo-first-order ($n = 1$), pseudo-second-order ($n = 2$), and a generalized power-law model, in which the reaction order (n) was treated as an adjustable parameter. Numerical integration and parameter estimation were carried out in the MATLAB® (R2025a) environment using the "*ode23s*" solver for differential equations and the "*lsqnonlin*" routine implementing the Levenberg–Marquardt algorithm for nonlinear regression. Confidence intervals for the fitted parameters were calculated using the "*nlparci*" function.

The thermodynamic aspects of phosphoric acid adsorption were further analyzed by fitting experimental data to four isotherm models—Langmuir, Freundlich, Sips, and Liu—at 25, 35, and 50 °C. From the temperature dependence of the equilibrium constant, the enthalpy (ΔH°) and entropy (ΔS°) of adsorption were determined using the linearized Van't Hoff equation, providing insight into the energetic and molecular interactions governing acid uptake. Additional methodological details are provided in **Paper II**.

2.2.6 Methanol test

To evaluate the stability of acid doping and to distinguish between free acid (F) and acid bound (B) to imidazole sites, a methanol washing test was performed. The membranes were first thoroughly dried, weighed, and then immersed for 30 minutes in phosphoric acid solutions of different concentrations. After the acid treatment, the samples were gently blotted and placed in an oven at 110 °C overnight to remove residual water. The next day, they were weighed to determine the initial acid doping level (ADL_0). Subsequently, the membranes were immersed in anhydrous methanol using a mass-to-volume ratio of 1:3000, and maintained in the bath for 24 hours. This washing step selectively removes the weakly bound or free phosphoric acid without affecting the acid molecules chemically bonded to the imidazole nitrogen atoms of PBI. After washing, the samples were recovered, vacuum-dried at 60 °C, and repeatedly weighed to determine the post-treatment acid doping level (ADL_{post}). The fraction of acid retained (B) — representing the amount of phosphoric acid stably bound to the PBI structure — was calculated according to Equation 2.7:

$$B = \frac{\mathrm{ADL}_{post}}{\mathrm{ADL}_0} \qquad \text{Eq. 2.7}$$

The complementary parameter (F = 1 – B) corresponds to the fraction of free acid not chemically bound to the polymer matrix.

2.2.7 High Temperature Fuel Cell Setup and Testing

Electrochemical characterization of the *m*-PBI membranes was carried out using a Scribner 850 Fuel Cell Test Station equipped with a 5 cm² single-cell fixture. The system integrates a programmable electronic load, mass-flow controllers (MFCs) for independent regulation of anode and cathode gas streams, and temperature-controlled endplates with embedded cartridge heaters and thermocouples. The station also includes a built-in Potentiostat/Galvanostat and a frequency response analyzer (FRA) for performing linear sweep voltammetry (LSV), polarization measurements, and electrochemical

impedance spectroscopy (EIS) under fully automated control via FuelCell® software. A schematic image of the experimental setup is shown in Figure 2.3.

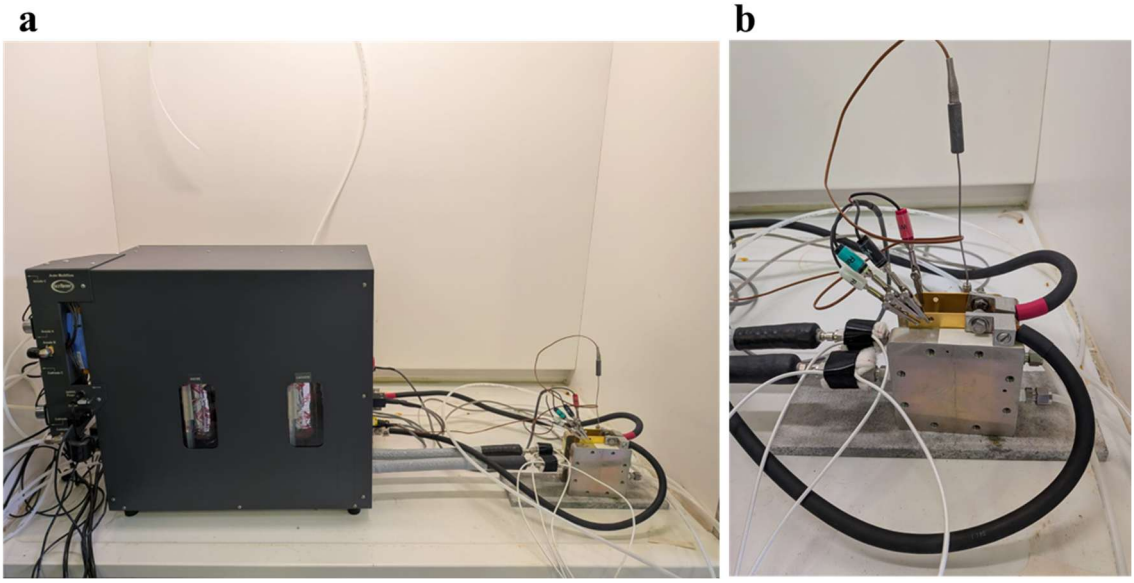

Figure 2.3 – Fuel cell testing setup. (a) Scribner 850 Fuel Cell Test Station equipped with electronic load, mass-flow controllers and temperature control for single-cell operation. (b) 5 cm² single-cell hardware with serpentine graphite flow-fields, gold-plated current collectors and integrated thermocouples, used for in-situ assembly and electrochemical testing of m-PBI membranes under HT-PEM conditions.

The cell hardware consisted of graphite flow-field plates (POCO graphite) with a serpentine gas-distribution pattern, gold-plated copper current collectors, and anodized aluminum endplates ensuring uniform temperature distribution across the active area. The fixture design, compatible with HT-PEM operation, allows precise control of membrane compression and sealing through four high-strength bolts. The Membrane–Electrode Assembly (MEA) was fabricated *in situ* (Figure 2.4) by positioning the electrospun *m*-PBI membrane between two commercial Celtec® HT-PEM electrodes (BASF/Fuel Cell Store), used respectively as anode and cathode. The two electrodes featured different catalyst loadings, with carbon-cloth gas diffusion layers (GDLs) and microporous layers (MPLs). Assembly was performed at room temperature using a cross-pattern tightening with a torque of 4 N m applied to each bolt; no external hot-pressing was used. The gas lines were then connected to the serpentine channels of the fixture, and leak-testing was conducted with nitrogen at low pressure prior to operation. All temperature, flow, and potential controls were managed by the Scribner 850 system.

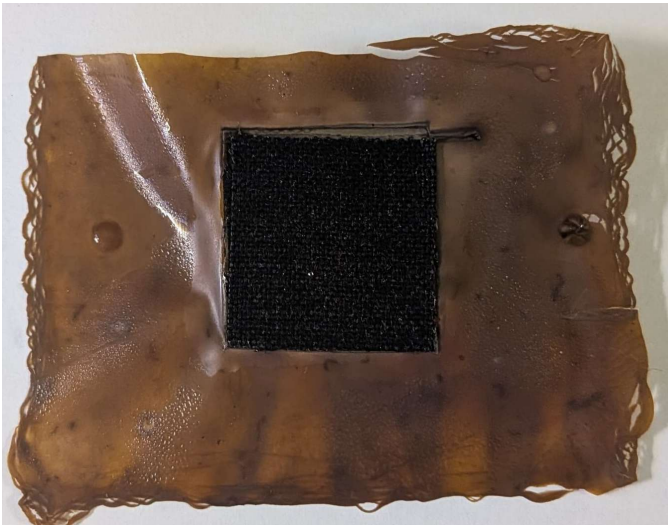

Figure 2.4 - Membrane Electrode Assembly (MEA) based on electrospun *m*-PBI membrane. The MEA was obtained by aligning the commercial BASF/Celtec electrodes with the membrane and assembling the cell under a torque of 4 N m. The applied pressure during cell assembly ensured proper interfacial contact between the membrane and the electrodes.

The testing protocol adopted for preliminary electrochemical evaluation is summarized in Table 2.2. All measurements were performed at ambient pressure using dry gases, under standard HT-PEM testing conditions. The analyses are considered preliminary and will be further optimized in future work.

Temperature [°C]	***Relative Humidity [%]***	***Gases***	***Treatment***	***Characterization***
30	0	H_2 (A) ; N_2 (C)	Pre-testing	LSV
150	0	H_2 (A) ; N_2 (C)	Pre-testing	LSV
150	0	H_2 (A) ; O_2 (C)	Testing	OCV, Polarization Curve, GEIS

Table 2.2 – Operational protocol adopted for preliminary electrochemical characterization of m-PBI-based membranes in single-cell configuration. The table summarizes the test conditions used for pre-testing and performance evaluation, including temperature, gas composition, and measurement type.

All electrochemical tests were conducted under atmospheric pressure and fully dry conditions. This combined approach, LSV for hydrogen crossover, EIS for impedance analysis, and polarization testing under H_2/O_2 provides a comprehensive assessment of the functional behavior of the electrospun *m*-PBI membranes under realistic high-temperature fuel cell operation.

2.3 Aminated Poly(2,6-dimethyl-1,4-phenyleneoxide)

2.3.1 Materials

For the synthesis of the aminated polymer (PPO–NH_2), the same base polymer used in the previous experiments was employed, namely commercial poly(2,6-dimethyl-1,4-phenylene oxide) (PPO, grade P6130, Sabic) in powder form. The polymer was dissolved in chloroform ($CHCl_3$, ≥99.8%, Sigma-Aldrich), selected for its high efficiency in dissolving PPO and its compatibility with the subsequent reaction steps. The functionalization of PPO into its aminated form was carried out through a multi-step chemical process involving both strong and weak acids. These included nitric acid (HNO_3, ≥65%, Sigma-Aldrich), sulfuric acid (H_2SO_4, ≥95–97%, Sigma-Aldrich), glacial acetic acid (CH_3COOH, ≥99.8%, VWR Chemicals), and hydrochloric acid (HCl, 37%, Sigma-Aldrich), which served as oxidizing agents, catalysts, or neutralizing media at different stages of the synthesis.

Tin(II) chloride dihydrate ($SnCl_2 \cdot 2H_2O$, ≥98%, Sigma-Aldrich) and potassium iodide (KI, ≥99%, VWR Chemicals) were also employed as reducing or promoting agents to facilitate the conversion of the functional groups introduced in the earlier reaction phases. The modified polymer was subsequently precipitated by adding methanol (CH_3OH, ≥99.9%, Sigma-Aldrich) and sodium hydroxide (NaOH, ≥98%, Sigma-Aldrich), which promoted the neutralization of residual acid and separation of the solid product.

Finally, the solubility of the aminated PPO was qualitatively tested in several organic solvents of different polarity, including chloroform, toluene ($C_6H_5CH_3$, ≥99.5%, Sigma-Aldrich), dimethyl sulfoxide (DMSO, $(CH_3)_2SO$, ≥99.9%, Carlo Erba), dimethylacetamide (DMAc, $CH_3CON(CH_3)_2$, ≥99.8%, Sigma-Aldrich), N-methylpyrrolidone (NMP, C_5H_9NO, ≥99.5%, Sigma-Aldrich), and dimethylformamide (DMF, C_3H_7NO, ≥99.8%, Sigma-Aldrich), in order to identify the most suitable solvent systems for subsequent membrane formulation.

2.3.2 Amination Reaction

The PPO amination reaction was carried out through a synthetic procedure consisting of two main steps, described in Scheme 2.3. The first involved the nitration of PPO, which was achieved through an acid solution treatment: specifically, 1g of PPO was dissolved in 25 mL of chloroform under magnetic stirring and at room temperature until a homogeneous solution was obtained. To this solution, an acidic mixture consisting of nitric acid and sulfuric acid (HNO_3/H_2SO_4) in a 3:1 v/v ratio was slowly added dropwise, a total of 8 mL, under constant stirring. The reactive mixture was allowed

to react for 30 minutes, after which it was precipitated in 600 mL of methanol to promote the precipitation of PPO nitrate (PPO-NO_2). The precipitate was left in methanol for 1 hour under stirring, and then separated by vacuum filtration. The solid obtained was again solubilized in chloroform and re-precipitated in a further 600 mL of fresh methanol to remove any acidic reaction residue. The PPO-NO_2 thus purified was finally recovered by filtration and dried in a vacuum oven at 40 °C overnight, resulting in an overall yield of 85% of the initial polymer. The second step involved the amination process of the obtained PPO-NO_2 by chemical reduction of the nitro group. Specifically, 0.5 g of the nitrate precursor was solubilized in 20 mL of chloroform at room temperature and under magnetic stirring. The solution was raised to 50 °C by heating in a thermostatic oil bath, monitoring the temperature with the aid of a thermocouple and using a reflux condenser to prevent evaporation of the solvent. Once the temperature was stabilized, a reactive solution consisting of 10 g of tin(II) chloride dihydrate ($SnCl_2 \cdot 2H_2O$), 0.3 g of potassium iodide (KI) dissolved in 12 mL of an acidic mixture of hydrochloric acid and acetic acid (HCl/CH_3COOH) in a 2:1 v/v ratio was added drop by drop.

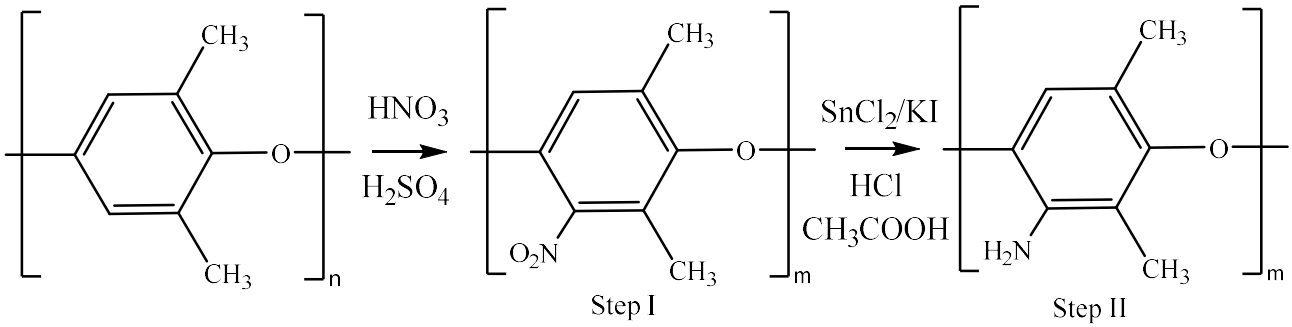

Scheme 2.3 - Two-step synthesis of aminated poly(2,6-dimethyl-1,4-phenylene oxide) (aPPO). In the Step I, PPO undergoes nitration in acidic medium (HNO_3/H_2SO_4), leading to the formation of nitrated PPO through an electrophilic aromatic substitution at the ortho and para positions relative to the methoxy group. In the Step II, the nitro groups are reduced to amino groups using the $SnCl_2$/KI system in HCl and acetic acid, yielding the aminated PPO derivative.

The overall reduction reaction (Step II) can be resumed as follows in Equation 2.8:

$$PPO\text{-}NO_2 + 3Sn^{2+} + 6H^{+} = PPO\text{-}NH_2 + 3Sn^{4+} + 2H_2O \qquad \text{Eq. 2.8}$$

The addition was carried out dropwise and the reaction was maintained at 50 °C for 5 hours. After about 1 hour, the formation of a precipitate was observed, which was redissolved by adding a small amount of methanol. At the end of the reaction, the solution turned from yellow to dark orange, qualitatively signaling reduction. The product was then precipitated in a 2M sodium hydroxide

(NaOH) solution, resulting in aminated PPO (aPPO), which was then vacuum filtered and dried in a vacuum oven at 40°C for 24 h. After heat treatment, the aPPO powder was dissolved in chloroform and again precipitated in methanol and stored in a vacuum oven at 40 °C for a further 24 hours. All the resulting polymeric material were subsequently characterized by spectroscopic and thermal techniques, including ATR-FTIR, ^{1}H-NMR, and WAXD analyses, in order to verify the success of the functionalization process, and finally stored in sealed glass containers at room temperature.

2.3.3 Solubility tests

The solubility behavior of the different PPO derivatives was evaluated to identify suitable solvent systems for subsequent processing steps, such as membrane casting, film formation, or further chemical functionalization. Solubility tests were carried out at a constant polymer concentration of 1 wt% in various solvents, including chloroform, toluene, DMSO, DMAc, NMP, and DMF, as listed in Section 2.3.1. The analyses were performed on neat PPO, nitrated PPO (PPO-NO_2), and aminated PPO (aPPO) powders. Each sample was magnetically stirred in sealed test tubes for 24 hours at room temperature. Solubility was assessed according to well-defined operational criteria: samples were classified as highly soluble (++) when the solution appeared optically clear and free of visible residues; as partially soluble (+) when persistent turbidity, gel formation, or residual solid was observed; and as insoluble (–) when no dissolution occurred. For aPPO, solubility tests were performed only after the purification step, since the presence of residual inorganic salts formed during the synthesis could otherwise cause apparent opalescence or sedimentation unrelated to the intrinsic solubility of the polymer.

CHAPTER III – CHARACTERIZATION TOOLS AND THEORY

This chapter describes the characterization techniques employed to investigate the chemical, structural, thermal, mechanical, and electrochemical properties of the functionalized polymeric membranes developed in this thesis. The analytical approaches were selected based on the specific goals outlined in Chapter II, where several functionalization and processing strategies were applied to poly(2,6-dimethyl-1,4-phenylene oxide) (PPO) and polybenzimidazole (PBI) to produce ion-conducting membranes suitable for use in proton exchange membrane fuel cells (PEMFCs). The techniques discussed here are divided into in-situ and ex-situ methods. In-situ analyses were performed during membrane operation in the fuel cell, providing direct information on performance and electrochemical behavior under realistic conditions. Ex-situ analyses, by contrast, were used to determine the intrinsic chemical and physical properties of the membranes, which were then correlated with the operational results to establish structure–property–performance relationships.

3.1 In-situ characterization

In-situ characterization techniques were employed to assess the electrochemical behavior of the membranes directly in PEMFC configuration. These measurements enable real-time assessment of the cell's performance, efficiency, and the electrochemical processes occurring within the system. The analyses were conducted under various gas feed conditions (inert or reactive) supplied to the Working Electrode (WE), allowing for a detailed evaluation of the system's dynamic behavior.

All electrochemical measurements were carried out using the single-cell setup described in Section 2.1.6 and 2.2.7, equipped with sPPO and *m*-PBI electrospun and cast membranes compared with Nafion® and Celtec®-based membrane–electrode assemblies (MEAs). The experimental techniques included open-circuit voltage (OCV), polarization curves, electrochemical impedance spectroscopy (EIS), linear sweep voltammetry (LSV), cyclic voltammetry (CV), and chronoamperometric and chronopotentiometry analyses.

3.1.1 Open Circuit Voltage (OCV)

The open-circuit voltage (OCV) represents the potential difference between the anode and cathode of the fuel cell when no external current is drawn. It reflects the maximum theoretical electromotive force of the system and provides a first diagnostic of membrane integrity and gas crossover.

Under standard conditions (25 °C, 1 atm), the theoretical potential (E^0) can be calculated from the change in Gibbs free energy, ΔG^0, associated with the water formation reaction (Eq. 3.1 and 3.2) as:

$$H_2 + ½\ O_2 = H_2O \qquad \text{Eq. 3.1}$$

$$E^0 = -\frac{\Delta G^0}{n\mathrm{F}} \qquad \text{Eq. 3.2}$$

Where the parameter ΔG^0 represents the standard free energy for the reaction (-237.2 kJ mol^{-1}), *n* is the number of moles of electrons transferred (equal to 2), and F is Faraday's constant (96485 C mol^{-1}). Based on these considerations, the theoretical OCV value for the reaction described in Eq. 8 is approximately parts to 1.23 V. However, the open circuit potential value is influenced by numerous factors such as temperature, pressure and concentration of the reactants as well as the presence of any problems in the cell setup. For this reason, a more general description of the OCV can be made based on the Nernst equation (Eq. 3.3):

$$*\mathrm{E} = E^0 + \frac{RT}{nF}\ln\left(\frac{p_{H2}\cdot p_{O2}^{0.5}}{p_{H2O}}\right) \qquad \text{Eq. 3.3}$$

Where R represents the gas constant (8.314 J mol^{-1} K^{-1}), T is the absolute temperature (in K) and p_{H2}, p_{O2} and p_{H2O} are the partial pressures of the input gas (H_2, O_2) and the product (H_2O). However, the experimentally observed OCV in PEMFCs typically ranges between 0.95 V and 1.10 V, due to inevitable gas permeation, catalyst losses, or membrane imperfections.. Knowing the OCV value is fundamental as it allows one to first understand any problems related to the polymer electrolyte, the state of the electrodes or manufacturing defects in the setup, offering a quick and essential diagnostic of the fuel cell. In this work, OCV measurements were particularly relevant for comparing sPPO membranes with different degrees of sulfonation (SD). As shown in Chapter II, the SD strongly affects the polymer's water uptake and ion exchange capacity (IEC). Higher IEC values increase proton conductivity but may also enhance gas permeability. The OCV test therefore provided an immediate indication of whether the functionalization improved or compromised the membrane's selectivity and gas permeability.

3.1.2 Polarization curve

The polarization curve is one of the most informative tests for assessing overall PEMFC performance. By progressively varying the cell voltage from the OCV down to 0.4–0.2 V, the corresponding current density is recorded, revealing the various loss mechanisms: activation, ohmic, and mass transport (Figure 3.1). Specifically, it is possible to divide a generic polarization curve (Figure 3.1) into three different regions, each of them is related to a specific loss:

I. Activation region, typically observed at low current densities, where the limiting factor is mainly related to the reaction kinetics, i.e., the energy required to initiate the electrochemical reaction, in particular the oxygen reduction reaction (ORR). The kinetics are generally described by the Buttler-Volmer equation that could be approximated using the Tafel expression at high overpotentials (η) (Eq. 3.4), where i_0 is the exchange current density, α is the charge-transfer coefficient and the parameters *a, b* are the Tafel intercept and slope, respectively.

$$|\eta| = \frac{2.303\ \mathrm{RT}}{\alpha\ \mathrm{F}} \log\left(\frac{|i|}{i_0}\right) = a + b \log|i| \qquad \text{Eq. 3.4}$$

The membrane plays an indirect but decisive role in that its degree of hydration and the distribution of the ionomer phase in the electrode condition the proton conductivity and hence the reaction itself. A dehydrated membrane increases local resistances while an excess of water hinders the diffusion of oxygen, penalizing the reaction kinetics;

II. Ohmic region, present in the intermediate current density zone, characterized by an almost linear decrease in voltage. This region is strongly influenced by the proton resistance of the membrane, which in turn is a function of temperature and the degree of humidification of the electrolyte. A well-hydrated membrane has very low proton resistance due to its high conductivity, which limits the slope of the curve in contrast to dry membranes that increase the resistance value with a consequent worsening of resistance in this region. Membrane design in terms of thickness control, water retention capacity and proton conduction properties is therefore crucial for limiting ohmic losses;

III. Concentration region, typically present at high current densities, mainly due to the transport of reactants to the catalytic sites. At such low voltages, the reaction is extremely fast and involves significant water formation; the excess water (flooding phenomenon) reduces the

oxygen diffusivity towards the catalytic surface of the electrode, accelerating the collapse of the curve and the entire cell. As before, there is a need for targeted tailoring of the membrane, which must be able to retain a good amount of water and balance it under extreme reaction conditions.

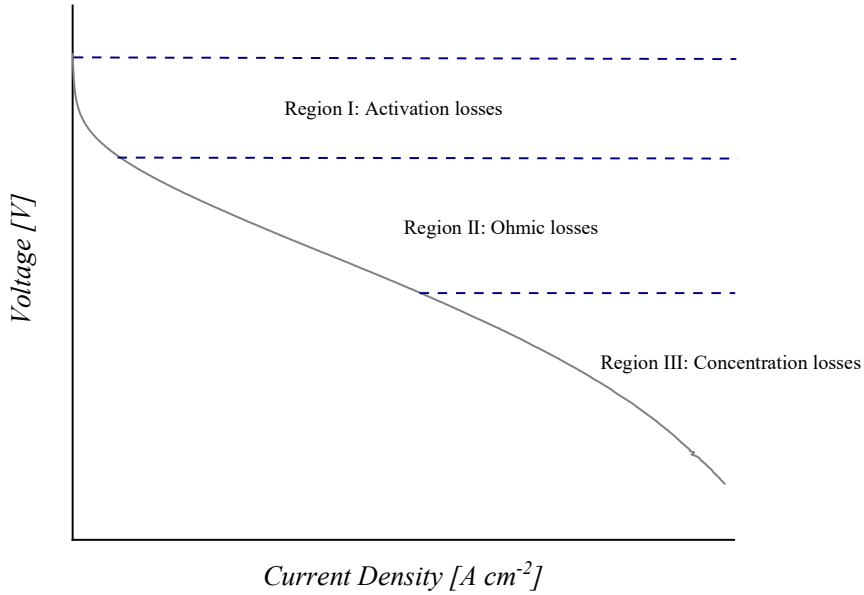

Figure 3.1 – Generic polarization curve in which the current density is plotted as a function of a decreasing potential starting from OCV and reaching typical values between 0.4-0.2 V. Three different regions are shown: I) Activation region; II) Ohmic region; III) Concentration region.

3.1.3 Electrochemical Impedance Spectroscopy (EIS)

Electrochemical impedance spectroscopy (EIS) provides a dynamic, frequency-dependent evaluation of all resistive and capacitive processes occurring within the fuel cell. In general, this technique applies a small-amplitude sinusoidal electrical signal to the cell, recording the response (Z) as a function of frequency (ω), as described in Equation 3.5:

$$Z(\omega) = Z^{real}(\omega) + jZ^{imag}(\omega) \qquad \text{Eq. 3.5}$$

From a mathematical point of view, it can be seen that the impedance (Z) is described by a real part (Z^{real}) related to energy dissipation processes, such as the ohmic resistance of the electrolyte, and an imaginary part (jZ^{imag}) associated with energy accumulation and release phenomena, such as diffusive ones. In particular, the high-frequency intercept with the real axis corresponds to the purely ohmic

resistance (R_Ω or *HFR*, High Frequency Resistance) of the membrane, providing important information on the efficiency of ion exchange. The graphical representation through the Nyquist or Bode plots provides a clear qualitative and quantitative interpretation of the phenomena occurring in the cell and associated with the various components of the MEA.

In this work, potentiostatic (PEIS) and galvanostatic (GEIS) modes were used to separate membrane-related phenomena from electrode kinetics. Under PEIS conditions the cell potential is kept constant and the current response following the sinusoidal response is measured. Specifically, the PEIS analysis obtained using hydrogen (H_2) at the RCE (Reference Counter Electrode) and nitrogen (N_2) at the WE (Working Electrode) allows for the elimination of the faradic contribution at the cathode, as there is no reaction. Under this condition, the PEIS analysis mainly reflects the resistive contribution of the membrane and ionomer present in the catalytic layer (CL) and hence their proton conductivity (σ_m) obtained by knowing fundamental parameters such as HFR values, thickness (T) and active area (A) involved in the electrochemical process (Eq. 3.6).

$$\sigma_m = \frac{T}{HFR \cdot A} \qquad \text{Eq. 3.6}$$

Under GEIS conditions the sinusoidal response is measured while maintaining a fixed current density at the cell. The special feature of this measurement is that the gases used are reactive, hydrogen at the anode and oxygen at the cathode, thus providing an impedance spectrum that simultaneously reflects all proton conduction processes occurring in the membrane and electrode. From here, it is possible to separate the ohmic contributions, activation losses and diffusive phenomena as the current increases, unpacking all regions of the polarization curve previously described. In particular, it is observed that at high current density the low-frequency arc of the Nyquist plot increases, signaling a worsening of oxygen transport at more critical water handling.

In conclusion, EIS served as a bridge between ex-situ transport properties (e.g., ionic conductivity, porosity) and in-situ electrochemical performance, validating the structural modifications introduced during functionalization.

3.1.4 Linear Sweep Voltammetry

The linear voltammetry technique is commonly used to determine intrinsic properties of the polymer membrane. Specifically, the potential between two electrodes (anode and cathode) is linearly varied over time and the resulting current is recorded. For PEMFC applications, this technique is generally used for the determination of non-faradic contributions such as hydrogen crossover. This

measurement is conducted by using hydrogen at the anode and an inert gas (N_2 or Ar) at the cathode in such a way as to isolate it from any other electrochemical reaction (as there is no oxygen) and using it as a working electrode to electrochemically oxidize the hydrogen crossing the membrane by diffusion. The LSV starts at a low potential (e.g. 0.1 V) and is pushed to relatively high values (between 0.6 and 0.8 V) in such a way that the reaction is controlled only by mass transport. In order to extrapolate the hydrogen crossover from a typical LSV curve (Figure 3.2), it is necessary to identify and 'remove' the contribution due to electrochemical hydrogen oxidation by fitting an equation in the linear section of the curve, and from whose intercept on the current density axis, the value i_{H2}, i.e. the current density associated with the hydrogen crossover, can be identified. From this value, it can be converted to molar flux (J_{H2}) via the Faraday equation (Eq. 3.7):

$$J_{H_2} = \frac{i_{H_2}}{n\,F} \qquad \text{Eq. 3.7}$$

Where n is the number of electrons per oxidized H_2 molecule (equal to 2) and F is Faraday's constant. To express the flux in terms of flux density (mol m^{-2} s^{-1}), it can be divided by normalizing for the active area (A).

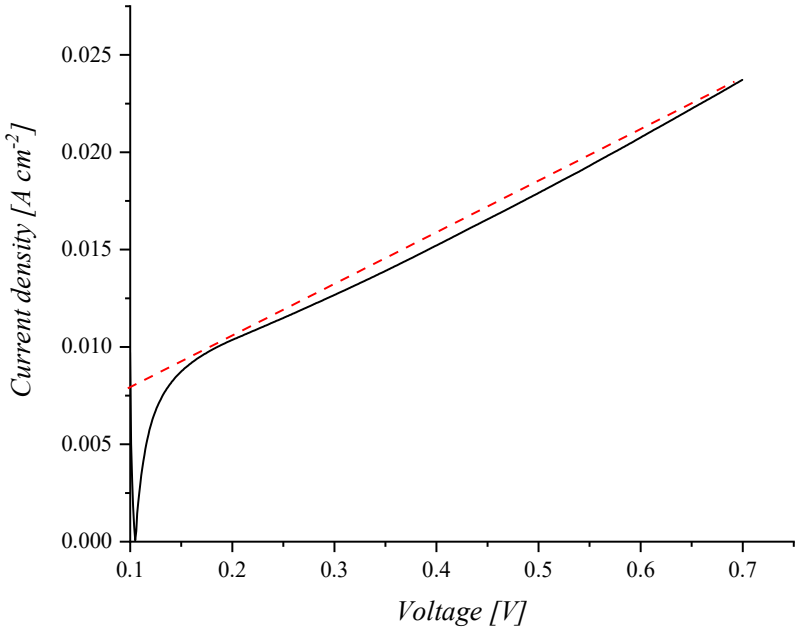

Figure 3.2 – Typical LSV curve in H_2/N_2 configuration: the current is measured as a function of the potential at the cathode. The dashed red line identifies the linear fit of the ohmic section whose intercept on the current density axis identifies the current density value associated with the hydrogen crossover (i_{H2}).

In addition to the crossover, it is also possible to determine the permeability of hydrogen through the membrane, understood as the intrinsic ability of the material to allow the gas to diffuse throughout its

thickness under a specific pressure gradient. A Fick's law combined with Faraday's law (Eq. 3.8) is defined in this context:

$$\Psi_{H_2} = \frac{J_{H_2}\ T}{p_{H_2}} \qquad \text{Eq. 3.8}$$

Where J_{H2} is the molar flux related to the hydrogen crossover, T is the thickness of the electrolyte and p_{H2} is the partial pressure of hydrogen across the membrane.

This analysis directly complemented the results of Chapter II, where the chemical functionalization of PPO (sulfonation, amination) and morphological control of PBI membranes (dense vs. electrospun) were expected to affect gas diffusion pathways. LSV measurements thus provided quantitative insight into how the functional group density, membrane porosity, and thickness jointly influenced gas barrier properties.

3.1.5 Cyclic Voltammetry

Cyclic voltammetry (CV) consists of linearly varying the potential of the working electrode in a cyclic manner and in a specific range (typically between 0.1 and 1.2 V). This technique is extremely effective for obtaining information on surface processes, reaction kinetics and charge build-up phenomena. In the fuel cell field, the use of CV using the H_2/N_2 pair at the anode and cathode respectively, is extremely functional for determining the electrochemically active area (ECSA) of the catalyst (Platinum). In fact, in the region between 0.05 and 0.4V characteristic peaks related to hydrogen adsorption and desorption phenomena on the catalyst surface are observed, and by integrating the current in one of these two regions by subtracting the capacitive contribution of the double layer, it is possible to obtain the charge associated with H_2-catalyst interaction phenomena. From a typical CV graph obtained using H_2/N_2 (Figure 3.3), it is possible to identify three main regions associated with different phenomena:

I. The first region is typically located in the 0-0.4 V range and is associated with H_2-catalyst interaction phenomena. Specifically, hydrogen adsorption peaks are observed during the anodic sweep (red curve) and desorption peaks during the cathodic sweep (green curve);
II. The second region is located in a range between 0.4-0.7 V and refers to the area of the double layer where there are no faradic reactions;
III. The third and last region, in the 0.7-1.2 V range, refers to the oxygen oxidation zone (green curve) characterized by the formation of surface oxides, and their reduction (red curve).

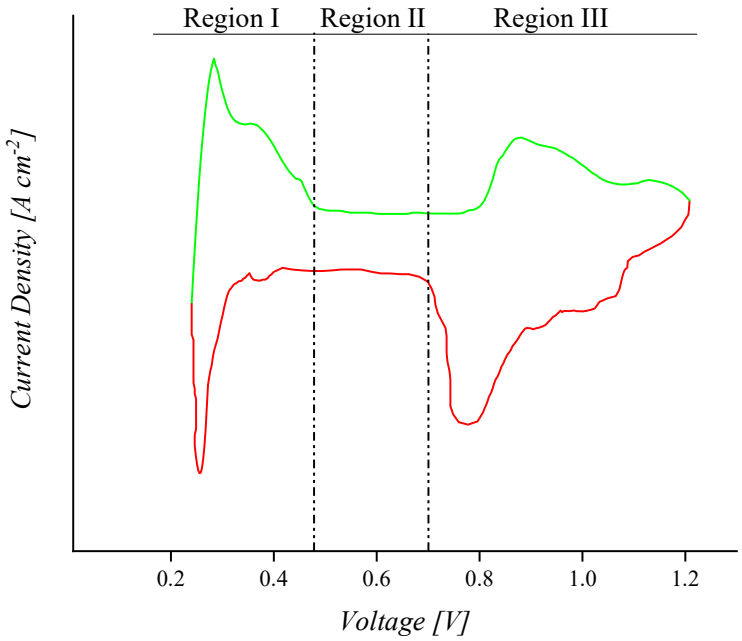

Figure 3.3 – Typical cyclic voltammogram (CV) for a PEMFC working in H_2/N_2 configuration. The green curve represents the cathodic oxidation sweep while the red curve refers to the anodic reduction sweep. Three distinct regions can be identified: I) Hydrogen adsorption/desorption zone on the catalyst; II) Double layer zone; III) Oxygen oxidation and reduction zone.

The electrical charge associated with hydrogen adsorption/desorption phenomena, Q_H, is calculated by integrating the area subtended by the curve in the identified region and subtracting the capacitive current of the bilayer. From here, knowing the theoretical charge to form a monolayer of H on polycrystalline platinum (q_{ref} = 210 µC cm^{-2}), the ECSA value is calculated by normalizing for the amount of charged platinum (m_{Pt}) on the MEA (Eq. 3.9):

$$ECSA\ [m^2\ g^{-1}] = \frac{Q_H}{q_{ref} \cdot m_{Pt}} \cdot 10^{-4} \qquad \text{Eq. 3.9}$$

This technique therefore validated the effectiveness of the Catalyst-Coated Membrane (CCM) fabrication method applied to functionalized PPO and provided a measure of the electrochemical utilization of the catalyst in the MEA.

3.1.6 Long-term Durability Tests

The long-term durability of polymeric membranes used in PEMFC applications is crucial to understanding their stability under operating conditions, i.e. in a reactive environment (H_2/O_2) under specific temperature and humidity conditions. Chronoamperometry (ChronoA) and chronopotentiometry (ChronoP) are two fundamental techniques that allow key parameters describing the functional and structural integrity of polymer electrolytes to be monitored over time. In chronopotentiometry, the cell is subjected to a constant current density, typically in the range 0.2-0.5 A cm^{-2}, recording potential changes over time. A stable membrane manifests itself with an almost constant potential, but an abrupt change in potential indicates an increase in the proton resistance of the membrane, which undergoes dehydration and/or degradation with the formation of micro-fractures or pinholes. The US DoE identifies for benchmark materials (e.g. Nafion 212) an operating range of over 10.000 hours with a resistance loss < 0.02 Ω cm^{-2} with a target for 2025 based on 20.000 operating hours. In chronoamperometry, on the other hand, one works in the reverse way as the technique consists of applying a constant potential to the cell while recording the current density over time. The current directly reflects the electrocatalytic activity of the MEA and the ability of the polymer electrolyte to ensure efficient proton transport. A gradual decrease in the current at constant potential identifies a deterioration of the membrane's conductive capacity and, thus, degradation phenomena. Tests conducted on Nafion 212, show under operating conditions of 80 °C and 100% RH a reduction in current of between 5-10% after about 5000 hours, thus showing how this technique is extremely functional for quantifying the residual “life” of membranes under realistic operating conditions.

3.2 Ex-situ characterization

Ex-situ characterization techniques include all analytical and experimental methods performed under conditions different from actual cell operation. Their main purpose is to obtain detailed information on the structure, chemical composition, morphology, and the mechanical and thermal properties of the synthesized polymer electrolytes. The data obtained from these analyses were used to establish correlations between the physicochemical characteristics of the membranes and their electrochemical performance under operating conditions.

3.2.1 X-Ray Diffraction (XRD)

Structural characterization of the membranes was performed by the WAXD (Wide,-Angle-X-Ray Diffraction) technique using the Malvern Panalytical Empyrean diffractometer with Cu Kα radiation (λ = 1.5418 Å). Measurements were conducted by means of continuous scanning, recording diffraction spectra in a range of 2θ angles between 5-40°, with a scanning speed of 0.05°/s.. The degree of crystallinity affects both mechanical properties and proton transport: highly crystalline structures tend to reduce water uptake and ionic mobility, whereas amorphous regions facilitate proton conduction. For example, comparing WAXD patterns before and after sulfonation or amination provided evidence of how chemical modification disrupted the polymer backbone, increasing amorphous content and improving ionic transport.

3.2.2 Attenuated Total Reflectance Fourier-Transform Infrared Spectroscopy (ATR/FTIR)

The chemical-structural characterization of the membranes was also conducted by means of Fourier transform infrared spectroscopy in ATR mode, using the Anton Paar Lyza 7000 instrument. Samples were placed on a diamond crystal, used as an optical element, recording 36 scans per sample with a spectral resolution of 4 cm^{-1} in a typical range between 400 to 4000 cm^{-1}. This technique makes it possible to identify the characteristic functional groups of each polymer and to detect any chemical changes due to functionalization treatments (sulfonation or acid impregnation), returning a complete analysis of the material's structure.

3.2.3 Thermogravimetric Analysis (TGA)

The thermal stability of the obtained membranes was assessed by thermogravimetric analysis (TGA) using the TA SDT650 instrument. Approximately 4-6 mg of sample was placed in an alumina crucible and heated in a nitrogen atmosphere (flow rate of 10 mL/min) with a temperature rise of 10 °C/min to 800 °C. These results provided critical information for defining the operating temperature window of the membranes and confirmed that the modifications introduced did not compromise their stability within the PEMFC range (up to 180 °C for PBI and aPPO, 100 °C for sPPO).

3.2.4 Mechanical Tests

The mechanical properties were determined at room temperature using the universal Instron instrument (model 5566H1543), following the guidelines of ASTM D638, in order to measure the tensile strength, Young's modulus and elongation at break. The specimens, with dimensions of 100x10 mm and a thickness of approximately 100 μm, were subjected to deformation at a rate corresponding to 10 times the initial length of the calibrated section (L_0) per minute for the recording of the stress-strain curves until failure. For the Young's modulus measurement, a reduced speed of 0.1 times the value of L_0 per minute was adopted in order to ensure better accuracy in the initial elastic stretch. The mechanical analysis provides insight into the robustness of the membrane and its ability to maintain its physical integrity under operational stresses, a crucial condition for fuel cell applications. Young's modulus (E) was determined from the slope of the initial linear section of the stress-strain curve, which corresponds to the elastic regime in which the deformation of a material is reversible and proportional to the applied stress. Beyond this region, the curve shows behaviour that deviates from linearity, identifying plastic behaviour, which deforms the material irreversibly. During this deformation, various phenomena can occur, such as strain hardening, due to the orientation of the chains along the stretching direction, or necking and pull-out, which quickly lead to fracture. Basic parameters for the description of mechanical properties include σ_{max} and ε_{break}, i.e. the maximum of the curve (maximum strength) and the deformation at the breaking point.

The motivation for these tests derived from the fact that functionalization and solvent processing can significantly alter polymer chain packing and flexibility. By comparing neat and sulfonated PPO, or dense and electrospun PBI, it was possible to assess how chemical modification and morphology affect the membrane's mechanical robustness—a prerequisite for maintaining integrity during fuel cell operation, especially under variable humidity.

3.2.5 Morphological characterization: Scanning Electron Microscopy

The morphological study of the membranes was conducted using scanning electron microscopy (SEM), a technique that allows high-resolution images of the surface and microstructure of the materials under investigation to be obtained. The analysis was performed using Nova Nanosem 450 instrumentation (FEI, Austin, TX, USA), with micrographs taken at different magnifications in order to characterize both the global surface characteristics and nanometric details. In addition, the assessment of membrane functionalisation (e.g. sulfonation or amination) was carried out by means of X-ray energy dispersion (EDX) analysis, integrated into the SEM instrumentation. This EDX

technique exploits the interaction of the electron beam with the atoms in the sample, generating characteristic X-rays whose energies are uniquely associated with each chemical element. Starting from the morphological evaluation conducted by SEM, for membranes obtained by electrospinning, a quantitative analysis of the fiber diameters was carried out using ImageJ software (Rasband, W.S., Image J, U.S. Nation Institute of Health, Bethesda, MD, USA) exploiting the linear measurement function calibrated according to the scalebar present in the SEM micrograph. For each sample, at least 30 randomly selected measurement points were performed on the entire micrograph.

In addition, Surface defects (D) present on the various materials such as beads, ribbon-like or dense droplets were identified on low-magnification (1000×) images and assimilated to equivalent circular areas, the percentage fraction of which was determined as the ratio of the summation of the i-example areas of the defects ($A_{D,i}$) to the total area of the micrograph (A_T) as reported in Eq. 3.10:

$$D = \frac{\sum_{i=1}^{n} A_{D,i}}{A_T} \cdot 100 \qquad \text{Eq. 3.10}$$

3.2.6 Porosity and Air Permeability Measurement

The porosity of the electrospun membranes was determined using the ethanol displacement technique, which is based on the determination of all pores accessible to ethanol (Sigma Aldrich, ρ_{EtOH} = 0.789 g/ml), i.e. as the ratio of the pore volume (V_{pore}) to the total sample volume (V_{tot}). The technique is gravimetric and consists of weighing the dry sample (m_{dry}) and then immersing it in ethanol (m_{wet}), estimating the porosity as shown in Eq. 3.11:

$$\varepsilon = \frac{m_{dry} - m_{dry}}{\rho_{EtOH} V_{tot}} \cdot 100 \qquad \text{Eq. 3.11}$$

Air permeability was assessed through the Gurley technique, using a Gurley Densometer (Model 4320, Troy, NY, USA). The test measures the time *t* required for a specific volume of air (V_{Air} =100 cm^3, μ=1.81·10^{-5} Pa·s) a known area of the sample (A = 1.58 cm^2) under an air column pressure considered constant (ΔP = 1220 Pa). The air permeation velocity (cm/s) is described in Eq. 3.12 and measured as:

$$v = \frac{V_{Air}}{A\,t} \qquad \text{Eq. 3.12}$$

3.2.7 Nuclear Magnetic Resonance (NMR)

Nuclear magnetic resonance (NMR) analysis was conducted using a Bruker Avance Ultrashield 400 spectrometer (Bruker Corporation, Billerica, MA, USA) with a nominal magnetic field corresponding to a frequency of 400 MHz for ^{1}H. NMR is a spectroscopic technique based on the interaction between nuclei with a magnetic moment and a static magnetic field. This interaction produces chemical shifts (expressed in ppm, δ) and signal intensities that reflect the nucleus' local electronic environment, making it possible to deduce information on molecular structure and the presence of specific functional groups. Indeed, in the case of the polymers proposed in this thesis work, the NMR technique was used to detect and quantify structural changes due to functionalisation processes such as sulfonation or amination. Depending on the solubility of the sample, solvents such as deuterated chloroform ($CDCl_3$) and deuterated dimethyl sulfoxide (DMSO-d_6) were used, which provide an internal reference signal and allow for adequate dissolution of the polymer without significant interference in the spectrum.

CHAPTER IV

SULFONATED POLY(2,6-DIMETHYL-1,4-PHENYLENE OXIDE) - sPPO

4.1 Fabrication of neat PPO membranes

The preparation of non-sulfonated poly(2,6-dimethyl-1,4-phenylene oxide) (PPO) membranes was carried out using the blade casting technique, with a Dr Blade on a flat glass substrate (See Section 2.1.2). Preliminary tests were conducted using a 7% wt. solution of PPO in chloroform, casting it on the glass substrate fixed on a vacuum plate. As a result of the solvent evaporation process, PPO membranes with an average thickness of 25 ± 5 μm were obtained, which were macroscopically homogeneous but characterized by the presence of irregularly distributed dotted areas on the surface, similar to a slight knurling (Figure 4.1-a). As the surface of the glass substrate is perfectly smooth, these defects may be attributable to the behavior of the polymer solution during the solvent evaporation process. Analysis of the phenomenon suggests that in such thin films, the rapid evaporation of chloroform induces strong concentration gradients. In particular, the high rate of solvent removal relative to the chloroform diffusion time from the interior to the surface of the melt can lead to the formation of a surface layer (skin). This layer tends to solidify rapidly, trapping the residual solvent present in the underlying layers. In addition, the low viscosity of the polymer solution makes it susceptible to Gibbs-Marangoni type convective flows, which occur when there is mass transfer along an interface between two phases. This is primarily due to surface tension gradients, mainly resulting from local concentration differences, which lead to micro-roughness and, consequently, local thickness variations. To mitigate this phenomenon, the next approach was to increase the solution concentration to 15 % wt. of PPO in chloroform, while keeping all other casting parameters (blade gap, casting speed and temperature) unchanged. The increase in concentration led to an increase in the viscosity of the solution, reducing the mobility of convective and surface flows and making the solution-film transition more uniform. Under the same casting conditions, the dry films obtained starting from a 15% wt. solution of PPO in chloroform and after the complete evaporation of the solvent is about 50 ± 5 μm. Under these conditions, the surface is smooth, compact and free of knurling, providing an excellent starting material for subsequent sulfonation steps (Figure 4.1).

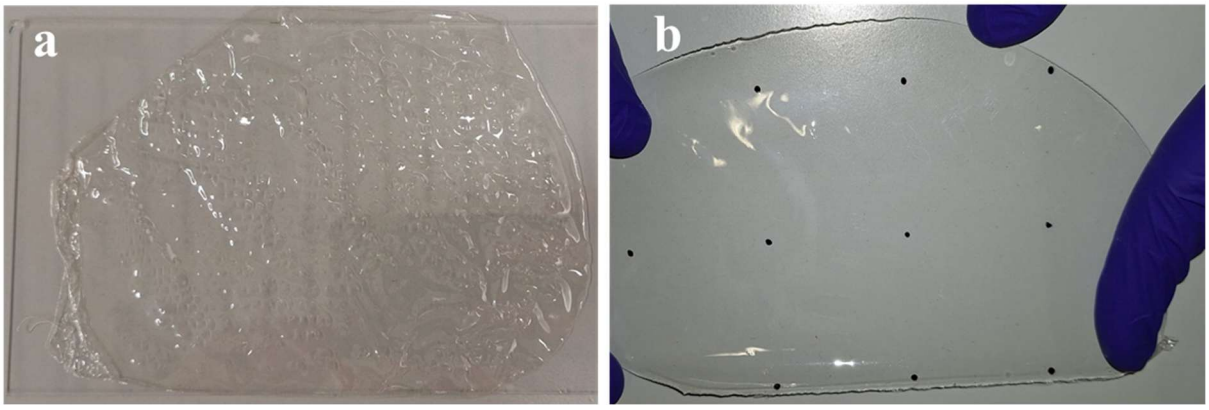

Figure 4.1 – Comparison of two PPO films obtained by the Dr. Blade technique using a minimum nominal gap of 0.05 mm and a feed rate of 20 from a 7% wt. (a) and 15% wt. (b) solution in chloroform. Film obtained at lower polymer concentration (a) were characterized by the presence of knurling and surface imperfections. In contrast, samples obtained at higher concentration (b), showed good surface homogeneity and absence of defects. The distance between black dots in Figure (b) is 5 cm.

Obtaining thicker membranes not only solves a problem from a surface, and therefore physical, point of view of the material, but also has functional advantages. Thicker membranes have greater mechanical strength, which facilitates handling during the various treatment steps and ensures greater stability of the material. In conclusion, we can say that this surface morphological variation is relevant in the development of PPO films by the blade casting technique, also because it can significantly influence the characterisation techniques to which the membranes will be subjected, particularly for electrochemical analysis. All the experimental considerations just described can be summarized in Table 4.1, which shows the main parameters used, the differences found and the experimental implications for membranes with thicknesses of 25 and 50 µm.

Parameter	***PPO membrane 25 µm***	***PPO membrane 50 µm***
Solution concentration [% wt.]	7	15
Solvent	Chloroform	Chloroform
Dr. Blade Height [mm]	0.05	0.05
Feed rate [-]	20	20
Support	Glass	Glass
Surface appearance	Visible surface streaks	Smooth and uniform surface

Main causes of defects	Rapid evaporation, superficial skin	No defects

Table 4.1 – Comparison of blade casting parameters and properties of the resulting dry PPO membranes.

4.2 PPO film functionalization

The functionalization of the PPO films was carried out through a solid-state sulfonation treatment using a 20% in volume solution of acylsulphate in cyclohexane as the sulphonating agent. The acylsulphate was obtained through a reaction between dodecanoic acid and chlorosulfonic acid in a molar ratio of 1.6:1 (see Section 2.1.3), left to react for 24 h. The choice of this sulphonating agent is justified by the ability to introduce sulfonic groups ($-SO_3H$) on the aromatic ring of PPO under relatively mild and controlled conditions, to prevent polymer chain degradation. In order to favor the diffusion of the sulphonating agent, the PPO films were immersed in pure cyclohexane for 24 h by exploiting the plasticizing effect of the solvent: this solvent locally lowers the T_g of the polymer by increasing the free volume, facilitating molecular transport of the sulphonating agent in the solid state. After the necessary time in cyclohexane had elapsed, the membranes were transferred to a closed system containing acylsulphate in cyclohexane (20% vol.) and left to react in specific time intervals at a temperature of 40 °C. The sulfonation conditions described above were applied to PPO films with thicknesses of 25 µm and 50 µm. The surface morphology of the films plays a crucial role in controlling the diffusion of the sulfonating agent and, consequently, affects the reproducibility of key parameters such as the ion exchange capacity (IEC) and water uptake (WU). Qualitatively, the sulfonation process produces a distinct color change in the polymer: pristine PPO films are transparent, whereas sulfonated PPO (sPPO) films become yellow to orange, with increasing color intensity corresponding to a higher degree of sulfonation (Figure 4.2). This behavior is characteristic of aromatic systems containing sulfonic acid groups. After the washing step with distilled water, the 25 µm membranes exhibit significant swelling—up to three times their original size—and show partial loss of dimensional stability. In contrast, the 50 µm membranes maintain their geometry and surface flatness despite undergoing similar swelling. This difference aligns with the morphological observations discussed earlier: thinner films are more fragile and show local variations in the degree of sulfonation, leading to uneven distributions of hydrophilic regions and, consequently, non-uniform swelling across the surface.

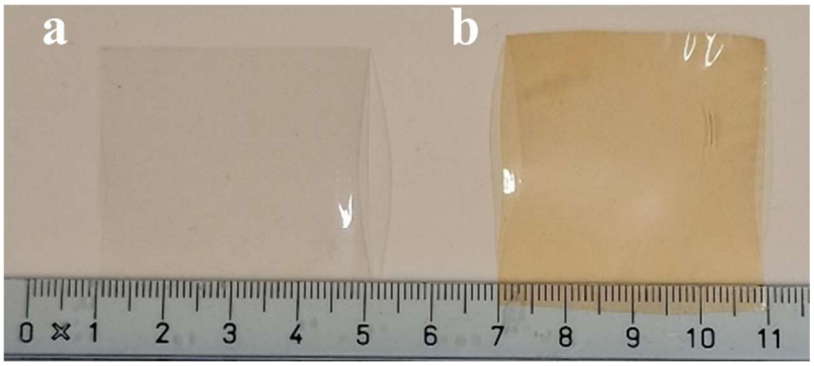

Figure 4.2 – Color change of PPO-based membranes: a) Transparent and colorless non-sulfonated neat membrane; b) Sulfonated PPO (sPPO) membranes obtained through a solid-state sulfonation with acylsulphate and characterized by a yellow/orange color.

4.2.1 Ion Exchange Capacity (IEC) and Water Uptake (WU)

The degree of sulfonation of the membranes was preliminarily assessed as described in Section 2.1.4 by measuring the ion exchange capacity (IEC) and water uptake (WU). As observed during the washing step, the quantitative trends of IEC and WU reflect the morphological features of the films described in the previous paragraph since in solid state processes even slight differences in morphology and thickness affect the diffusion of the sulfonating agent and, consequently, the dimensional stability of the resulting sPPO membranes.

In the thinner films (25 μm), sulfonated for 15 and 30 minutes, a pronounced variability in IEC values was detected even for samples obtained from the same film. As shown in Table 4.2 (rows 1–2), samples treated for 15 minutes exhibited IEC values ranging from 0.63 to 0.93 meq g^{-1}, while those treated for 30 minutes reached higher but still very dispersed values (between 0.98 and 2.0 meq g^{-1}). This large variation, unexpected for samples obtained from the same film, could be explained to the largely heterogeneous surface morphology of the film (Figure 4.1-a), and characterized by micro-roughened regions where the sulfonating agent penetrates more readily. These local differences in thickness and accessibility lead to uneven sulfonation rates across the membrane, resulting in zones of significantly higher and lower IEC. WU follows a similar trend: as IEC increases, so does the membrane's hydrophilicity and swelling capacity. However, the 25 μm membranes exhibit non-uniform swelling, with localized expansion and loss of flatness already apparent after washing.

In contrast, the 50 μm membranes display regular and reproducible behavior (Table 4.2, rows 3–4). After 195 minutes of sulfonation, the IEC reaches approximately 1.2 ± 0.05 meq g^{-1}, increasing to 2.1 ± 0.05 meq g^{-1} after 255 minutes, accompanied by proportionally higher and consistent WU values.

The correlation between IEC and WU is essential for understanding water conduction and retention in membranes designed for PEMFC applications. In the 25 µm samples, this correlation remains localized and irregular due to morphological defects that either facilitate or hinder reagent penetration in different regions. Conversely, the more uniform surface and bulk morphology of the 50 µm films minimizes these effects, ensuring a more homogeneous degree of sulfonation throughout the membrane thickness.

Thickness	*Sulfonation time [min]*	*IEC [meq g^{-1}]*	*WU [%]*	*Reproducibility*
25 µm	15	0.63 - 0.93	25 – 38	Low
25 µm	30	0.98 – 2	40 – 85	Low
50 µm	195	1.20 ± 0.05	45 ± 3	High
50 µm	255	2.10 ± 0.05	90 ± 5	High

Table 4.2 – Ion Exchange Capacity (IEC) and Water Uptake (WU) of sPPO membranes functionalized in the solid state and at different immersion times in the sulphonating agent.

In conclusion, we can say that solid-state functionalization requires skillful control of the initial morphology of the samples if reproducible IEC and WU values are desired, a necessary condition for reliable and efficient electrochemical performance.

4.3 Characterization of sulfonated membranes

The characterization of sPPO membranes aims to describe the structure-property relationship induced by the sulfonation process. Analyses were conducted using spectroscopic, structural, thermal, and mechanical analysis techniques to obtain a comprehensive description of each specific aspect.

4.3.1 Spectroscopic analysis: FTIR-ATR

Fourier Transform Infrared spectroscopy with Attenuated Total Reflectance (FTIR-ATR) was used to characterize the chemical structure of pristine PPO and of sulfonated sPPO samples to confirm the introduction of sulfonic groups and the degree of sulfonation. Figure 4.3 shows the spectra of non-sulfonated PPO and two sPPO samples with IEC of 1.3 and 2.0 meq g^{-1}. In the full spectrum of neat PPO (Figure 4.3-a, black curve), the typical bands of the PPO polymer are first observed. Prominent among these are the intense aromatic C=C stretching bands in the range 1600-1500 cm^{-1}, the aromatic and aliphatic C-H bond stretching signals at 3050 and 2900 cm^{-1}, respectively, and the aromatic ether

C-O-C bond vibrations located around 1250-1180 cm^{-1}. In sPPO spectra (red and blue curves) a very important aspect is the appearance of new signals, absent in neat PPO, starting with the presence of a broad band centered at around 3300 cm^{-1} which can be attributed to the stretching of the O-H bond of sulfonic acids and water adsorbed by hydrogen bond interaction. The individual FTIR spectra of each sample can be found in Annex A.1.

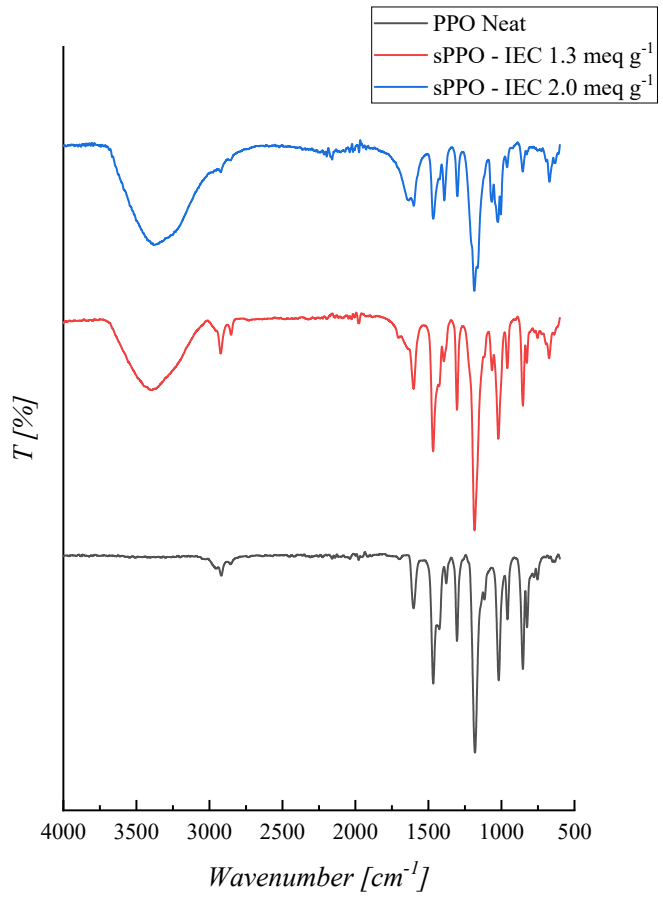

a)

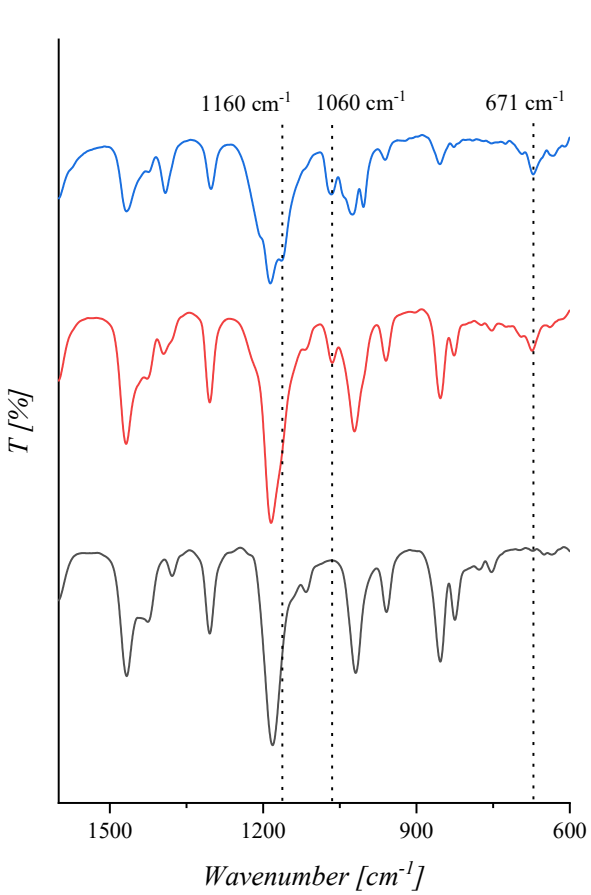

Figure 4.3 – FTIR spectra of neat PPO (black) and sulfonated membranes with IEC 1.3 (red) and 2.0 (blue) meq g^{-1}: a) full spectrum; b) magnification of the spectral region where diagnostic bands of sulfonation are present.

Figure 4.3-b allows us to observe the spectral regions in more detail that are most characteristic of the identification of sulfonic groups. In particular, in respect to the FT-IR spectrum of pristine PPO, new characteristic bands appear in the sulfonated samples:

- Signal related to asymmetric stretching of the S=O bond in the range ~1040-1060 cm^{-1};
- Signal related to the symmetrical stretching of the S=O bond at approximately 1160 cm^{-1}, which partially overlaps with the C-O-C vibrations of the PPO;
- A weaker signal attributable to the S-O sulfonic group bound to the aromatic ring at about 670 cm^{-1}.

To facilitate the interpretation of the spectra, Table 4.3 shows the main characteristic bands of all the samples analyzed, with their respective vibrational assignments. It can be seen that the relative

intensity of these bands increases from IEC 1.3 to IEC 2.0 meq g^{-1}, in accordance with the increasing degree of functionalization. This trend confirms that the FTIR technique is able to provide qualitative feedback on the level of membrane sulfonation.

Vibrational Assignment	*PPO Neat [cm^{-1}]*	*sPPO [cm^{-1}]*
O-H Stretching	-	~ 3300
C-H Aromatic Stretching	~ 3050	~ 3050
C-H Aliphatic Stretching	~ 2920-2850	~ 2920-2850
C=C Aromatic Stretching	~ 1600-1500	~ 1600-1500
C-O-C Stretching (Ether)	~ 1250-1180	~ 1250-1180
S=O Symmetric Stretching	-	~ 1160
S=O Asymmetric Stretching	-	~ 1060
S-O on the Aromatic Ring	-	~ 670

Table 4.3 – Characteristic FTIR bands of neat PPO and sulfonated sPPO samples.

4.3.2 Structural Analysis (XRD)

The structural properties of PPO and sulfonated PPO (sPPO) membranes were analyzed using Wide-Angle X-ray Diffraction (WAXD) to investigate the possible presence of crystalline domains and to evaluate the effect of sulfonation on the polymer matrix organization. Figure 4.4 compares the diffraction pattern of pristine PPO (black curve) with that of an sPPO sample exhibiting an IEC of 2.0 meq g^{-1}. Both materials display typical amorphous behavior, as evidenced by the presence of a broad diffuse maximum centered at $2\theta \approx 18–20°$, accompanied by a weak shoulder around $2\theta \approx 22–25°$, which is attributed to diffuse scattering from the aromatic chains. No sharp peaks are observed, confirming the absence of long-range crystalline order. Moreover, the diffraction profiles recorded for sPPO samples at different degrees of sulfonation are nearly identical, indicating that the incorporation of sulfonic groups does not substantially alter the microstructural organization of the polymer. All WAXD spectra are reported in Annex A.2.

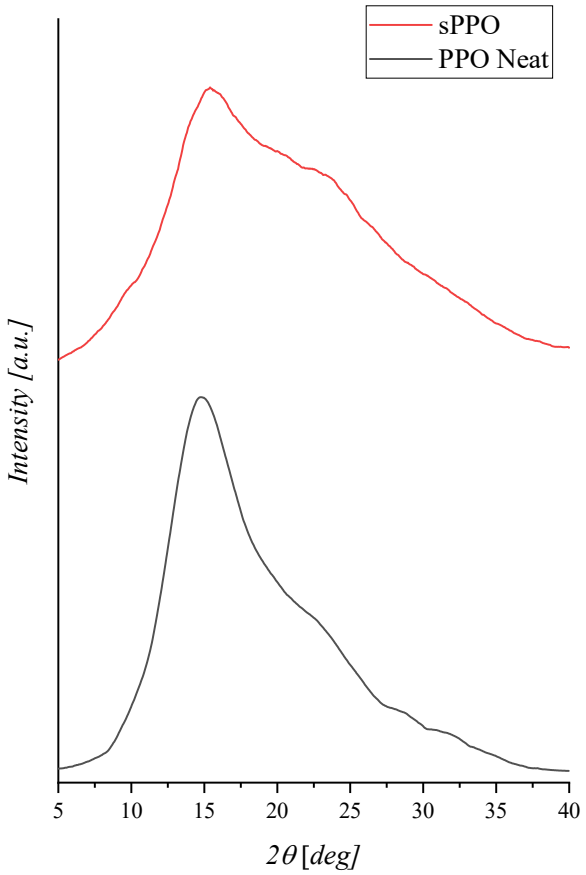

Figure 4.4 – XRD diffraction patterns of PPO neat and sPPO membranes.

Although the introduction of sulfonic acid groups (–SO_3H) does not affect the position or relative intensity of the main diffraction maximum, suggesting that the average chain packing remains unchanged, it may still influence the material at the nanometric scale. However, the formation of these hydrophilic microdomains, typically associated with ionic clustering, cannot be detected by WAXD but could be investigated through Small-Angle X-ray Scattering (SAXS) analysis [134].

4.3.3 Thermo-gravimetric analysis: TGA

Thermogravimetric analysis (TGA) is a crucial tool for evaluating the thermal stability and nature of functional groups present in polymers. Figure 4.5 shows the comparison of the thermal behavior of neat PPO and of sPPO with IEC 2.0 meq g^{-1}. The thermogram highlights the percentage weight loss

as a function of temperature, revealing substantial differences between the starting and functionalized materials.

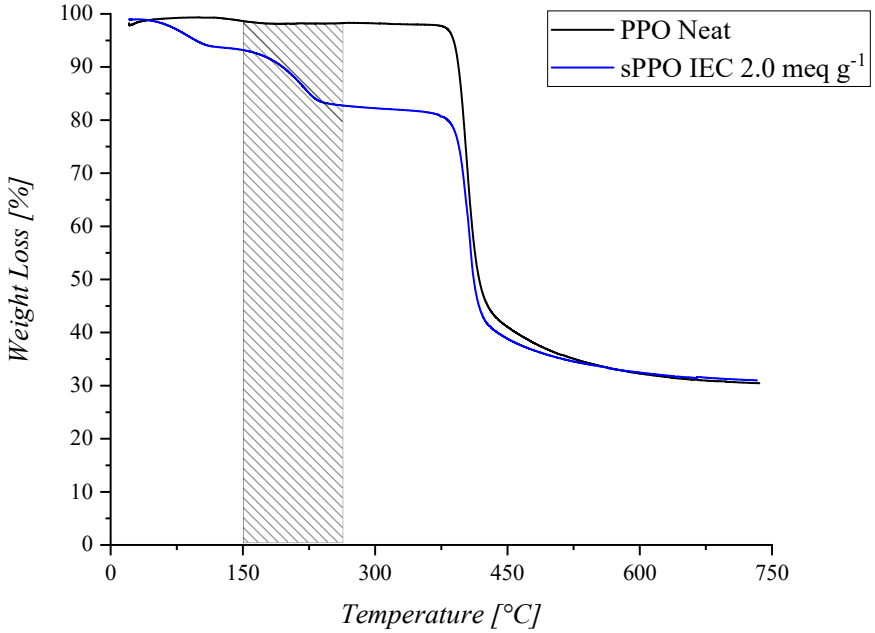

Figure 4.5 – Thermogravimetric analysis (TGA) recorded in air at 20°C/min heating rate, of neat PPO (black curve) and sulfonated sPPO (IEC 2.0 meq g^{-1}, blue curve). In dashed area in the range 150-250 °C the weight loss attributable to the degradation of sulfonic groups.

Neat PPO (black curve) shows excellent thermal stability, with negligible mass loss up to about 380°C where a rapid mass decay is observed, attributable to the polymer chain breakage. At the end of the process, the final residual mass is around 30%, a value in line with the aromatic nature of the polymer [122]. Differently, the TGA curve of sulfonated sample (sPPO, blue curve) shows an initial loss already around 100 °C, likely attributable to the loss of water absorbed (that is absent in ta case of the neat PPO due to its hydrophobic nature). In addition, we note the presence of a significant loss in the 150-250 °C range (dashed area in Figure 4.5), which can be attributed to the thermal degradation of the -SO_3H groups bound to the aromatic ring.

This process results in a progressive mass loss, directly proportional to the degree of sulfonation of the material, which is around 30%. Beyond this range, the material presents a final loss, consistent with what occurs with neat PPO and corresponding to the degradation of the aromatic backbone. We can therefore say that the introduction of sulfonated units on the PPO structure does not compromise the overall thermal stability of the material. The sPPO can, therefore, be used for LT-PEM fuel cell

applications since the typical operating range is in the 60-80 °C range. In this operative condition, the polymer fully retains its sulfonic functionalization and thus its proton exchange capacity, ensuring stable and durable performance. To better quantify these observations, Table 4.4 summarizes the estimated weight losses for the main temperature intervals and their corresponding thermal events. The sulfonated polymer exhibits a two-step degradation profile, with an early mass loss due to the decomposition of ionic groups and a subsequent degradation associated with the polymer chain. Despite the earlier onset of degradation, sPPO retains a comparable char yield to PPO neat, indicating that the modification does not significantly alter the carbonaceous residue content after complete pyrolysis.

Temperature range [°C]	***Thermal degradation process***	***Neat PPO Weight loss [%]***	***sPPO Weight loss [%]***
25-150	Removal of residual moisture or solvent	~ 1	~ 6
130-300	Decomposition of sulfonic acid groups ($-SO_3H$)	-	~ 15
350-500	Degradation of PPO backbone	~ 70	~ 60
500-750	Formation of carbonaceous residue	~ 30	~ 30

Table 4.4 - Estimated weight loss of PPO and sPPO (IEC = 2.0 meq g^{-1}) in different temperature intervals.

4.4 Electrochemical Characterization

The electrochemical performance of the sulfonated PPO (sPPO) membranes was evaluated using a single-cell fuel cell setup. The experimental procedure followed a stepwise approach, beginning with preliminary diagnostic measurements aimed at identifying any intrinsic limitations of the material, and progressing to the assessment of overall fuel cell performance under operational conditions. In the initial diagnostic phase, linear sweep voltammetry (LSV), cyclic voltammetry (CV), and potentiostatic electrochemical impedance spectroscopy (PEIS) were performed under inert gas atmospheres (H_2/N_2). These tests provided quantitative information on hydrogen crossover, electrochemically active surface area (ECSA), and electrolyte resistance. Such analyses are essential to isolate the specific contributions of the membrane from those of other cell components, offering a clear understanding of the intrinsic properties and limitations of the newly developed materials. The results of these diagnostic measurements served as the basis for interpreting subsequent open-circuit voltage (OCV) determinations, polarization curves (PC), and impedance analyses carried out under reactive conditions (H_2/O_2).

Durability testing was conducted exclusively on the 50 µm membranes, which demonstrated suitable stability during both diagnostic and operational phases. In contrast, the 25 µm membranes were excluded from long-term testing due to their non optimal performance and safety concerns under fuel cell operating conditions.

4.4.1 Pre-testing characterization: Linear Sweep Voltammetry

Linear Sweep Voltammetry (LSV) analysis was used to evaluate the crossover of hydrogen in H_2/N_2 configuration, supplying 50 sscm of hydrogen at the anode and 100 sscm of nitrogen at the cathode. The potential at the cathode was varied in a range of 0.1-0.7 V with a scan rate of 1 mV s^{-1}: under these conditions, the current measured at the cathode is exclusively related to the electrochemical oxidation of the hydrogen permeating through the membrane, hence the plateau typically observed in LSV curves. Three independent replicates were performed for each membrane, and the hydrogen molar flux values refer to the mean value with the corresponding standard deviation interval. Table 4.5 summarizes the limiting current density values i_L obtained for different samples and from this the corresponding molar flux J_{H2}, calculated from Faraday's law. For ease of comparison, the H_2 crossover values were normalized to the Nafion® 212 (50.8 µm thick) used as a benchmark for electrochemical measurements and taken as a reference (1x).

Sample	***i_L [mA cm^{-2}]***	***J_{H2} [µmol cm^{-2} s^{-1}]***	***Comparison with benchmark***
Nafion® 212	8.0 ± 0.2	0.041 ± 0.001	1x
sPPO 25 µm – IEC ~ 0.69 meq g^{-1}	3.3 ± 0.4	0.017 ± 0.002	0.41x
sPPO 25 µm – IEC ~ 1.3 meq g^{-1}	8.0 ± 0.8	0.041 ± 0.004	0.99x
sPPO 25 µm – IEC ~ 2.0 meq g^{-1}	15.0 ± 0.2	0.08 ± 0.01	1.88x
sPPO 50 µm – IEC ~ 2.1 meq g^{-1}	1.0 ± 0.1	0.0046 ± 0.0005	0.13x

Table 4.5 – Crossover limit current (i_L) and H_2 molar flux (J_{H2}) calculated according to Faraday's law, for the tested membranes compared the commercial benchmark Nafion® 212. All values are normalized to Nafion 212 and expressed as multiplication factors: values below 1x indicate lower hydrogen crossover, while values above 1x indicate higher crossover relative to the benchmark.

Data reported in Table 4.5 are also shown in Fig. 4.6, where the complete LSV curves, the boundary current and H_2 molar flux values (b) and a scatter plot of the crossover as a function of IEC (c) are reported. Analysis of the data highlights two fundamentally important aspects: the 25 μm sPPO membranes show a crossover that increases as the degree of sulfonation increases. The membrane exhibiting an IEC ~ 0.69 meq g^{-1} has a crossover molar flux about 60% lower than the benchmark Nafion 212. At IEC ~ 1.3 meq $g^{-1,}$ it is almost identical to that of Nafion, while at IEC ~ 2 meq $g^{-1,}$ the crossover is almost double. This trend can be attributed to the increased hydrophilicity of the membranes (as demonstrated by a high IEC and WU) because of the increased concentration of sulfonic groups (-SO_3H), on the polymer backbone. This increase in WU favors the formation of aqueous macrodomains that in such thin membranes are likely to generate preferential pathways for gas permeation. Furthermore, as solid-state functionalization is a diffusive phenomenon, this is strongly influenced by non-uniform surface area of the original membrane, resulting in a non-uniform distribution of functional groups that could create "high sulfonated isles" characterized by very high permeability. In contrast, the 50 μm sample (IEC ~ 2.1 meq g^{-1}) exhibits extremely low crossover values when compared to the benchmark. This result is not surprising since the greater thickness, the absence of surface defects and the nature of the hydrocarbon polymer backbone all contribute to lower permeability, as widely reported in the literature [135].

It is worth noting that the significantly higher crossover current density observed in the 25 μm membranes from LSV measurements indicates increased permeation of fuel species through the membrane, which can directly affect the subsequent cell performance. The diffusive crossover current reaching the cathode produces a mixed potential that lowers the open-circuit voltage (OCV) and causes instability in the polarization behavior. In contrast, the lower crossover current measured for the 50 μm membrane leads to higher OCV values and markedly improved polarization stability. These findings show that although reducing membrane thickness enhances proton conductivity and decreases ohmic resistance, it could also severely compromise transport selectivity. For all these reasons, these results suggest that thicker membranes provide a better balance between proton conduction and fuel crossover, maintaining both functionalization efficiency and morphological integrity. This balance has direct implications for the electrochemical performance of the cell, leading to improved OCV stability and polarization reproducibility under the tested conditions, as shown in the next paragraphs. All the LSV curves of each sample are reported in Annex A.4.

a)

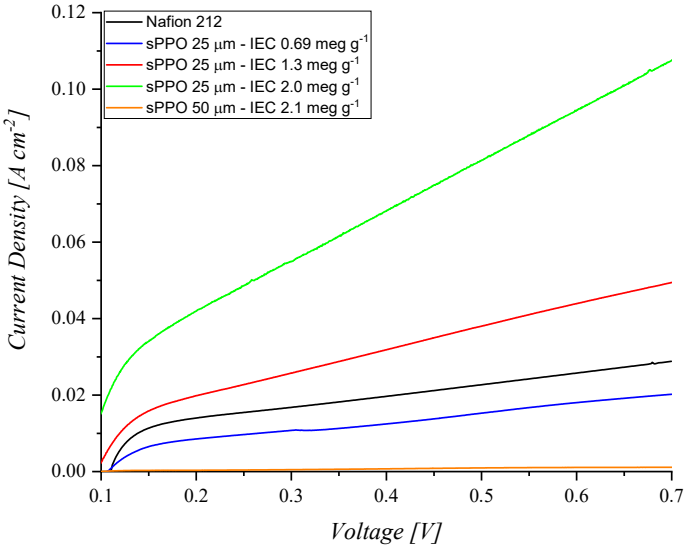
Nafion 212
sPPO 25 μm - IEC 0.69 meq g-1
sPPO 25 μm - IEC 1.3 meq g-1
sPPO 25 μm - IEC 2.0 meq g-1
sPPO 50 μm - IEC 2.1 meq g-1
Current Density [A cm-2]
Voltage [V]
0.12
0.10
0.08
0.06
0.04
0.02
0.00
0.1
0.2
0.3
0.4
0.5
0.6
0.7

b)

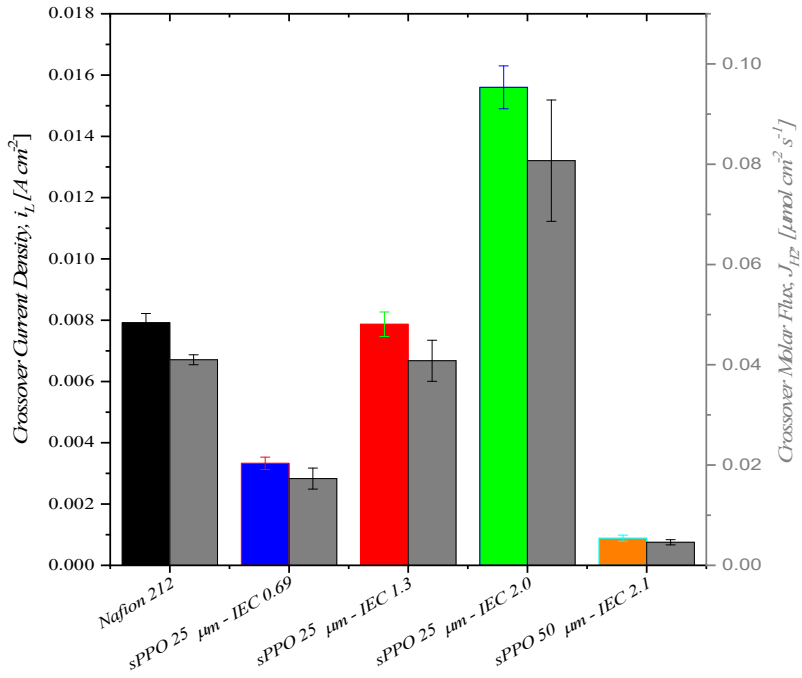
Crossover Current Density, iL [A cm2]
Crossover Molar Flux, JH2 [μmol cm-2 s-1]
0.018
0.016
0.014
0.012
0.010
0.008
0.006
0.004
0.002
0.000
0.10
0.08
0.06
0.04
0.02
0.00
Nafion 212
sPPO 25 μm - IEC 0.69
sPPO 25 μm - IEC 1.3
sPPO 25 μm - IEC 2.0
sPPO 50 μm - IEC 2.1

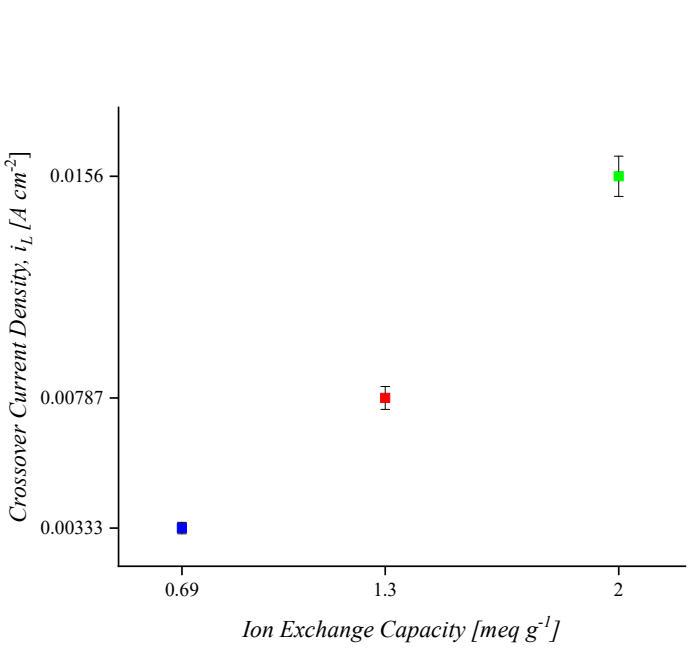

Figure 4.6 – LSV electrochemical characterization of hydrogen crossover for Nafion 212 and sPPO membranes at different thicknesses and IEC values: (a) linear voltammetry curves in H_2/N_2 configuration from which the limiting current, i_L, could be derived; (b) comparison of the limiting current densities (left axis) and the corresponding crossover molar fluxes, J_{H2} (right axis), measured via Faraday's law for each sample; (c) comparison of the crossover performance of the 25 μm sPPO samples as the IEC values change.

4.4.2 Pre-testing characterization: Cyclic Voltammetry

Cyclic voltammetry was used to estimate the electrochemically surface active area of platinum catalyst (ECSA) post-MEA fabrication. Measurements were conducted using the H_2/N_2 configuration at 80 °C and RH = 90 %, using 5 continuous cycles with a scan rate of 50 mV s^{-1} in the measurement protocol. In particular, the ECSA calculation was performed on the 3rd cycle, post-stabilization, by integrating the hydrogen desorption charge in the 0.05-0.4V *vs* RHE window, after subtraction of the capacitive contribution. The value measured in this way was then normalized for the platinum content present on the membrane (0.4 mg cm^{-2}), yielding the values shown in Table 4.6, both in areal (cm^2 $_{Pt}$/cm^2 $_{geo}$) and mass (m^2 g^{-1}) form to allow a comparative analysis with literature data.

Sample	*ECSA [cm^2_{Pt} / cm^2_{geo}]*	*ECSA [$m^2 g^{-1}$]*
Nafion® 212	180	45.0
sPPO 25 µm – IEC ~ 0.69 meq g^{-1}	165	41.2
sPPO 25 µm – IEC ~ 1.3 meq g^{-1}	122	30.5
sPPO 25 µm – IEC ~ 2.0 meq g^{-1}	150	37.6
sPPO 50 µm – IEC ~ 2.1 meq g^{-1}	163	40.8

Table 4.6 – ECSA calculated from cyclic voltammetry data (T=80 °C, RH=90%, H_2/N_2, scan rate 50 mV s^{-1}). Platinum loading of 0.4 mg cm^{-2}, Active area of 0.98 cm^2.

The ECSA values obtained for Nafion 212 fall within the typical range reported for commercial MEAs at low platinum loadings, providing a solid reference for the interpretation of subsequent data. The sPPO-based membranes, with a thickness of 50 µm (IEC ~2.1 meq g^{-1}), also show an ECSA comparable to that of Nafion at the same loading. This indicates a substantially homogeneous sulfonation, which again confirms that the smooth, defect-free membrane surface ensures good ionic contact at the catalyst/ionomer interface while preserving the accessibility of platinum for the electrochemical reaction. In contrast, the 25 µm membranes exhibit a more variable picture: at a low IEC (~0.69 meq g^{-1}), the ECSA value is approximately 41 m^2 g^{-1}, indicating that a low degree of sulfonation does not significantly affect catalyst distribution. At intermediate IECs (~1.3 meq g^{-1}), on the other hand, a significantly lower ECSA value is observed, plausibly due to a combination of non-uniform swelling and local sulfonation gradients (as described above) that penalize ionic percolation and the quality of contact between the ionomer and platinum. Finally, at high IEC (~ 2.0 meq g^{-1}), ECSA increases to slightly lower values that that recorded for the benchmark: also in this case, the combination of micro-defects and the large swelling of the membranes could limit platinum access.

It should also be considered that the MEAs were carried out using an automatic spray-coating technique, which ensures high macroscopic reproducibility but also local heterogeneity in the destruction of the catalytic ink. These aspects, combined with the described morphological differences, help to explain the observed case histories.

4.4.3 Pre-testing characterization: Potentiostatic Electrochemical Impedance Spectroscopy

Potentiostatic Electrochemical Impedance Spectroscopy (PEIS) in the H_2/N_2 configuration represent is an essential method for evaluating membrane both conduction properties of the membrane and the ionomer behavior at the electrode/membrane interface. The measurements were carried out in potentiostatic mode at 0.4 V, over a frequency range from 100 kHz to 0.1 Hz, under steady-state conditions at 80 °C and 90% relative humidity. The main parameter extracted from this technique is the high-frequency resistance (HFR), which reflects the protonic resistance of the membrane and ionomer phases. The HFR value is determined from the intercept of the real axis at zero imaginary impedance ($-Z_{imag} = 0$). Table 4.7 summarizes the HFR and calculated proton conductivity (σ_m) for the benchmark Nafion® 212 and the sulfonated PPO (sPPO) membranes. Figure 4.7 compares the corresponding Nyquist plots (Fig. 4.7-a), focusing on the high-frequency region (Fig. 4.7-b) where clear differences in ohmic resistance appear. These data confirm the high conductivity of Nafion® and, conversely, the higher resistances measured for the thinner sPPO films.

Sample	***HFR [Ω cm^2]***	***σ_m [S cm^{-1}]***
Nafion 212	0.080 ± 0.004	0.062 ± 0.005
sPPO 25 µm – IEC ~ 0.69 meq g^{-1}	1.11 ± 0.06	0.0020 ± 0.0001
sPPO 25 µm – IEC ~ 1.3 meq g^{-1}	0.45 ± 0.02	0.0060 ± 0.0002
sPPO 25 µm – IEC ~ 2.0 meq g^{-1}	0.26 ± 0.01	0.010 ± 0.001
sPPO 50 µm – IEC ~ 2.1 meq g^{-1}	0.130 ± 0.007	0.038 ± 0.003

Table 4.7 – HFR and proton conductivity (σ_m) values in H_2/N_2 configuration obtained from PEIS analysis at 0.4V, 80 °C, RH 90%.

a)

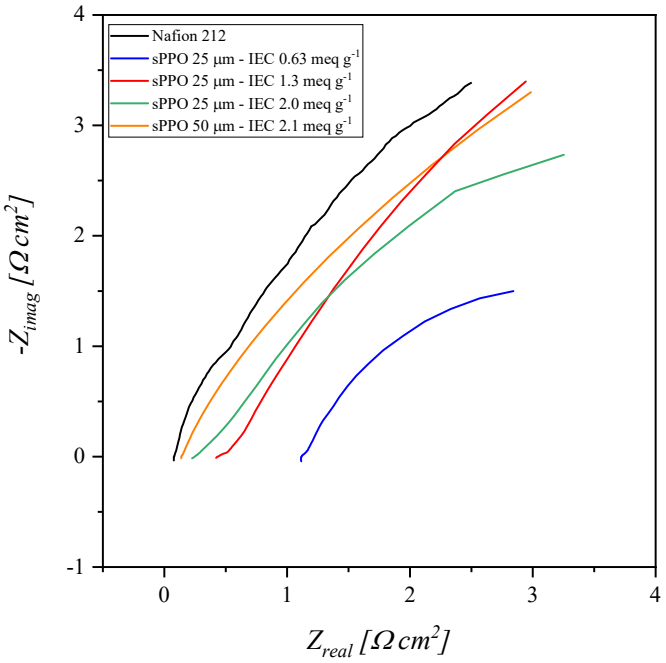

b)

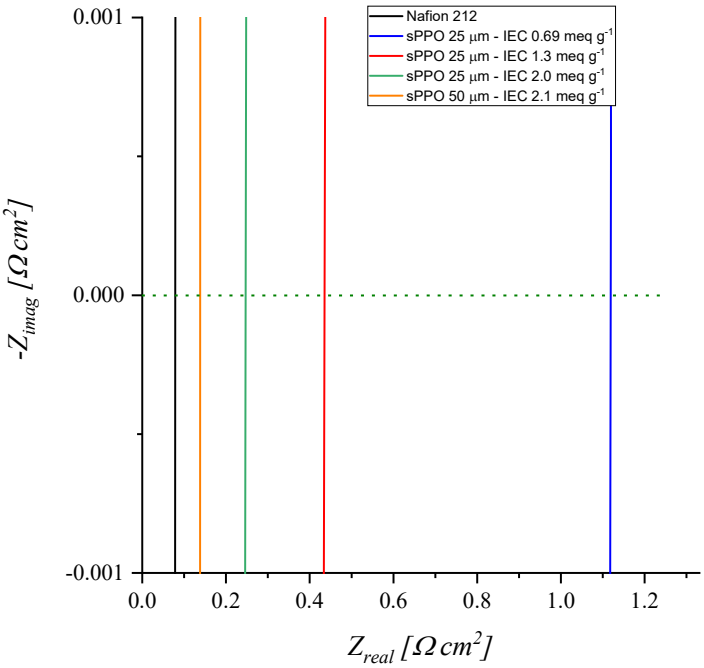

Fig. 4.7 – Potentiostatic electrochemical impedance spectra (PEIS) in H_2/N_2 configuration for Nafion 212 and sPPO membranes at different IEC values (a). The enlarged high-frequency region (b) highlights differences in ohmic resistance (HFR), obtained from the intercept at $-Z_{imag} = 0$ (dashed line).

The impedance analysis reveals a clear and systematic trend in the ohmic resistance of the tested electrolytes. For the 25 μm membranes, increasing the IEC from 0.69 to 2.0 meq g^{-1} progressively reduces the HFR from 1.11 to 0.256 Ω·cm^2. This behavior is consistent with the higher concentration of sulfonic acid groups in the polymer backbone, which enhances proton conduction. However, even the highly sulfonated 25 μm membranes show resistances about three times higher than the benchmark Nafion 212 (0.256 vs. 0.080 Ω cm^2), despite being thinner. This indicates that sulfonation alone cannot explain the relatively high resistance values; interfacial effects between the membrane and electrode also play a key role, especially those related to surface roughness and morphological inhomogeneity.

Supporting this interpretation, the 50 μm membrane with a similar IEC (≈ 2.1 meq g^{-1}) exhibits particularly interesting behavior. Despite its nearly doubled thickness compared to the 25 μm films, it shows an HFR of only 0.130 Ω cm^2, approaching the value of Nafion 212. This improvement is attributed to the smoother and more homogeneous surface morphology of the thicker membrane, which promotes better adhesion with the catalytic layer and ensures continuous ionic pathways across the interface. The more uniform sulfonation throughout the film results in a tangible electrochemical advantage, improving both conductivity and operational stability.

The comparison with Nafion 212 remains particularly significant: its low HFR (0.080 Ω cm^2) reflects the intrinsically high proton conductivity of perfluorosulfonic acid (PFSA) membranes under hydrated conditions. Furthermore, the perfect chemical compatibility between the Nafion membrane and the Nafion-based ionomer used in the catalyst ink ensures seamless interfacial proton exchange, a condition not met in sPPO/Nafion systems. This observation highlights the need for developing hydrocarbon-based sulfonated ionomers that are chemically and conductively compatible with the sPPO membrane structure. The proton conductivities (σ_m) calculated from the HFR values follow the same trend observed for the resistances. Nafion 212, as expected, shows the highest conductivity due to its strongly acidic and highly hydrated structure. The 25 μm sPPO membranes display initially low conductivity values, which increase with the degree of sulfonation up to 0.010 S cm^{-1}. Nevertheless, in thin films, the presence of morphological irregularities still hinders efficient charge transport.

Conversely, the 50 μm sPPO membrane at IEC ≈ 2.1 meq g^{-1} reaches a significantly higher conductivity (0.038 S cm^{-1}), close to that of Nafion 212. These results confirm that solid-state sulfonation can successfully produce non-fluorinated aromatic membranes with competitive proton-conducting properties, provided that both film thickness and morphological uniformity are carefully controlled.

4.4.4 Testing characterization: Open Circuit Potential and Polarization Curves

The open-circuit potential (OCV) is one of the primary indicators of the electrochemical performance of the studied membranes, as it reflects both gas crossover through the electrolyte and the quality of membrane–electrode contact. OCV values were recorded in an H_2/O_2 configuration, using a stoichiometric gas ratio of 2:1 (100 sccm hydrogen and 50 sccm oxygen), under operating conditions of 80 °C and 90% relative humidity. For each measurement cycle, the OCV was monitored for 120 s to ensure signal stabilization and reliable comparison between samples. Subsequently, polarization curves were acquired from OCV down to 0.2 V with a scan rate of 1 mV s^{-1}.

Due to the instability and low OCV values of the 25 µm sPPO membranes, long-term durability tests were not performed. Instead, a protocol of 50 consecutive measurement cycles was adopted to monitor the evolution of their performance and assess their proton exchange capacity. The 50 µm membranes, showing higher stability, were tested for reproducibility too. Table 4.8 summarizes the evolution of OCV values over 50 cycles.

Sample	***Initial OCV [V]***	***Final OCV [V]***	***Δ% over 50 Cycles***
Nafion 212	0.96	0.96	N.D.
sPPO 25 µm – IEC 0.69 meq g^{-1}	0.75	0.73	-2.7 %
sPPO 25 µm – IEC 1.3 meq g^{-1}	0.78	0.75	-3.8 %
sPPO 25 µm – IEC 2.0 meq g^{-1}	0.79	0.71	-10.1 %
sPPO 50 µm – IEC 2.1 meq g^{-1}	0.94	0.94	N.D.

Table 4.8 – OCV values measured in H_2/O_2 configuration with a stoichiometric ratio of 2:1 (80 °C, 90% RH, 100/50 sscm)

Nafion 212 confirmed a high and stable OCV of 0.96 V, indicating negligible crossover and an optimal electrode interface. In contrast, the 25 µm sPPO membranes started from lower values and exhibited a progressive decline in OCV, increasingly pronounced with higher IEC. This behavior correlates with the enhanced gas permeability discussed previously, due to higher sulfonic group density and less effective water management. In particular, the 25 µm membrane with IEC ≈ 2.0 meq g^{-1} showed an OCV decrease of about 10%, revealing severe permeability and structural instability aggravated by surface irregularities that facilitate gas diffusion.

The 50 µm sPPO membrane, on the other hand, displayed a high and stable OCV (0.94 V), comparable to Nafion 212 and constant across replicates. Its greater thickness and more homogeneous sulfonation minimize gas crossover and stabilize hydration, making cyclic testing unnecessary.

The OCV trends are confirmed by the polarization curves in Figure 4.8a. Nafion 212, used as benchmark, showed excellent performance across the entire current density range, maintaining stability up to 3 A cm^{-2} with a smooth and consistent voltage decay, typical of efficient charge transfer and well-balanced mass transport. The thinner, low-IEC sPPO membranes (0.69 and 1.3 meq g^{-1}) exhibited significantly poorer behavior, reaching maximum current densities below 0.5 and 0.7 A cm^{-2}, respectively, due to high internal resistance and gas crossover.

a)

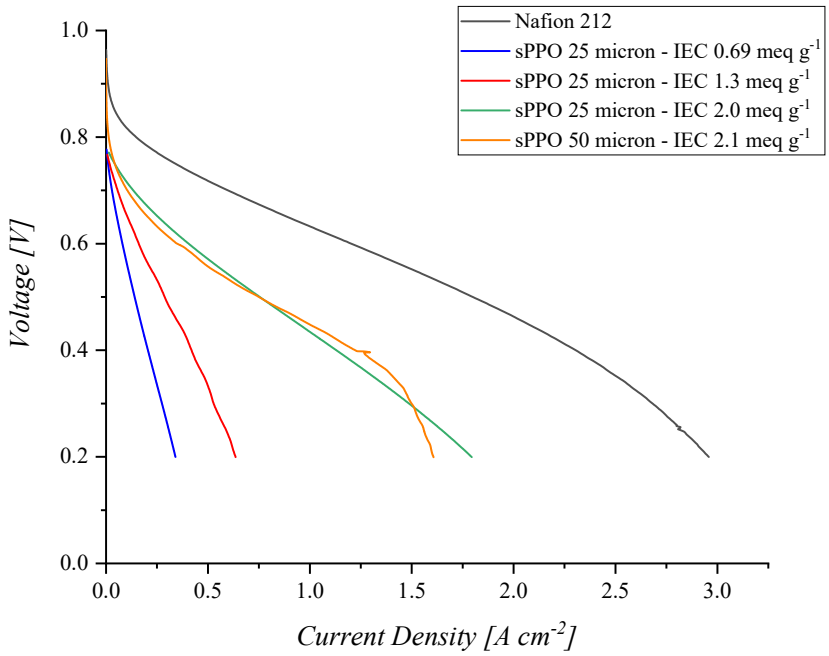

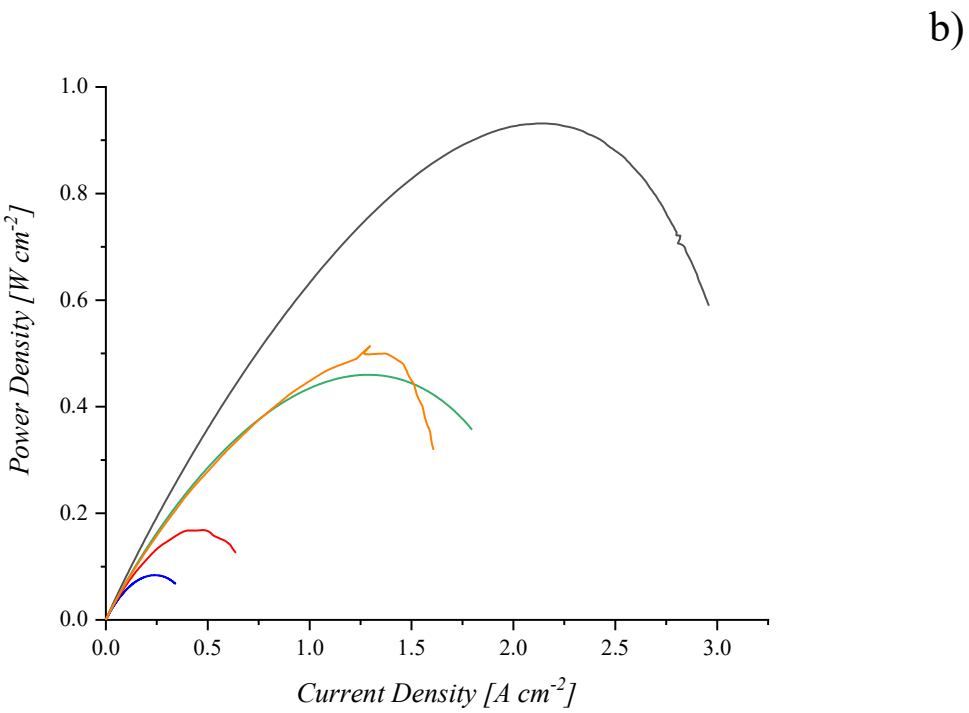

Fig. 4.8 – Comparison of the electrochemical performance of the membranes: a) polarization curves recorded in H_2/O_2 configuration at 80 °C and 90% RH; b) power density curves derived from the corresponding data.

The increase in IEC produced visible improvements in performance, although the highly sulfonated 25 µm membrane (≈ 2.0 meq g^{-1}) still started from a modest OCV. Interestingly, this membrane and the 50 µm film displayed similar polarization behavior, reaching comparable current densities (≈ 1.7 A cm^{-2} at 0.2 V). In the thin membrane, high proton conductivity is counterbalanced by excessive crossover, whereas in the thick film, improved selectivity and morphological uniformity compensate for the higher thickness. The corresponding power density curves (Figure 4.8b) confirm these observations. The thin sPPO membranes showed low peak power densities: 0.12, 0.18, and 0.47 W cm^{-2} for IEC ≈ 0.69, 1.3, and 2.0 meq g^{-1}, respectively. The 50 µm membrane with IEC ≈ 2.1 meq g^{-1} achieved a slightly higher maximum power (≈ 0.52 W cm^{-2}), with stable and reproducible output. The combined analysis of OCV, polarization, and power curves demonstrates that high IEC alone is insufficient to ensure stable performance in thin membranes. The combination of high IEC with increased thickness provides a better compromise, reducing crossover and total resistance, and yielding sPPO membranes whose behavior approaches that of commercial benchmarks.

4.4.5 Testing characterization: Potentiostatic Electrochemical Impedance Spectroscopy (PEIS)

Potentiostatic Electrochemical Impedance Spectroscopy (PEIS) in reactive H_2/O_2 conditions is a powerful technique for distinguishing the resistive and capacitive contributions of the cell under realistic operation. This analysis allows separation of the ohmic resistance (HFR), charge-transfer resistance (intermediate-frequency semicircle), and low-frequency diffusion effects. Measurements were performed at 0.4 V, corresponding to a high current density regime that highlights material differences. Figure 4.9-a shows the complete Nyquist plots for all samples, while Figure 4.9b highlights the region comparing Nafion 212 and the 50 µm sPPO membrane (IEC ≈ 2.1 meq g^{-1}). Two distinct behaviors emerge. The 25 µm membranes exhibit large, incomplete semicircles shifted toward high resistance values. The low-IEC sample (≈ 0.69 meq g^{-1}) shows small but highly resistive arcs due to poor proton conductivity, while the intermediate IEC (≈ 1.3 meq g^{-1}) exhibits a wide semicircle indicating significant charge-transfer resistance. The IEC ≈ 2.0 meq g^{-1} membrane shows an intermediate profile with visible capacitive scattering and diffusion limitations.

a)

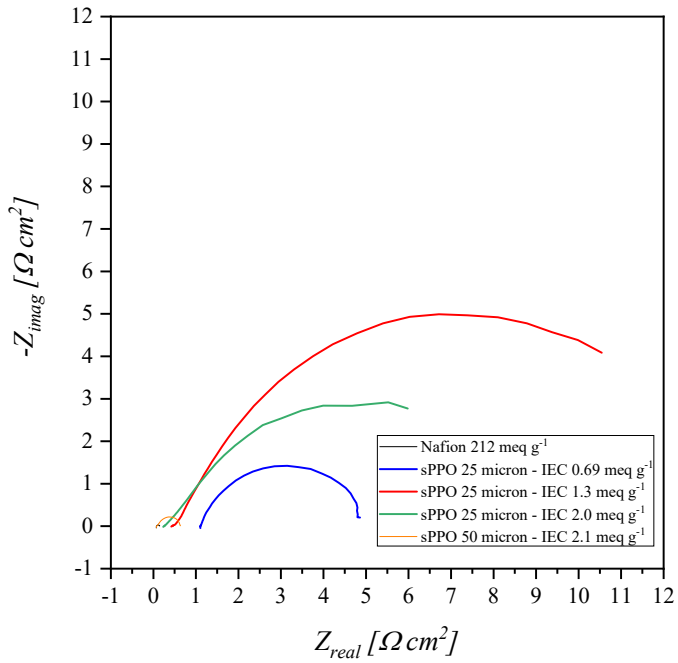

b)

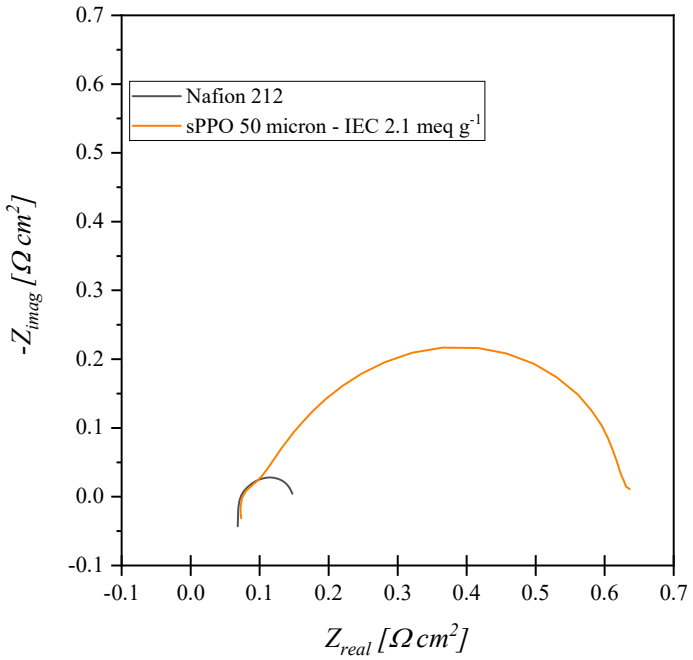

Figure 4.9 – Nyquist diagrams from PEIS 0.4V in reactive H_2/O_2 configuration (100/50 sscm, 80 °C, 90% RH). (a) Comparison of all samples showing higher resistances for the 25 µm membranes; (b) magnified view of Nafion 212 and sPPO 50 µm (IEC ~ 2.1 meq g^{-1}) with similar HFRs.

Nafion 212 and the 50 µm sPPO membrane exhibit much lower HFRs, with compact semicircles, typical of efficient charge transfer. This finding is important, as it demonstrates that thicker sPPO membranes retain good conductivity and interfacial contact despite their hydrocarbon nature.

The incomplete semicircles observed for the 25 µm membranes result from several combined effects. At 0.4 V, the cell operates close to the transport-limited regime. The low-frequency tail shows finite-length Warburg behavior, indicating restricted diffusion of reactants and mass transport limitations. This is further aggravated by hydration instability (localized flooding) and capacitive dispersion caused by structural inhomogeneity (surface knurling). Additionally, high hydrogen crossover induces parasitic currents, preventing regular arc closure.

Another factor is the Nafion-based ionomer in the catalyst layer, which, though standard in MEA fabrication, may introduce higher interfacial resistances with hydrocarbon membranes like sPPO. This mismatch particularly affects the thinner films, which are more sensitive to structural and interfacial discontinuities. The 50 µm membranes, by contrast, mitigate this chemical incompatibility through greater structural robustness and uniform sulfonation, resulting in more consistent

electrochemical performance. Table 4.9 shows the HFR values derived from the high-frequency intercept of each sample.

Sample	*HFR [Ω cm²]*
Nafion 212	0.065 ± 0.003
sPPO 25 µm – IEC ~ 0.69 meq g^{-1}	1.10 ± 0.08
sPPO 25 µm – IEC ~ 1.3 meq g^{-1}	0.465 ± 0.005
sPPO 25 µm – IEC ~ 2.0 meq g^{-1}	0.254 ± 0.004
sPPO 50 µm – IEC ~ 2.1 meq g^{-1}	0.078 ± 0.002

Table 4.9 – Ohmic resistances (HFR) estimated from Potentiostatic PEIS analysis at 0.4V in H_2/O_2 (100/50 sscm, 80 °C, 90% RH)

In conclusion, PEIS under reactive conditions demonstrates that the combination of high IEC, increased thickness, and homogeneous morphology enables a drastic reduction in electrochemical limitations, bringing sPPO performance close to that of commercial membranes.

4.4.6 Stability test: Chrono Amperometry

Long-term stability was evaluated through chronoamperometry in reactive H_2/O_2 conditions under the same flow, temperature, and humidity settings presented before. The cell voltage was fixed at 0.4 V for approximately 15 h, balancing performance and operational stress. Nafion 212 was not included in this test, as its durability is already well-documented in the literature. The 25 µm sPPO membranes were also excluded due to their strong instability, as evidenced by OCV decay below 0.5 V during the 50-cycle tests, indicating advanced structural degradation. For safety and consistency, only the 50 µm sPPO membrane (IEC ≈ 2.1 meq g^{-1}) was tested.

Figure 4.10 shows the current density trend over time (@0.4V). Initially, the current stabilizes around 0.6 A cm^{-2}, increasing to a local maximum of about 0.8 A cm^{-2} within the first 10 ks, corresponding to the a decreasing of HFR associated with progressive hydration of the membrane and ionomer. This is followed by a sharp decrease below 0.1 A cm^{-2} after ~25 ks, likely due to severe mass transport limitations and flooding phenomena. Oxygen starvation and partial anode dry-out may also contribute to higher ohmic resistance and performance loss.

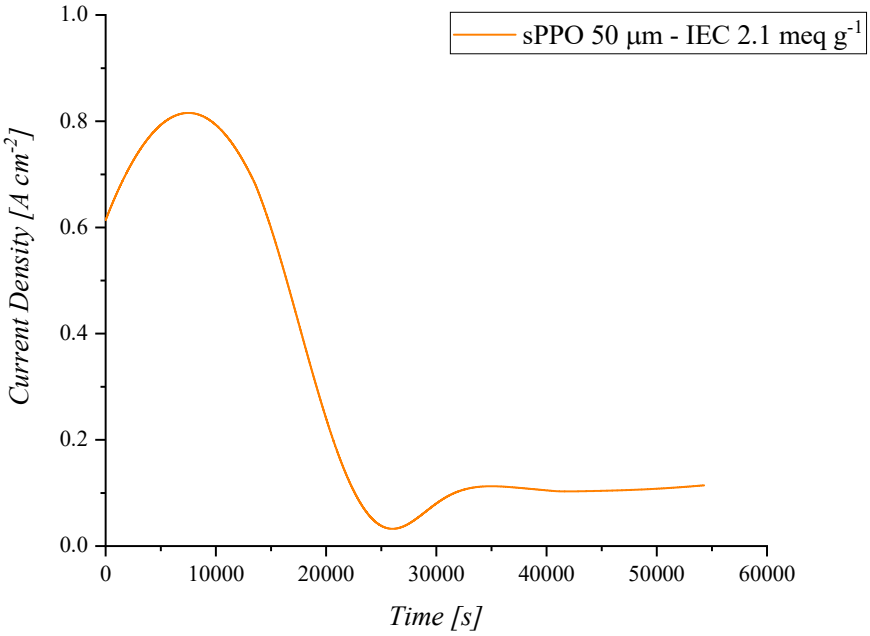

Figure 4.10 – Chronoamperometry profile at 0.4V of the 50 µm sPPO membrane (IEC ~ 2.1 meq g^{-1}).

Subsequently, a partial recovery occurs, with the current stabilizing around 0.1 A cm^{-2} and slowly increasing toward the end of the test (54 ks). However, full recovery is not achieved, implying partial degradation of the active area.

The final current remains below the initial peak, reflecting the complex interplay between water management and the interfacial resistance arising from the chemical mismatch between the Nafion ionomer and the hydrocarbon-based sPPO membrane.

4.5 Future Outlook

The overall results allow identification of key design directions for future sPPO-based membranes. The 25 µm membranes, although exhibiting low ohmic resistance at high IEC, suffer from excessive gas crossover, unstable water management, and rapid degradation, preventing long-term operation. In contrast, the 50 µm films display robust performance, with stable OCV, promising polarization and power behavior, and low HFRs comparable to commercial standards. Nonetheless, chronoamperometric results highlight limitations associated with activation, flooding, and partial recovery, suggesting the need to balance structural strength and protonic resistance. Future work should focus on developing thinner yet mechanically reinforced membranes—through the

incorporation of inorganic fillers (e.g., hydrophilic oxides or functionalized nanoparticles) or polymeric reinforcements (e.g., ePTFE supports or scaffolded composites)—to enhance water management, mechanical integrity, and dimensional stability without sacrificing conductivity. Another key aspect is the interfacial compatibility between the membrane and the catalyst layer. The use of a Nafion-based ionomer, though common in MEA fabrication, likely increases interfacial resistance with hydrocarbon membranes. The development of alternative ionomers chemically and conductively compatible with sPPO could ensure continuous proton transport and reduced ohmic losses, paving the way for fully fluorine-free MEAs with competitive performance and durability.

CHAPTER V

POLY[2,2'-(m-PHENYLENE)-5,5'-BISBENZIMIDAZOLE] – PBI

In this work, electrospun *m*-polybenzimidazole (*m*-PBI) mats were investigated as potential polymer electrolytes for high-temperature proton exchange membrane fuel cells (HT-PEMFCs). In the first stage, the electrospinning parameters were carefully identified, designed, and optimized to obtain uniform nanofibrous materials free from macroscopic defects. The resulting fibrous membranes were then characterized from a physicochemical standpoint using spectroscopic, thermal, and mechanical analyses. Their morphology, porosity, and air permeability were also evaluated. Subsequently, the membranes were impregnated with phosphoric acid to assess their acid retention capacity, and, for the first time, the mechanisms of acid adsorption were examined through kinetic and thermodynamic modeling. Finally, the proton conductivity of the doped membranes was measured as a function of temperature, allowing a correlation between morphology, acid content, and functional performance. All results were compared with those of their dense, solution-cast counterparts.

5.1 Electrospinning trial and morphological verification (SEM)

The development of *m*-PBI–based nanofibrous membranes began with exploratory electrospinning tests using the commercial S26 solution (26 wt% in DMAc with LiCl). This solution exhibited very high viscosity (~2100 Poise), which prevented the formation of a stable jet and resulted in dense or bead-rich deposits (globular defects) instead of a continuous and homogeneous fibrous mat. Dilution with DMAc proved to be the only effective approach to restore the proper balance among viscosity, surface tension, conductivity, and solvent evaporation rate, thereby re-establishing a stable electrospinning regime. The first trials were performed with a 15 wt% solution (Table 5.1), allowing us to investigate the combined effects of temperature, relative humidity, applied voltage, needle-collector distance, and flow rate. At this early stage, it became evident that lowering the flow rate and controlling the humidity inside the electrospinning chamber promoted the transition from dense morphologies to interconnected fibrous mats, although some defects remained. This confirmed the critical influence of environmental parameters on jet stability and solvent evaporation during the polymer's flight time.

Sample	*Temperature*	*Relative Humidity*	*V Ejector*	*V Collector*	*Needle-collector distance*	*Flow rate*
PBI_Trial A	25 °C	40 %	20 kV	-20 kV	125 mm	5 mL h^{-1}
PBI_Trial B	35 °C	25 %	20 kV	-20 kV	125 mm	0.4 mL h^{-1}
PBI_Trial C	40 °C	25 %	20 kV	-20 kV	125 mm	1 mL h^{-1}
PBI_Trial D	45 °C	20 %	20 kV	-20 kV	125 mm	1 mL h^{-1}

Table 5.1 – Exploratory electrospinning conditions for a 15 wt% solution of *m*-PBI in DMAc.

The SEM micrographs in Figure 5.1 illustrate the combined effect of temperature, relative humidity, and flow rate on fiber quality and distribution. All images were taken at the same magnification (10000×) to enable direct comparison. In micrograph (a) (sample PBI_Trial A, ambient conditions), solvent evaporation was incomplete during jet flight, leading to dense, film-like structures with poorly defined fibers. The high viscosity and relatively high humidity favored the formation of compact, non-fibrous deposits. Micrograph (b) (PBI_Trial B) shows a marked improvement. Thin, intertwined fibers begin to appear, though still embedded in a dense matrix. The lower humidity and higher temperature enhanced solvent evaporation and promoted a partial transition to a fibrous morphology.

Micrograph (c) (PBI_Trial C, 40 °C and 25 % RH) displays a predominantly fibrous structure, consisting of interconnected filaments with occasional beads—evidence of a jet in a partially stabilized whipping regime. The fibers are more continuous and uniform than in the previous samples, indicating a better balance among surface tension, viscosity, and evaporation rate. Finally, micrograph (d) (PBI_Trial D, 45 °C and 20 % RH) shows the most homogeneous morphology. The fibers are numerous, continuous, and evenly distributed, with very few defects. The higher temperature accelerates solvent evaporation, while the lower humidity promotes proper jet solidification. Under these conditions, the resulting structure closely resembles a true fibrous mat with well-developed porosity, serving as a basis for subsequent process optimization.

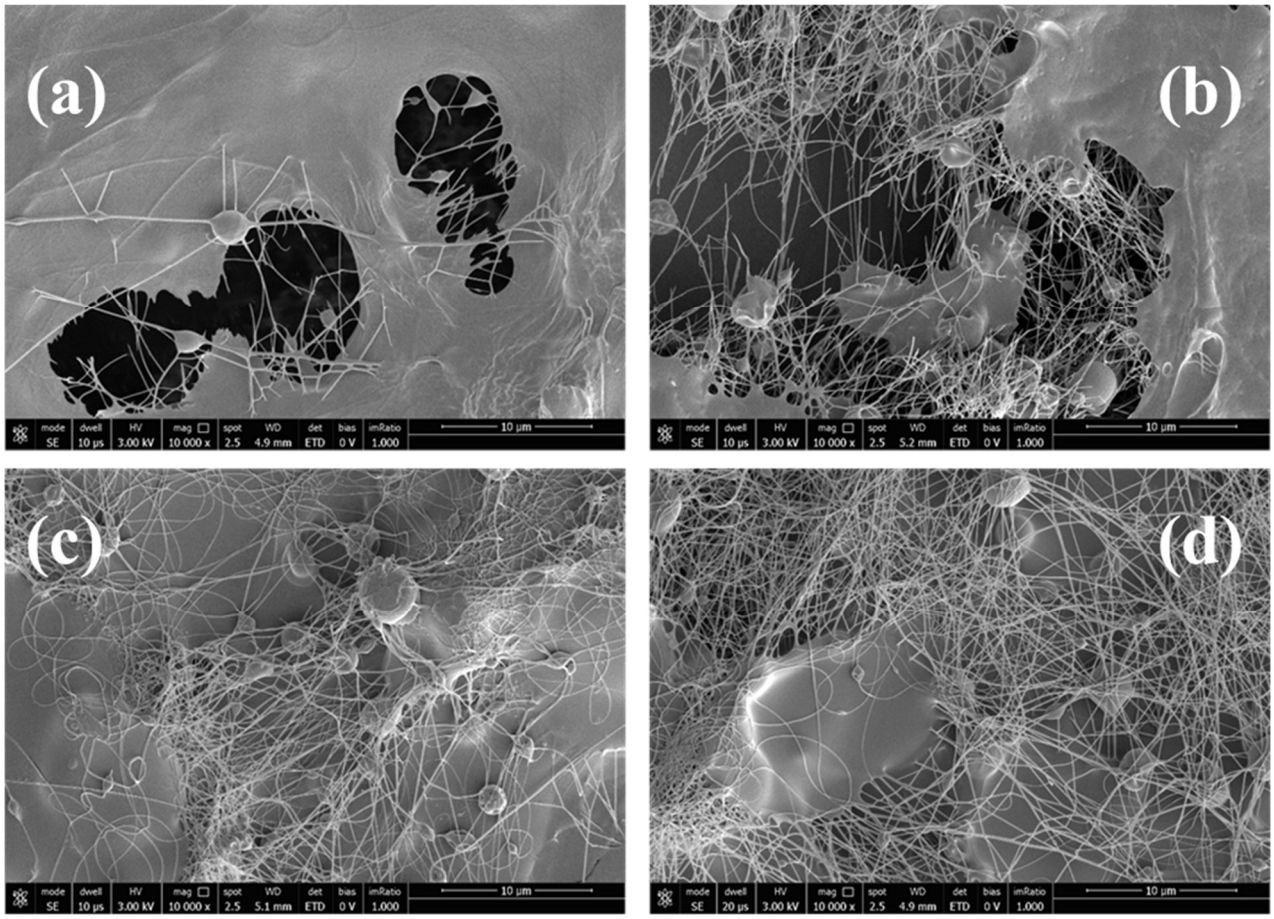

Figure 5.1 – SEM micrographs of electrospun *m*-PBI mats obtained from a 15 wt% solution in DMAc (10000× magnification): (a) PBI_Trial A, (b) PBI_Trial B, (c) PBI_Trial C, and (d) PBI_Trial D. The images illustrate the evolution of fiber morphology under different operating conditions, showing a progressive increase in fiber uniformity, continuity, and density.

These preliminary trials highlighted an essential point: when using a high-boiling solvent such as DMAc, careful control of the electrospinning environment is crucial to ensure adequate solvent evaporation and jet stabilization. Based on these findings, a centered operating condition was selected (45 °C, 20 % RH, –20 kV at the collector), and a 2k factorial Design of Experiments (DOE) approach was implemented to quantitatively assess the combined effects of polymer concentration, voltage, distance, and flow rate.

5.2 Optimization of the Electrospinning Parameters through a Design of Experiments (DOE) Approach

Preliminary trials demonstrated that using a high-boiling-point solvent requires careful control of the electrospinning environment to ensure the formation of a stable fibrous network. To systematically optimize the electrospinning parameters, a Design of Experiments (DOE) approach was employed.

Compared to a traditional single-factor approach, DOE enables the simultaneous investigation of multiple process variables (x_i) and their interactions, allowing the development of a predictive model for specific responses (y_i). This method is particularly suitable for complex processes such as electrospinning, where several parameters interact to influence fiber morphology and mat quality.

A 2^k factorial design (k = 4) with a central point was implemented, resulting in a total of 17 experiments. The factors and their levels are summarized in Table 5.2. For data processing, the variables were normalized using the standard –1/0/+1 coding system, which enables the comparison of regression coefficients and facilitates ANOVA and linear regression analyses. Level 0 represents the midpoint of each factor range and serves to detect possible curvature in the response surface (i.e., deviations from linearity), thereby increasing the robustness of the model.

Factor (x_i)	***Unit***	***Low Level (-1)***	***High Level (+1)***	***Central Level (0)***
Solution concentration	%wt.	14	16	15
V Ejector	kV	17	20	18.5
Height	mm	115	135	125
Flow rate	mL h^{-1}	1.0	2.0	1.5

Table 5.2 – Factors and levels used for the 2^4 factorial DOE model. Normalized coding (–1/0/+1) allows the regression coefficients to be compared directly, facilitating statistical analysis.

Each sample corresponds to a unique combination of process parameters (Table 5.3), selected to clearly separate the main effects of each factor (x_i) and highlight their interactions. This design makes it possible to determine whether the relationship between process variables and measured responses (y_i) is linear or requires the inclusion of higher-order (quadratic) terms in the model.

Sample	*Flow rate [mL h^{-1}]*	*V Ejector [kV]*	*Height [mm]*	*Concentration [% wt.]*	*Temperature [°C]*	*Humidity [%]*	*V Collector [kV]*
PBI_01	1	17	135	14	45	20	-20
PBI_02	2	17	135	14	45	20	-20
PBI_03	1	20	135	14	45	20	-20
PBI_04	2	20	135	14	45	20	-20
PBI_05	1	17	115	14	45	20	-20
PBI_06	2	17	115	14	45	20	-20
PBI_07	1	20	115	14	45	20	-20
PBI_08	2	20	115	14	45	20	-20
PBI_09	1	17	135	16	45	20	-20
PBI_10	2	17	135	16	45	20	-20
PBI_11	1	20	135	16	45	20	-20
PBI_12	2	20	135	16	45	20	-20
PBI_13	1	17	115	16	45	20	-20
PBI_14	2	17	115	16	45	20	-20
PBI_15	1	20	115	16	45	20	-20
PBI_16	2	20	115	16	45	20	-20
PBI_17	1.5	18.5	125	15	45	20	-20

Table 5.3 – Experimental matrix of the 2^4 factorial DOE with a central point for the preparation of electrospun *m*-PBI membranes. Temperature, relative humidity and collector voltage were kept constant across all experiments.

Five response parameters were selected to evaluate the quality and microstructural characteristics of each fibrous mat since, unlike dense, non-porous films, the performance of electrospun materials strongly depends on their microstructure. The selected parameters are described below:

- ***Average fiber diameter (y_1):*** the key morphological parameter defining the structural scale of the mat. Smaller fibers yield a higher surface-to-volume ratio and larger specific area, enhancing adsorption and impregnation capacity. However, excessively thin fibers can compromise mechanical strength. Thus, the average diameter reflects a balance between surface area and stability.
- ***Fiber Diameter standard deviation (y_2):*** provides information on fiber size uniformity. A large standard deviation indicates heterogeneous fiber formation and irregular porosity, which may lead to uneven impregnation or preferential transport paths. A narrow distribution reflects a stable and reproducible process.
- ***Total porosity (y_3):*** represents the volume fraction of voids, which determines fluid uptake and the number of accessible proton-conduction sites. High porosity enhances absorption but may reduce mechanical integrity if excessive. Interconnected porosity is essential for continuous transport through the membrane thickness.
- ***Air permeability (y_4):*** complements porosity by describing the degree of pore interconnection and the resistance to fluid flow through the membrane. It distinguishes between open and closed porosity and is a useful indicator of impregnation homogeneity. Measurements were performed using the Gurley method, which is simple, reproducible, and suitable for thin porous materials.
- ***Morphological Defects Fraction (y_5):*** bead formation is a common defect in electrospinning and a direct indicator of suboptimal operating conditions. Beads reduce mat uniformity, increase local density, and decrease effective surface area. Quantifying bead fraction is therefore essential for assessing fiber quality and process reliability.

5.2.1 Effect of Electrospinning Parameters on Fiber Morphology and Structural Properties

The characterization of the 17 samples obtained through the factorial experimental design allowed for a systematic evaluation of how process parameters influence the morphology and structural properties of the electrospun m-PBI membranes. Table 5.4 reports the five measured responses for each sample, with process factors expressed in dimensionless coded units. Additional statistical details are discussed in ***Paper I*** attached to this thesis.

Sample	x_1* [-]	x_2* [-]	x_3* [-]	x_4* [-]	y_1 [nm]	y_2 [nm]	y_3 [cm s^{-1}]	y_4 [%]	y_5 [%]
PBI_01	-1	-1	1	-1	132	30	1.20	76	1.06
PBI_02	1	-1	1	-1	125	33	1.52	75	1.07
PBI_03	-1	1	1	-1	100	25	0.75	83	22.2
PBI_04	1	1	1	-1	102	25	0.91	82	6.56
PBI_05	-1	-1	-1	-1	105	28	0.84	82	46.7
PBI_06	1	-1	-1	-1	89	22	1.11	83	6.79
PBI_07	-1	1	-1	-1	83	20	0.52	72	52.2
PBI_08	1	1	-1	-1	89	20	0.68	76	8.23
PBI_09	-1	-1	1	1	133	33	0.95	74	0
PBI_10	1	-1	1	1	116	27	1.27	84	49.3
PBI_11	-1	1	1	1	174	28	0.91	85	0
PBI_12	1	1	1	1	156	26	0.79	85	0
PBI_13	-1	-1	-1	1	143	35	1.16	70	14.6
PBI_14	1	-1	-1	1	132	29	0.89	77	1.89
PBI_15	-1	1	-1	1	114	28	0.59	76	13.7
PBI_16	1	1	-1	1	130	40	0.55	68	3.99
PBI_17	0	0	0	0	139	41	0.59	79	9.81

Table 5.4 – Experimental matrix with coded process factors (x_i*) and measured responses (y_i): y_1 = mean fiber diameter, y_2 = diameter standard deviation, y_3 = air permeability (Gurley test), y_4 = total porosity, y_5 = surface fraction of beads. Samples PBI_01–PBI_16 correspond to the vertices of the factorial design, while PBI_17 represents the midpoint.

The analysis of mean fiber diameter reveals a clear dependence on solution concentration. Increasing the PBI concentration from 14 to 16 wt% led to a significant rise in average fiber diameter (y_1), from approximately 100 nm to 140 nm. This trend is consistent with the increase in solution viscosity, which reduces the polymer jet's stretching and results in thicker fibers. The diameter standard deviation (y_2) provides complementary information about process stability. Low values (20–25 nm) correspond to uniform fiber thickness and stable spinning conditions, whereas higher values (35–41 nm) indicate heterogeneous fiber formation and a less homogeneous microstructure, often accompanied by localized dense areas or defects.

The total porosity (y_3) values are generally high (72–85%), confirming the open fibrous nature of the electrospun mats. However, porosity alone does not fully capture microstructural quality. In samples with numerous beads (e.g., PBI_07), porosity tends to decrease due to local densification, while in others (e.g., PBI_10), high porosity can result from macrovoids or non-interconnected pores. These differences demonstrate that porosity must be evaluated together with morphological uniformity to assess membrane quality.

Air permeability (y_4) reflects this relationship. In general, higher porosity corresponds to greater air permeability. Morphologically regular samples with low defect content and well-connected pores show moderate to high permeability values (0.8–1.2 cm s^{-1}). In contrast, samples such as PBI_07 and PBI_10 exhibit two opposite behaviors: extremely low permeability (0.52 cm s^{-1}) when beads obstruct flow channels, or artificially high permeability (1.27 cm s^{-1}) when macrovoids create preferential flow paths—neither of which indicates true membrane quality.

Taken together, these five responses provide an integrated picture of membrane performance. The mean fiber diameter defines the nanoscale morphology, its standard deviation describes process uniformity, porosity quantifies the void fraction, permeability reflects functional connectivity through the membrane thickness, and the bead fraction (y_5) directly indicates process stability. However, a complete understanding of these effects requires correlation with the actual microstructure, as shown by the representative SEM micrographs in Figure 5.2.

For simplicity, only the most representative samples are discussed here; the full set of SEM images for all 17 membranes is provided in Annex B.1.

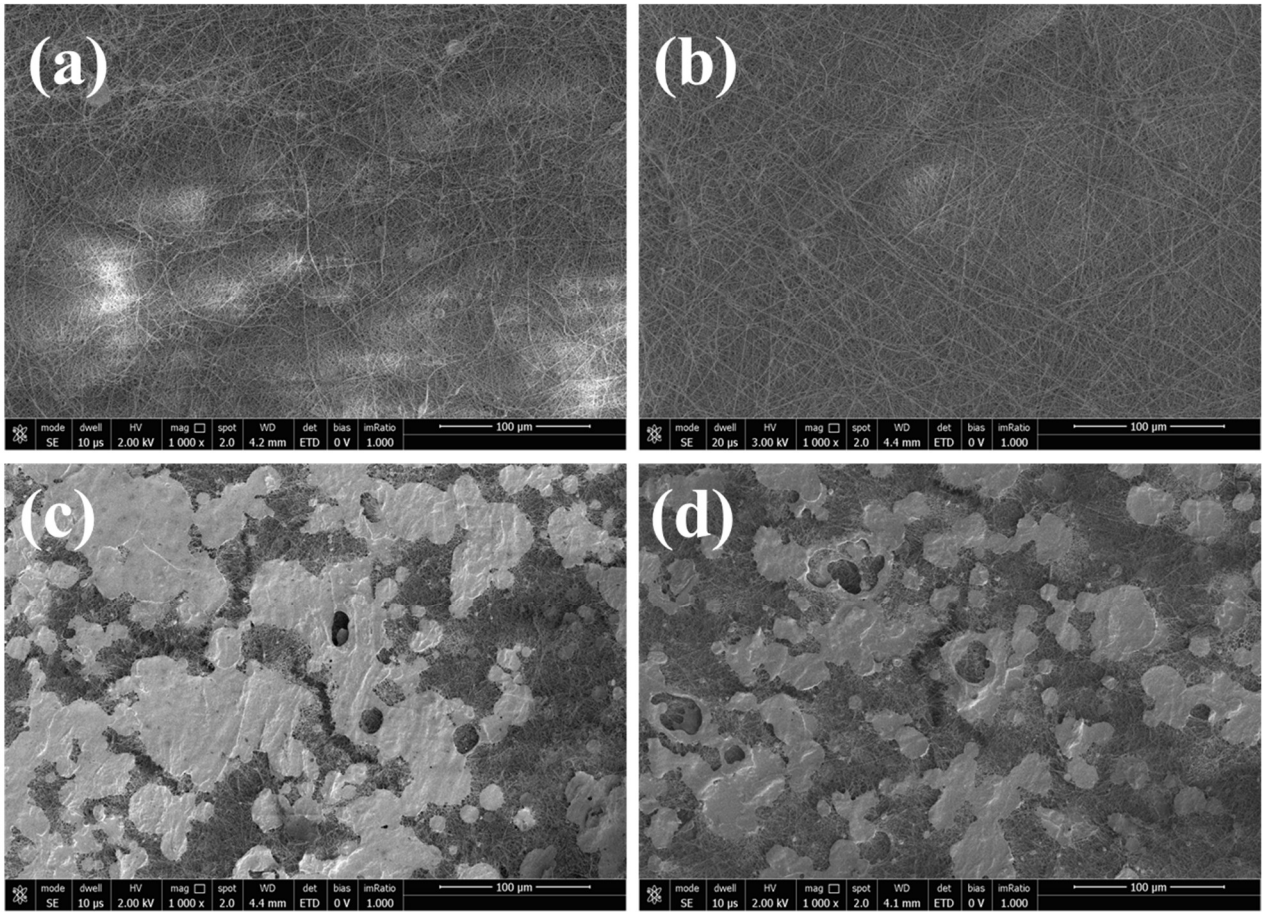

Figure 5.2 – Representative SEM micrographs of electrospun *m*-PBI membranes: (a) best-case 14 % wt. (FD= 132 nm, D= 1.06%, PBI_01); (b) best-case 16% wt. (FD= 156 nm, D= <0.5%, PBI_12); (c) worst-case 14 %wt. (FD= 83 nm, D= 52.2%, PBI_07), (d) worst-case 16% wt. (FD= 116 nm, D= 49.3 %, PBI_10). FD= Fiber diameter; D= Defect fraction.

The micrograph in Figure 5.2a shows a membrane electrospun under optimized conditions from a 14 wt% PBI solution. It represents the best morphology at this concentration, with fine, uniform fibers and minimal defects. ImageJ (Rasband, W.S., Image J, U.S. Nation Institute of Health, Bethesda, MD, USA) analysis confirms the narrow fiber diameter distribution, reflecting stable electrospinning conditions and a good balance between viscosity and solvent evaporation..

Similarly, Figure 5.2b shows the optimized sample obtained from a 16 wt% solution. The higher viscosity produces thicker but still regular fibers, with low defect content and enhanced jet stability. ImageJ analysis confirms both the increased average fiber diameter and reduced structural irregularities. The worst-case samples, shown in Figures 5.2c and 5.2d, highlight the effects of non-optimal conditions. The 14 wt% sample (Fig. 5.2c) exhibits numerous beads and irregularities, leading to a tortuous air path and reduced permeability. The 16 wt% worst-case sample (Fig. 5.2d) displays similar instability, with irregular, deformed fibers and a high density of morphological

defects. Despite the nominally larger fiber diameter, ImageJ analysis reveals reduced effective cross-section and increased jet instability, confirming the correlation between poor process control and deteriorated membrane morphology.

5.2.2 Statistical analysis of electrospinning parameters interaction (ANOVA)

In accordance with the adopted experimental design, each membrane was synthesized from a unique combination of the factors x_i. The operational domain of each variable was discretized into three levels, coded as –1, 0, and +1, corresponding to the lower, central, and upper settings, respectively (Tab. 5.4). Each experimental run thus generated a response y_i, whose dependence on the x_i factors and their interactions was systematically assessed by means of analysis of variance (ANOVA).

The best-fitting models proposed for the responses y_1, y_2, y_3, y_4 and y_5 are summarized in Table 5.5, together with the corresponding coefficients of determination (R^2) and adjusted coefficients of determination (R_{adj}^2). The predicted values exhibit a strong correlation with the experimental data, confirming the adequacy of the models. This high predictive accuracy is also attributable to the inclusion of binary (e.g., x_1x_2) and ternary (e.g., $x_1x_2x_3$) interaction terms, which substantially enhance the explanatory power of the final models. Statistical models were developed using JMP software, adopting a *stepwise regression* approach for the automatic selection of the most significant terms, ensuring greater predictive accuracy and robustness.

Output Response	***Model Equation***	R^2	R^2_{adj}
Y_1	$Y_1 = 120.2 + 9.47\,X_3 + 16.9\,X_4 + 5.01\,X_2X_3 + 7.90\,X_2X_4 + 9.04\,X_2X_3X_4$	0.918	0.8687
Y_2	$Y_2 = 28.11 - 1.440\,X_2 + 2.653\,X_4 + 1.492\,X_1X_2 - 0.759\,X_2X_3 + 1.317\,X_2X_4 - 2.661\,X_3X_4 - 1.442\,X_1X_2X_3 + 1.257\,X_1X_2X_4 - 1.472\,X_1X_3X_4$	0.983	0.936
Y_3	$Y_3 = 0.9149 - 0.2031\,X_2 + 0.1231\,X_3 - 0.0644\,X_1X_4$	0.833	0.778
Y_4	$Y_4 = 78.11 + 0.831\,X_1 + 2.436\,X_3 - 0.692\,X_4 - 1.434\,X_1X_2 + 2.957\,X_2X_3 + 0.767\,X_2X_4 + 2.255\,X_3X_4 - 1.824\,X_1X_2X_4 + 1.035\,X_1X_3X_4 - 0.886\,X_2X_3X_4$	0.978	0.943

Y_5	$Y_5 = 14.01 - 4.54\,X_1 - 4.24\,X_3 - 3.83\,X_4 - 4.13\,X_1X_2 + 8.75\,X_1X_3 + 7.9\,X_1X_4 + 6.13\,X_3X_4 - 3.99\,X_1X_2X_3 - 4.39\,X_2X_3X_4$	0.954	0.876

Table 5.5 – Statistical models (in coded form) for the responses chosen for the experimental electrospinning design of the *m*-PBI. The selected significant terms, as well as the coefficients of determination R^2 and R_{adj}^2 are given for each equation.

All the proposed models are expressed in coded units, and the intercept represents the expected response at the midpoint ($x_i = 0$). The average fiber diameter, y_1, shows a picture very consistent with the physics of the process: concentration has the most pronounced effect ($x_4 >> 0$), i.e. that more viscous solutions generate thicker average fibers. Distance also contributes positively ($x_3 >> 0$) as a longer "time of flight" of the polymer jet favors complete evaporation. A particular aspect of this model is the binary interactions, especially the interactions involving the voltage applied to the ejector. If we take a look at the x_2x_3 interaction (> 0), it describes the fact that a high voltage only really favors stretching of the polymer jet if it is accompanied by a "high" distance. Similarly, the x_2x_4 interaction (> 0) indicates that increased tension, on more viscous solutions, leads to the formation of fibers with a larger average diameter. Finally, the ternary $x_2x_3x_4$ interaction, which is positive, synthesizes and confirms the experimentally observed optimum working region (20 kV, 135 mm, 16%wt.) capable of ensuring a thicker and more regular fiber. The quality of the model is, in turn, reported by the high coefficients of determination, a sign that these interactions explain much of the observed variance.

For the y_2 response, i.e. the standard deviation of the fiber diameter, the model is rich in binary and ternary interactions. This confirms that there is no single dominant factor, but rather a kind of balance between different electrospinning operating conditions. However, some interactions are indicative, such as, for example, the combination of high voltage with high flow ($x_1x_2 > 0$) and high concentration ($x_2x_4 > 0$). Such conditions do indeed trigger whipping instabilities by promoting dimensional dispersion. However, increasing the distance under high concentration conditions ($x_3x_4 < 0$) negatively affects the diameter distribution by narrowing it, as the longer time of flight favors more uniform solidification. Finally, the negative ternary terms indicate the extent to which the dimensional variability is a purely interactional phenomenon.

The permeability y_3 is described by a rather consistent model in which two relevant pieces of information stand out: high tension reduces the average permeability ($x_2 < 0$) as it tends to deposit the fibers more densely, creating accumulation zones that partially close the pores. Similarly, increasing

the distance affects the increase in permeability ($x_3 > 0$) as it ensures proper evaporation of the solvent during deposition, producing a more open and continuous fibrous network. The binary flow-concentration interaction ($x_1x_4 < 0$) penalizes the average permeability, a sign that the microstructure has defects or tortuous pores resulting from non-homogeneous solidification. However, the coefficients of determination are excellent and consistent with experimental observations.

On the other hand, needle-collector distance is the main driver describing the porosity behaviour, y_4, since, as extensively described above, the longer time of flight ensures better pore distribution ($x_3 > 0$). Concentration, taken individually, tends to reduce porosity ($x_4 < 0$), but this effect is compensated for when combined with a high distance ($x_3x_4 > 0$). Similarly, the positive interaction between voltage and distance ($x_2x_3 > 0$) confirms once again how the presence of a high electric field only really works if the polymer jet has more time to develop. The ternary terms tell us of two opposite conditions: the $x_1x_2x_4$ interaction is negative, symbolizing that at high flow rate, voltage and concentration, porosity tends to decrease unless a high distance is acted upon. Conversely, the $x_1x_2x_3$ interaction (> 0) signals that high flow and concentration conditions can be employed if the distance is sufficient to support the viscosity gradients of the polymer solution. Thus, in general, we can say that porosity is described by a balance between the evaporation kinetics of the solvent during ejection and the mechanics of the polymer jet. Finally, the descriptive model of the fraction of surface defects on electrospun samples, y_5, is the most informative in terms of process robustness. The linear terms are all negative, indicating that increasing flow rate, distance and concentration reduces the presence of defects overall. However, the core of the model is the binary interactions x_1x_3 and x_1x_4, which makes us realize how high flow rate becomes dangerous when associated with high distance or high concentration, as they promote strong polymer jet instability. However, the negative ternary terms involving distance and applied tension ($x_2x_3x_4$) show a kind of "solution": the high tension and greater distance, combined with an appropriate viscosity of the polymer solution, drastically reduce the presence of defects as they allow for stable stretching and more uniform evaporation of the polymer jet. This explains the clear difference between the best and worst cases at the two concentrations, observed in the SEM micrographs. Operationally, these models provide comprehensive guidelines for maximizing sample regularities and reducing defects. The combination of high voltage-high distance plays a key role in the production of the samples, followed by the correct balance between flow rate and concentration of the polymer solution. Thus, the use of cross-national terms is not only justified from a statistical point of view, but is physically necessary in order to describe the best conditions between electric field, flow rate, time of flight and solidification of the jet.

The analysis of the statistical models yielded descriptive and predictive models with sufficiently high R^2 and R_{adj}^2 values, confirming the validity of the fitting. However, in order to assess the factors really determining the y_i responses, it was necessary to supplement the study of the coefficients with the p-value analysis shown in Figure 5.3. This parameter, *p*-value, represents the probability that a certain observed effect is due to chance rather than a real influence of the factor (x_i) under consideration. Values of *p*-value below the imposed threshold indicate that a specific parameter or interaction is statistically relevant. In this thesis work, the significance level was set at 0.1, a deliberately less stringent threshold than typical values of 0.05. This choice is motivated by the small dataset and the exploratory nature of the experimental design.

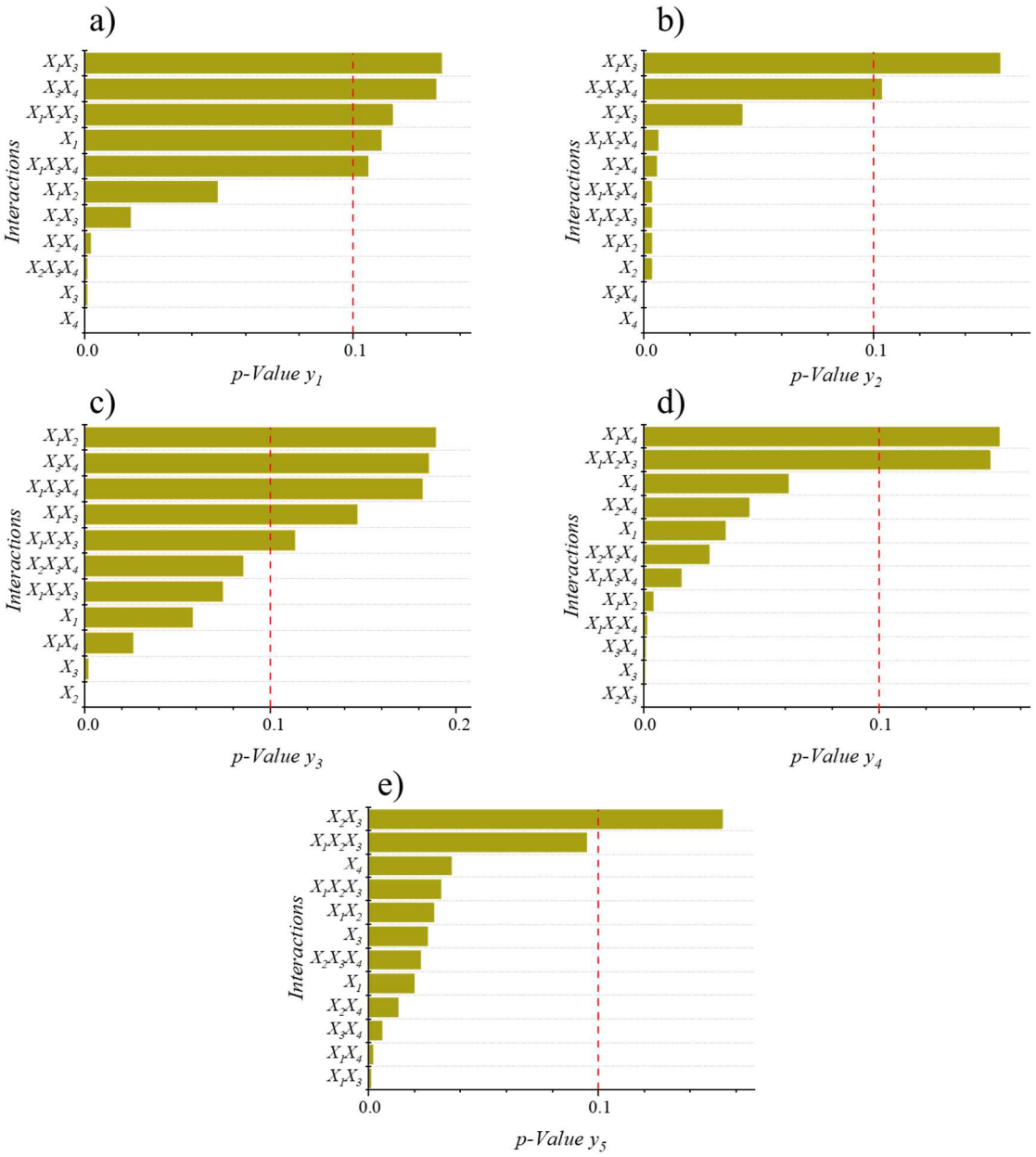

Figure 5.3 – Analysis of *p*-values for the main factors and interactions of the five responses considered: a) mean fiber diameter, y_1; b) standard deviation of diameter, y_2; c) air permeability, y_3; d) membrane porosity,

y_4; e) surface fraction of defects, y_5. The dashed red line indicates the statistical significance threshold set at $p = 0.1$. All the interactions below this threshold are statistically significant.

The most relevant aspect that emerged from the graphs is the confirmation that the truly significant effects coincide with the key interactions highlighted by the models, such as, for example, the strong reduction of *p*-values in the tension-distance interaction (x_2x_3) for the y_4 response (porosity); a similar discourse for the particularly low values for the flow-distance interaction (x_1x_3) and flow-concentration (x_1x_4) for the y_5 response (air permeability). On the other hand, the lack of significant p-values referring to the standard deviation of the defect diameter (y_2) highlights the heterogeneity of the phenomenon, which cannot therefore be explained consistently. We can therefore say that the statistical analysis of the *p*-value reinforces the validity of the previously described models by allowing the effects of the various interactions to be distinguished with greater certainty. The full *p*-values for each factor and each response, together with the detailed ANOVA regressions, are given in the ***Annex B*.2** and further described in ***Paper I*.**

5.2.3 Effect of Calendering on the Morphology and Functional Properties of electrospun *m*-PBI membranes

After identifying the optimal electrospinning conditions through the DOE approach—yielding membranes with uniform, continuous morphology and minimal defects—a further optimization step was introduced through calendering. This post-treatment technique serves as a complementary strategy to electrospinning, enabling fine control over the membrane microstructure in the post-production stage. The main goal is to reduce porosity and air permeability while improving the mechanical integrity and functional stability of the material, making it more suitable for use in high-temperature proton exchange membrane fuel cells (HT-PEMFCs). Sample PBI_12 was selected for the calendering study, as it represented the best-performing sample from the DOE campaign in terms of morphological uniformity, absence of defects, and consistent fiber dimensions.

Figure 5.4 shows the evolution of porosity and air permeability as a function of the lamination ratio (LR), defined as the ratio between the initial and final membrane thicknesses. The transition from the untreated membrane (LR = 1) to the calendered membrane (LR = 2) results in a sharp reduction in both parameters: porosity decreases from typical fibrous values above 80% to around 35–40%, while permeability drops proportionally. A further increase in compression (LR = 3) leads to even more pronounced densification, with residual porosity around 10% and nearly zero air permeability. This

indicates a substantial microstructural transformation, where the membrane gradually loses its fibrous porosity and approaches a partially dense configuration.

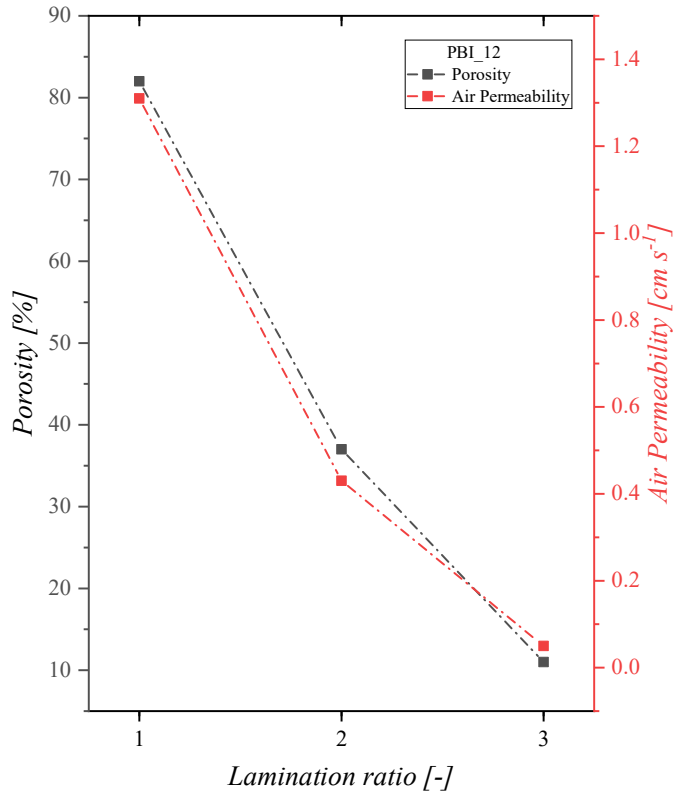

Figure 5.4 – Variation in porosity (black squares) and air permeability (red squares) in the electrospun PBI_12 membrane as a function of the lamination ratio (LR)

The morphological evolution is clearly visible in the SEM micrographs shown in Figure 5.5. At LR = 2 (Fig. 5.5a), the membrane retains a recognizable fibrous structure, although local compaction of fibers and slight thickening due to the applied pressure are evident. The network remains largely open and interconnected, suggesting that moderate compression can enhance contact between fibers without compromising the fibrous character. When the lamination ratio is increased to LR = 3 (Fig. 5.5b), the morphology changes drastically: regions of fiber collapse and fusion ("welding") appear, accompanied by a substantial reduction in inter-fiber voids. Although some traces of the fibrous origin remain, the membrane now exhibits an intermediate morphology between an electrospun network and a dense film, indicative of extensive structural reorganization.

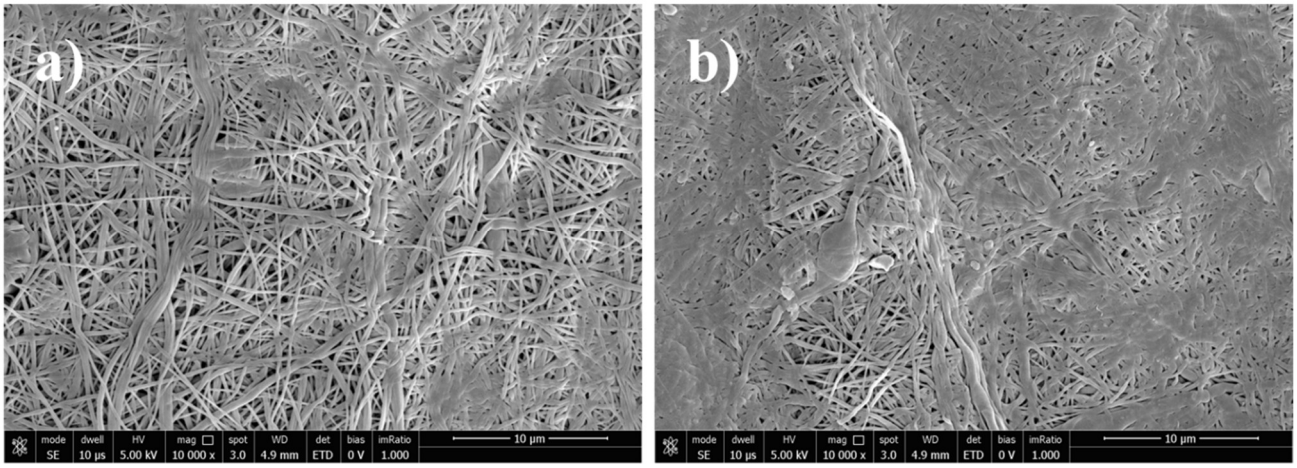

Figure 5.5 – SEM micrographs of electrospun *m*-PBI membranes after calendering: a) LR=2, a fibrous morphology structure is still visible, with partially compacted fibers; b) LR=3, the sample shows extensive compaction and fiber welding, with a transition toward a dense structure.

Overall, these results demonstrate that calendering is an effective tool for tailoring the microstructure of electrospun *m*-PBI membranes. By adjusting the lamination ratio, it is possible to fine-tune the balance between impregnation capacity—linked to surface area and residual porosity—and mechanical robustness, while preserving some of the beneficial characteristics of the original fibrous morphology, such as high specific surface area and good acid uptake capability.

5.3 Chemical and physical characterization of *m*-PBI membranes

After identifying the optimal electrospinning conditions and analyzing how the processing parameters affect membrane morphology, it was necessary to evaluate the chemical and physical stability of the material. The goal of this section is to confirm that the electrospinning process, although it changes the microstructure of the polymer, does not alter its chemical composition or thermal behavior. To this end, several instrumental analyses were carried out, including Wide-Angle X-ray Diffraction (WAXD), FTIR/ATR and NMR spectroscopy, thermogravimetric analysis (TGA), and mechanical testing. Each technique provides complementary information and helps confirm that the membranes maintain suitable mechanical and physical properties for potential use in high-temperature fuel cell environments.

All the analyses described in this section—and in the following sections on phosphoric acid impregnation and electrochemical testing—refer to sample PBI_12, identified as the best among the 17 samples produced. This sample was selected as representative of the entire experimental series because it showed the most favorable morphological and structural characteristics, including uniform

fiber diameter distribution and absence of defects. Therefore, PBI_12 was chosen for full characterization and functional testing.

5.3.1 Structural analysis: X-Ray Diffraction (WAXD)

High-angle X-Ray Diffraction (WAXD) analysis was conducted to assess whether the electrospinning process induces any structural changes to *m*-PBI. As shown in Figure 5.6, the diffractogram is characterized by the presence of a broad halo with a maximum localized around 2θ=20°. No characteristic peaks associated with crystalline phases are present. This profile indicates an amorphous material.

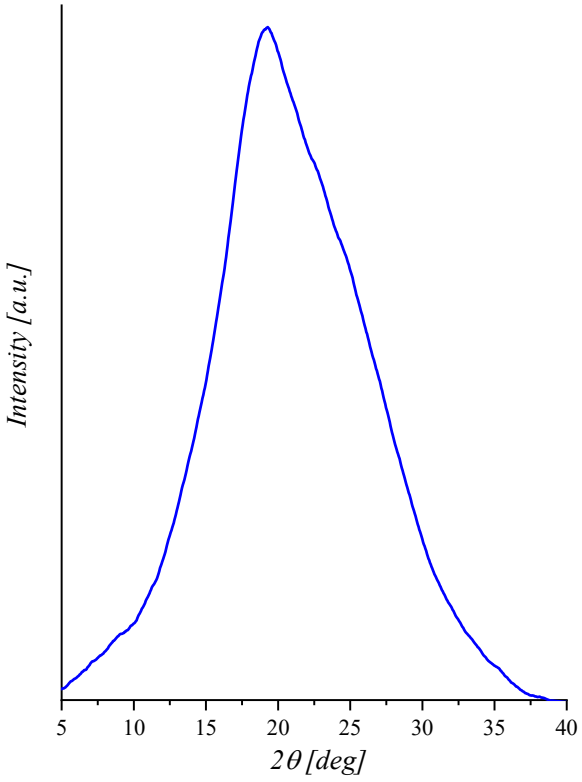

Figure 5.6 – Cu-Kα WAXD diffraction pattern of *m*-PBI electrospun membrane.

The amorphous nature of *m*-PBI is widely documented in the literature and represents an intrinsic feature of the polybenzimidazole family. It is worth pointing out that although the absence of crystallinity implies a lower degree of structural order, it also facilitates phosphoric acid uptake: the

disordered and loosely packed polymer chains allow greater interaction with acid molecules, promoting deeper and more uniform impregnation. This feature is particularly advantageous for HT-PEMFC applications, where efficient acid retention and homogeneous distribution within the polymer matrix are essential to achieve high proton conductivity.

5.3.2 Spectroscopic analyses: FTIR/ATR and NMR

The FTIR/ATR spectrum of the electrospun m-PBI membrane shown in Figure 5.7 clearly highlights the main absorption bands characteristic of the benzimidazole structure. The region between 3200 and 3400 cm^{-1} exhibits a broad and intense band, characteristic of N-H stretching vibrations associated with imidazole rings. The considerable amplitude of the signal indicates a strong presence of intermolecular hydrogen bonds, a characteristic of polybenzimidazoles, which significantly contribute to its mechanical and thermal stability. Moving towards lower wave numbers, a set of bands between 1638-1442 cm^{-1} is observed, attributable to stretching vibrations of the C=C and C=N bonds of the aromatic system and the imidazole heterocyclic ring. This region is certainly representative of the polymer, as it encompasses all the conjugate vibrations of the condensed aromatic systems that make up the polymer backbone.

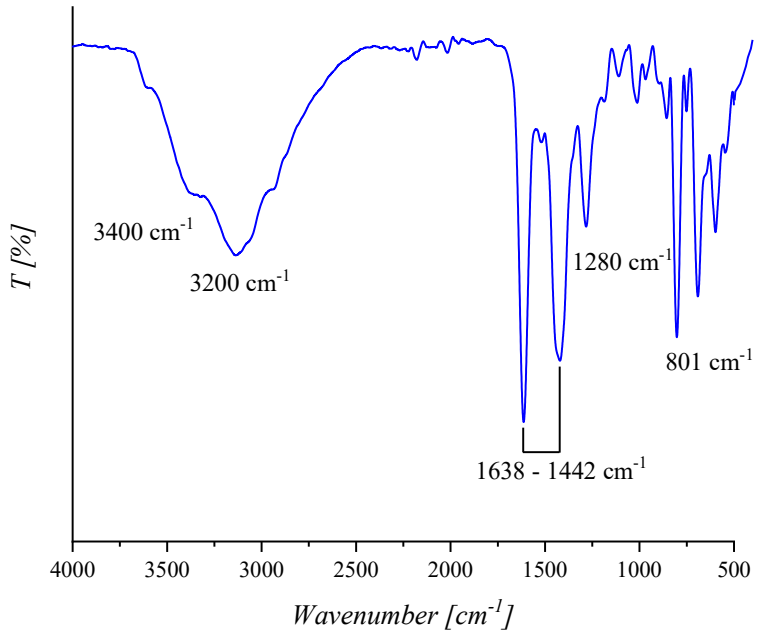

Figure 5.7 – FTIR/ATR spectrum of the electrospun membrane of *m*-PBI (PBI_12). The bands together confirm the aromatic and imidazole nature of the polymer, demonstrating that the electrospinning process does not alter the chemical structure of the polymer.

A further significant signal is found at 1280 cm^{-1} and is generally associated with the C-N stretching vibration of the imidazole ring. Its presence is crucial as it confirms the integrity of the imidazole functional groups that play a key role in the polymer's ability to interact with phosphoric acid during the impregnation phase. Finally, in the region near the fingerprints, we find a signal at around 801 cm^{-1}, which can be traced back to the out-of-plane (*oop*) bending vibrations of the aromatic C-H bonds. To complement the spectroscopic analysis conducted via FTIR/ATR, which allowed the identification of the polymer's main functional groups, a proton nuclear magnetic resonance.

^{1}H-NMR analysis was conducted in DMSO-d_6. This technique allows complementary infrared information to be obtained, providing direct confirmation of the chemical nature of the protons present in the polymer backbone. Figure 5.8-a shows the full NMR spectrum, showing the typical signals associated with the deuterated solvent, while Figure 5.8-b represents a detailed zoom into the 14-7 ppm region, where the diagnostic signals of the polybenzimidazole structure are concentrated.

a)

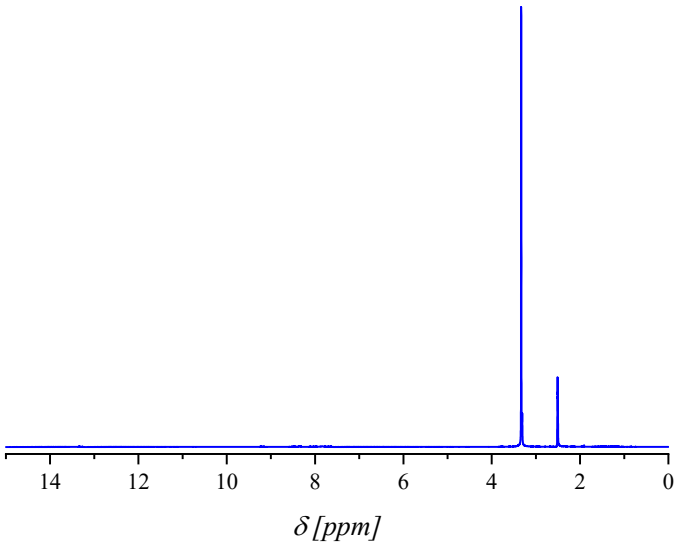

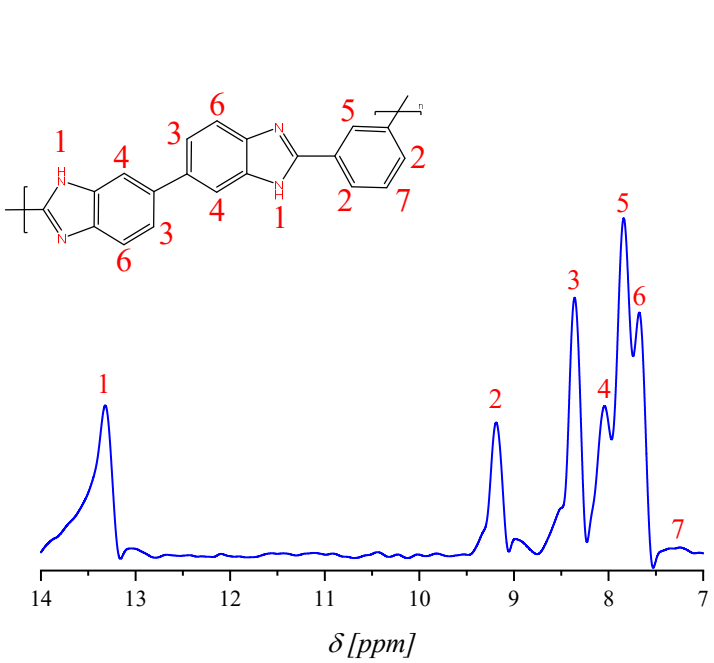

Figure 5.8 – ^{1}H-NMR spectra of *m*-PBI recorded in DMSO-d_6: (a) full spectrum in which the characteristic signals of the deuterated solvent are visible; (b) zoom in on the 14-7 ppm region, highlighting the main aromatic and imidazole signals of the polymer backbone.

The most deshielded signal, observed in the 14-12 ppm region (signal 1), corresponds to the N-H proton bound to the imidazole ring; its position in such a low field region is justified by a strong electron-attracting character of the C=N double bond and the possibility of forming intermolecular hydrogen bonds, as also suggested by FTIR analysis in the 3200-3400 cm^{-1} region. Proceeding to higher ranges (low ppm), characteristic signals of the aromatic hydrogens of the benzimidazole structure (signal 2) are observed at about 9.1 ppm, attributable to protons in the *ortho* position with respect to the imidazole group. This is followed by signal 3, at approx. 8.8-8.6 ppm, referring to hydrogens in the *para* position with respect to the imidazole group, which is less affected by the deshielding effect. Signals 4, 5, 6 in the 8.2-7.6 ppm region are associated with the remaining aromatic protons of the condensed benzimidazole system. The partial overlapping of the signals indicates a symmetry of the structure, but above all, a strong electronic conjugation. Finally, a less intense signal localized between 7.2-7 ppm corresponds to more shielded aromatic protons located in positions far from the electron-attracting centers of the structure (signal 7).

In conclusion, both techniques demonstrate the aromatic and imidazole nature of the polymer, allowing any differences in the macroscopic properties of the membranes to be attributed solely to the morphology resulting from the manufacturing process.

5.3.3 Thermo-gravimetric analysis: TGA

The thermal stability of the electrospun PBI samples was evaluated under an inert environment (N_2) from room temperature up to 800 °C. A representative thermogram is shown in Figure 5.9 for sample PBI_12. As apparent, the mass loss curve shows a profile that could be schematically divided into three distinguishable stages, fully consistent with literature data on the thermal degradation behavior of polybenzimidazoles:

- **Stage I:** A modest and gradual mass loss (-17 %wt.) is observed in a typical range between room temperature up to ~ 150-180 °C. This can be attributed to the removal of moisture and weakly retained water in the polymer matrix. It is important to remember that in *m*-PBI, the basic sites and the dense network of hydrogen bonds favor the adsorption of water molecules.;
- **Stage II:** In the range ~200-400 °C, a further mass loss (-7 %wt.) occurs. Possible reasons for this step in mass loss are the presence of traces of solvent (DMAc) retained in sub-micrometer volumes and/or desorption of physically adsorbed/chemisorbed atmospheric CO_2 on the basic imidazole sites of the polymer;
- **Stage III:** Finally, in the range between ~500-800 °C lies the primary degradation of the polybenzimidazole backbone. Indeed, in an inert atmosphere, PBI does not melt but undergoes cleavage and dehydrogenation followed by a further carbonization phenomenon. This results in the formation of a carbonaceous char that persists up to 800 °C and justifies the presence of solid residue at the end of the analysis (~40%wt).

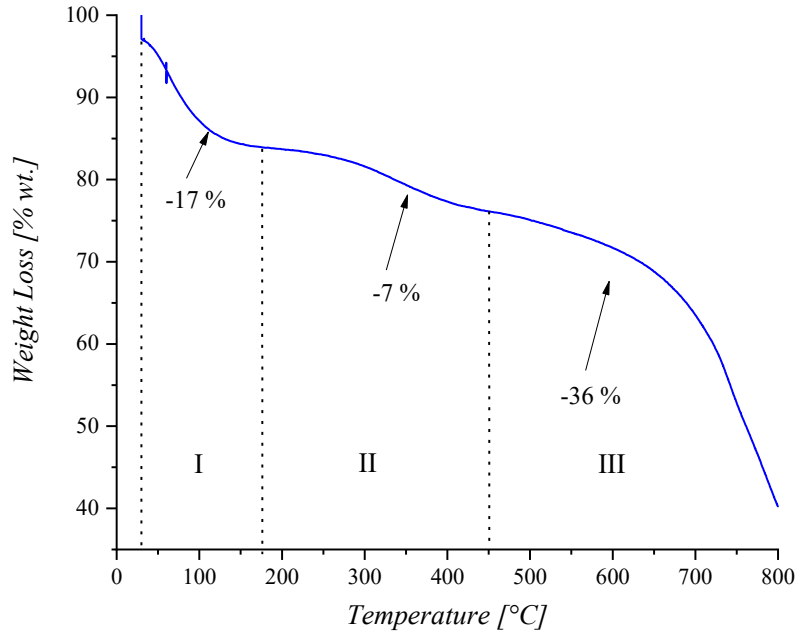

Figure 5.9 – TGA curve (RT-to-800 °C) of PBI_12 electrospun mat as recorded under N_2-flow at 20°C/min heating rate.

5.3.4 Mechanical Characterization of Dense and Electrospun *m*-PBI membranes

Figure 5.10 shows the stress–strain curves of *m*-PBI membranes produced either as dense films by solution casting (PBI_Cast) or as fibrous mats by electrospinning (PBI_ES). The curves are reported in terms of engineering stress (σ) and strain (ε), from which the Young's modulus—representing the material's stiffness—was determined from the initial linear region. The comparison highlights a clear difference consistent with the distinct morphologies of the two membranes. The dense PBI_Cast film exhibits a high Young's modulus of approximately 1 GPa, a maximum tensile strength of 7–7.5 MPa, and an elongation at break of 33–35%. The curve displays an initial linear elastic region followed by pronounced strain hardening, associated with polymer chain orientation along the tensile direction, and fracture occurring in the advanced plastic regime.

In contrast, the electrospun PBI_ES membrane shows a Young's modulus roughly an order of magnitude lower (0.1 GPa), a maximum strength of about 3.8–4.0 MPa, and an elongation at break of 11–12%. Its stress–strain curve reaches a peak followed by a rapid drop, indicating localized instability (such as necking or inter-fiber creep) and failure governed by its porous architecture.

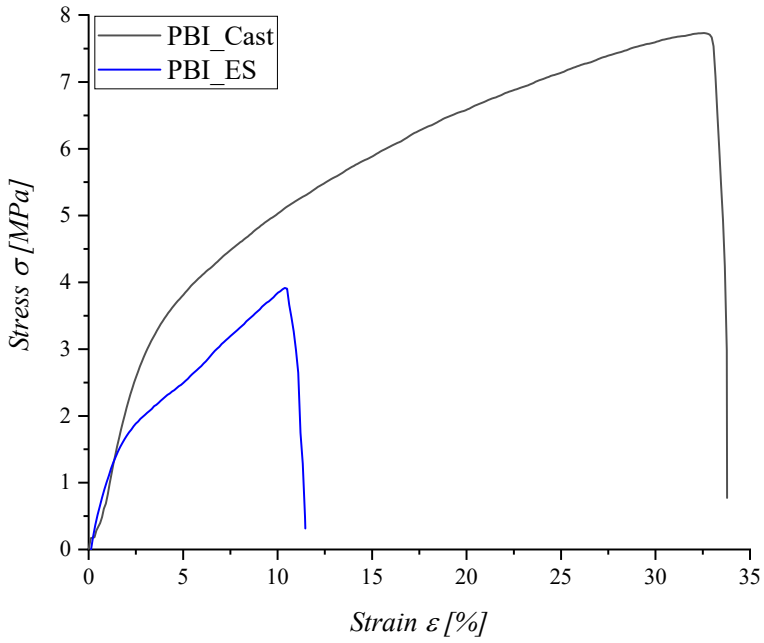

Figure 5.10 – Stress–strain curves of PBI_Cast and PBI_ES membranes obtained from tensile tests at room temperature.

These differences can be fully explained by the underlying morphology. Electrospun membranes contain interconnected pores that reduce the effective load-bearing cross-section and introduce stress concentration zones along the pore edges. Consequently, load transfer between fibers is incomplete, promoting local deformation and crack initiation. In contrast, the continuous structure of the cast film allows efficient stress transfer between polymer chains, resulting in higher stiffness and tensile strength before failure. It is worth emphasizing that the lower mechanical strength of fibrous membranes does not compromise their suitability for HT-PEMFC applications. Their large surface area enhances interfacial contact with the electrodes during MEA fabrication and improves phosphoric acid uptake. This acid impregnation has a plasticizing effect, increasing segmental mobility and inter-fiber adhesion, thereby reducing the mechanical gap relative to dense films while maintaining the functional benefits—high acid doping and proton conductivity—of the fibrous structure. Moreover, in HT-PEMFC operation, membranes mainly experience compressive forces (due to cell clamping) and moderate shear stresses, conditions under which a lower Young's modulus remains adequate for maintaining mechanical integrity.

Sample	*Young's Modulus E [GPa]*	σ_{max} *[MPa]*	ε_{break} *[%]*
PBI_Cast	1.02 ± 0.08	7.3 ± 0.4	34.1 ± 2.0
PBI_ES	0.11 ± 0.02	3.9 ± 0.3	11.2 ± 1.1

Table 5.6 – Mechanical parameters obtained from stress–strain curves for PBI_Cast and PBI_ES samples. Values represent averages of five independent tests with standard deviations. Young's modulus (E), maximum strength (σ_{max}) and elongation at break (ε_{break}) are reported.

5.4 Phosphoric Acid Doping and Impregnation Behavior of Dense and Electrospun *m*-PBI Membranes

Phosphoric acid (H_3PO_4) impregnation is a key step in enabling proton conduction in *m*-PBI membranes for high-temperature polymer electrolyte membrane fuel cells (HT-PEMFCs). In these systems, proton transport is ensured by the presence of free phosphoric acid molecules uniformly distributed within the polymer matrix. The membrane's ability to retain and stabilize these molecules over time is crucial for achieving long-term durability. This section discusses the acid-doping and impregnation behavior of both solution-cast and electrospun *m*-PBI membranes. While dense films offer high dimensional and chemical stability, electrospun membranes exhibit a much higher acid retention capacity due to their large surface area and interconnected porosity, leading to distinctive morphological and structural changes. A dedicated impregnation protocol was developed for the fibrous samples to manage their rapid absorption and prevent structural degradation when exposed to concentrated phosphoric acid (85 wt%, ~15 M). Alongside experimental analyses, a kinetic and thermodynamic model was developed to describe the impregnation process as the adsorption of phosphoric acid molecules on the polymer's active sites, neglecting bulk absorption phenomena. This model enables a quantitative evaluation linking the structural features of the membranes to their effective acid-doping capacity.

5.4.1 Development of the impregnation protocol

Initial impregnation tests followed the classical procedure used for dense PBI films, consisting of direct immersion in concentrated phosphoric acid (~15 M). Standardized 2 × 2 cm^2 samples with an average thickness of 50 ± 5 μm were used. Under these conditions, the dense solution-cast membranes remained stable, showing no visible structural or mechanical degradation. However, the same treatment proved unsuitable for electrospun membranes: even after less than one minute of contact, the fibrous structure completely disintegrated, dissolving in the acid medium and losing all

mechanical integrity. This striking difference can be explained by the distinct morphologies of the two materials. In cast PBI, the compact matrix limits acid penetration, resulting in slow kinetics and limited swelling. In contrast, the high porosity and surface area of electrospun membranes promote extremely rapid interaction with phosphoric acid, leading to uncontrolled swelling and total loss of cohesion. In this case, the main advantage of fibrous materials—their open, accessible structure—becomes a drawback during impregnation.

To overcome this issue, a dedicated protocol was developed to carefully control acid concentration, immersion time, and temperature, allowing gradual stabilization of the fibrous structure during contact with phosphoric acid. The optimized protocol consists of three main steps:

- **Water Uptake (WU) determination** – Membranes were immersed in deionized water for up to 30 minutes. At fixed intervals, samples were removed, blotted to remove surface water, and weighed. The increase in mass relative to the dry weight provides the water uptake.
- **Stepwise acid impregnation** – The same membranes were subsequently immersed in phosphoric acid solutions of increasing concentration (0.1–5 M), maintaining the same immersion times as in the WU tests. At each interval, membranes were removed, blotted, and weighed to monitor the impregnation kinetics. No thermal treatments have been performed on the membranes at this stage.
- **Drying and equilibrium determination** – After 30 minutes of impregnation, samples were dried in a vacuum oven at 110 °C for 24 h to remove residual water and determine the equilibrium acid content. This step validates the amount of adsorbed acid, free from water contributions.

It is worth pointing out that the new impregnation protocol was specifically designed to avoid intermediate drying steps in an oven, which are instead included in the conventional procedure for dense PBI films. This modification was introduced to prevent significant dimensional variations in the electrospun membranes that could occur as a result of repeated impregnation and drying cycles. Indeed, as discussed in the following section, electrospun mats exhibit a very high WU, which makes them particularly sensitive to dimensional instability when subjected to repeated wetting and drying processes. For this reason, the dynamic impregnation tests were conducted entirely without thermal treatments between steps, thus preserving the morphological integrity of the samples. However, at the end of the dynamic study, the membranes were finally dried in an oven, following the standard procedure, in order to validate the new method and ensure the accuracy of the equilibrium acid content determined by the protocol.

The experimental conditions used in developing this protocol are summarized in Table 5.7. Different acid concentrations and contact times were tested to identify the parameters that maximize doping capacity while maintaining morphological stability. To allow a consistent comparison, the same protocol was applied to both dense and fibrous membranes.

Experiment	*H_3PO_4 [mol L^{-1}]*	*Temperature [°C]*
1	0.1	25
2	0.5	25
3	1	25
4	3	25
5	5	25

Table 5.7 – Experimental conditions used for the development of the acid-impregnation protocol applied to dense and electrospun *m*-PBI membranes (2x2 cm^2 samples, thickness 50 ± 5 μm).

5.4.2 Water Uptake and Acid Doping Level of *m*-PBI membranes

Water Uptake (WU) is a key parameter describing the ability of *m*-PBI membranes to retain polar species and represents a first step in understanding their interaction with phosphoric acid. WU was determined as described in Section 2 by immersing the membranes in deionized water and measuring their mass gain at fixed intervals. The results were normalized to the moles of polymer repeat units to eliminate effects of membrane thickness or mass.

Figure 5.11 shows the WU results for (a) dense and (b) electrospun membranes. Dense solution-cast samples exhibited reproducible behavior, with stable values reached within 30 minutes of immersion. The 18 tested samples displayed consistent results, confirming the homogeneity of the polymer matrix and the absence of swelling or mechanical alteration. The relatively low WU values confirm the compact, “closed” structure typical of cast *m*-PBI films and agree well with literature data. Water uptake in these membranes is mainly governed by slow bulk diffusion and limited hydrogen bonding with imidazole groups, with negligible morphological changes.

In contrast, electrospun membranes showed markedly higher WU values—about one order of magnitude greater than those of dense films—yet remained reproducible across 18 independent tests. This increase can be attributed to their fibrous, porous architecture, which allows water to penetrate not only the polymer matrix but also the inter-fiber voids, resulting in substantially higher water

retention per mole of PBI. It is important to highlight that the slight variability observed among fibrous samples reflects normal microstructural differences, such as variations in fiber diameter or pore interconnection, rather than methodological uncertainty.

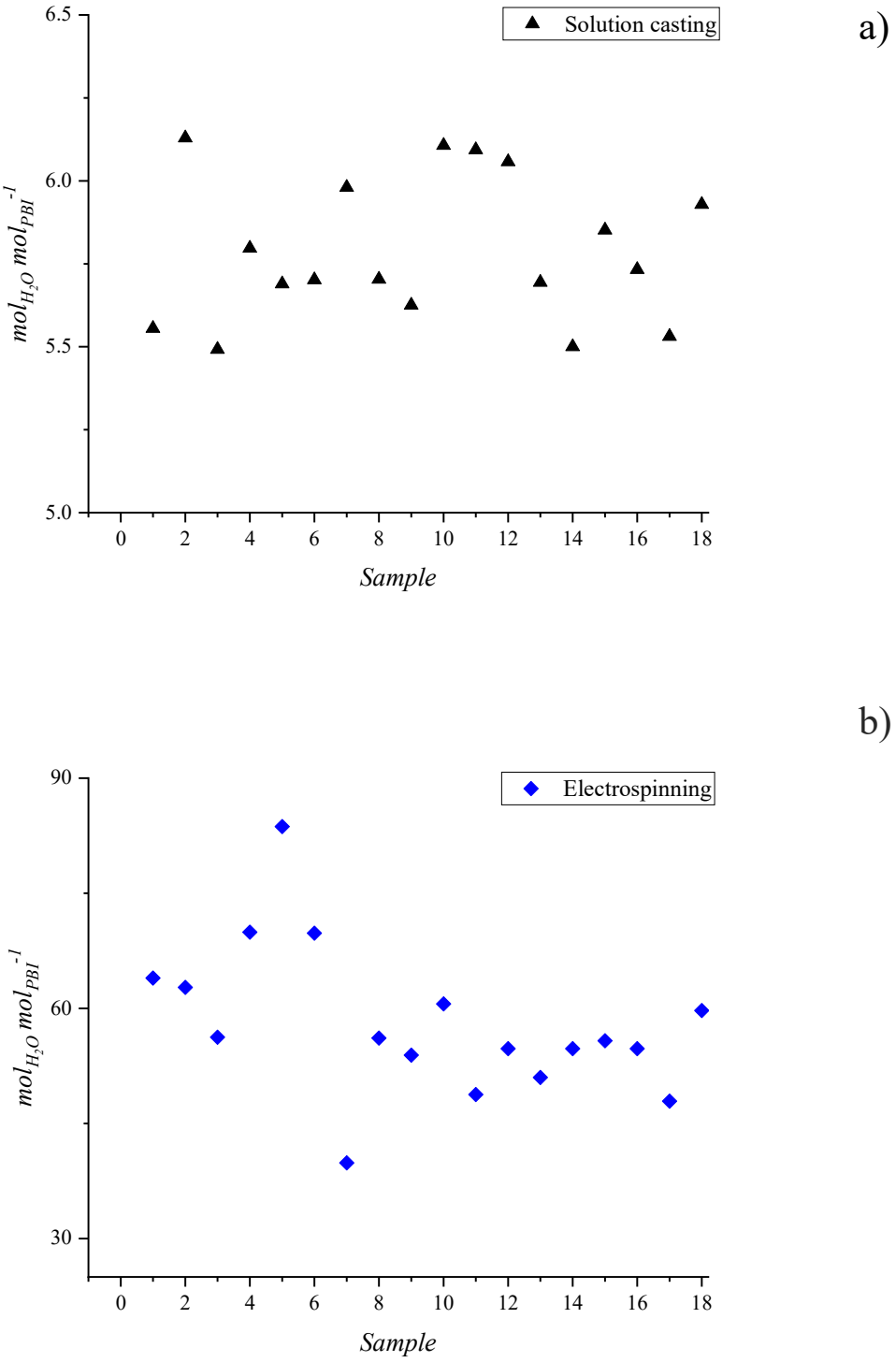

Figure 5.11 – Water Uptake (WU) of *m*-PBI membranes after doping with phosphoric acid solutions of different concentrations (30 min immersion): electrospun mats (blue squares) and dense films (black circles). Literature data from Li et al. [134] are included for comparison (red triangles).

The relationship between water uptake and phosphoric acid concentration provides further insight into the interaction mechanisms. As shown in Figure 5.12, dense membranes exhibit nearly constant WU values (≈ 5 mol H_2O/mol PBI) over the entire range of acid concentrations, indicating that their compact morphology limits water retention. This behavior is consistent with previous studies (Li et al., [133]). Electrospun membranes, however, display a more complex trend. At low acid concentrations (0.1–0.5 M), WU increases sharply, reaching 40–60 mol H_2O/mol PBI, followed by a slight decrease at 1 M and a new increase and stabilization at higher concentrations (3–5 M). This non-monotonic behavior results from two competing effects: (i) at low concentrations, phosphoric acid binds to imidazole sites, acting as a plasticizer and attracting additional water molecules; (ii) at higher concentrations, the reduced availability of free water in the solution limits further uptake. The point around 1 M likely represents the equilibrium between these two opposing effects.

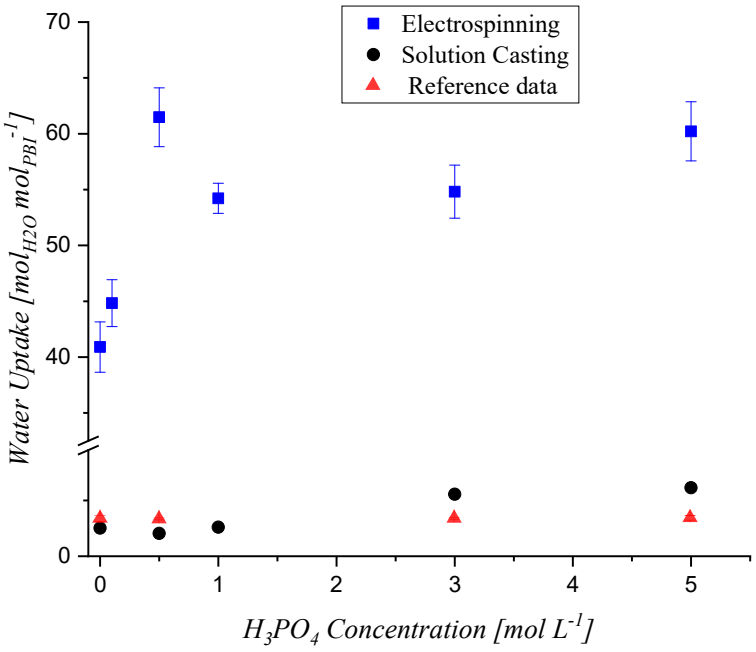

Figure 5.12 – Water Uptake (WU) evaluation of different PBI membranes after doping treatments with phosphoric acid at different concentrations for 30 min: electrospun mats (blue squares) and dense membranes obtained by solution casting (black circles). Literature data from ref. [134] (red triangles) are reported for comparison.

5.5 Acid adsorption on *m*-PBI membranes: Kinetic Evaluation

The application of the experimental protocol for the acid impregnation of membranes developed in this thesis work made it possible to dynamically monitor over time the amount of phosphoric acid that actually interacts with m-PBI. In particular, it was decided to neglect diffusive phenomena of the fluid in the matrix, describing only the adsorption process of the acid on the membranes, a crucial aspect governing the final functional properties of the material. From a mathematical point of view, a reactive differential kinetic model described by an *n*-order power law was adopted, in which the adsorption phenomenon is described as a function of the adsorbent concentration over time and at equilibrium (see section 2.2.4).

This approach has the great advantage of being sufficiently general to include specific cases such as pseudo-first-order (PFO, *n*=1) and pseudo-second-order (PSO, *n*=2) kinetics, widely used in the literature to describe adsorption phenomena in polymeric and/or porous materials. Specifically, three conditions were estimated: a) *n*=1, corresponding to a simple exponential decay towards equilibrium; b) *n*=2, which introduces a square dependence with respect to saturation equilibrium; c) *n* variable, estimated as a free parameter from experimental data and minimizing an objective function in order to obtain the best possible correlation coefficients (R^2 and R_{adj}^2).

5.5.1 Adsorption of dense *m*-PBI membranes

The WU analysis is already indicative of the impregnation behaviour of the two types of membranes (dense and fibrous), especially when read in perspective with subsequent acid doping tests. Such values, in fact, provide a direct measure of the membrane's propensity to accommodate polar molecules and maintain a retention equilibrium. In support of this, it was possible to measure a fundamental parameter for this type of treatment, namely the Acid Doping Level (ADL), which quantifies the moles of phosphoric acid retained in relation to the moles of *m*-PBI. The two parameters (WU and ADL) are complementary in that, based on the protocol developed, they are correlated by Equation 5.1, already shown in Section 2.2.4 (Eq. 2.4):

$$ADL = \frac{\text{mol H}^+}{\text{mol PBI}} = [\frac{m_{tot} - m_{dry} \cdot (1+WU)}{m_{dry}}]/(\frac{308}{98}) \qquad \text{Eq. 5.1}$$

The introduction of the term (1 + WU), where WU is the experimentally measured water uptake under the same conditioning protocol adopted for acid impregnation, reflects the fact that phosphoric acid impregnation occurs in a hydrated polymer matrix, whose effective mass and free volume are influenced by water sorption. This definition therefore accounts for the actual swollen state of the

membrane during acid uptake, rather than referring exclusively to the dry polymer backbone. This relationship is crucial as it allows us to normalize against the WU value for each membrane, making the comparison between the various morphologies more informative and functional. In this way, in fact, we only and exclusively observe the fixed acid contribution per unit of absorbed water. It is a measure, in essence, of the intrinsic affinity of the fibrous system towards the acid, diverted from the purely volumetric effect of the imbibition process.

The use of the described acid impregnation protocol developed in this thesis work made it possible to determine the amount, and thus the moles, of H_3PO_4 present in the dense membrane of *m*-PBI as a function of time. From here, it is possible to determine Acid Doping Level (ADL) time curves that reflect the progress of the adsorption phenomenon. It is important to underline that this formulation does not rely on the assumption that the water uptake is identical for all membranes or independent of the acid doping level. On the contrary, WU is experimentally determined for each membrane type and morphology, and it is implicitly coupled to the microstructural features of the material, such as porosity, fiber diameter distribution, and degree of compaction. Especially in electrospun membranes, even small variations in local porosity or fiber packing density can significantly influence the extent of hydration and, consequently, the apparent acid retention. The present definition of ADL was therefore adopted to provide an internally consistent normalization within the investigated sample set, rather than to enforce a universal comparison across different membrane architectures.

The doping level over time was calculated from the mass change of the membranes, normalized for WU, while the ADL at equilibrium was determined following a prolonged 24-hour heat treatment to remove water and quantify only the component actually retained by the polymer matrix. The dense membranes show a classical behaviour of diffusion-limited systems, as shown in Figure 5.13. The dynamic curves (a) show a relatively slow initial phase, followed by an essentially asymptotic trend identifying an equilibrium situation. However, even at increasing concentrations of H_3PO_4, the system requires almost 24 h of imbibition to stabilize, a behaviour that is consistent throughout the range of concentrations analyzed, confirming that the kinetics are dominated by mass transfer in the bulk of the membrane. In addition, the low porosity and small specific area limit acid access to the internal active sites, with diffusion predominantly localized in the amorphous regions of the polymer. The values at ADL equilibrium (Figures 5.13-b) obtained after drying the membranes further clarify an increasing trend in its values as the concentration increases, even though, overall, they remain very low. The dense structure, therefore, imposes not only long impregnation times but also physical limits related to the actual amount of acid accessible to the polymer.

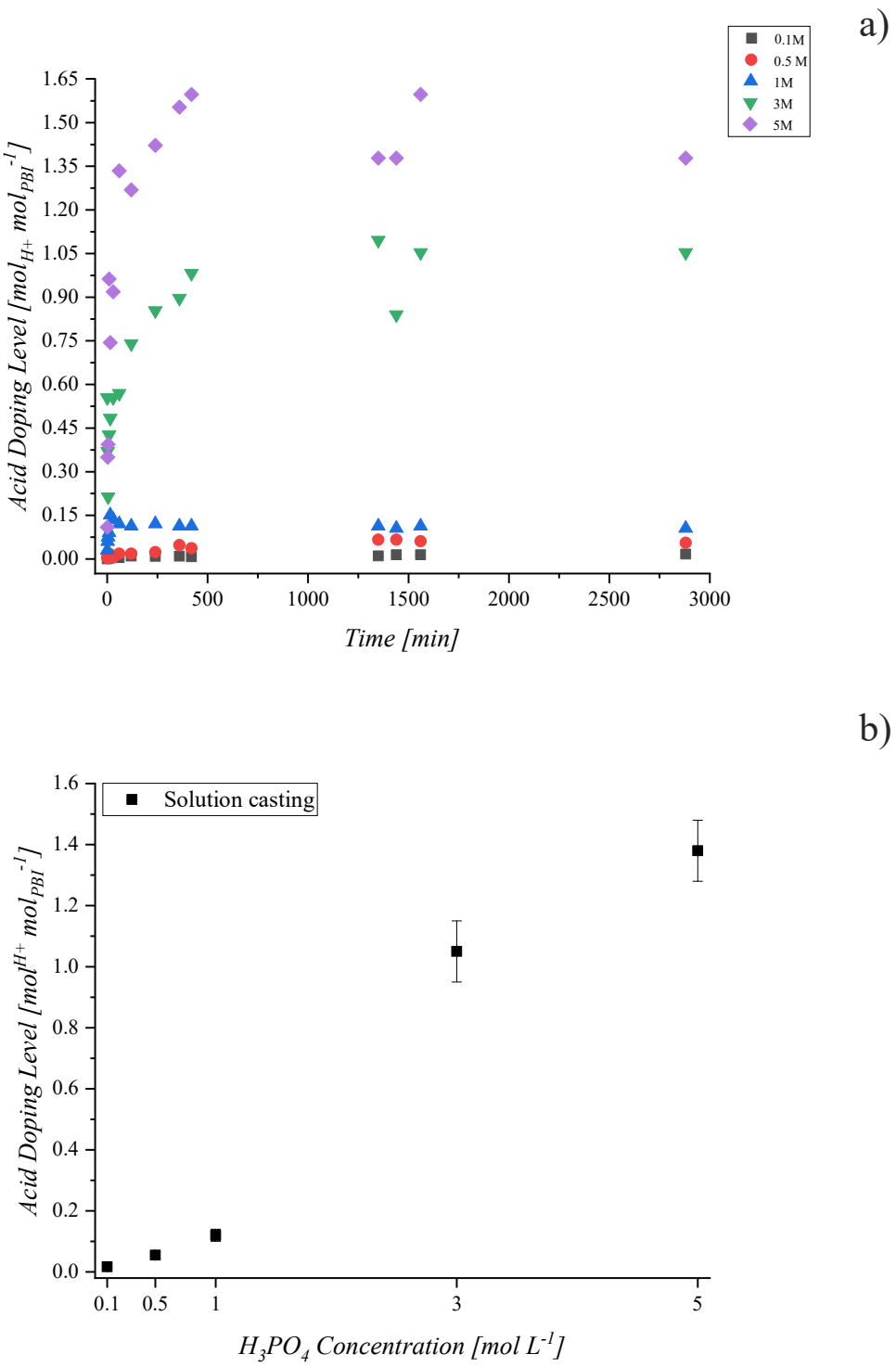

Figure 5.13 – Dynamic trend of the Acid Doping Level (ADL) of *m*-PBI membranes obtained through solution casting as time (a) and H_3PO_4 concentration (b) change at equilibrium.

From a physico-chemical point of view, the membranes are characterized by a strong tortuosity, due to the dense packing of the polymer chains, and a sustained swelling capacity that lengthen the characteristic impregnation time. Initially, the capture of phosphoric acid molecules is limited to the

imidazole sites immediately present on the sample surface. Subsequently, the slow migration and diffusion of the acid proceeds towards the bulk of the membrane until it reaches the entire thickness of the film. The dependence of ADL at equilibrium on acid concentration deserves a separate comment.

The increase shown in Fig. 5.13-b from 0.1 to 5M has a sub-linear trend: at low concentrations, the increase in acid in solution results in a modest increase in ADL values, whereas at higher concentrations this parameter increases but not in proportion to the external driving force. This behaviour can be explained by a limited population of accessible sites and the absence of a structure capable of "dragging'" the acid deep into the membrane. In other words, the architecture of the material forces the system into an equilibrium governed by an acid-imidazole interaction and considerable diffusive difficulties. This consistently explains why ADL levels are substantially low even under high-concentration conditions. From a purely kinetic and modelling point of view, this slow and almost monotonous evolution lacking an initial "'informative" section on the reactive plane (the first linear and sloping section of an adsorption curve allows key parameters such as the kinetic constant to be identified) does not allow for the estimation and distinction between PFO, PSO and *n*-order model. Since, in such a case, the process is dominated by diffusion, the application of a reactive model could produce parameters with an ambiguous interpretation of little practical significance.

When comparing the acid doping levels reported in this work with values commonly found in the literature for dense PBI membranes, lower ADL values are generally observed. For instance, the higher acid doping levels reported in Fig. 2 of Aili et al. 2020 [136] are obtained on dense PBI membranes with substantially different thickness and morphological homogeneity. In such systems, phosphoric acid retention is dominated by bulk absorption mechanisms, whereas in electrospun membranes acid uptake is strongly affected by local microstructural heterogeneities and accessible pore volume.

As a consequence, a direct quantitative comparison of ADL values between dense and fibrous membranes should be approached with caution, as identical numerical values do not necessarily correspond to comparable acid distribution or proton conduction pathways. This apparent discrepancy should not be interpreted as an intrinsic limitation of the impregnation protocol, but rather as a consequence of structural and geometrical differences between the investigated membranes. In particular, dense cast PBI membranes reported in the literature typically exhibit significantly larger thicknesses and reduced internal surface accessibility, which favor higher apparent acid retention per unit dry mass. In contrast, the electrospun membranes investigated in this study are characterized by a highly porous fibrous architecture, where acid distribution and retention are governed by capillary

effects, pore connectivity, and fiber-scale confinement. Further details about the ADL values are reported in **Annex B**.

5.5.2 Adsorption of electrospun *m*-PBI membranes

The kinetic behaviour of *m*-PBI membranes obtained by electrospinning is drastically different from those obtained by solution casting. In particular, the morphological change characterized by a network of nanometric fibers woven into a dimensional lattice has a direct and substantial impact on the kinetics of acid impregnation. At 25 °C, the dynamic analysis of the amount of phosphoric acid adsorbed per unit mass of PBI, shown in Figures 5.14-a, as the concentration of H_3PO_4 changes, reveals a highly distinctive trend: the curves show an extremely rapid initial phase, in which the membrane rapidly captures a significant fraction of the acid, followed by a rapid attainment of an equilibrium condition. The remarkable aspect of these curves is that equilibrium itself is reached within a few minutes for all the concentrations studied, in stark contrast to the films obtained from casting, which, as discussed above, take almost 24 hours to approach an equilibrium condition. From a purely interpretative point of view, it is possible to distinguish a two-stage process: i) an initial phase in which a rapid capture of acid molecules by the immediately accessible surface sites takes place; ii) a subsequent phase, characterized by intrafiber diffusive phenomena in which the progressive plasticization of the polymer regulates the acid-polymer interaction until a plateau is reached. The combination of porosity and plasticization explains the overall rapidity of the kinetics and the ability to reach such high doping values, confirming the substantial role of the fibrous microstructure in membrane impregnation capabilities.

a)

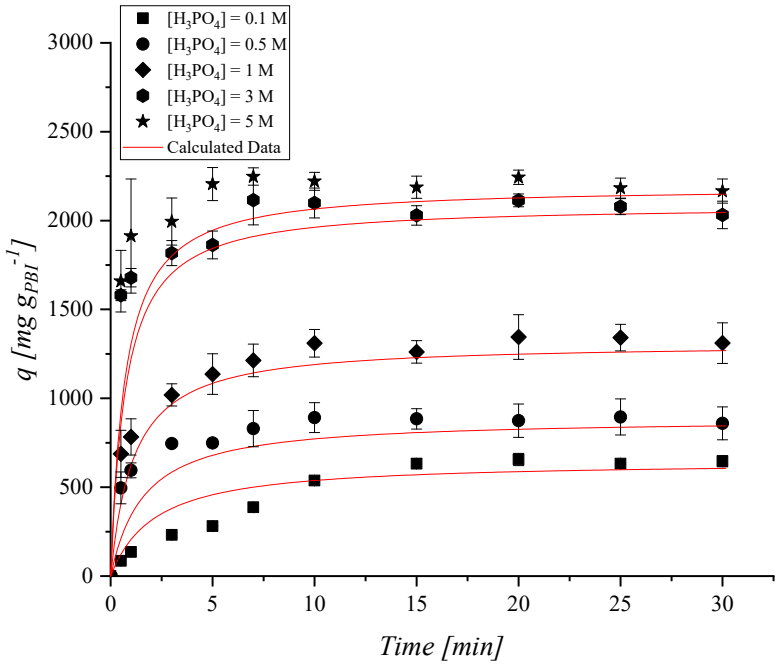

b)

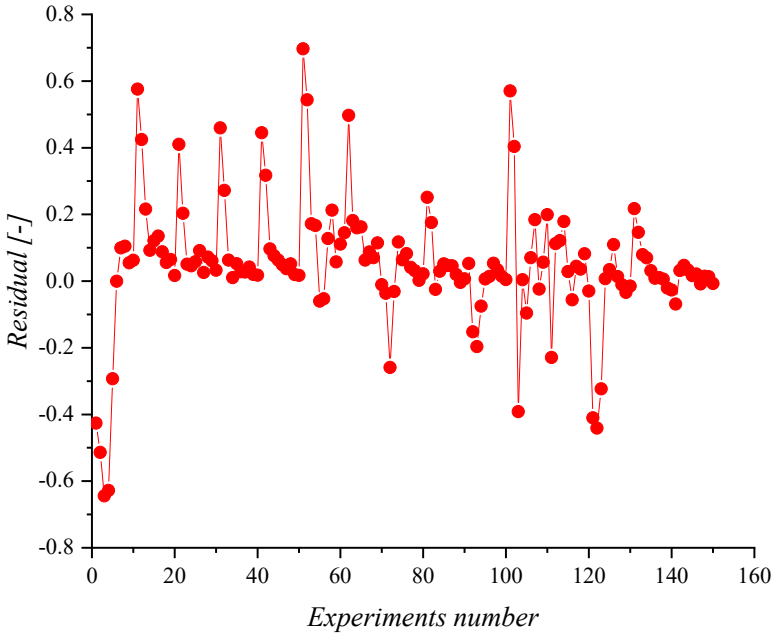

Figure 5.14 – Adsorption of phosphoric acid on electrospun membranes based on *m*-PBI at 25 °C: (a) dynamic trend of the specific amount of phosphoric acid per mass of membrane, at different concentrations; (b) distribution of residuals resulting from the comparison of the experimental data and the values calculated with the model used at 25 °C.

Another crucial aspect that emerged from the experimental data is the intrinsic reproducibility of the adsorption phenomenon, shown in Figure 5.14-b, which reports the trend of the residuals obtained by comparing the experimental data and the values calculated with the model adopted. The distribution of the points, oscillating around zero, demonstrates that the model correctly describes the phenomenon analysed and that the residual error is marginal, reinforcing the experimental protocol developed. This guarantees not only the reliability of the experimental data, but also of the kinetic and thermodynamic analyses derived from them.

This result reinforces the conclusion that the observed trend is not affected by any microstructural variations in the samples, but represents a characteristic trait of the morphology obtained by electrospinning. This robustness is crucial in view of practical applications, as it ensures that the extracted kinetic parameters can be used as a reliable basis for large-scale impregnation protocols. In addition, it should be noted that all kinetic tests were replicated at higher temperatures (35 and 50 °C) with the same phosphoric acid concentration conditions in order to confirm the validity of the model and to estimate the energy parameters by linearizing the Arrhenius equation. Equilibrium measurements conducted at higher temperatures (35 and 50 °C) showed an increase in the level of acid doping as the temperature increases, as shown in Figure 5.15. This behaviour is symptomatic of a clearly endothermic process, in which the imbibition of phosphoric acid into the polymer matrix is favored by an increase in available thermal energy. This is consistent with an interaction that breaks the intermolecular bonds between the polymer chains, with a subsequent formation of new interactions with the acid.

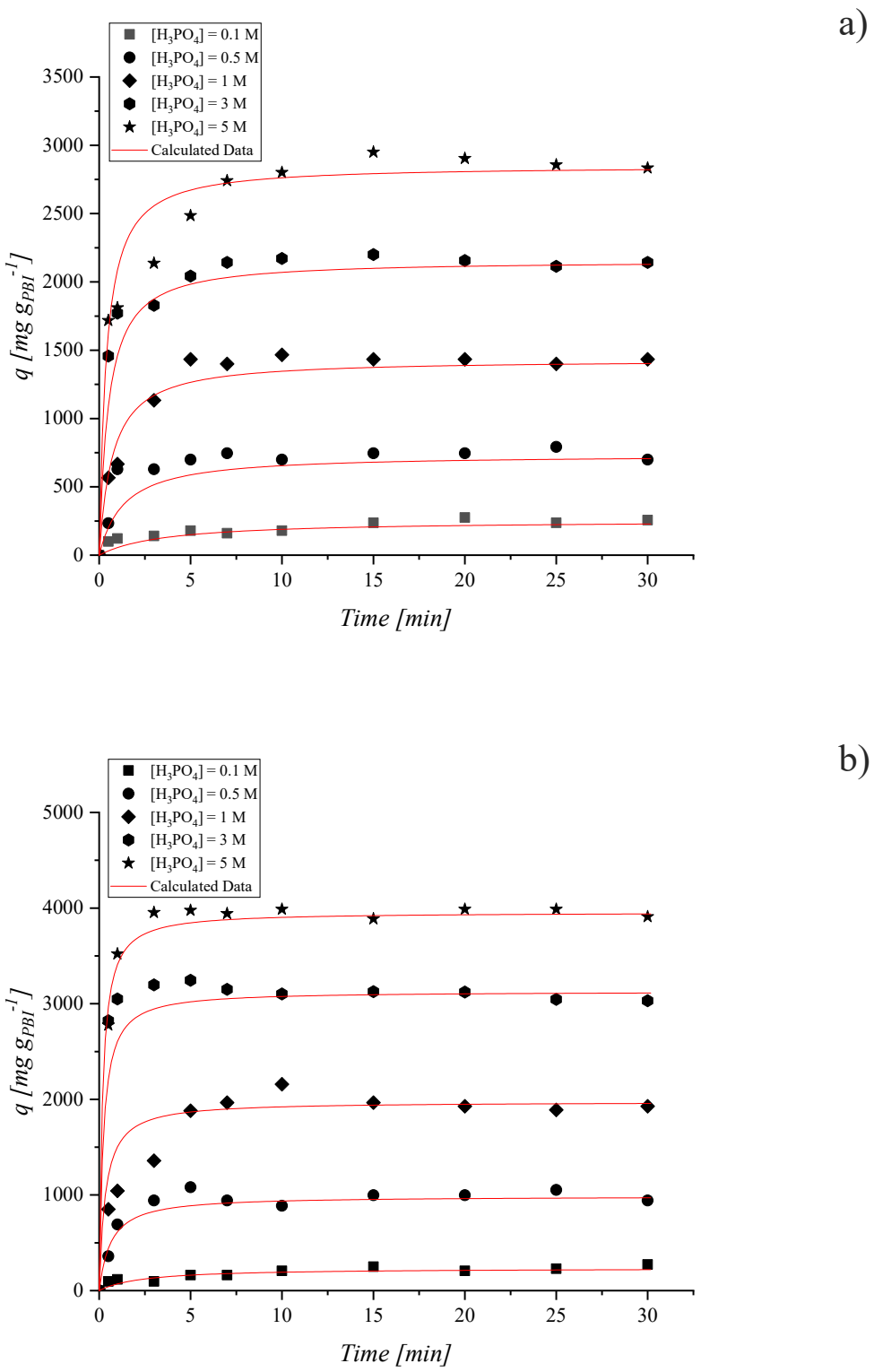

Figure 5.15 - Adsorption kinetics at 35 °C (a) and 50 °C (b) for electrospun membranes. Experimental data are reported as black scatter symbols while calculated model fits are reported with red lines.

From a quantitative point of view, kinetic modelling involved the use of power-law differential reactive models, analyzing the data at equilibrium. As previously introduced, three models were used: pseudo first-order kinetics (PFO, n=1), pseudo second-order kinetics (PSO, n=2) and n-order law. Systematic comparison showed that the first-order hypothesis fails to adequately reproduce the initial transient, underestimating the capture rate in the early stages of the interaction. The second-order model significantly improves the quality of the fit, correctly describing both the first linear stretch and the subsequent slowdown towards the equilibrium condition. However, the best agreement is found for an n-order, with an estimate very close to second order (n=1.91 ± 0.03) whose numerical evaluation is shown in Table 5.8. This conclusion is of great significance, not only from a mathematical point of view (R_{adj}^2=0.977), but also from a chemical-physical point of view, as it describes a process governed by cooperative and complex mechanisms, in which the simultaneous interaction of several factors such as the availability of active sites, intrafiber diffusion and the phenomenon of plasticization, results in a quasi-quadratic dependence of the interaction speed. In addition, the model made it possible to estimate energy and kinetic parameters with a strong statistical robustness. The activation energy (E_a) exhibited moderate and intermediate values, falling between those typical of physisorption and chemisorption, which is consistent with the nature of the material.

The correlation analysis of the kinetic parameters for phosphoric acid adsorption on electrospun PBI-based membranes reveals significant interdependencies that suggest a complex adsorption mechanism influenced by both energetic and structural factors. A moderate negative correlation between the pre-exponential factor A_0 and the activation energy E_a (-0.4440) indicates a possible enthalpy–entropy compensation effect. This suggests that an increase in the frequency of effective collisions is associated with a decrease in the energy barrier, a behavior often observed in systems where molecular mobility partially offsets energetic requirements. The strong positive correlation between the reaction order n and E_a (0.8437) implies that the adsorption process becomes more energy-demanding as the dependence on acid concentration increases. This may reflect a mechanism involving multiple interacting species or site saturation effects that limit the overall rate of adsorption. The negative correlation between A_0 and n (-0.6329) suggests that the frequency of effective collisions decreases with increasing reaction order, likely due to steric or diffusional constraints. As the reaction order rises, the simultaneous interaction of multiple H_3PO_4 molecules may become less favorable, particularly in a porous medium. Overall, the estimated kinetic parameters support a complex adsorption mechanism with a possible rate-limiting step influenced by acid concentration and membrane microstructure.

Parameter	*Value ± C.I. 95 %*	*Correlation Matrix*			*Adj-R^2*
		A_0	E_a	n	
A_0	0.85 ± 0.02	1			
E_a	26597 ± 605	-0.4440	1		0.9770
n	1.91 ± 0.03	-0.6329	0.8437	1	

Table 5.8 - Estimated kinetic parameters for the interaction between H_3PO_4 and *m*-PBI electrospun membranes at 25 °C, obtained by MATLAB modelling on a non-linear *n*-order differential model regression. A_0= [$L^{0.91}$ $mol^{-0.91}$ s^{-1}]; E_a = [J mol^{-1}]; *n* = [-].

To understand the improvement of the fibrous morphology, Figure 5.16 shows a comparison between the equilibrium ADL values as a function of H_3PO_4 concentration for both dense and fibrous membranes. As expected, the ADL increases systematically for electrospun membranes to a greater extent than for the dense counterpart. This behaviour is again justified by the greater accessibility of imidazole sites, which reduces diffusional limitations by allowing the acid to reach them rapidly. Furthermore, the normalization for WU makes us realize how, with the same amount of water retained, the ADL/WU ratio is more favorable for the material with a fibrous morphology due to the confinement of acid in the pores of the material and the local density of accessible basic sites that lead to the formation of acidic inter-fiber domains. This means that, from a practical point of view, for the same time and temperature, the final ADL after impregnation treatment will certainly be higher in electrospun samples, which is reflected in a better proton conductivity and lower ohmic membrane resistance. For completeness, all tested kinetic models and their fit curves are given in the **Annex B**.

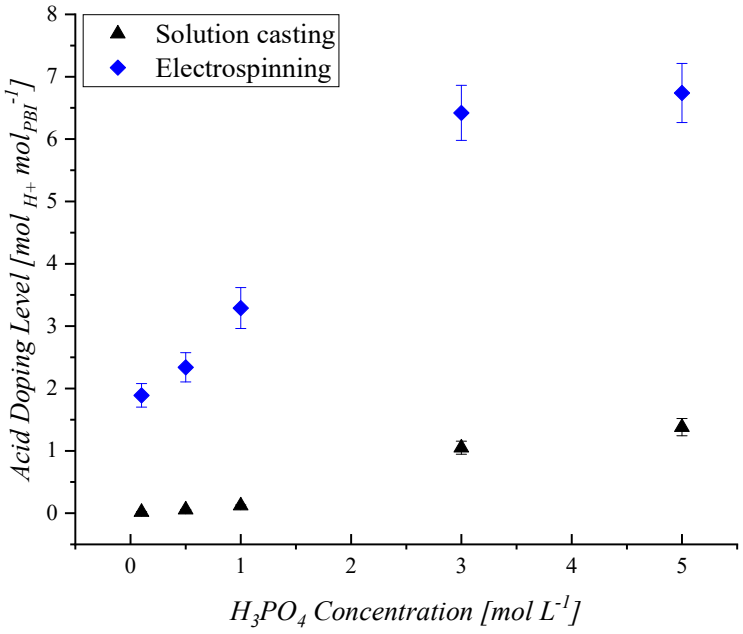

Figure 5.16 – Equilibrium Acid Doping Level (ADL) as a function of H_3PO_4 concentration for both dense and fibrous *m*-PBI membranes. The amount of acid in contact with the membrane increases with concentration for both morphologies. Still, it is significantly higher for electrospun membranes, indicating a higher acid retention and fixation efficiency per unit of water.

5.5.3 Acid doping stability and nature of the bond: methanol test

To gain a deeper understanding of the nature of acid doping and to distinguish between physiosorbed and chemisorbed contributions, electrospun *m*-PBI membranes impregnated with phosphoric acid were subjected to a selective methanol (MeOH) treatment, as described in Section 2.2.5. Owing to its polar and protic character, methanol can effectively remove weakly bound H_3PO_4 molecules, allowing the quantification of the acid fraction that is strongly bound to the polymer via acid–base interactions or cooperative hydrogen bonding. The comparison of the Acid Doping Level (ADL) before and after methanol treatment, shown in Table 5.9, enables the differentiation between the bound acid fraction (B, resistant to methanol) and the free acid fraction (F, extractable by the solvent), the latter likely residing within membrane pores or weakly adsorbed on the surface. The experiments were performed at 25 °C using acid concentrations of 1, 3, and 5 M. Lower concentrations (0.1 and 0.5 M) were excluded due to the strong influence of water, which would complicate data interpretation.

Acid Concentration [mol/L]	*Starting ADL [-]*	*Post-MetOH ADL [-]*	*Bounded acid fraction (B)*	*Free acid fraction (F)*
1	2.34 ± 0.12	1.14 ± 0.08	0.509	0.491
3	6.18 ± 0.25	3.14 ± 0.17	0.508	0.492
5	8.12 ± 0.40	4.61 ± 0.11	0.568	0.432

Table 5.9 - Results of the methanol test on electrospun *m*-PBI membranes: initial and post-treatment ADL values, and calculated bound (B) and free (F) acid fractions.

The results clearly show that electrospun *m*-PBI membranes retain a significant amount of phosphoric acid after methanol treatment, indicating strong and stable interactions between the acid and the polymer matrix. Even at 1 M, a residual ADL of 1.14 is observed, increasing to over 4 at higher concentrations. As the acid concentration rises, both the total uptake and the proportion of strongly bound acid increase, suggesting that concentrated H_3PO_4 enhances the formation of stable acid–imidazole complexes. This behavior contrasts sharply with that of dense PBI films obtained by solution casting. As reported by Li et al. [133], dense membranes typically retain an ADL of about 2 after methanol washing—consistent with the stoichiometric number of imidazole sites—while excess acid is readily removed. In electrospun membranes, however, a substantially higher amount of acid remains even after solvent extraction, highlighting the stabilizing effect of the fibrous architecture. The high surface area and interconnected porosity promote greater accessibility of imidazole sites and facilitate the formation of extended hydrogen-bonding networks.

These observations are fully consistent with the kinetic analysis discussed earlier. The reaction order close to 2 and the moderate activation energy ($E_a \approx 26.6$ kJ/mol) support a mixed adsorption mechanism—not purely physical adsorption, nor limited to acid–base neutralization—but involving cooperative hydrogen bonding in addition to classical proton–imidazole interactions.

The ability of electrospun *m*-PBI membranes to retain phosphoric acid stably beyond the stoichiometric limit of imidazole sites represents a key advantage for their application in high-temperature proton exchange membrane fuel cells (HT-PEMFCs). A higher bound acid fraction enhances long-term proton conductivity while minimizing the migration of free acid toward the catalyst layer, thereby improving the membrane's durability and operational stability.

5.5.4 Adsorption Thermodynamic

Dynamic analysis and stability tests in methanol have shown that only part of the acid content is actually relevant to membrane performance, as it clearly quantifies the fraction of acid that stably interacts with imidazole sites. In order to fully describe the acid-membrane interaction, it is essential to delve into thermodynamics, which makes it possible to elucidate the mechanisms of interaction between acid and polymer at varying concentration and temperature. To quantitatively describe the behaviour at equilibrium at different temperatures, several isothermal models have been used, such as Langmuir, Freundlich, Sips and Liu. The first three, although widely used in the literature, showed significant deviations from the experimental trend, especially at high phosphoric acid concentrations. In particular, Langmuir's model, based on the assumption of energetically equivalent sites and a monolayer adsorption, is too restrictive for a porous matrix and a microstructure as complex as that displayed by electrospun membranes. Freundlich's model, while describing heterogeneous systems, does not allow for explicit saturation while Sips provides a compromise but introduces uncertainties in the fit parameters. Liu's model, which is an evolution of Langmuir with the introduction of an empirical exponent n_L to capture the deviation from the monolayer ideal, provided the best fit to the data: Eq. 5.2 describes the Liu isotherm model where q is the amount of acid adsorbed at equilibrium (mol g^{-1}), Q_{max} is the theoretical maximum adsorption capacity (mol g^{-1}), K is the affinity constant (L mol^{-1}), C_e is the equilibrium concentration of phosphoric acid (mol L^{-1}) and n_L is an empirical parameter related to the adsorption sites.

$$q = \frac{Q_{max}\,(KC_e)^{n_L}}{1+(KC_e)^{n_L}} \qquad \text{Eq. 5.2}$$

This model assumes a heterogeneous distribution of adsorption energies and finite sorption capacity (Q_{max}). Even if Liu's isotherm model is a combination of Langmuir and Freundlich isotherm models, the monolayer assumption from Langmuir and the infinite adsorption assumption from the Freundlich are discharged [ref.]. Figure 5.17 shows the experimental isotherms and the corresponding Liu model fits at 25, 35, and 50 °C: increasing temperature leads to an increase in adsorption capacity at the same initial phosphoric acid concentration, with the plateau of the isotherm tending to shift towards higher adsorption capacities. It can be pointed out that increasing temperature shifts the isotherms upward, suggesting an endothermic process, where the increase in temperature facilitates the interaction between the PBI functional groups and phosphoric acid.

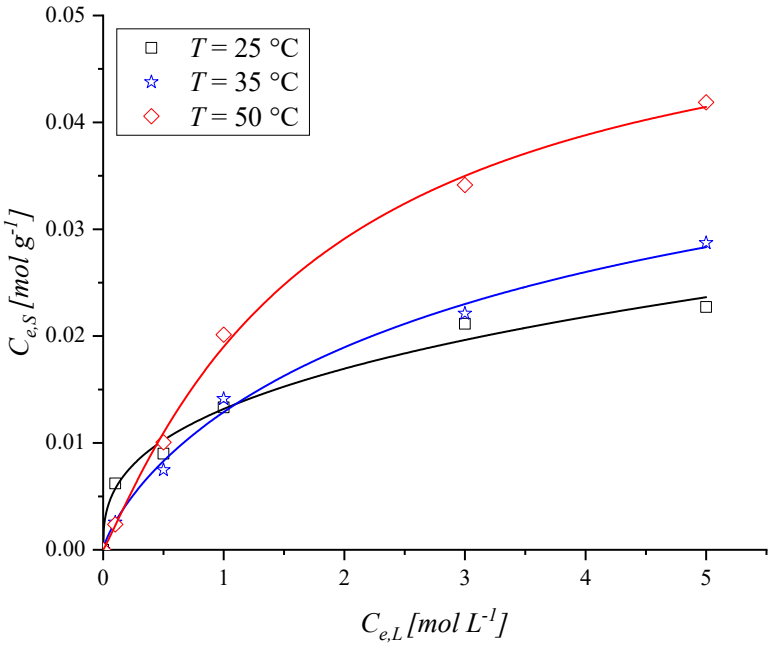

Figure 5.17 – Adsorption isotherms of phosphoric acid (scatter symbols) and interpolating Liu model fits (lines) at 25 (black), 35 (blue), and 50 (red) °C for PBI electrospun membranes.

Liu's parameters estimated at the three temperatures analyzed are shown in Table 5.10 in which an increase in the equilibrium constant *K* can be observed as the temperature increases, signaling an increase in the membrane's affinity for acid. The Qmax parameter remains constant and in a range of 0.05-0.06 mol g^{-1}, indicating a substantially constant maximum doping capacity, while the nL exponent increases from sub-uniform values (0.495 at 25 °C) to values of a few above 1 at 50 °C. This result is extremely interesting in that at low temperatures the process appears to be dominated by a heterogeneous distribution of sites, but as the temperature increases, the system behaves homogeneously and cooperatively, with acid-polymer interactions that are energetically more uniform. The linearization of the Vant' Hoff equation shown in Figure 5.18 also made it possible to calculate reference thermodynamic quantities such as the enthalpy of adsorption (ΔH) and entropy (ΔS).

	Liu Parameters				*Thermodynamic*	
T (°C)	***K (L/mol)***	***Q_{max} (mol/g)***	***n_L (-)***	***Adj-R^2***	***ΔS (J/mol K^{-1})***	***ΔH (J/mol)***
25	0.079 ± 0.006	0.060 ± 0.001	0.495 ± 0.004	0.9975		
35	0.24 ± 0.03	0.05 ± 0.01	0.8 ± 0.2	0.9917	185.58	61337
50	0.6 ± 0.2	0.055 ± 0.007	1.1 ± 0.2	0.9962		

Table 5.10 - Liu's isotherm parameters at different temperatures (25, 35, 50 °C) and estimated values of enthalpy and entropy of adsorption, calculated by means of a Vant' Hoff linearization.

The positive sign of the enthalpy of adsorption confirms the endothermic nature of the process and the absolute value of this parameter identifies a stronger interaction than a "simple" physisorption. This is consistent with the interpretation of a weak and cooperative chemisorption mechanism, with the formation of a sort of network of stable hydrogen bonds in the polymer matrix. The strong, positive entropic contribution, on the other hand, reflects the increase in disorder associated with the process, as the entry of acid into the fibrous structure necessarily entails a reorganization of the polymer chains, increasing the overall configurational freedom of the system.

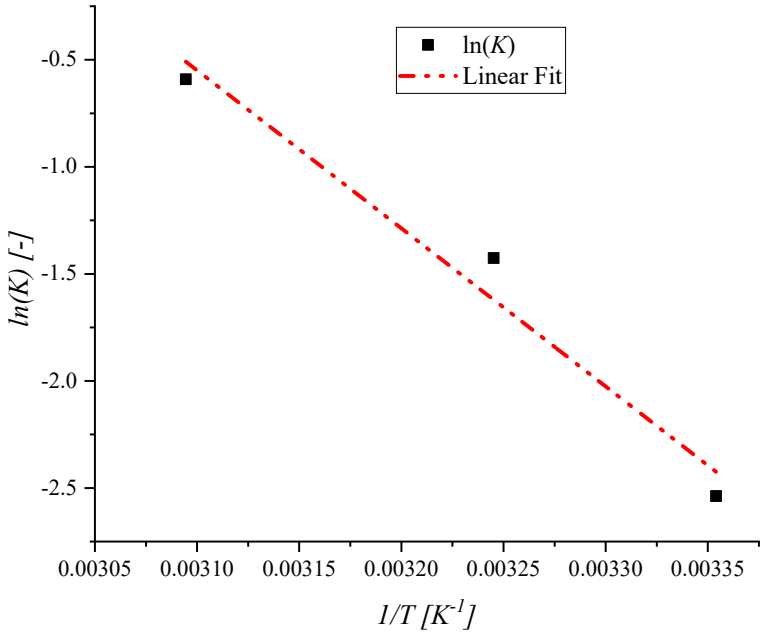

Figure 5.18 – Linearized van't Hoff plot for estimation of *ΔH* and *ΔS*, obtained from the equilibrium constant (*K*) derived from Liu's isotherm at different temperatures (25, 35, 50 °C).

Doping is therefore a thermodynamically favored process and made even more spontaneous with increasing temperature, further confirming that electrospun membranes are particularly promising for

applications in HT-PEM, where doping stability must be maintained at high temperature. The results of the different isotherm models tested (Langmuir, Freundlich and Sips), together with their fit parameters and determination coefficients, are given in the **Annex B.**

5.6 Post-doping Microstructural Evaluation

The kinetic and thermodynamic discussion has shed light on the mechanisms by which phosphoric acid interacts with PBI, highlighting how electrospun membranes are characterized by a rapid impregnation process. However, to fully understand the impact of this interaction, it is necessary to extend the analysis to the mechanical, morphological and chemical-structural properties of post-doping membranes. Such an evaluation allows on the one hand to assess the stability and integrity of the polymeric material for its future applications, and on the other hand provides independent and complementary evidence on the acid-polymer interaction mechanisms already discussed in the previous section.

5.6.1 SEM Morphological evaluation

The morphological analysis was conducted using scanning electron microscopy (SEM). This technique enabled the observation of the material's surface microstructure, highlighting the changes induced by the doping process. In particular, dense and fibrous membrane samples were compared before and after impregnation at different H_3PO_4 concentrations, to assess variations in material continuity, fiber diameter, and the integrity of the polymer network. The observations obtained provide critical insights for interpreting the differences in adsorption kinetics and doping levels across the different membrane types, serving as a fundamental support for the kinetic analysis. The SEM image of the neat dense PBI membrane (Fig. 5.19-a) reveals a compact, continuous film with a smooth surface and no significant porosity or discernible fibrous features. This uniform structure is typical of solvent-cast membranes and results in low permeability and limited specific surface area due to the absence of internal voids. In contrast, the SEM micrograph of the neat (undoped) electrospun PBI membrane (Fig. 5.19-b) displays a highly porous, three-dimensional network of thin, interconnected fibers. This morphology is characteristic of electrospun materials and originates from the rapid solidification of a polymer jet subjected to a high-voltage electric field during fabrication. The resulting fibrous architecture significantly enhances the membrane's porosity, specific surface area, and permeability.

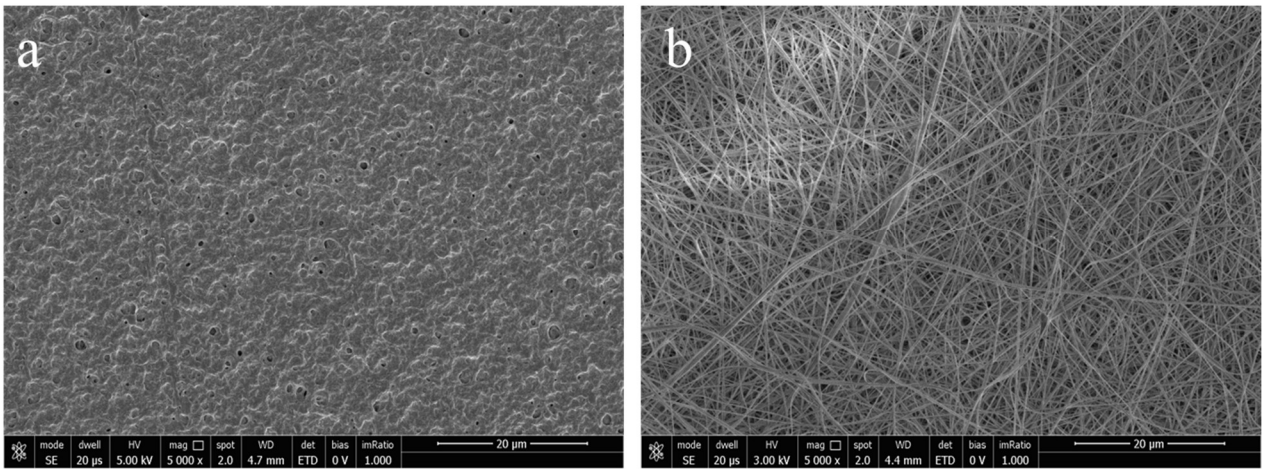

Figure 5.19 – SEM micrographs at 5000x magnification of neat dense (a) and undoped electrospun (b) PBI membranes.

Following impregnation with 1 M H_3PO_4 for 30 min (Fig. 5.20-a), the electrospun membrane undergoes moderate but noticeable morphological changes. While the fibrous network remains largely intact, a slight increase in average fiber diameter and partial adhesion between adjacent fibers are observed. These changes indicate that phosphoric acid has penetrated the fibers, inducing swelling due to polymer chain plasticization. In some regions, coalescence of adjacent fibers occurs, evidenced by permanent contact points or "welded" junctions where polymer softening has facilitated fusion during treatment. However, the relatively low concentration of acid limits the total amount of absorbed liquid (and the extent of polymer protonation), resulting in a mild reduction in porosity. Nonetheless, the overall structure remains largely preserved: most fibers are still distinguishable, and a substantial fraction of inter-fiber voids persists. This suggests that 1 M H_3PO_4 is sufficient to induce doping and partial morphological rearrangement without compromising the fibrous architecture.

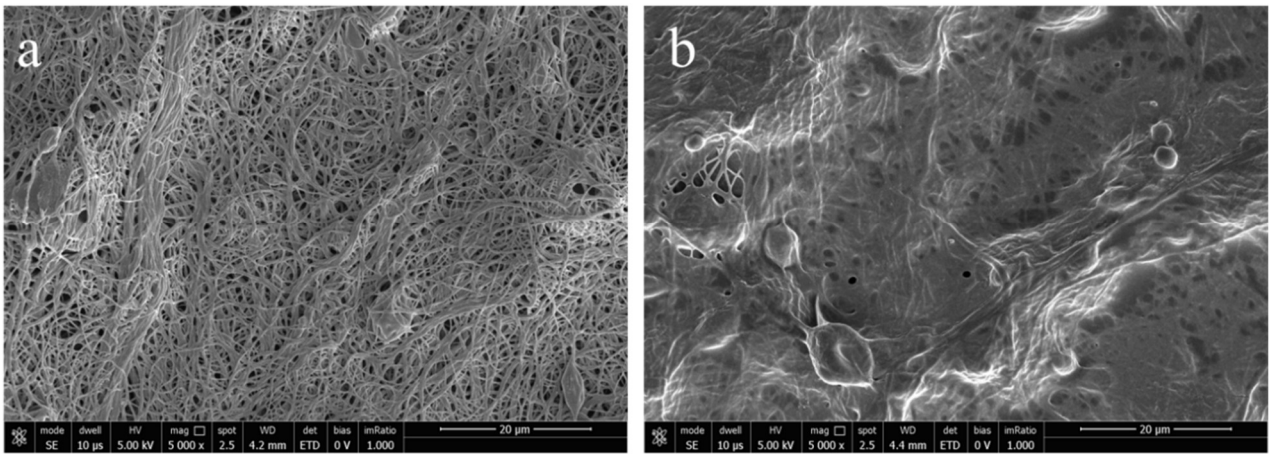

Figure 5.20 – SEM micrographs at 5000 magnifications of electrospun PBI membranes after acid treatment for 30 min: (a) 1 M H_3PO_4, (b) 5 M H_3PO_4.

In contrast, treatment with 5 M H_3PO_4 for 30 min (Fig. 5.20-b) results in pronounced morphological transformation. The SEM image reveals significant fiber swelling and extensive fusion between adjacent fibers, which now appear as thickened, indistinct bundles or continuous plates. The clear outlines of individual fibers are largely lost, indicating that the polymer has undergone partial flow or reorganization during acid exposure. This leads to a marked densification of the membrane, with the structure increasingly resembling a compact film rather than a fibrous mat. Consequently, the inter-fiber porosity is dramatically reduced: many of the original voids are eliminated, and those that remain are notably smaller. This progressive coalescence of fibers with increasing acid concentration demonstrates a concentration-dependent transition from a porous to a dense morphology. Importantly, this acid-induced structural evolution has significant implications for membrane performance in fuel cell applications. The densification and reduced porosity resulting from high-concentration acid treatment could effectively minimize gas crossover, making the membranes promising candidates for proton exchange membrane fuel cells.

5.6.2 Post-doping FTIR spectroscopic analysis

To complement the morphological analysis, a spectroscopic investigation of the interactions between phosphoric acid and the polymer matrix was carried out using the FTIR-ATR technique. The analysis was performed on samples doped at two representative acid concentrations and compared to the neat material, to highlight the progressive protonation of the polymer and the presence of adsorbed phosphate species. The resulting spectra provide a qualitative understanding of the acid–polymer

interactions at the molecular level and are essential for interpreting the thermodynamic and kinetic mechanisms discussed above. Moreover, the analysis confirms the effective presence of phosphate species within the membrane structure. Figure 5.21 presents the spectra of electrospun PBI membranes treated with 1 M and 5 M H_3PO_4 for 30 min, compared to the undoped (neat) electrospun PBI sample. New absorption bands are observed in the region of 954–962 cm^{-1}, corresponding to the symmetric stretching vibrations of P–O bonds, indicating the presence of phosphate species either adsorbed on the surface or chemically bound to the polymer matrix [137]. Additionally, a prominent signal appears around 1110 cm^{-1}, attributed to P=O stretching, further confirming the incorporation of phosphoric acid within the membrane. Significant spectral changes are also detected in the 2350–2400 cm^{-1} range, where new bands emerge that are absent in the neat membrane [137]. These are associated with protonation of the imidazole rings in the PBI backbone, providing direct evidence of acid–base interactions between H_3PO_4 and the polymer's nitrogen-containing functional groups. The intensity of these bands increases with acid concentration, suggesting a progressive and structurally relevant protonation process, which can alter the electronic distribution and rigidity of the polymer chains. Finally, the region between 3500 and 3850 cm^{-1} exhibits a broad, intense band attributed to O–H stretching vibrations. This feature reflects both hydrogen-bonded hydroxyl groups (O–H···N) and free hydroxyls from phosphoric acid or absorbed water. The increase in intensity and width of this band with rising H_3PO_4 concentration is indicative of enhanced doping efficiency and higher adsorbate uptake, correlating with the morphological changes discussed earlier.

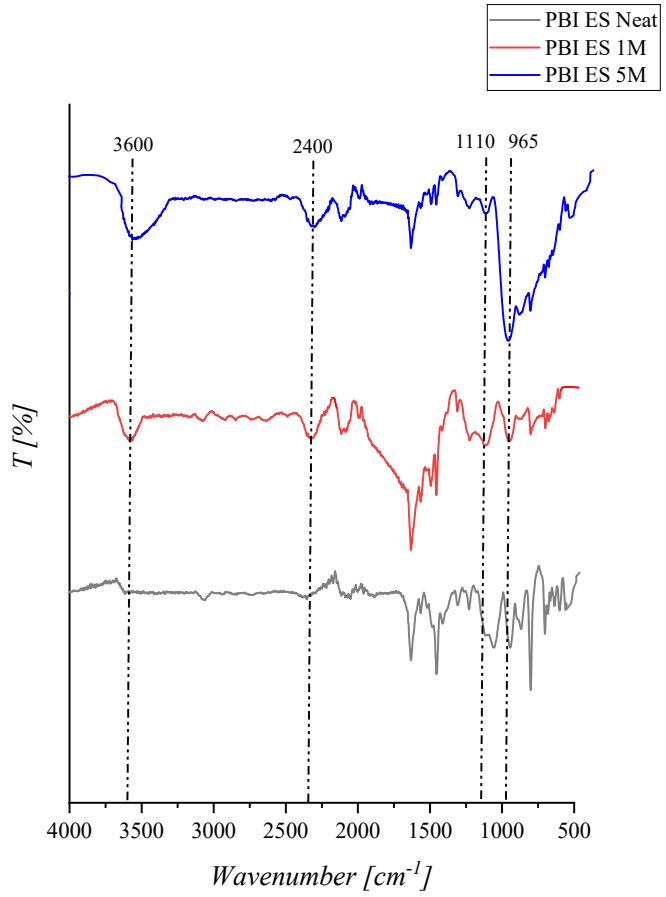

Figure 5.21 – FTIR-ATR spectra of electrospun PBI membranes: neat (grey line), doped with 1 M H_3PO_4 (red line), and doped with 5 M H_3PO_4 (blue line).

These spectroscopic observations confirm that the interaction between H_3PO_4 and the PBI matrix is not limited to simple physisorption but involves stronger acid-base interactions. In particular, the protonation of the imidazole rings indicates the formation of specific and relatively stable bonds, consistent with a partial chemisorption contribution, supporting what has already been described in the previous paragraphs.

5.6.3 Effect of acid doping on mechanical behaviour

Figure 5.22 shows the stress-strain curves of electrospun PBI membranes before and after acid impregnation with 1M and 5M solutions of H_3PO_4. A qualitative analysis already shows that the introduction of the acid has a significant effect on the mechanical behaviour of the material, with a reduction in both Young's modulus (initial linear region of the curve) and elongation at break. The

1M doping immediately shows a decrease in these parameters, while maintaining a well-defined elastic response with a Young's modulus of approximately 46 ± 6 MPa and an elongation at break of 8 ± 1 %. As the concentration increases (5M), the decrease becomes more pronounced and the material assumes a brittle character with a net reduction in modulus (23 ± 2 MPa) and elongation at break (4 ± 0.5 %). This behaviour finds a natural explanation in the doping mechanism: phosphoric acid penetrates the fibrous matrix, breaking the intermolecular interactions between the polymer chains and forming dynamic interactions with the imidazole groups. This necessarily results in a lowering of the elastic modulus, also due to local swelling phenomena, which reduce the material's ability to sustain high levels of deformation. Despite this apparent penalization of mechanical properties, it is essential to emphasize that the observed behaviour does not significantly compromise the application of these HT-PEMFC membranes. It is important to emphasize that the working conditions of HT-PEMFCs do not require mechanical stresses on the membrane, as the membrane is not subjected to significant tensile loads. In this context, therefore, even low values of modulus and elongation at break are largely sufficient to guarantee the mechanical stability of the system, which is, in general, secondary to the proton conduction capacity of the membranes.

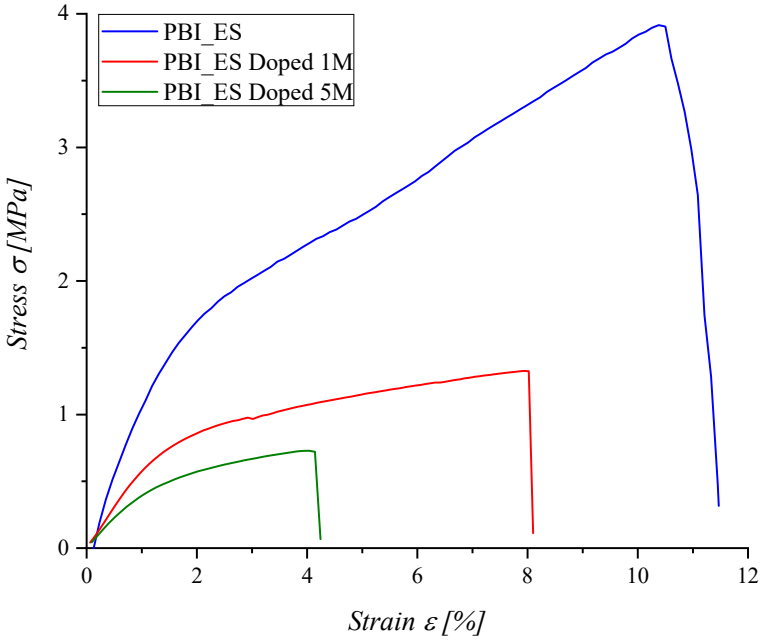

Figure 5.22 – Stress-strain curves of electrospun PBI membranes before (PBI_ES) and after acid doping in 1M and 5M H_3PO_4 solutions. The impregnation significantly reduces the elastic modulus and elongation at break, clearly showing the plasticizing effect of phosphoric acid.

The reduction in mechanical properties should therefore not be interpreted as a defect but as a functional adaptation of the material. The acid-induced plasticization allows a reorganization of the polymer network (see Section 5.6.1) favoring the formation of stable proton-conductive domains. The decrease in elastic modulus, for example, is simply a direct consequence of a mechanism that improves and enhances the desired electrochemical properties of the material. However, it should be emphasized that the mechanical behaviour of the presented membranes is sufficiently in line with what has been reported in the literature for membranes obtained through the electrospinning technique and/or treated with plasticizing agents [102].

5.7 Electrochemical evaluation: Proton conductivity

Preliminary proton conductivity measurements were performed to explore the relationship between membrane morphology, acid adsorption mechanisms, and overall functional performance. As shown in Figure 5.23, the electrospun m-PBI membrane (PBI_ES) exhibits markedly higher conductivity than the dense, solution-cast membrane (PBI_Cast), even though both samples have comparable thickness and similar acid doping levels (ADL ≈ 11). The conductivity of the PBI_ES membrane increases significantly with temperature, reaching a maximum near 150 °C.

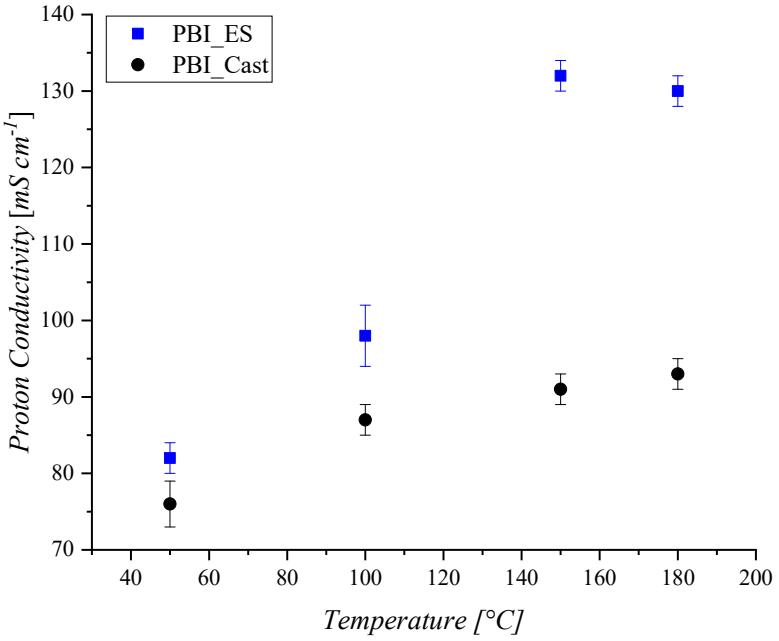

Figure 5.23 – Proton conductivity tests performed under anhydrous conditions for electrospun (PBI_ES, blue rhombus) and cast (PBI_Cast, black triangle) PBI membranes at different temperatures.

At 50 °C, both membranes display similar conductivity values. However, as temperature rises, their behavior diverges sharply: at 150 °C, the electrospun membrane achieves a proton conductivity of approximately 132 mS cm^{-1}, higher than that of the cast membrane under the same conditions. This superior performance is attributed to the fibrous and highly porous morphology of the electrospun mat, as confirmed by SEM analysis. The interconnected fiber network facilitates rapid and homogeneous diffusion of phosphoric acid throughout the structure, improving site accessibility and the formation of continuous proton-conducting pathways. Conversely, the compact morphology of cast membranes restricts acid diffusion and leads to a less uniform distribution of protonic sites.

Temperature also enhances ion mobility within the polymer matrix, contributing to the progressive conductivity increase observed across the studied range. Overall, these results demonstrate that the enhanced proton transport in electrospun membranes is not solely due to their higher acid-doping capacity but, more importantly, to the favorable morphology that enables continuous and efficient ionic conduction.

This distinctive feature makes electrospun *m*-PBI membranes particularly promising for anhydrous, high-temperature applications such as HT-PEMFC systems, where stable proton conductivity under dry conditions is a key requirement for durable operation.

5.8 Electrochemical evaluation: Fuel Cell Testing

Following optimization of the electrospun *m*-PBI membranes in terms of morphology, mechanical stability, and acid-doping capability, their electrochemical performance was evaluated under real fuel cell operating conditions. This section presents the preliminary single-cell tests designed to assess the functionality of the developed membranes when integrated into a Membrane Electrode Assembly (MEA) operating in a hydrogen–oxygen environment. The objectives of these tests were to evaluate hydrogen permeability, electrochemical stability, and proton conduction behavior under typical HT-PEMFC conditions. Measurements included:

- Linear Sweep Voltammetry (LSV) to quantify hydrogen crossover,
- Electrochemical Impedance Spectroscopy (EIS) to analyze internal resistance and charge transfer,
- Polarization curve analysis to assess overall cell performance.

These results should be regarded as preliminary, providing a baseline for the validation of the electrospun architecture and for future optimization of MEA design and testing protocols.

5.8.1 Hydrogen Crossover Assessment via LSV

Hydrogen crossover through the electrospun *m*-PBI membrane was investigated by Linear Sweep Voltammetry (LSV) under inert conditions using a Scribner 850 test station. The measurements were performed by feeding hydrogen to the anode (100 sccm) and nitrogen to the cathode (200 sccm), both under dry conditions and at ambient pressure, while maintaining the cell at the target temperature. The cathode potential was scanned from 0.1 to 0.8 V versus the anode reference at a slow rate of 1 mV/s to ensure quasi-steady-state gas diffusion through the membrane. Under these conditions, the limiting current density (i_{H2}) is governed by hydrogen diffusion and solubility in the membrane, thus providing a quantitative measure of gas crossover. Measurements were carried out at 30 °C and 150 °C to assess the temperature dependence of hydrogen permeation through the electrospun m-PBI network. The resulting LSV curves exhibited a low and nearly flat current response at 30 °C, consistent with limited gas permeation and the expected insulating behavior of the dry polymer. At 150 °C, the current magnitude increased by more than one order of magnitude, indicating enhanced hydrogen transport due to increased molecular diffusivity and possible microstructural relaxation of the fibrous mat. The limiting current densities, molar fluxes, and derived permeabilities are summarized in Table 5.11.

Temperature [°C]	i_{H2} ***[mA cm^{-2}]***	J_{H2} ***[mol s^{-1} cm^{-2}]***	Ψ_{H2} ***[mol m^{-1} s^{-1} Pa^{-1}] · 10^{-15}***
30	0.197	$1.02 \cdot 10^{-9}$	5.10
150	2.09	$1.08 \cdot 10^{-8}$	54.0

Table 5.11 – Limiting current densities (i_{H2}) and derived hydrogen molar flux (J_{H2}) and permeability (Ψ_{H2}) of the electrospun *m*-PBI membrane determined from LSV curves under H_2/N_2 conditions.

The results indicate an approximately tenfold increase in hydrogen permeability between 30 °C and 150 °C, consistent with the thermally activated nature of gas diffusion in polymeric matrices. This increase can also be attributed to enhanced segmental mobility of the PBI chains and a possible expansion of inter-fiber free volume at elevated temperatures. Nevertheless, the absolute permeability values remain comparatively low, confirming that the fibrous m-PBI membrane retains effective gas-barrier properties suitable for HT-PEM operation, while benefiting from its high acid uptake and mechanical flexibility. It should be noted that these crossover measurements represent preliminary tests performed during protocol optimization and system calibration. The data therefore provide a first qualitative indication of the membrane's gas impermeability and electrochemical stability, while further refinement of the testing procedure is expected to yield more reproducible and quantitatively accurate results in future studies.

5.8.2 Fuel Cell Performance: Open Circuit Voltage and Polarization Curves

After establishing the morphological and physicochemical properties of the electrospun *m*-PBI membranes, their electrochemical performance was assessed under functional HT-PEMFC conditions. Single-cell tests were carried out to evaluate gas impermeability, proton conductivity, and overall electrochemical stability when integrated into a Membrane Electrode Assembly (MEA).

The polarization behavior of the electrospun *m*-PBI membrane (PBI_ES) was compared with that of the dense, solution-cast membrane (PBI_Cast) and the commercial Celtec®-PBI benchmark (PBI_Celtec). The MEA was assembled directly in the test fixture, with the membrane positioned between the electrodes and compressed using a torque of 4 N·m to ensure uniform mechanical contact while avoiding excessive deformation of the fibrous structure. Although this simplified procedure allows fast assembly, the lack of hot pressing or preconditioning can result in small interfacial gaps or partial contact non-uniformities, which may influence the apparent electrochemical performance.

The cell was operated with dry hydrogen and oxygen feeds at 140 and 70 sccm, respectively, corresponding to a stoichiometric ratio of about 2:1. The system was stabilized at 150 °C for 30 minutes under open-circuit conditions prior to testing. The recorded Open Circuit Voltage (OCV) was 0.8336 V — slightly below the theoretical Nernst potential (0.85–1.0 V) expected for similar PBI-based systems. This small deviation can be attributed to a combination of factors: (i) measurable hydrogen crossover through the membrane, as evidenced by the LSV tests; (ii) reduced interfacial proton conductivity due to the dry operating mode; (iii) small microgaps introduced during assembly without hot pressing; and (iv) minor instrumental offsets or temperature gradients during this preliminary testing phase.

When compared to the Celtec® benchmark, which typically achieves OCV values close to 1.0 V under similar conditions, the electrospun membrane's performance remains within the expected range for an unoptimized system. The dense PBI_Cast membrane exhibited a slightly higher OCV (~0.96 V), likely due to improved gas tightness and interfacial contact. Nonetheless, the electrospun PBI membrane maintained a stable open-circuit potential, confirming adequate sealing and protonic continuity despite its fibrous morphology.

Following the OCV measurement, the polarization curve was recorded through a galvanostatic sweep (1 mV/s) under the same dry gas conditions. The polarization and power density curves are shown in Figure 5.24a–b.

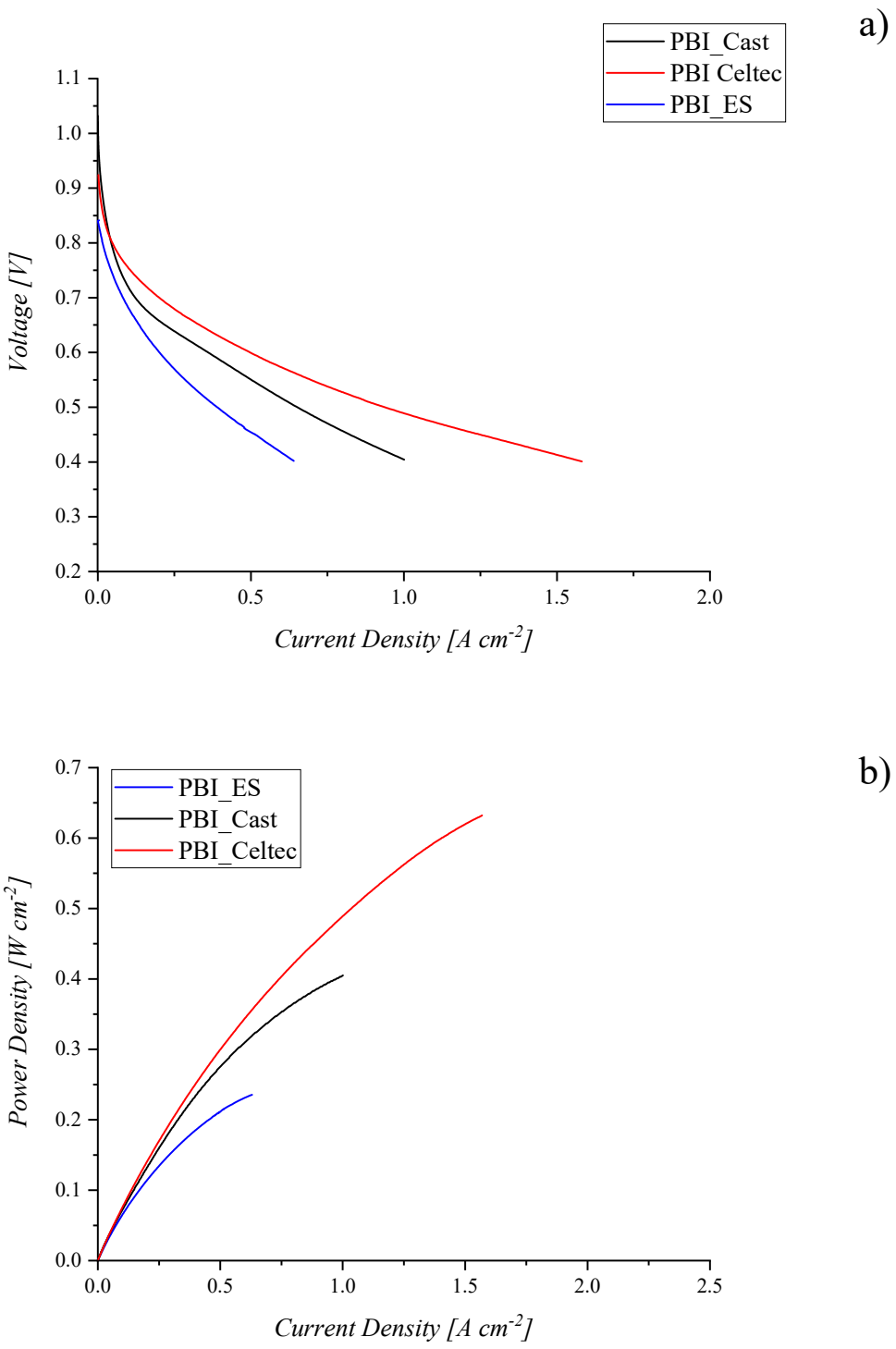

Figure 5.24 - Polarization (a) and power density curves (b) of electrospun (PBI_ES), dense solution-cast (PBI_Cast), and commercial Celtec®-PBI membranes, tested at 150 °C under dry H_2/O_2 operation.

The voltage–current curve exhibits the characteristic profile of polymer electrolyte membrane fuel cells, encompassing three distinct regions: activation, ohmic, and mass-transport losses.

At low current densities (≤ 0.1 A cm^{-2}), the voltage drop is dominated by activation overpotentials, primarily due to sluggish cathodic kinetics. In dry operation, limited water availability hinders proton hydration and reduces catalyst utilization. The electrospun PBI membrane, although possessing high acid retention, was not preconditioned prior to testing, meaning full acid redistribution across the fibrous network and electrode interfaces was likely incomplete. This contributes to the higher activation losses observed. In contrast, both the PBI_Cast and Celtec® MEAs showed smaller activation overpotentials, with Celtec® reaching linear behavior around 0.2 A cm^{-2}, indicative of optimized catalyst utilization.

In the ohmic region (approximately 0.1–0.7 A cm^{-2}), a linear voltage decrease is observed. This regime is governed by ionic transport through the membrane and interfacial contact resistance. Because the cell was assembled without hot pressing, incomplete compression may have introduced localized contact resistances. Furthermore, the use of dry gases means that proton transport relies entirely on the intrinsic mobility of phosphoric acid within the polymer matrix. The fibrous morphology introduces tortuous conduction pathways, contributing to slightly higher total resistance. Quantitatively, the ohmic slope for PBI_ES is steeper than for PBI_Cast, which in turn remains higher than for Celtec®, reflecting the increasing optimization of interfacial contact and transport pathways across the three systems.

At high current densities (> 0.8 A cm^{-2}), the cell enters the mass-transport-limited region, where diffusion resistance and local acid redistribution become dominant. Although the serpentine gas flow field ensures fairly uniform reactant distribution, oxygen depletion and local water accumulation at the cathode can modify acid concentration and viscosity, leading to transient polarization effects. The electrospun membrane shows an earlier deviation from linearity (~0.5 A cm^{-2}), consistent with partial gas transport limitations through its porous structure. Nevertheless, it maintains stable operation up to significant current densities, confirming its suitability for HT-PEM operation. The corresponding power density curve displays a typical parabolic shape, with a maximum of ~0.24 W·cm^{-2} at ~0.8 A·cm^{-2}. Although lower than Celtec® (~0.65 W·cm^{-2}) and PBI_Cast (~0.45 W·cm^{-2}), this value represents 60–70% of benchmark performance under identical, non-optimized, and dry conditions — an excellent result for a first unconditioned electrospun MEA. Moreover, the power curve of the PBI_ES membrane was still increasing at the voltage cut-off of 0.4 V, suggesting that higher output could be achieved with improved interfacial compaction and acid equilibration. In conclusion, the electrospun *m*-PBI membrane demonstrates coherent MEA integration, stable operation, and promising power output under anhydrous high-temperature conditions. The observed performance

gap compared to benchmark systems is primarily linked to assembly and conditioning factors rather than intrinsic material limitations.

5.8.3 Through-Plane Impedance Characterization and Evaluation

Further insights into the electrochemical behavior of the electrospun *m*-PBI membrane were obtained through Galvanostatic Electrochemical Impedance Spectroscopy (GEIS) performed at 150 °C under dry H_2/O_2 operation. Measurements were conducted at total current loads of 0.5, 1.0, 1.5, and 3.0 A, corresponding to current densities of 0.10, 0.20, 0.30, and 0.60 $A \cdot cm^{-2}$ over a 5 cm^2 active area. A perturbation amplitude of 5% of the DC current was applied, with frequencies ranging from 10 kHz to 0.1 Hz, enabling resolution of resistive and capacitive components within the MEA while maintaining response linearity.

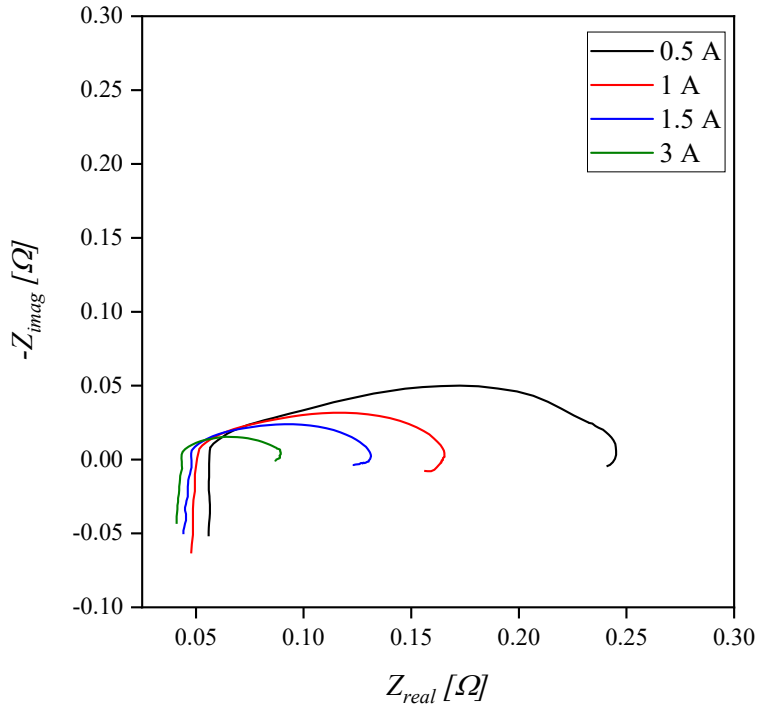

Figure 5.25 – Nyquist plots of electrospun *m*-PBI membranes at 150 °C under dry H_2/O_2 operation, recorded at total current loads of 0.5 A (0.10 A cm^{-2}), 1.0 A (0.20 A cm^{-2}), 1.5 A (0.30 A cm^{-2}), and 3.0 A (0.60 A cm^{-2}). The spectra are shown in absolute impedance (Ω); corresponding normalized values (Ω·cm^2) are discussed in the text.

At low current density (0.10 $A \cdot cm^{-2}$), the Nyquist plot displays a wide, nearly symmetrical semicircle with a high overall magnitude, reflecting the predominance of activation and ohmic losses. The high-

frequency intercept corresponds to 0.045–0.050 Ω (0.23–0.25 $\Omega \cdot cm^2$ when normalized), which remains nearly constant across all current densities, indicating stable ionic transport through the membrane and uniform mechanical contact within the MEA. At higher current densities (≥0.6 $A \cdot cm^{-2}$), the semicircular arc becomes smaller, indicating reduced charge-transfer resistance as the electrode interfaces reach full activation. A low-frequency tail, inclined by 45°–60° to the real axis, appears at high loads, corresponding to diffusion-related (Warburg-type) processes. This feature arises from mass transport limitations and local acid redistribution within the catalyst layer under dry, high-temperature operation. The fibrous membrane morphology, combined with slight variations in local porosity or compression, can also contribute to this behaviour by creating small spatial variations in acid concentration and proton transport resistance. The absence of hot-pressing during assembly likely enhanced such effects by introducing small local contact variations.

Using the membrane thickness (~60 μm), the apparent through-plane proton conductivity ($\sigma\perp$) was estimated to be 24–26 $mS \cdot cm^{-1}$ under operating conditions. This value represents the effective conductivity of the full MEA, including minor interfacial and contact resistances. The intrinsic membrane conductivity is therefore expected to be somewhat higher. The observed $\sigma\perp$ is lower than the in-plane conductivity (100–130 $mS \cdot cm^{-1}$ at 150 °C) measured previously, consistent with the known anisotropy of electrospun structures, where fibers preferentially align parallel to the substrate, facilitating lateral but not transverse proton transport. This anisotropy, while typical, highlights an important design consideration: optimizing fiber interconnection across the membrane thickness (e.g., via post-treatment or mild thermal fusion) could substantially enhance through-plane conduction without sacrificing porosity or acid uptake.

It should be noted that these GEIS tests were performed during early-stage calibration of the instrumentation. Small uncertainties in potentiostat response and local temperature control may slightly affect the absolute values. Nonetheless, the overall consistency of the spectra supports the reliability of the data and provides meaningful insight into the electrochemical properties of the electrospun membrane.

5.9 Potentials and future developments of electrospun membranes

The results discussed in this chapter clearly demonstrate that the fabrication of *m*-PBI-based membranes by electrospinning is a particularly promising approach for application in HT-PEM fuel cells. Compared to conventional dense films, electrospun membranes exhibit markedly faster acid impregnation kinetics, a higher phosphoric acid uptake, and, most importantly, the ability to form stable acid–polymer domains. In light of these findings, future research could focus on optimizing the fibrous microstructure to further improve membrane durability and stability under realistic operating conditions. One possible direction involves the design of sandwich-like architectures, combining multiple fibrous layers—possibly with different fiber diameters or densities—to balance mechanical integrity and acid retention. Another promising route could be the development of core–shell or concentric fiber structures, where phosphoric acid or functional additives are selectively confined within specific regions of the fiber. The incorporation of ionic liquids within such architectures could further stabilize proton conduction over time and reduce acid leaching during operation. Moreover, the preliminary results obtained from calendering treatments have shown that a simple post-processing step can drastically reduce membrane porosity and permeability. This offers a valuable route for microstructural refinement, enabling the production of fibrous membranes with tailored density and improved mechanical robustness, without compromising their functional properties. Taken together, these strategies—whether applied individually or in combination—offer a dual advantage: maximizing electrochemical performance through high acid doping levels, while simultaneously enhancing durability and resistance to degradation. Electrospun PBI membranes therefore represent not only an innovative alternative to traditional cast films but also a versatile platform for the development of next-generation proton exchange membranes for high-temperature fuel cells.

CHAPTER VI

AMINATED POLY(2,6-DIMETHYL-1,4-PHENYLENE OXIDE) – aPPO

This chapter presents the results of the synthesis and characterization of polyphenylene oxide functionalized with amine groups (aPPO). As discussed in a previous chapter, the introduction of polar groups onto PPO chains represents an effective strategy to modulate their interaction with acids or bases and to make them suitable for electrochemical (fuel cell) applications. In particular, the functionalization introduced with the amination reaction allows two promising avenues to be pursued: i) the possibility of establishing acid-base bonds with phosphoric acid, a fundamental feature for improving the durability and exchange properties of a membrane; ii) the use of aPPO as a precursor for the synthesis of anion-exchange membranes (AEM) for alkaline fuel cell applications. The synthesis strategy, described in detail in Section 2.3.2, is based on an initial nitration step that introduces -NO_2 groups onto the polymer chain, followed by a subsequent reduction reaction to form primary amine groups (-NH_2). The intermediates and the final polymer were analysed by FTIR/ATR spectroscopy, nuclear magnetic resonance (NMR) and high-angle X-ray diffraction (WAXD), to confirm the functionalization and assess its impact on the polymer structure. Solubility and impregnation tests in phosphoric acid are also reported to understand how the structural change affects the polymer's overall properties and its ability to establish acid-base interactions. The reaction pathway, previously reported in Section 2.3.2 (Scheme 2.3), is reproduced here as Scheme 6.1.

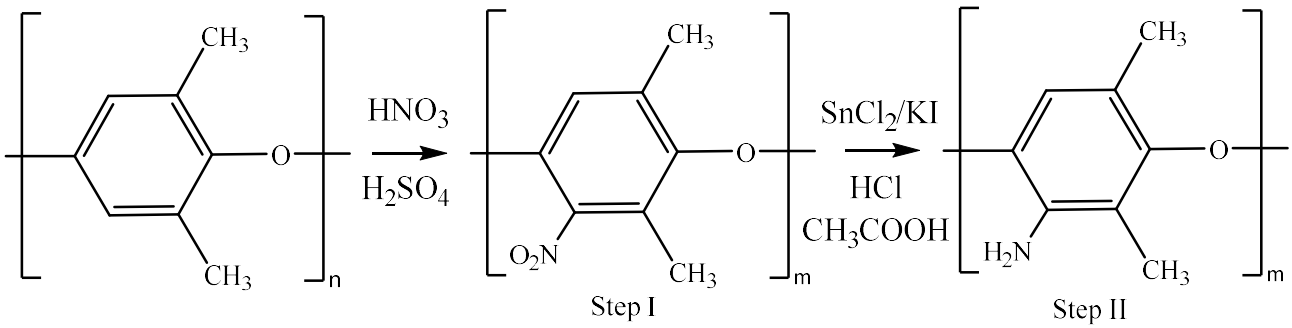

Scheme 6.1. Synthetic route for the preparation of aPPO starting from poly(2,6-dimethylphenylene oxide). The process involves a two-step sequence: nitration with HNO_3/H_2SO_4 (Step I), followed by reduction with $SnCl_2$/KI in acidic medium (Step II).

6.1 Comparative spectroscopic analysis: FTIR/ATR and NMR

The FTIR/ATR spectra of the three samples shown in Figure 6.1-a, describe a two-step reaction sequence involving an initial nitration step followed by a subsequent reduction. The profile curve of the starting material provides the reference for the interpretation of the subsequent transformations: in the PPO neat one recognizes, with good definition, the aromatic C-H stretching around ~3050 cm^{-1}, the aliphatic C-H bands of the methyl's at position 2.6 between ~2920 and 2850 cm^{-1}, the broad aromatic C=C region between ~1600 and 1500 cm^{-1} and, above all, the characteristic C-O-C aromatic ether imprint in the ~1250-1180 cm^{-1} domain, which remains readable in all samples and serves as a useful internal reference for comparing relative intensities. The whole is consistent with what has already been documented for PPO in previous sections of the thesis and with the reference literature on the base polymer. The nitrate sample (PPO-NO_2) obtained during the first reaction step shows typical signals of the nitro aromatic group, which are absent in the starting PPO and clearly distinguishable.

In particular, an intense band centered at about 1530 cm^{-1} appears in the 1600-1400 cm^{-1} region, attributable to asymmetric stretching of the N-O bond, flanked by the signal at about 1365 cm^{-1}, partially superimposed on the backbone fingerprint. The combination of these bands constitutes a clear sign of the nitration of PPO, indicating a functionalization that selectively affects the aromatic ring without altering its integrity. In the aminated sample (aPPO), the spectrum changes substantially, showing typical signals attributable to the reduction of the nitro group in primary amine. In fact, characteristic signals are noted in the 3300-3500 cm^{-1} region attributable to the symmetrical and asymmetrical stretching of the N-H bond, with localized bending bands around the 1620-1650 cm^{-1} region. In addition, a significant reduction in the diagnostic signal of the nitro group (~ 1530 cm^{-1}) is detected in the amine sample, with a weak residue compatible with traces of unreduced nitro units. In general, we can say that the presence of well-developed N-H signals confirms the reduction to primary amine, in agreement with what is reported in the literature.

a)

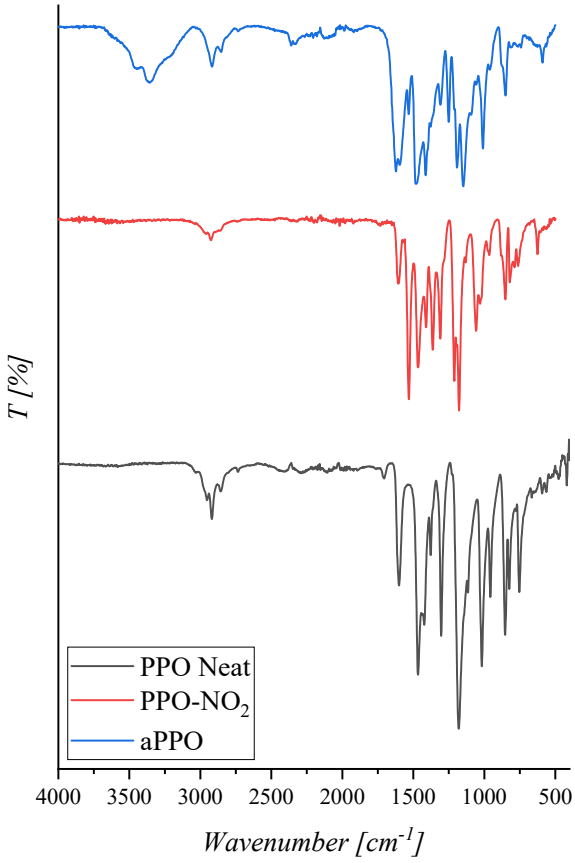
T [%]
PPO Neat
PPO-NO2
aPPO
4000 3500 3000 2500 2000 1500 1000 500
Wavenumber [cm-1]

b)

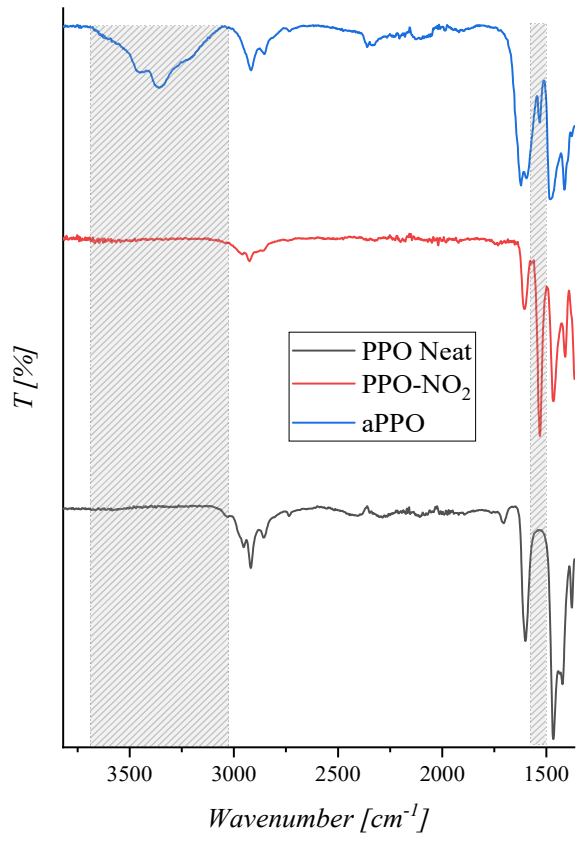
T [%]
PPO Neat
PPO-NO2
aPPO
3500 3000 2500 2000 1500
Wavenumber [cm-1]

Figure 6.1 – Comparative FTIR/ATR spectra of PPO neat (black), PPO-NO_2 (red) and aPPO (blue): (a) full spectrum in the 4000-400 cm^{-1} region; (b) zoom of the diagnostic regions of the main functional groups introduced in the backbone.

For a more immediate view of the functional markers, Figure 6.1-b shows the spectra zoomed in on the two diagnostic areas, highlighted in grey: starting from the left, the 3300-3500 cm^{-1} region is visible only in the amine sample (aPPO) and here it is possible to appreciate the double hump of the N-H stretching, absent in the other two samples. The second highlighted area captures the ~1530 cm^{-1} region of the nitro group (NO_2), showing its strong intensity in the nitrate sample and its reduction in the reduced sample. Overall, the three profiles document the sequential transition from PPO→ PPO-NO_2 →aPPO, while maintaining chemical identity throughout the reaction pathway.

The ^{1}H-NMR spectra recorded on neat PPO ($CDCl_3$), PPO-NO_2 ($CDCl_3$) and aPPO (DMSO-d_6) are shown in Figures 6.2-a and in greater detail in subfigures 6.2-b&c. Starting with the unfunctionalized PPO, we can generally say that its spectrum is characterized by the presence of characteristic signals of the protons bound to the aromatic ring in the range 6.2-7 ppm and the aliphatic (methyl) signals in the range 2-2.5 ppm (Fig. 6.2-b). The absence of additional resonances and the compactness of the aromatic area provide the reference for interpreting the changes induced by functionalization.

a)

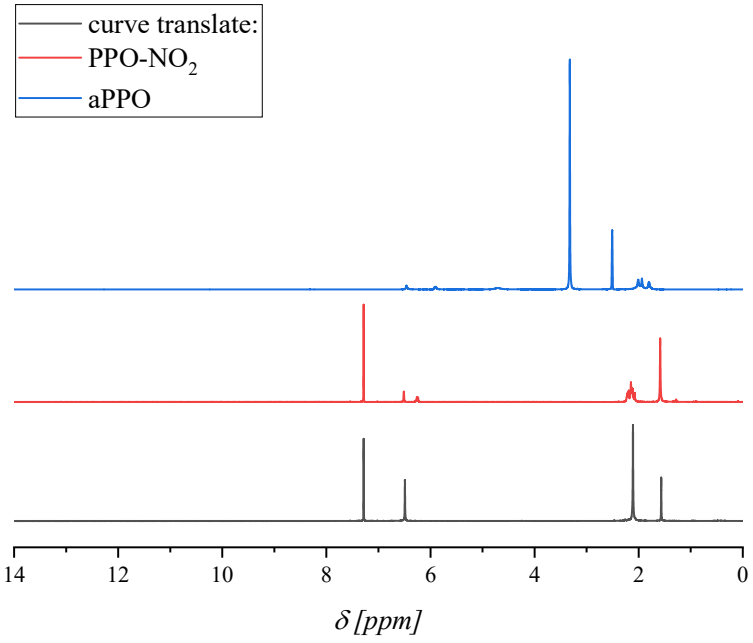

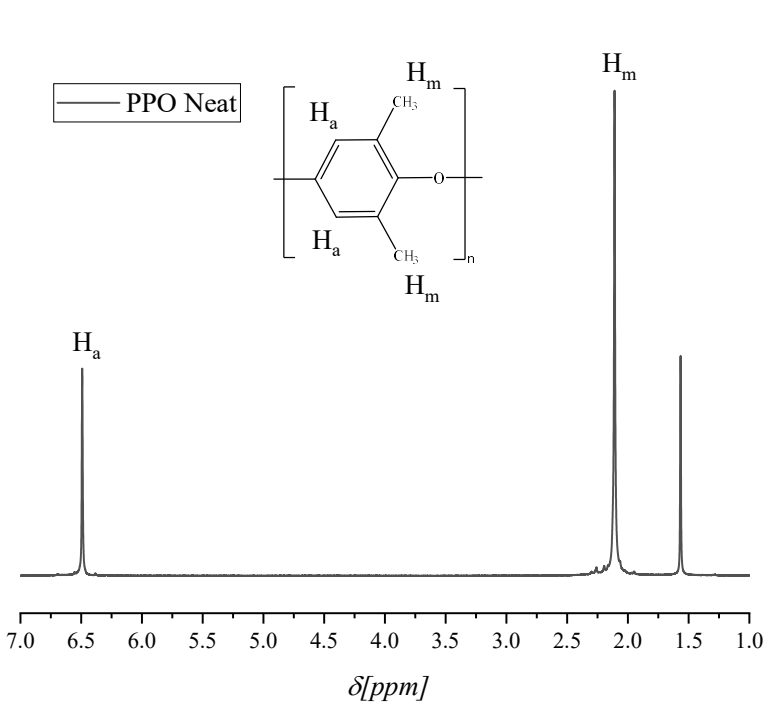

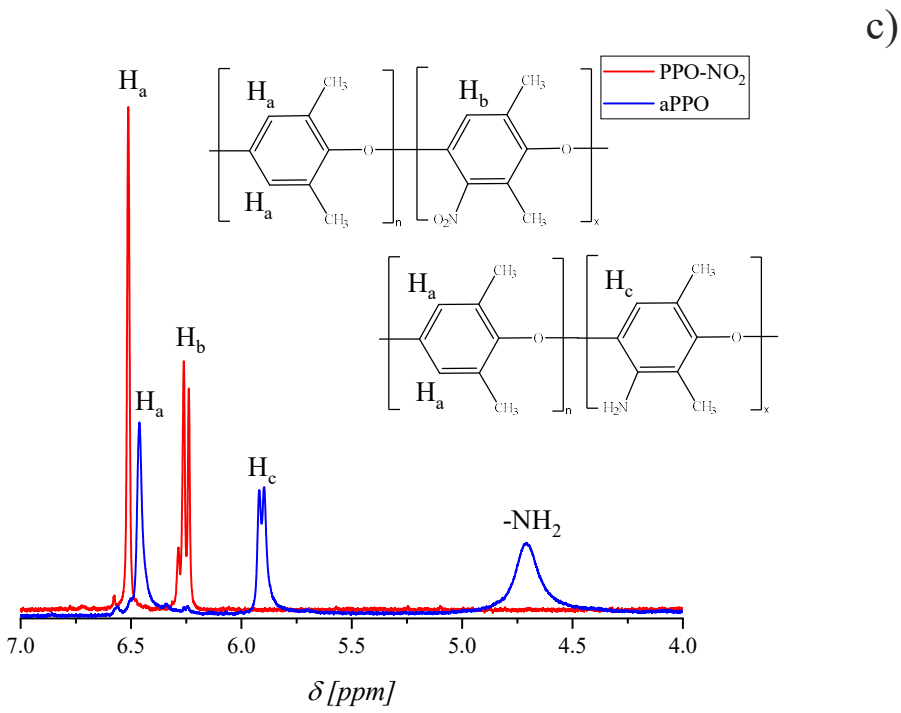

Figure 6.2 – Comparative ^{1}H-NMR spectra of PPO neat (black curve, $CDCl_3$), PPO-NO_2 (red curve, $CDCl_3$) and aPPO (blue curve, DMSO-d_6): a) full spectra in the range 0-14 ppm; b) zoom in the region 7-4 ppm with assignment of the unsubstituted units (H_a), substituted nitro group (H_b) and aminated unit (H_c).

In the nitrate sample (PPO-NO_2, red curve), the 6.7-6.0 ppm region shows a marked shift in the area associated with the aromatic protons, which slip to lower ranges and split into two distinct components, labelled H_a (unsubstituted units) and H_b (nitrate units), as shown in Fig. 6.2-c. The separation is essentially attributable to the deshielding effect of the nitro units on the protons at ortho and para positions with respect to the substituted site. The signal area of the methyl groups also underwent partial broadening with respect to neat PPO, a behavior already described in the literature for random copolymers and attributed to the statistical distribution of the units along the chain. For this reason, the quantitative determination of the degree of substitution was conducted from the protons positioned on the aromatic ring. In the amine sample (aPPO, blue curve), the aromatic zone recomposes itself towards higher ranges, showing two clearly distinguishable signals: H_a for the unsubstituted units, again centered around 6.5 ppm, and H_c, i.e. the proton relating to the substituted units of the amine group, located at around 6.0 ppm.

Furthermore, only for the aPPO sample, a broad signal is present in the 4.6-4.8 ppm region, consistent with the presence of an -NH_2 site exchangeable in DMSO-d_6. The observed behavior coincides with Pan et al.'s [138] observation that the N-H proton may be unassignable or confused with the solvent resonance, making the interpretation unreliable for quantitative purposes. As mentioned above, the degree of substitution was therefore determined by considering only the aromatic portion of the spectrum: the degree X of mono-substitution was derived from the integration ratios of the aromatic resonances alone, using the same approach as Pan et al. In particular, $\boldsymbol{I_a}$ was defined as the integral attributable to the H_a protons of the unsubstituted units and $\boldsymbol{I}$ as the integral of the protons of the substituted units (H_b for nitrate and H_c for amine) using Equation 6.1:

$$X = \frac{\mathrm{I}}{0.5\ \mathrm{I}_a + I} \qquad \text{Eq. 6.1}$$

This relationship takes into account the stoichiometry of the aromatic protons and allows an estimate independent of the absolute concentration of the sample. It is important to emphasize that solvent differences do not hinder the procedure, as the calculation makes use of area ratios within each sample and, in addition, the spectra were calibrated against solvent residues, baseline corrected and integrated over narrow windows to minimize spurious contributions. In the PPO-NO_2 sample, calculation of the integrals yields a value of I_a=1.0 and I_b=0.95, which gives, via Eq. 6.1, a degree of substitution X_{NO2}=0.655. In parallel, in the aPPO sample, we measure I=1 and I_c=0.93 which gives, applying the same relationship, an X_{NH2}=0.650. The two practically coinciding estimates indicate that the reduction process in the nitrate sample is essentially quantitative, with a small residue of nitrate sample also confirmed by the FTIR observation of the signal at ~1530 cm^{-1} in the aminated sample.

6.2 Structural analysis: X-Ray Diffraction

Figure 6.3-a shows the X-ray diffraction (XRD) patterns of the three analyzed samples — PPO neat, PPO-NO_2, and aPPO — to allow a direct structural comparison of the materials. The PPO neat sample exhibits a broad amorphous halo centered around $2\theta \approx 20°$, which is characteristic of amorphous aromatic polymers. The diffraction profile is smooth and lacks any sharp reflections that could be associated with crystalline domains, in agreement with the results discussed in Chapter 4. The PPO-NO2 sample displays a diffraction pattern nearly identical to that of the pristine polymer, maintaining an amorphous halo of similar position and shape. This indicates that the nitration process, although it introduces nitro groups onto the aromatic rings, does not generate sufficient structural heterogeneity to induce crystallization. This finding is consistent with the FTIR and ^{1}H-NMR analyses, which confirmed that the main polymer backbone remains essentially unaltered by the synthetic modification. In contrast, the aminated sample (aPPO) exhibits a markedly different diffraction pattern. Along with the broad amorphous halo, several sharp and well-defined peaks appear at various 2θ angles, which are absent in both the PPO neat and PPO-NO_2 spectra. These reflections correspond to crystalline phases and are attributed to inorganic residues, likely tin or tin salts, arising from the use of $SnCl_2$ as a reducing agent in the conversion of nitro to amino groups ($–NO_2 \rightarrow –NH_2$). Based on this evidence, the aPPO sample was subjected to an additional purification step as described in Section 2.3.2, involving dissolution in chloroform followed by precipitation in methanol. The XRD pattern obtained after purification, shown in Figure 6.3-b, reveals the disappearance of crystalline peaks and the persistence of a single amorphous halo, comparable to those observed in PPO neat and PPO-NO_2. These results confirm the effectiveness of the purification procedure in removing inorganic residues and restoring the intrinsic amorphous nature of the polymer. Furthermore, the XRD analysis demonstrates the utility of this technique not only for structural characterization but also as a sensitive indicator of sample purity and the presence of crystalline contaminants.

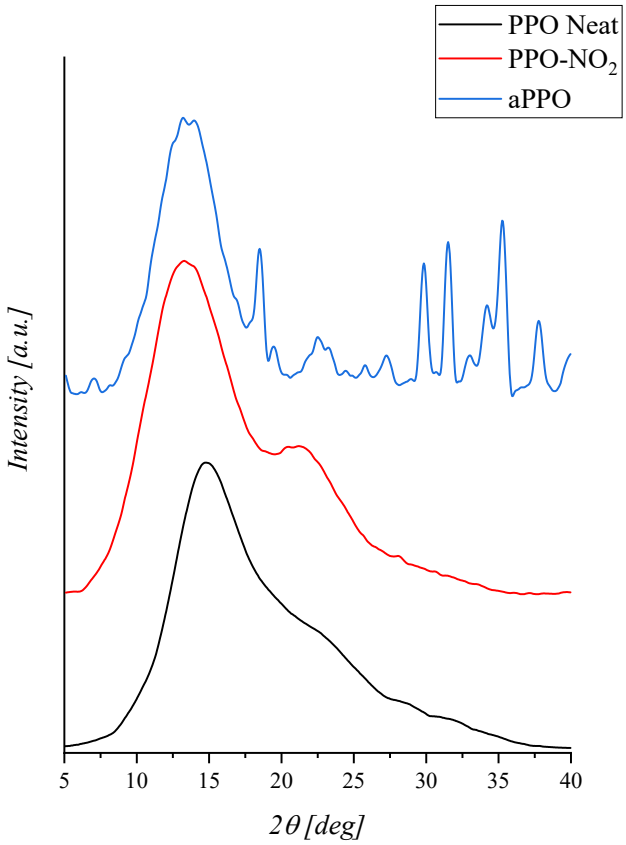
PPO Neat
PPO-NO2
aPPO
Intensity [a.u.]
5
10
15
20
25
30
35
40
2θ [deg]

a)

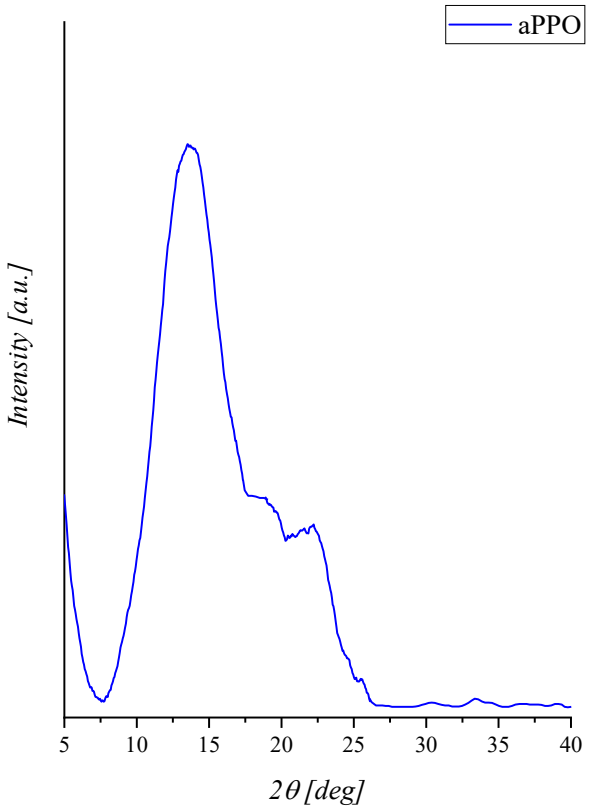
aPPO
Intensity [a.u.]
5
10
15
20
25
30
35
40
2θ [deg]

b)

Figure 6.3 – XRD diffraction patterns in the 5–40° 2θ range: (a) Comparison between PPO neat (black), PPO-NO_2 (red), and aPPO (blue). Crystalline peaks appear only in the aminated sample, attributable to inorganic residues from the reduction step. (b) aPPO after purification, showing the disappearance of crystalline reflections and confirming the effectiveness of the treatment and the amorphous nature of the polymer.

6.3 Solubility test results

The solubility analysis shown in Table 6.1 of the samples produced allowed a direct relationship between the functionalization of PPO and the transition from the nitro group to the amine group, showing affinity towards solvents of different polarity. PPO neat confirms the expected behavior of an apolar aromatic polymer: it is highly soluble in chloroform and toluene while being insoluble in medium-polar solvents such as dimethyl sulphoxide (DMSO) and dimethylacetamide (DMAc). This solubility justifies the use of chloroform in analytical and process steps of the starting material and, above all, provides the reference with which to read the effect of the introduced groups. Nitration shifts change the situation markedly: PPO-NO_2 remains highly soluble in chloroform and toluene, but also acquires affinity for polar aprotic solvents as partial solubility is observed in DMSO and DMAc, which is absent in PPO.

The most pronounced jump occurs after amination: aPPO (post-purification) becomes insoluble in chloroform and toluene, while it is highly soluble in DMSO, DMAc, NMP and DMF, allowing clear and stable solutions suitable for film casting and subsequent acid impregnation tests. The overall trend is thus monotonic towards polar aprotic solvents along the functionalization sequence, with a reversal of preference that is consistent with the introduction of first a strongly electron-attracting substituent (-NO_2) and then a basic, hydrogen-binding substituent (-NH_2). On a practical level, the purification of aPPO is decisive: the absence of inorganic residues is reflected in perfectly clear solutions in DMSO/DMAc/NMP/DMF, without opalescence or sediments that would otherwise interfere with fine filtration and film quality.

Solvent	*PPO neat*	*PPO-NO_2*	*aPPO*
Chloroform ($CHCl_3$)	++	++	-
Toluene (C_7H_8)	++	++	-
DMSO (C_2H_6OS)	-	+	++
NMP (C_5H_9NO)	n.d.	n.d	++
DMF (C_3H_7NO)	n.d.	n.d.	++
DMAc (C_4H_9ON)	-	+	++

Table 6.1 – Results of solubility tests of PPO neat, PPO-NO_2 and aPPO samples in solvents of different polarity. All tests were performed at the same concentration, temperature and polymer/solvent mass ratio (1 % wt.). Legend: ++, totally soluble; +, partially soluble; -, unsoluble; n.d., not detected.

6.4 aPPO film preparation and acid treatment

Immediately after the purification step and following the solubility tests described above, the solvent used for the production of aPPO films from solution casting is DMSO. This choice is motivated by its high solvation capacity and thermal stability, which allows gradual evaporation of the solvent, avoiding local precipitation or formation of concentration gradients in the final film. A 5% wt. solution of aPPO in DMSO was prepared at room temperature and under magnetic stirring for about 2h until a clear solution with no visible residue was obtained. The solution was then centrifuged and then cast onto a Petri dish and allowed to evaporate at 60 °C overnight until the solvent was completely removed. The resulting film, translucent and about 100 μm thick, shown in Figure 6.4 shows a smooth surface with amber coloration. However, the material is found to be extremely brittle and rigid, with a marked tendency to fracture under minimal mechanical stress. This behavior is consistent with the polymer structure of aPPO, which is rigid and poorly plasticized, with the free amine groups capable of establishing interchain interactions (H-bond) limiting the mobility of the chains themselves.

Figure 6.4 – Optical image of the aPPO film obtained by solution casting from a 5% wt. solution of aPPO in DMSO. The film shows good surface homogeneity and brown-translucent coloration.

To improve the mechanical flexibility and evaluate the material's ability to establish acid-base interactions, the resulting films were subjected to imbibition in concentrated phosphoric acid (85 % wt.). Each sample was first cut into 2x2 cm squares and weighed in order to identify its dry mass (w_{dry}), and then they were immersed in H_3PO_4 for 24h after which the films were rapidly removed from the acid solution, dried superficially with filter paper and weighed again (w_{wet}). From the weight gain measured following imbibition, the moles of phosphoric acid (n_{H3PO4}) retained by the aPPO film could be determined, and from the degree of amine monosubstitution calculated via NMR, the moles of aPPO (n_{aPPO}) were also calculated. The Acid Doping Level (ADL) was calculated according to the classical relationship described in Equation 6.1:

$$ADL = \frac{n_{H3PO4}}{n_{aPPO}} \qquad \text{Eq. 6.1}$$

The average value obtained from three independent tests is approximately 2.52 ± 0.20, indicating a significant interaction between the polymer and the acid, albeit lower than typical values for benchmark materials such as polybenzimidazole (PBI). Nevertheless, this result demonstrates the presence of stable acid-base bonds between the amine groups of aPPO and the proton species of phosphoric acid, confirming the reactivity of the functional sites introduced into the polymer backbone. A relevant aspect is also the behavior of the film after imbibition. In particular, marked swelling was detected with an increase in film size of about 3-fold compared with the initial size.

This was also accompanied by a noticeable mechanical change as the material was found to be more flexible and malleable than the starting film, although structurally weakened. This plasticization, however, resulted in the film breaking in several places, a sign that the swelling was accompanied by internal stresses and a strong non-uniform thickness alteration. This behavior, however, is in line with what has been observed with other amine-treated polymers treated in acidic solutions, in which the formation of acid-base hydrogen bridges lead to a partially plasticized but unstable polymer lattice, characterized by cracking or partial matrix dissolution phenomena. Overall, the value of ADL ~ 2.52 suggests the formation of an overall stable acid-base complex of NH_3^+ $H_2PO_4^-$ type, as discussed in the following section with reference to the spectroscopic results.

6.5 FTIR/ATR Analysis after the acid treatment

FTIR analysis in ATR mode was used to identify structural changes associated with the interaction between the amine groups of aPPO and phosphoric acid. Figure 6.5 shows the FTIR spectra of the original sample (red curve) and the one doped with phosphoric acid (gray curve), which is useful for highlighting changes in the characteristic bands of the $-NH_2$ group and the appearance of new signals attributable to the phosphate species. In the untreated film, the 3700-3200 cm^{-1} region shows the typical double shoulder of the primary amine group, with maxima at about 3350 and 3270 cm^{-1}, which can be associated with the asymmetric and symmetric N-H stretching vibrations, respectively, as discussed extensively in the previous paragraphs. The clear separation between the two bands indicates the presence of $-NH_2$ groups that are free and not strongly involved in hydrogen bonds. After imbibition in H_3PO_4, the double shoulder disappears and a broad, unstructured band centered around 3500 cm^{-1} appears, extending to about 3200 cm^{-1}. This spectral profile is characteristic of strong, distributed hydrogen bonds, in which the N-H vibrations are de-tuned due to an interaction with phosphate oxygens. The absence of a sharp band at 3100 cm^{-1}, typical of the $-NH_3^+$ ammonium group, suggests that complete protonation does not occur, and that the amines are involved in hydrogen-bonded acid-base complexes rather than true ammonium salts. The band at 3500 cm^{-1} can thus be interpreted as the superposition of contributions from N-H---O=P bonds of different intensities, where the proton is partially shared between the nitrogen and oxygen of the phosphate. This picture is consistent with a partially proton--reversible interaction mechanism in equilibrium between molecular and ionic forms proposed in Equation 6.2:

$$R–NH_2+H_3PO_4 \rightleftharpoons R–NH_2\cdots H_3PO_4 \rightleftharpoons R–NH_3^+H_2PO_4^-$$ Eq. 6.2

Further confirmation comes from the mid-infrared region (1700-900 cm^{-1}): in the aPPO neat film, the band related to N-H bonding is located at about 1615 cm^{-1} and tends to decrease in intensity and shift toward lower values (1600 cm^{-1}) after treatment, an indication of a weakening of N-H bonding due to interaction with the acid. At the same time, new bands appear in the 1250-950 cm^{-1} region, which were absent in the spectrum of the untreated sample. In particular:

- a band at 1240-1220 cm^{-1} attributable to vibrational stretching of the partially coordinated P=O group;
- a set of signals between 1150 and 950 cm^{-1} traceable to the P-O and P-O-H vibration modes of H_3PO_4 and its dissociated anions;
- a secondary signal at about 1080 cm^{-1}, which may be associated with P-O-C vibrations, indicative of a closer interaction or partial proton transfer.

The appearance of these new bands, together with the disappearance of the double N-H shoulder, provides direct evidence for the formation of acid-base bonds and multiple hydrogen bonds between aPPO chains and phosphoric acid molecules. In addition, the spectrum shows no significant changes in the characteristic bands of the aromatic backbone of PPO, such as the C=C vibrations of phenylene (~1500-1450 cm^{-1}) and C-O-C vibrations of ether (~1240-1180 cm^{-1}) confirming how the interaction with the acid is localized only on the amine groups and does not affect the chemical stability of the main chain.

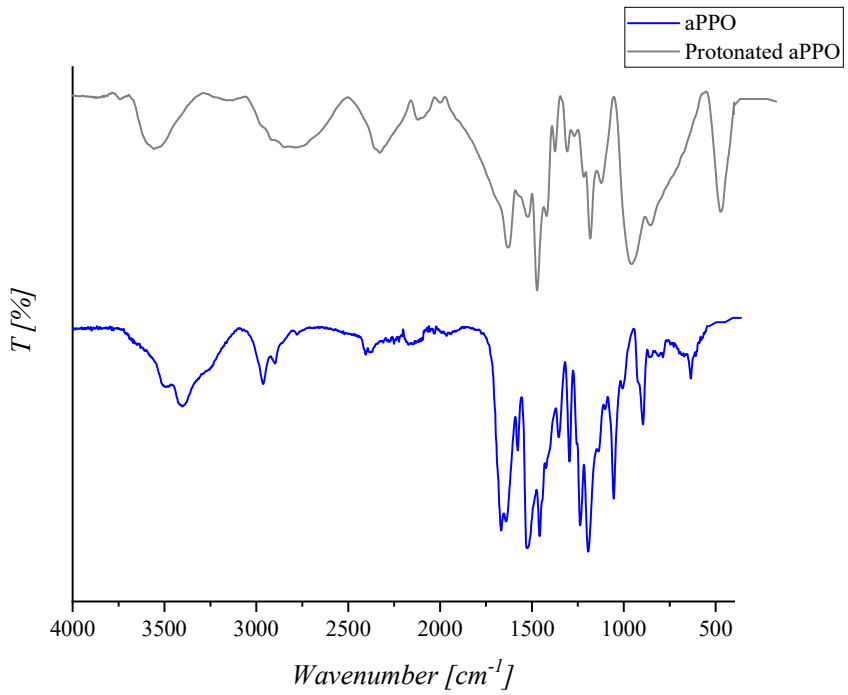

Figure 6.5 - FTIR/ATR spectrum of difference between doped and undoped aPPO in H_3PO_4. The characteristic double shoulder of amine N-H vibrations (3350-3270 cm^{-1}) disappears after imbibition, leaving a broad band centered at ~3500 cm^{-1}, indicative of strong hydrogen bonds with H_3PO_4. New bands also emerge at 1240 and 1150-950 cm^{-1}, attributable to the P=O and P-O-H vibrations of the phosphate groups.

6.6 Mechanism of interaction and proton conduction of aPPO

Spectroscopic and morphological analysis conducted on aPPO doped with phosphoric acid allows the mechanism of acid-base interaction to be clearly delineated, enabling it to be compared with that of the reference material for high-temperature fuel cells, polybenzimidazole (PBI). Although belonging to two different polymer classes, both systems share the ability to establish strong interactions with phosphoric acid and to stabilize mobile proton species within them, albeit with different modes and intensities. In the case of aPPO, the amine functionalization of the aromatic backbone of PPO gives the chain the ability to interact with H_3PO_4 through a combination of hydrogen bonds and partial protonation. The acid molecules coordinate to the amine groups through N-H---O=P or O-H---N interactions, generating a complex network of hydrogen bonds of varying strength. This network, although less dense than that of PBI, is extensive enough to allow proton transfer within the matrix. Indeed, FTIR/ATR analysis showed the disappearance of the double shoulder typical of free amines and the appearance of a broad, unstructured band centered at about 3500 cm^{-1}, a clear sign of the establishment of strong and diffuse hydrogen bonds, with only a partial protonation contribution. The

interaction with the acid results in a profound reorganization of the polymeric lattice, leading to a macroscopic swelling of the film and a significant softening of the matrix, which from rigid and brittle becomes flexible and malleable. This plasticized behavior is compatible with the insertion of H_3PO_4 molecules between the chains and the formation of a dynamic structure, capable of harboring free protons. Proton transfer in doped aPPO cannot be attributed to a single mechanism, but rather to a coexistence of two synergistic processes. On the one hand, acid molecules adsorbed in the polymeric lattice are free to move partially, carrying associated protons, following a typical carrier-like process; on the other hand, protons can migrate along the network of hydrogen bonds between the amine and phosphate groups, through a Grotthuss-like proton hopping mechanism. Such dynamics requires a flexible but not fully protonated structure, such as that actually observed in aPPO. The presence of an Acid Doping Level of about 2.5 after 24 h of imbibition, although lower than typical PBI values, testifies to the formation of a chemically active environment capable of promoting a proton conduction mechanism in the anhydrous environment. In the PBI/H_3PO_4 system, on the other hand, the situation is more defined and the strength of the acid-base interaction is markedly higher because the imidazole groups present in the PBI chain, act as very strong basic sites and form stable NH^+-$H_2PO_4^-$ type ion pairs with phosphoric acid. Protonation is thus more pronounced and diffuse, leading to the formation of a true three-dimensional ion network, in which protons are strongly delocalized between imidazole groups and phosphate anions ($H_2PO_4^-/HPO_4^{2-}$). The resulting proton conductivity is mainly governed by a Grotthuss-type mechanism, in which the proton moves along a chain of hydrogen bonds that rearrange continuously. The high density of proton sites (2 per monomer unit) and high acid imbibition capacity allow PBI to reach Acid Doping Level values above 5, providing conductivities up to 10^{-1} S cm^{-1} at temperatures of 160-200 °C. However, such high interaction with acid also results in a significant degree of plasticization and, in some cases, a deterioration in the mechanical stability of the film, which must be compensated for by cross-linking or composite reinforcement processes. In comparison with PBI, aPPO represents a weaker system from the acid-base point of view, but with structural and technological characteristics of considerable interest. The partial protonation of amines, coupled with their random distribution along the PPO chain, generates a more disordered but chemically active network in which protons can move due to fluctuating hydrogen bonds. This type of interaction, described in Scheme 6.2, while less intense, offers advantages in chemical stability and potential durability, as it reduces the risk of acid leaching and limits the degradation phenomena associated with the strong internal acidity of the PBI system.

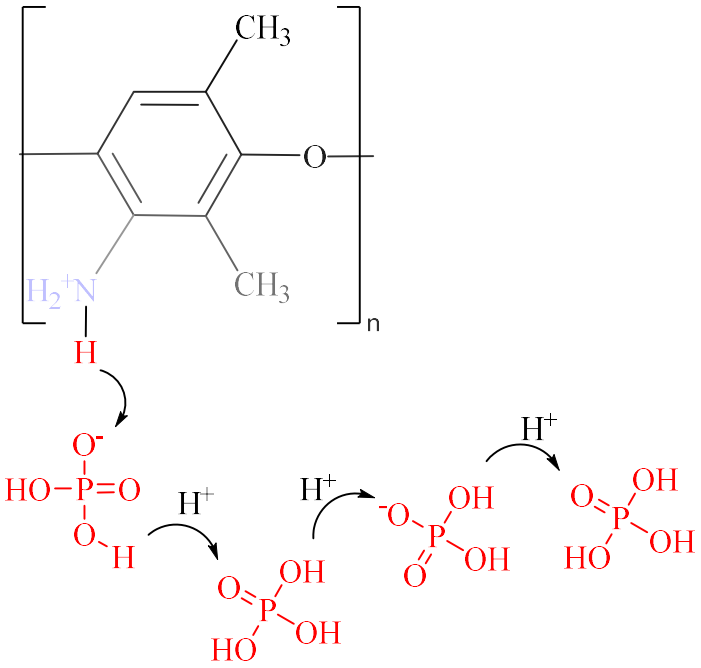

Scheme 6.2 - Proposed mechanism of acid–base interaction and proton conduction in aPPO doped with H_3PO_4. Hydrogen bonding and partial proton transfer occur between amine groups and phosphoric acid, facilitating proton hopping along the H-bond network.

In other words, aPPO exhibits a milder but more tolerant cooperative chemistry, capable of retaining acid while retaining minimal structural cohesion even under high imbibition. Functionally, the behavior observed in aPPO can be considered complementary to that of PBI. While the latter provides high conductivities due to a high density of proton sites, aPPO offers an alternative approach based on affordability, synthetic simplicity and sustainability. Indeed, the PPO backbone, which is thermally stable, nonfluorinated, and already commercially available, enables the design of low-cost conducting membranes that are potentially scalable on a large scale, reducing the environmental impact associated with the use of fluoropolymers and specialty monomers. The challenge remains to increase the degree of interaction with the acid without sacrificing the mechanical stability of the film, a goal that can be achieved through blending strategies or targeted structural modifications, which will be discussed in the following section.

6.7 Future outlook and improvement

The evidence gathered in the present work provides a solid basis for interpreting H_3PO_4-doped aPPO as a novel and promising material for applications in high-temperature polymer membrane fuel cells (HT-PEMFC). The ability to establish acid-base interactions with phosphoric acid, confirmed by spectroscopic analysis, is the most relevant result and opens up several prospects for scientific and technological development. The first key message that emerges is that the effectiveness of a material for HT-PEMFC applications depends not only on the high Acid Doping Level value, but also on the nature of the interactions that are established between the polymeric and acid phases. In the case of aPPO, partial protonation and the formation of an extensive network of hydrogen bonds ensure a balanced combination of acid retention and chemical stability, which are essential features for the long-term operation of a membrane. The absence of excessive ionization also reduces matrix plasticization and acid leaching, making the system inherently more durable over time. A second crucial aspect concerns the scalability and economic viability of the material: aPPO is in fact derived from a commercial aromatic polymer, PPO, modified by a simple amination reaction that can be performed with inexpensive reagents and common solvents. Unlike specialty polymers such as PBI, whose synthesis requires drastic conditions and expensive precursors, aPPO can be obtained by industrially compatible processes, setting the stage for low-cost, environmentally friendly proton membranes. The non-fluorinated nature of the material is also a strategic advantage, in line with European directives aimed at reducing the use of fluorinated compounds and promoting more sustainable technologies. From a technological point of view, the main directions for improvement are in mechanical stability and imbibition capacity. The fragility observed in pure aPPO films can be mitigated by post-treatment with weak acids such as TFA (Tri-fluoro acetic acid), which promote controlled protonation and partial chain relaxation, making the membrane more flexible. Further improvements may result from the introduction of copolymers or functional blends, in which aPPO is combined with more flexible polymers or with stronger basic groups, which can increase the density of proton sites and the value of ADL. The use of cross-linking agents or side chains containing ethereal or imidazole groups could also stabilize the structure during imbibition, preventing film rupture and improving thermomechanical strength. Looking forward, the possibility of creating aPPO-based hybrid membranes, in which the polymer acts as a scaffold for immobilization of H_3PO_4 or other conducting phases, represents a highly promising research direction. Indeed, the combination of stability, cost-effectiveness and ability to interact with phosphoric acid makes aPPO a versatile platform for the development of next-generation proton-conducting materials.

In conclusion, the present study demonstrates that a nonfluorinated, inexpensive, and easily processable polymer such as aPPO, synthesized here for the first time through the reaction pathway proposed in this thesis specifically for HT-PEMFC applications, can establish effective acid–base interactions with H_3PO_4, thereby laying the foundation for proton conduction under anhydrous conditions. Even with a lower Acid Doping Level than commercial benchmarks, the observed behavior highlights a remarkable potential for further enhancement through material engineering and the implementation of blending or crosslinking strategies. This pioneering synthetic approach positions aPPO as a novel and cost-effective material platform for high-temperature fuel cells, combining adequate performance with economic and environmental sustainability, and thus paving the way for a new generation of low-cost, nonfluorinated proton-conducting membranes.

CONCLUSIONS

The work presented in this PhD thesis has explored the development of new non-fluorinated polymer electrolyte membranes as a sustainable and technologically viable alternative to perfluorosulfonated (PFAS) systems, such as Nafion, that have dominated the fuel cell market for decades. This research aligns with the broader framework of the ongoing energy transition and the global effort to decarbonize power generation, where hydrogen and fuel cell technologies are increasingly recognized as strategic components of a clean, circular, and efficient energy system. The gradual restriction on the use of PFAS by regulatory authorities in Europe and the United States represents not only an environmental necessity but also a profound industrial challenge, as it requires rethinking the design of ionomeric membranes and the chemistry of proton-conducting materials from first principles. The aim of this work was therefore to contribute to this transformation by developing high-performance polymer electrolytes based on hydrocarbon backbones, derived from commercially available and inexpensive monomers, and to demonstrate their applicability both in low-temperature and high-temperature PEM fuel cell architectures.

The first experimental section was dedicated to the synthesis and characterization of sulphonated poly(2,6-dimethyl-1,4-phenylene oxide) (sPPO) membranes. Starting from commercial PPO, a common amorphous thermoplastic polymer, a solid-state sulphonation protocol was developed to introduce controlled amounts of sulfonic groups on the aromatic rings. The process, based on the use of acyl sulfates in non-aqueous media, allowed fine-tuning of the degree of sulfonation while preserving the mechanical integrity of the films. The resulting membranes exhibited an ion exchange capacity and water uptake behaviour strongly dependent on the sulfonation time and the membrane's morphology, confirming the possibility to modulate their hydrophilic character and, consequently, their proton conductivity. The electrochemical validation in single-cell PEM configuration demonstrated proton conductivities comparable to those of Nafion® 212 under humidified conditions, while maintaining the intrinsic advantage of being fully fluorine-free. The main limitation observed was the tendency to excessive swelling at high degrees of sulfonation, a common issue among hydrocarbon-based membranes, but one that can be addressed through crosslinking strategies or the introduction of inorganic nanofillers. From a broader perspective, the sPPO system has proven that high-performing ionomeric membranes can be derived from simple, low-cost commercial materials through relatively mild chemical treatments, paving the way for scalable and environmentally sustainable manufacturing processes.

The second part of the thesis investigated the electrospinning of *m*-polybenzimidazole (*m*-PBI) to produce fibrous membranes for high-temperature proton exchange membrane fuel cells (HT-PEMFCs). The change in morphology from dense films to nanofibrous mats significantly improved the surface area, porosity, and consequently, the acid impregnation capacity of the material. The fibrous PBI membranes showed high phosphoric acid uptake, leading to improved proton conductivity and reduced ohmic resistance in terms of proton conductivity. The results highlight the importance of morphology engineering in optimizing both the kinetic and thermodynamic parameters governing acid adsorption and retention. Surprisingly, the interaction between the electrospun membranes of *m*-PBI and phosphoric acid showed the formation of an interconnected network of hydrogen bonds and phosphate anions that provides good chemical and mechanical stability. The electrospinning approach also demonstrated its versatility and scalability, offering a potential pathway to industrially relevant membranes with tunable thickness and fiber alignment. Moreover, the electrochemical measurements performed in single-cell configuration revealed a consistent reduction in the overall ohmic resistance and a stable proton conductivity over time, indicating that the fibrous architecture effectively promotes continuous proton-transport pathways. When combined with the inherently scalable nature of the electrospinning process, these results suggest that this approach could be extended to membranes of larger active area without compromising performance. This work contributes to a growing body of research demonstrating that structural design—rather than only chemical modification—can be a decisive factor in the functional performance of HT-PEM materials. The PBI-based fibrous systems developed here confirm the robustness, durability, and excellent electrochemical behaviour that make PBI the benchmark polymer for high-temperature fuel cell applications.

The final section focused on the synthesis of aminated poly(2,6-dimethyl-1,4-phenylene oxide) (aPPO), a new polymeric platform designed to merge the chemical versatility of PPO with the acid-binding capability typical of PBI. The introduction of amine groups into the PPO backbone generated a basic polymeric matrix capable of interacting with phosphoric acid to form stable ammonium phosphate complexes. This acid-base interaction mechanism enables efficient proton transport even under anhydrous conditions, suggesting the potential of aPPO as a viable electrolyte for HT-PEMFCs. The dual functionality of this polymer—its ability to act as a proton-conducting matrix at high temperature and as a precursor for quaternized anion-exchange membranes—positions aPPO as a truly multifunctional material. The synthesis pathway developed is based on commercially accessible PPO and simple amination reactions, making this route both cost-effective and adaptable to large-scale production. In essence, the aPPO system bridges two traditionally distinct technological areas—

acidic and alkaline electrochemical devices—reinforcing the concept of PPO as a molecular platform for next-generation, fluorine-free energy materials.

Overall, the research presented in this thesis demonstrates a coherent and systematic approach towards the development of environmentally sustainable and economically viable polymer electrolytes for fuel cell applications. Each of the polymers investigated—sPPO, electrospun PBI, and aPPO—addresses a specific aspect of membrane functionality: the first optimizes proton conductivity and cost for low-temperature systems; the second enhances structural and electrochemical performance at high temperatures through morphological design; and the third introduces a new class of hybrid materials capable of operating in multiple electrochemical environments. Together, they define a roadmap for the rational design of polymer electrolytes based on hydrocarbon matrices that are free of fluorine and compatible with the forthcoming regulatory landscape.

This work reinforces the idea that the next generation of fuel cell membranes should no longer rely on perfluorinated precursors and materials, but on sustainable ones derived from widely available aromatic polymers. The use of PPO and PBI as base materials exemplifies this approach: they are inexpensive, commercially accessible, and chemically modifiable, allowing the creation of membranes that combine high proton conductivity, mechanical robustness, and chemical stability without compromising environmental compatibility. The experimental results confirm that it is possible to achieve conductivities on the order of 10^{-1} S cm^{-1} using non-fluorinated backbones, while maintaining acceptable dimensional stability and durability. These achievements bring the prospect of fully hydrocarbon-based fuel cells closer to industrial reality, with the additional benefit of drastically reducing material costs and environmental impact.

In conclusion, the work carried out throughout this Ph.D. project provides both scientific and technological insights into how polymer chemistry, processing, and electrochemical evaluation can converge to develop new generations of PFAS-free membranes. By exploiting commercially available polymers, adopting low-impact synthesis protocols, and applying advanced processing techniques such as electrospinning, it is possible to produce materials that are not only competitive with current benchmarks but also aligned with the principles of green chemistry and circular economy. Future research should focus on the long-term stability and integration of these membranes into complete fuel cell stacks, the optimization of composite architectures, and the coupling of these materials with renewable hydrogen production systems. The key message emerging from this work is that the transition to non-fluorinated, cost-effective, and sustainable polymer membranes is not

only feasible but necessary for the evolution of hydrogen technologies and for their large-scale deployment in a decarbonized energy future.

REFERENCES

[1] F. Johnsson, J. Kjärstad, e J. Rootzén, «The threat to climate change mitigation posed by the abundance of fossil fuels», *Climate Policy*, vol. 19, fasc. 2, pp. 258–274, feb. 2019, doi: 10.1080/14693062.2018.1483885.

[2] P. A. Owusu e S. Asumadu-Sarkodie, «A review of renewable energy sources, sustainability issues and climate change mitigation», *Cogent Engineering*, vol. 3, fasc. 1, p. 1167990, dic. 2016, doi: 10.1080/23311916.2016.1167990.

[3] T. He, P. Pachfule, H. Wu, Q. Xu, e P. Chen, «Hydrogen carriers», *Nat Rev Mater*, vol. 1, fasc. 12, p. 16059, ott. 2016, doi: 10.1038/natrevmats.2016.59.

[4] A. Züttel, A. Remhof, A. Borgschulte, e O. Friedrichs, «Hydrogen: the future energy carrier», *Phil. Trans. R. Soc. A.*, vol. 368, fasc. 1923, pp. 3329–3342, lug. 2010, doi: 10.1098/rsta.2010.0113.

[5] J. Lindorfer, D. C. Rosenfeld, e H. Böhm, «Fuel Cells», in *Future Energy*, Elsevier, 2020, pp. 495–517. doi: 10.1016/B978-0-08-102886-5.00023-2.

[6] J. Brouwer, «On the role of fuel cells and hydrogen in a more sustainable and renewable energy future», *Current Applied Physics*, vol. 10, fasc. 2, pp. S9–S17, mar. 2010, doi: 10.1016/j.cap.2009.11.002.

[7] Q. Hassan, I. D. J. Azzawi, A. Z. Sameen, e H. M. Salman, «Hydrogen Fuel Cell Vehicles: Opportunities and Challenges», *Sustainability*, vol. 15, fasc. 15, p. 11501, lug. 2023, doi: 10.3390/su151511501.

[8] Y. Manoharan *et al.*, «Hydrogen Fuel Cell Vehicles; Current Status and Future Prospect», *Applied Sciences*, vol. 9, fasc. 11, p. 2296, giu. 2019, doi: 10.3390/app9112296.

[9] M. W. Ellis, M. R. Von Spakovsky, e D. J. Nelson, «Fuel cell systems: efficient, flexible energy conversion for the 21st century», *Proc. IEEE*, vol. 89, fasc. 12, pp. 1808–1818, dic. 2001, doi: 10.1109/5.975914.

[10] M. Secanell, R. Songprakorp, N. Djilali, e A. Suleman, «Optimization of a proton exchange membrane fuel cell membrane electrode assembly», *Struct Multidisc Optim*, vol. 40, fasc. 1–6, pp. 563–583, gen. 2010, doi: 10.1007/s00158-009-0387-z.

[11] O. Okur, Ç. İyigün Karadağ, F. G. Boyacı San, E. Okumuş, e G. Behmenyar, «Optimization of parameters for hot-pressing manufacture of membrane electrode assembly for PEM (polymer electrolyte membrane fuel cells) fuel cell», *Energy*, vol. 57, pp. 574–580, ago. 2013, doi: 10.1016/j.energy.2013.05.001.

[12] E. Santos e W. Schmickler, «Electrocatalysis of Hydrogen Oxidation—Theoretical Foundations», *Angew Chem Int Ed*, vol. 46, fasc. 43, pp. 8262–8265, nov. 2007, doi: 10.1002/anie.200702338.

[13] J. Fan *et al.*, «Bridging the gap between highly active oxygen reduction reaction catalysts and effective catalyst layers for proton exchange membrane fuel cells», *Nat Energy*, vol. 6, fasc. 5, pp. 475–486, mag. 2021, doi: 10.1038/s41560-021-00824-7.

[14] L. Yang *et al.*, «Carbon-Based Metal-Free ORR Electrocatalysts for Fuel Cells: Past, Present, and Future», *Advanced Materials*, vol. 31, fasc. 13, p. 1804799, mar. 2019, doi: 10.1002/adma.201804799.

[15] A. J. Appleby, «Fuel cell electrolytes: evolution, properties and future prospects», *Journal of Power Sources*, vol. 49, fasc. 1–3, pp. 15–34, apr. 1994, doi: 10.1016/0378-7753(93)01790-O.

[16] L. Carrette, K. A. Friedrich, e U. Stimming, «Fuel Cells: Principles, Types, Fuels, and Applications», *ChemPhysChem*, vol. 1, fasc. 4, pp. 162–193, dic. 2000, doi: 10.1002/1439-7641(20001215)1:4%3C162::AID-CPHC162%3E3.0.CO;2-Z.

[17] C. Vallejo-Cervantes, M. Espinoza-Andaluz, e A. Iranzo, «Technical review of commercial LT-PEMFC technologies: Performance, applications and challenges», *International Journal of Hydrogen Energy*, vol. 176, p. 151480, ott. 2025, doi: 10.1016/j.ijhydene.2025.151480.

[18] R. E. Rosli *et al.*, «A review of high-temperature proton exchange membrane fuel cell (HT-PEMFC) system», *International Journal of Hydrogen Energy*, vol. 42, fasc. 14, pp. 9293–9314, apr. 2017, doi: 10.1016/j.ijhydene.2016.06.211.

[19] M. M. Tellez-Cruz, J. Escorihuela, O. Solorza-Feria, e V. Compañ, «Proton Exchange Membrane Fuel Cells (PEMFCs): Advances and Challenges», *Polymers*, vol. 13, fasc. 18, p. 3064, set. 2021, doi: 10.3390/polym13183064.

[20] H. Zhang e P. K. Shen, «Recent Development of Polymer Electrolyte Membranes for Fuel Cells», *Chem. Rev.*, vol. 112, fasc. 5, pp. 2780–2832, mag. 2012, doi: 10.1021/cr200035s.

[21] O. N. Primachenko, E. A. Marinenko, A. S. Odinokov, S. V. Kononova, Y. V. Kulvelis, e V. T. Lebedev, «State of the art and prospects in the development of proton-conducting perfluorinated membranes with short side chains: A review», *Polymers for Advanced Techs*, vol. 32, fasc. 4, pp. 1386–1408, apr. 2021, doi: 10.1002/pat.5191.

[22] M. Hasan, «On characterizing mechanical degradation of polymer electrolyte fuel cell membranes using numerical simulations», University of Delaware, Ph.D. Thesis Dissertation, Elsevier LTD, ISSN: 0142-1123, 2021

[23] M. Mariani, A. Basso Peressut, S. Latorrata, R. Balzarotti, M. Sansotera, e G. Dotelli, «The Role of Fluorinated Polymers in the Water Management of Proton Exchange Membrane Fuel Cells: A Review», *Energies*, vol. 14, fasc. 24, p. 8387, dic. 2021, doi: 10.3390/en14248387.

[24] W. Zhang, S. Zhao, R. Wang, A. Zhang, Y. Huang, e H. Tang, «Proton-conductive channels engineering of perfluorosulfonic acid membrane via in situ acid–base pair of metal organic framework for fuel cells», *Adv Compos Hybrid Mater*, vol. 6, fasc. 2, p. 60, apr. 2023, doi: 10.1007/s42114-023-00637-0.

[25] A. Kusoglu e A. Z. Weber, «New Insights into Perfluorinated Sulfonic-Acid Ionomers», *Chem. Rev.*, vol. 117, fasc. 3, pp. 987–1104, feb. 2017, doi: 10.1021/acs.chemrev.6b00159.

[26] S. Singha e T. Jana, «Proton-Conducting Channels in Polybenzimidazole Nanocomposites», Journal of the Indian Institute of Science, vol. 96, fasc. 4, pp. 351-364, dec. 2016.

[27] X. Sun, S. Simonsen, T. Norby, e A. Chatzitakis, «Composite Membranes for High Temperature PEM Fuel Cells and Electrolysers: A Critical Review», *Membranes*, vol. 9, fasc. 7, p. 83, lug. 2019, doi: 10.3390/membranes9070083.

[28] M. Klingele, M. Breitwieser, R. Zengerle, e S. Thiele, «Direct deposition of proton exchange membranes enabling high performance hydrogen fuel cells», *J. Mater. Chem. A*, vol. 3, fasc. 21, pp. 11239–11245, 2015, doi: 10.1039/C5TA01341K.

[29] R. Borup *et al.*, «Scientific Aspects of Polymer Electrolyte Fuel Cell Durability and Degradation», *Chem. Rev.*, vol. 107, fasc. 10, pp. 3904–3951, ott. 2007, doi: 10.1021/cr050182l.

[30] H. Tang, X. Wang, M. Pan, e F. Wang, «Fabrication and characterization of improved PFSA/ePTFE composite polymer electrolyte membranes», *Journal of Membrane Science*, vol. 306, fasc. 1–2, pp. 298–306, dic. 2007, doi: 10.1016/j.memsci.2007.09.008.

[31] Y. Prykhodko, K. Fatyeyeva, L. Hespel, e S. Marais, «Progress in hybrid composite Nafion®-based membranes for proton exchange fuel cell application», *Chemical Engineering Journal*, vol. 409, p. 127329, apr. 2021, doi: 10.1016/j.cej.2020.127329.

[32] L.-Y. Zhu, Y.-C. Li, J. Liu, J. He, L.-Y. Wang, e J.-D. Lei, «Recent developments in high-performance Nafion membranes for hydrogen fuel cells applications», *Petroleum Science*, vol. 19, fasc. 3, pp. 1371–1381, giu. 2022, doi: 10.1016/j.petsci.2021.11.004.

[33] A. M. Arnold, J. Su, e E. M. Sabolsky, «Influence of environmental conditions and voltage application on the electromechanical performance of Nafion-Pt IPMC actuators», *Smart Mater. Struct.*, vol. 31, fasc. 11, p. 115031, nov. 2022, doi: 10.1088/1361-665X/ac986f.

[34] A. Sharma, L. Đelević, e K. Herkendell, «Next-Generation Proton-Exchange Membranes in Microbial Fuel Cells: Overcoming Nafion's Limitations», *Energy Tech*, vol. 12, fasc. 6, p. 2301346, giu. 2024, doi: 10.1002/ente.202301346.

[35] M. Di Virgilio, A. Basso Peressut, V. Arosio, A. Arrigoni, S. Latorrata, e G. Dotelli, «Functional and Environmental Performances of Novel Electrolytic Membranes for PEM Fuel Cells: A Lab-Scale Case Study», *Clean Technol.*, vol. 5, fasc. 1, pp. 74–93, gen. 2023, doi: 10.3390/cleantechnol5010005.

[36] A. Kelarakis, «Nafion in Biomedicine and Healthcare», *Polymers*, vol. 17, fasc. 15, p. 2054, lug. 2025, doi: 10.3390/polym17152054.

[37] D. Dias, J. Bons, A. Kumar, M. Kabir, e H. Liang, «Forever Chemicals, Per-and Polyfluoroalkyl Substances (PFAS), in Lubrication», *Lubricants*, vol. 12, fasc. 4, p. 114, mar. 2024, doi: 10.3390/lubricants12040114.

[38] K. A. Mauritz e R. B. Moore, «State of Understanding of Nafion», *Chem. Rev.*, vol. 104, fasc. 10, pp. 4535–4586, ott. 2004, doi: 10.1021/cr0207123.

[39] A. Dias, «JRC Science for Policy Report».

[40] S. Chakraborty *et al.*, «A Review on the Numerical Studies on the Performance of Proton Exchange Membrane Fuel Cell (PEMFC) Flow Channel Designs for Automotive Applications», *Energies*, vol. 15, fasc. 24, p. 9520, dic. 2022, doi: 10.3390/en15249520.

[41] J. Li, M. Pan, e H. Tang, «Understanding short-side-chain perfluorinated sulfonic acid and its application for high temperature polymer electrolyte membrane fuel cells», *RSC Adv.*, vol. 4, fasc. 8, pp. 3944–3965, 2014, doi: 10.1039/C3RA43735C.

[42] A. C. Fernandes e E. A. Ticianelli, «A performance and degradation study of Nafion 212 membrane for proton exchange membrane fuel cells», *Journal of Power Sources*, vol. 193, fasc. 2, pp. 547–554, set. 2009, doi: 10.1016/j.jpowsour.2009.04.038.

[43] H. Tang, S. Peikang, S. P. Jiang, F. Wang, e M. Pan, «A degradation study of Nafion proton exchange membrane of PEM fuel cells», *Journal of Power Sources*, vol. 170, fasc. 1, pp. 85–92, giu. 2007, doi: 10.1016/j.jpowsour.2007.03.061.

[44] T. H. Yu, Y. Sha, W.-G. Liu, B. V. Merinov, P. Shirvanian, e W. A. Goddard, «Mechanism for Degradation of Nafion in PEM Fuel Cells from Quantum Mechanics Calculations», *J. Am. Chem. Soc.*, vol. 133, fasc. 49, pp. 19857–19863, dic. 2011, doi: 10.1021/ja2074642.

[45] A. Zucconi, J. Hack, R. Stocker, T. A. M. Suter, A. J. E. Rettie, e D. J. L. Brett, «Challenges and opportunities for characterisation of high-temperature polymer electrolyte membrane fuel cells: a review», *J. Mater. Chem. A*, vol. 12, fasc. 14, pp. 8014–8064, 2024, doi: 10.1039/D3TA06895A.

[46] R. C. McDonald, C. K. Mittelsteadt, e E. L. Thompson, «Effects of Deep Temperature Cycling on Nafion® 112 Membranes and Membrane Electrode Assemblies», *Fuel Cells*, vol. 4, fasc. 3, pp. 208–213, ago. 2004, doi: 10.1002/fuce.200400015.

[47] C. Chen e T. F. Fuller, «The effect of humidity on the degradation of Nafion® membrane», *Polymer Degradation and Stability*, vol. 94, fasc. 9, pp. 1436–1447, set. 2009, doi: 10.1016/j.polymdegradstab.2009.05.016.

[48] R. K. Ahluwalia e X. Wang, «Effect of CO and CO2 impurities on performance of direct hydrogen polymer-electrolyte fuel cells», *Journal of Power Sources*, vol. 180, fasc. 1, pp. 122–131, mag. 2008, doi: 10.1016/j.jpowsour.2008.01.087.

[49] M. Mukaddam, E. Litwiller, e I. Pinnau, «Gas Sorption, Diffusion, and Permeation in Nafion», *Macromolecules*, vol. 49, fasc. 1, pp. 280–286, gen. 2016, doi: 10.1021/acs.macromol.5b02578.

[50] J. Peron *et al.*, «Properties of Nafion® NR-211 membranes for PEMFCs», *Journal of Membrane Science*, vol. 356, fasc. 1–2, pp. 44–51, lug. 2010, doi: 10.1016/j.memsci.2010.03.025.

[51] A. Bosnjakovic e S. Schlick, «Nafion Perfluorinated Membranes Treated in Fenton Media: Radical Species Detected by ESR Spectroscopy», *J. Phys. Chem. B*, vol. 108, fasc. 14, pp. 4332–4337, apr. 2004, doi: 10.1021/jp037519c.

[52] T. Sugawara, N. Kawashima, e T. N. Murakami, «Kinetic study of Nafion degradation by Fenton reaction», *Journal of Power Sources*, vol. 196, fasc. 5, pp. 2615–2620, mar. 2011, doi: 10.1016/j.jpowsour.2010.10.043.

[53] D. C. Lee, H. N. Yang, S. H. Park, e W. J. Kim, «Nafion/graphene oxide composite membranes for low humidifying polymer electrolyte membrane fuel cell», *Journal of Membrane Science*, vol. 452, pp. 20–28, feb. 2014, doi: 10.1016/j.memsci.2013.10.018.

[54] A. K. Sahu, K. Ketpang, S. Shanmugam, O. Kwon, S. Lee, e H. Kim, «Sulfonated Graphene–Nafion Composite Membranes for Polymer Electrolyte Fuel Cells Operating under Reduced Relative Humidity», *J. Phys. Chem. C*, vol. 120, fasc. 29, pp. 15855–15866, lug. 2016, doi: 10.1021/acs.jpcc.5b11674.

[55] Z. Jie, T. Haolin, e P. Mu, «Fabrication and characterization of self-assembled Nafion–SiO2–ePTFE composite membrane of PEM fuel cell», *Journal of Membrane Science*, vol. 312, fasc. 1–2, pp. 41–47, apr. 2008, doi: 10.1016/j.memsci.2007.12.025.

[56] Z. Wang *et al.*, «Synthesis of Nafion/CeO2 hybrid for chemically durable proton exchange membrane of fuel cell», *Journal of Membrane Science*, vol. 421–422, pp. 201–210, dic. 2012, doi: 10.1016/j.memsci.2012.07.014.

[57] M. P. Rodgers, Z. Shi, e S. Holdcroft, «Transport properties of composite membranes containing silicon dioxide and Nafion®», *Journal of Membrane Science*, vol. 325, fasc. 1, pp. 346–356, nov. 2008, doi: 10.1016/j.memsci.2008.07.045.

[58] C. Yang, «A comparison of physical properties and fuel cell performance of Nafion and zirconium phosphate/Nafion composite membranes», *Journal of Membrane Science*, vol. 237, fasc. 1–2, pp. 145–161, lug. 2004, doi: 10.1016/j.memsci.2004.03.009.

[59] S.-J. Shin, A. I. Balabanovich, H. Kim, J. Jeong, J. Song, e H.-T. Kim, «Deterioration of Nafion 115 membrane in direct methanol fuel cells», *Journal of Power Sources*, vol. 191, fasc. 2, pp. 312–319, giu. 2009, doi: 10.1016/j.jpowsour.2009.01.101.

[60] V. D. Cong Tinh e D. Kim, «Enhancement of oxidative stability of PEM fuel cell by introduction of HO• radical scavenger in Nafion ionomer», *Journal of Membrane Science*, vol. 613, p. 118517, nov. 2020, doi: 10.1016/j.memsci.2020.118517.

[61] Q. Lin, X. Sun, X. Chen, e S. Shi, «Effect of Pretreatment on Microstructure and Mechanical Properties of Nafion™ XL Composite Membrane», *Fuel Cells*, vol. 19, fasc. 5, pp. 530–538, ott. 2019, doi: 10.1002/fuce.201900064.

[62] S. Shi *et al.*, «Temperature-dependent fatigue crack growth mechanisms of fuel cell membranes», *International Journal of Fatigue*, vol. 154, p. 106554, gen. 2022, doi: 10.1016/j.ijfatigue.2021.106554.

[63] H. Tang, X. Wang, M. Pan, e F. Wang, «Fabrication and characterization of improved PFSA/ePTFE composite polymer electrolyte membranes», *Journal of Membrane Science*, vol. 306, fasc. 1–2, pp. 298–306, dic. 2007, doi: 10.1016/j.memsci.2007.09.008.

[64] A. Veziroglu e R. Macario, «Fuel cell vehicles: State of the art with economic and environmental concerns», *International Journal of Hydrogen Energy*, vol. 36, fasc. 1, pp. 25–43, gen. 2011, doi: 10.1016/j.ijhydene.2010.08.145.

[65] N. Esmaeili, E. MacA. Gray, e C. J. Webb, «Non-Fluorinated Polymer Composite Proton Exchange Membranes for Fuel Cell Applications – A Review», *ChemPhysChem*, vol. 20, fasc. 16, pp. 2016–2053, ago. 2019, doi: 10.1002/cphc.201900191.

[66] V. Mehta e J. S. Cooper, «Review and analysis of PEM fuel cell design and manufacturing».

[67] S. Mo *et al.*, «Recent Advances on PEM Fuel Cells: From Key Materials to Membrane Electrode Assembly», *Electrochem. Energy Rev.*, vol. 6, fasc. 1, p. 28, dic. 2023, doi: 10.1007/s41918-023-00190-w.

[68] D. Cha, W. Yang, e Y. Kim, «Performance improvement of self-humidifying PEM fuel cells using water injection at various start-up conditions», *Energy*, vol. 183, pp. 514–524, set. 2019, doi: 10.1016/j.energy.2019.06.154.

[69] S. R. Narayanan, T. I. Valdez, e S. Firdosy, «Analysis of the Performance of Nafion-Based Hydrogen–Oxygen Fuel Cells», *J. Electrochem. Soc.*, vol. 156, fasc. 1, p. B152, 2009, doi: 10.1149/1.3008015.

[70] X. Zhang, D. Yang, M. Luo, e Z. Dong, «Load profile based empirical model for the lifetime prediction of an automotive PEM fuel cell», *International Journal of Hydrogen Energy*, vol. 42, fasc. 16, pp. 11868–11878, apr. 2017, doi: 10.1016/j.ijhydene.2017.02.146.

[71] M. Gandiglio, A. Lanzini, M. Santarelli, e P. Leone, «Design and optimization of a proton exchange membrane fuel cell CHP system for residential use», *Energy and Buildings*, vol. 69, pp. 381–393, feb. 2014, doi: 10.1016/j.enbuild.2013.11.022.

[72] J. Wang, H. Wang, e Y. Fan, «Techno-Economic Challenges of Fuel Cell Commercialization», *Engineering*, vol. 4, fasc. 3, pp. 352–360, giu. 2018, doi: 10.1016/j.eng.2018.05.007.

[73] T. Wilberforce *et al.*, «Effect of humidification of reactive gases on the performance of a proton exchange membrane fuel cell», *Science of The Total Environment*, vol. 688, pp. 1016–1035, ott. 2019, doi: 10.1016/j.scitotenv.2019.06.397.

[74] H. Li *et al.*, «A review of water flooding issues in the proton exchange membrane fuel cell», *Journal of Power Sources*, vol. 178, fasc. 1, pp. 103–117, mar. 2008, doi: 10.1016/j.jpowsour.2007.12.068.

[75] L. Xing, S. Du, R. Chen, M. Mamlouk, e K. Scott, «Anode partial flooding modelling of proton exchange membrane fuel cells: Model development and validation», *Energy*, vol. 96, pp. 80–95, feb. 2016, doi: 10.1016/j.energy.2015.12.048.

[76] L. Dubau *et al.*, «A review of PEM fuel cell durability: materials degradation, local heterogeneities of aging and possible mitigation strategies», *WIREs Energy & Environment*, vol. 3, fasc. 6, pp. 540–560, nov. 2014, doi: 10.1002/wene.113.

[77] S. Cui, G. Zhu, L. He, X. Wang, e X. Zhang, «Analysis of the fire hazard and leakage explosion simulation of hydrogen fuel cell vehicles», *Thermal Science and Engineering Progress*, vol. 41, p. 101754, giu. 2023, doi: 10.1016/j.tsep.2023.101754.

[78] C. Sonne *et al.*, «EU need to protect its environment from toxic per- and polyfluoroalkyl substances», *Science of The Total Environment*, vol. 876, p. 162770, giu. 2023, doi: 10.1016/j.scitotenv.2023.162770.

[79] R. C. Buck, S. H. Korzeniowski, E. Laganis, e F. Adamsky, «Identification and classification of commercially relevant per- and poly-fluoroalkyl substances (PFAS)», *Integrated Environmental Assessment and Management*, vol. 17, fasc. 5, pp. 1045–1055, mag. 2021, doi: 10.1002/ieam.4450.

[80] I. T. Cousins *et al.*, «The concept of essential use for determining when uses of PFASs can be phased out», *Environ. Sci.: Processes Impacts*, vol. 21, fasc. 11, pp. 1803–1815, 2019, doi: 10.1039/C9EM00163H.

[81] F. Borchert, R. Figuière, I. T. Cousins, C. Rudén, e M. Ågerstrand, «Identifying non-essential uses to phase out substances of very high concern under REACH», *Front. Toxicol.*, vol. 6, p. 1488336, nov. 2024, doi: 10.3389/ftox.2024.1488336.

[82] Hydrogen Europe, "Hydrogen Europe Position Paper on PFAS - The importance of fluoropolymers across the hydrogen value chain, and impacts of the proposed PFAS restriction for the hydrogen sector", Brussels, 2023.

[83] Fuel Cells and Hydrogen Joint Undertaking, "A Sustainable Pathway for the European Energy Transition", 2019, doi:10.2843/249013.

[84] Environmental Protection Agency, 40 CFR Part 705, "Perfluoroalkyl and Polyfluoroalkyl Substances (PFAS) Data Reporting and Recordkeeping Under the Toxic Substances Control Act (TSCA); Change to Submission Period", U.S. Federal Register, vol. 90(91), 2025.

[85] Y. Duan, C. Ru, Y. Pang, J. Li, B. Liu, e C. Zhao, «Crosslinked PAEK-based nanofiber reinforced Nafion membrane with ion-paired interfaces towards high-concentration DMFC», *Journal of Membrane Science*, vol. 655, p. 120589, ago. 2022, doi: 10.1016/j.memsci.2022.120589.

[86] R.S. Raja Rafidah, W. Rashmi, M. Khalid, W.Y. Wong and J. Priyanka, «Recent Progress in the Development of Aromatic Polymer-Based Proton Exchange Membranes for Fuel Cell Applications», *Polymers*, vol. 12(5), 1061, 2020, doi: 10.3390/polym12051061.

[87] C. Spreafico e N. Thonemann, «Prospective life cycle assessment of proton exchange membrane fuel cell. Comparing data from patents and papers», *International Journal of Hydrogen Energy*, vol. 99, pp. 45–52, gen. 2025, doi: 10.1016/j.ijhydene.2024.12.211.

[88] M. Salimi, E. Degoli, e R. Magri, «Aqueous Nafion-Platinum Interface for Pem Fuel Cells; an Ab-Initio Perspective», 2025, *SSRN*. doi: 10.2139/ssrn.5112963.

[89] M. Yusro e V. Hacker, «Insight into aligned nanofibers improving fuel cell performances: strategies, rationalities, and opportunities», *Mater. Adv.*, vol. 5, fasc. 12, pp. 4974–4995, 2024, doi: 10.1039/D4MA00120F.

[90] M. M. Gomaa, I. Requena-Leal, M. R. M. Elsharkawy, M. A. Rodrigo, e J. Lobato, «Eco-friendly non-fluorinated membranes for renewable energy storage», *International Journal of Hydrogen Energy*, vol. 90, pp. 328–341, nov. 2024, doi: 10.1016/j.ijhydene.2024.09.431.

[91] S. Jacobs *et al.*, «Assessment of Fluoropolymer Production and Use With Analysis of Alternative Replacement Materials», SRNL--STI-2023-00587, 2370520, gen. 2024. doi: 10.2172/2370520.

[92] Z. G. Abdi, J. Chen, T. Chiu, H. Yang, e H. Yu, «Synthesis of ionic polybenzimidazoles with broad ion exchange capacity range for anion exchange membrane fuel cell application», *Journal of Polymer Science*, vol. 59, fasc. 18, pp. 2069–2081, set. 2021, doi: 10.1002/pol.20210409.

[93] S. Li, S. Zhang, e Q. Shen, «Effect of Flow Field with Baffles on Performance of High Temperature Proton Exchange Membrane Fuel Cells», *JMSE*, vol. 13, fasc. 3, p. 456, feb. 2025, doi: 10.3390/jmse13030456.

[94] A. Mekkad e V. M. Janardhanan, «Performance evaluation of high temperature polymer electrolyte membrane fuel cells: an experimental investigation», *J Appl Electrochem*, vol. 55, fasc. 4, pp. 931–941, apr. 2025, doi: 10.1007/s10800-024-02226-5.

[95] D. Konovalov, I. Tolstorebrov, Y. Iwamoto, e J. J. Lamb, «Hydrogen and Japan's Energy Transition: A Blueprint for Carbon Neutrality», *Hydrogen*, vol. 6, fasc. 3, p. 61, ago. 2025, doi: 10.3390/hydrogen6030061.

[96] A. Unnikrishnan, N. Rajalakshmi, e V. M. Janardhanan, «Mechanistic modeling of electrochemical charge transfer in HT-PEM fuel cells», *Electrochimica Acta*, vol. 261, pp. 436–444, gen. 2018, doi: 10.1016/j.electacta.2017.12.150.

[97] T. J. Schmidt e J. Baurmeister, «Properties of high-temperature PEFC Celtec®-P 1000 MEAs in start/stop operation mode», *Journal of Power Sources*, vol. 176, fasc. 2, pp. 428–434, feb. 2008, doi: 10.1016/j.jpowsour.2007.08.055.

[98] Y. Chen, D. Aili, W. Zhang, K. Azizi, L. N. Cleemann, e Q. Li, «Reinforced Polybenzimidazole Membranes by Crosslinked Fiber Mats for High Temperature Polymer Electrolyte Membrane Fuel Cells», *Electrochimica Acta*, vol. 529, p. 146260, lug. 2025, doi: 10.1016/j.electacta.2025.146260.

[99] Y. Wang *et al.*, «Anchoring Highly Sulfonated Hyperbranched PBI onto oPBI: Fast Proton Conduction with Low Leaching», *ACS Appl. Energy Mater.*, vol. 5, fasc. 9, pp. 10802–10814, set. 2022, doi: 10.1021/acsaem.2c01491.

[100] S. Rigal, A. Jaafar, C. Turpin, T. Hordé, J.-B. Jollys, e P. Kreczanik, «An Air Over-Stoichiometry Dependent Voltage Model for HT-PEMFC MEAs», *Energies*, vol. 17, fasc. 12, p. 3002, giu. 2024, doi: 10.3390/en17123002.

[101] K. Fishel, G. Qian, e B. C. Benicewicz, «PBI Membranes Via the PPA Process», in *High Temperature Polymer Electrolyte Membrane Fuel Cells*, Q. Li, D. Aili, H. A. Hjuler, e J. O. Jensen, A c. di, Cham: Springer International Publishing, 2016, pp. 217–238. doi: 10.1007/978-3-319-17082-4_10.

[102] X. Liu, M. Cheng, Y. Zhao, e Y. Qiu, «Theoretical Studies on the Chemical Degradation and Proton Dissociation Property of PBI used in High-Temperature Polymer Electrolyte Membrane Fuel Cells», *J. Phys. Chem. B*, vol. 128, fasc. 25, pp. 6167–6177, giu. 2024, doi: 10.1021/acs.jpcb.4c00882.

[103] N. Seselj *et al.*, «Performance degradation and mitigation of high temperature polybenzimidazole-based polymer electrolyte membrane fuel cells», *Chem. Soc. Rev.*, vol. 52, fasc. 12, pp. 4046–4070, 2023, doi: 10.1039/D3CS00072A.

[104] T. Guo *et al.*, «High PA retention proton exchange membranes based on polybenzimidazole/SiO2 composites for high-temperature fuel cells», *Journal of Membrane Science*, vol. 735, p. 124545, nov. 2025, doi: 10.1016/j.memsci.2025.124545.

[105] Y. Devrim e G. N. Bulanık Durmuş, «Composite membrane by incorporating sulfonated graphene oxide in polybenzimidazole for high temperature proton exchange membrane fuel cells», *International Journal of Hydrogen Energy*, vol. 47, fasc. 14, pp. 9004–9017, feb. 2022, doi: 10.1016/j.ijhydene.2021.12.257.

[106] A. Javed, P. Palafox Gonzalez, e V. Thangadurai, «A Critical Review of Electrolytes for Advanced Low- and High-Temperature Polymer Electrolyte Membrane Fuel Cells», *ACS Appl. Mater. Interfaces*, vol. 15, fasc. 25, pp. 29674–29699, giu. 2023, doi: 10.1021/acsami.3c02635.

[107] L. A. Briceno-Mena, C. G. Arges, e J. A. Romagnoli, «Machine learning-based surrogate models and transfer learning for derivative free optimization of HT-PEM fuel cells», *Computers & Chemical Engineering*, vol. 171, p. 108159, mar. 2023, doi: 10.1016/j.compchemeng.2023.108159.

[108] N. Seselj, S. M. Alfaro, E. Bompolaki, L. N. Cleemann, T. Torres, e K. Azizi, «Catalyst Development for High-Temperature Polymer Electrolyte Membrane Fuel Cell (HT-PEMFC) Applications», *Advanced Materials*, vol. 35, fasc. 40, p. 2302207, ott. 2023, doi: 10.1002/adma.202302207.

[109] S. Celik, B. Timurkutluk, U. Aydin, e M. Yagiz, «Development of titanium bipolar plates fabricated by additive manufacturing for PEM fuel cells in electric vehicles», *International Journal of Hydrogen Energy*, vol. 47, fasc. 89, pp. 37956–37966, nov. 2022, doi: 10.1016/j.ijhydene.2022.08.282.

[110] J. Peng, X. Fu, J. Luo, Y. Liu, L. Wang, e X. Peng, «Constructing novel cross-linked polybenzimidazole network for high-performance high-temperature proton exchange membrane», *Journal of Membrane Science*, vol. 643, p. 120037, mar. 2022, doi: 10.1016/j.memsci.2021.120037.

[111] L. Zhang *et al.*, «Double cross-linked 3D layered PBI proton exchange membranes for stable fuel cell performance above 200 °C», *Nat Commun*, vol. 15, fasc. 1, p. 3409, apr. 2024, doi: 10.1038/s41467-024-47627-4.

[112] C.-Y. Lee, F.-B. Weng, C.-Y. Yang, C.-W. Chiu, e S.-M. Nawale, «Real-Time Monitoring of HT-PEMFC», *Membranes*, vol. 12, fasc. 1, p. 94, gen. 2022, doi: 10.3390/membranes12010094.

[113] E. O. Eren, N. Özkan, e Y. Devrim, «Preparation of polybenzimidazole/ZIF-8 and polybenzimidazole/UiO-66 composite membranes with enhanced proton conductivity», *International Journal of Hydrogen Energy*, vol. 47, fasc. 45, pp. 19690–19701, mag. 2022, doi: 10.1016/j.ijhydene.2021.11.045.

[114] Y. Zhang *et al.*, «Inorganic Lewis Base-Modified Polybenzimidazole for High-Temperature Proton-Exchange Membrane Fuel Cell Applications», *ACS Appl. Energy Mater.*, vol. 7, fasc. 12, pp. 5275–5284, giu. 2024, doi: 10.1021/acsaem.4c00891.

[115] Y. N. Yusoff e N. Shaari, «An overview on the development of NANOFIBER-BASED as polymer electrolyte membrane and electrocatalyst in fuel cell application», *Int J Energy Res*, vol. 45, fasc. 13, pp. 18441–18472, ott. 2021, doi: 10.1002/er.7020.

[116] T. Xu, D. Wu, e L. Wu, «Poly(2,6-dimethyl-1,4-phenylene oxide) (PPO)—A versatile starting polymer for proton conductive membranes (PCMs)», *Progress in Polymer Science*, vol. 33, fasc. 9, pp. 894–915, set. 2008, doi: 10.1016/j.progpolymsci.2008.07.002.

[117] H. Yang e A. S. Hay, «Synthesis and characterization of poly(2,6-diarylphenylene oxide)s», *J. Polym. Sci. A Polym. Chem.*, vol. 31, fasc. 5, pp. 1261–1273, apr. 1993, doi: 10.1002/pola.1993.080310522.

[118] F. E. Karasz, W. J. MacKnight, e J. Stoelting, «Dielectric Properties of Poly(2, 6-Dimethyl Phenylene Oxide)», *Journal of Applied Physics*, vol. 41, fasc. 11, pp. 4357–4360, ott. 1970, doi: 10.1063/1.1658467.

[119] H. Hwang, S. Hsu, C. Wang, "Synthesis and Physical Properties of Low-Molecular-Weight Redistributed Poly(2,6-dimethyl-1,4-phenylene oxide) for Epoxy Resin", Journal of Applied Polymer Science, vol. 110, pp. 1880-1890, 2008. https://doi.org/10.1002/app.28770

[120] B. Nagendra *et al.*, «Two Nanoporous Crystalline Forms of Poly(2,6-dimethyl-1,4-phenylene)oxide and Related Co-Crystalline Forms», *Macromolecules*, vol. 52, fasc. 24, pp. 9646–9656, dic. 2019, doi: 10.1021/acs.macromol.9b01911.

[121] O. Tarallo, "Clathrates", *Encyclopedia of Polymer Science and Technology*, Wiley, 2013.

[122] C. Daniel, S. Longo, G. Fasano, J. G. Vitillo, e G. Guerra, «Nanoporous Crystalline Phases of Poly(2,6-Dimethyl-1,4-phenylene)oxide», *Chem. Mater.*, vol. 23, fasc. 13, pp. 3195–3200, lug. 2011, doi: 10.1021/cm200546r.

[123] B. Nagendra, M. Golla, C. Daniel, P. Rizzo, e G. Guerra, «Melting of nanoporous-crystalline and co-crystalline solution cast films of poly(2,6-dimethyl-1,4-phenylene) oxide», *Polymer*, vol. 228, p. 123935, lug. 2021, doi: 10.1016/j.polymer.2021.123935.

[124] I. Petreanu, D. Ebrasu, C. Sisu, e M. Varlam, «Thermal analysis of sulfonated polymers tested as polymer electrolyte membrane for PEM fuel cells», *J Therm Anal Calorim*, vol. 110, fasc. 1, pp. 335–339, ott. 2012, doi: 10.1007/s10973-012-2442-z.

[125] B. Nagendra *et al.*, «Poly(phenylene oxide) Films with Hydrophilic Sulfonated Amorphous Phase and Physically Cross-Linking Hydrophobic Crystalline Phase», *ACS Appl. Polym. Mater.*, vol. 5, fasc. 5, pp. 3489–3498, mag. 2023, doi: 10.1021/acsapm.3c00152.

[126] Y. S. Bhole, P. B. Karadkar, e U. K. Kharul, «Nitration and amination of polyphenylene oxide: Synthesis, gas sorption and permeation analysis», *European Polymer Journal*, vol. 43, fasc. 4, pp. 1450–1459, apr. 2007, doi: 10.1016/j.eurpolymj.2007.01.017.

[127] M. Serin, D. Sakar, H. Cankurtaran, O. Cankurtaran, and F. Karaman, «Doping effect on electrical properties of poly(2,6-dimethyl- 1,4-phenylene oxide) films», Journal of Optoelectronics and Advanced Materials, vol. 7(6), pp. 3121-3125, 2005.

[128] J.-H. Kim, S. Ryu, J.-Y. Lee, e S.-H. Moon, «Preparation of high-conductivity QPPO (quaternary-aminated poly (2,6-dimethyl-1,4-phenyleneoxide)) membranes by electrical treatment», *Journal of Membrane Science*, vol. 553, pp. 82–89, mag. 2018, doi: 10.1016/j.memsci.2017.12.009.

[129] Y. Wang, T. Yang, K. Fishel, B. C. Benicewicz, e T.-S. Chung, «Polybenzimidazole», 2016.

[130] K. A. Perry, K. L. More, E. Andrew Payzant, R. A. Meisner, B. G. Sumpter, e B. C. Benicewicz, «A comparative study of phosphoric acid-doped *m* -PBI membranes», *J Polym Sci B Polym Phys*, vol. 52, fasc. 1, pp. 26–35, gen. 2014, doi: 10.1002/polb.23403.

[131] J. A. Asensio, S. Borrós, e P. Gómez-Romero, «Polymer Electrolyte Fuel Cells Based on Phosphoric Acid-Impregnated Poly(2,5-benzimidazole) Membranes», *J. Electrochem. Soc.*, vol. 151, fasc. 2, p. A304, 2004, doi: 10.1149/1.1640628.

[132] J. Thisuwan, P. Promma, e K. Sagarik, «The Grotthuss mechanism for bifunctional proton transfer in poly(benzimidazole)», *R. Soc. open sci.*, vol. 8, fasc. 12, p. 211168, dic. 2021, doi: 10.1098/rsos.211168.

[133] Q. Li, R. He, J. O. Jensen, e N. J. Bjerrum, «PBI-Based Polymer Membranes for High Temperature Fuel Cells – Preparation, Characterization and Fuel Cell Demonstration», *Fuel Cells*, vol. 4, fasc. 3, pp. 147–159, ago. 2004, doi: 10.1002/fuce.200400020.

[134] G. Gebel, «Structure of Membranes for Fuel Cells: SANS and SAXS Analyses of Sulfonated PEEK Membranes and Solutions», *Macromolecules*, vol. 46, fasc. 15, pp. 6057–6066, ago. 2013, doi: 10.1021/ma400314c.

[135] H. Nguyen *et al.*, «Hydrocarbon-based Pemion^{TM} proton exchange membrane fuel cells with state-of-the-art performance», *Sustainable Energy Fuels*, vol. 5, fasc. 14, pp. 3687–3699, 2021, doi: 10.1039/D1SE00556A.

[136] D. Aili, J. Yang, K. Jankova, D. Henkensmeier, e Q. Li, «From polybenzimidazoles to polybenzimidazoliums and polybenzimidazolides», *J. Mater. Chem. A*, vol. 8, fasc. 26, pp. 12854–12886, 2020, doi: 10.1039/D0TA01788D.

[137] R. Zeis, «Materials and characterization techniques for high-temperature polymer electrolyte membrane fuel cells», *Beilstein J. Nanotechnol.*, vol. 6, pp. 68–83, gen. 2015, doi: 10.3762/bjnano.6.8.

[138] Y. Pan, Y. Huang, B. Liao, e G. Cong, «Synthesis and characterization of aminated poly(2,6-dimethyl-1,4-phenylene oxide)», *J. Appl. Polym. Sci.*, vol. 61, fasc. 7, pp. 1111–1115, ago. 1996, doi: 10.1002/(SICI)1097-4628(19960815)61:7%3C1111::AID-APP6%3E3.0.CO;2-P.

[139] G. A. Giffin *et al.*, «Interplay between structure and properties in acid-base blend PBI-based membranes for HT-PEM fuel cells», *Journal of Membrane Science*, vol. 535, pp. 122–131, ago. 2017, doi: 10.1016/j.memsci.2017.04.019.

[140] J. Lobato, P. Cañizares, M. A. Rodrigo, e J. J. Linares, «PBI-based polymer electrolyte membranes fuel cells», *Electrochimica Acta*, vol. 52, fasc. 12, pp. 3910–3920, mar. 2007, doi: 10.1016/j.electacta.2006.11.014.

[141] K. Y. Wang, M. Weber, e T.-S. Chung, «Polybenzimidazoles (PBIs) and state-of-the-art PBI hollow fiber membranes for water, organic solvent and gas separations: a review», *J. Mater. Chem. A*, vol. 10, fasc. 16, pp. 8687–8718, 2022, doi: 10.1039/D2TA00422D.

[142] J. Lin e C. Korte, «PBI-type Polymers and Acidic Proton Conducting Ionic Liquids – Conductivity and Molecular Interactions», *Fuel Cells*, vol. 20, fasc. 4, pp. 461–468, ago. 2020, doi: 10.1002/fuce.201900201.

[143] J. Lin, S. Willbold, T. Zinkevich, S. Indris, e C. Korte, «Ionic (Proton) transport and molecular interaction of ionic Liquid–PBI blends for the use as electrolyte membranes», *Journal of Molecular Liquids*, vol. 342, p. 116964, nov. 2021, doi: 10.1016/j.molliq.2021.116964.

[144] Y. J. Chendake e U. K. Kharul, «Transport of inorganic acids through polybenzimidazole (PBI) based membranes by chemo-dialysis», *Desalination and Water Treatment*, vol. 38, fasc. 1–3, pp. 96–103, gen. 2012, doi: 10.1080/19443994.2012.664270.

[145] H. Schoeman, H. M. Krieg, A. J. Kruger, A. Chromik, K. Krajinovic, e J. Kerres, «H2SO4 stability of PBI-blend membranes for SO2 electrolysis», *International Journal of Hydrogen Energy*, vol. 37, fasc. 1, pp. 603–614, gen. 2012, doi: 10.1016/j.ijhydene.2011.09.113.

[146] J. A. Asensio, E. M. Sánchez, e P. Gómez-Romero, «Proton-conducting membranes based on benzimidazole polymers for high-temperature PEM fuel cells. A chemical quest», *Chem. Soc. Rev.*, vol. 39, fasc. 8, p. 3210, 2010, doi: 10.1039/b922650h.

[147] M. Mamlouk e K. Scott, «Phosphoric acid-doped electrodes for a PBI polymer membrane fuel cell», *Int. J. Energy Res.*, vol. 35, fasc. 6, pp. 507–519, mag. 2011, doi: 10.1002/er.1708.

[148] Q. Dai *et al.*, «High-performance PBI membranes for flow batteries: from the transport mechanism to the pilot plant», *Energy Environ. Sci.*, vol. 15, fasc. 4, pp. 1594–1600, 2022, doi: 10.1039/D2EE00267A.

[149] L. A. Murdock e B. C. Benicewicz, «Preparation of Dense Polybenzimidazole Films without Organic Solvents», *Macromolecules*, vol. 56, fasc. 7, pp. 2729–2735, apr. 2023, doi: 10.1021/acs.macromol.3c00038.

[150] Z. Liu, Y.-M. Tsou, G. Calundann, e E. De Castro, «New process for high temperature polybenzimidazole membrane production and its impact on the membrane and the membrane electrode assembly», *Journal of Power Sources*, vol. 196, fasc. 3, pp. 1055–1060, feb. 2011, doi: 10.1016/j.jpowsour.2010.08.026.

[151] J. Chen, F. Rong, e Y. Xie, «Fabrication, Microstructures and Sensor Applications of Highly Ordered Electrospun Nanofibers: A Review», *Materials*, vol. 16, fasc. 9, p. 3310, apr. 2023, doi: 10.3390/ma16093310.

[152] S. Shi *et al.*, «Recent Progress in Protective Membranes Fabricated via Electrospinning: Advanced Materials, Biomimetic Structures, and Functional Applications», *Advanced Materials*, vol. 34, fasc. 17, p. 2107938, apr. 2022, doi: 10.1002/adma.202107938.

[153] J. Wang, C. You, Y. Xu, T. Xie, e Y. Wang, «Research Advances in Electrospun Nanofiber Membranes for Non-Invasive Medical Applications», *Micromachines*, vol. 15, fasc. 10, p. 1226, set. 2024, doi: 10.3390/mi15101226.

[154] Y. Wang, W. Zhai, J. Li, H. Liu, C. Li, e J. Li, «Friction behavior of biodegradable electrospun polyester nanofibrous membranes», *Tribology International*, vol. 188, p. 108891, ott. 2023, doi: 10.1016/j.triboint.2023.108891.

[155] H. Matsumoto e A. Tanioka, «Functionality in Electrospun Nanofibrous Membranes Based on Fiber's Size, Surface Area, and Molecular Orientation», *Membranes*, vol. 1, fasc. 3, pp. 249–264, ago. 2011, doi: 10.3390/membranes1030249.

[156] S. Wu, X. Qin, e M. Li, «The structure and properties of cellulose acetate materials: A comparative study on electrospun membranes and casted films», *Journal of Industrial Textiles*, vol. 44, fasc. 1, pp. 85–98, lug. 2014, doi: 10.1177/1528083713477443.

[157] W. Hu, P. Zhang, L. Zhao, e Z. Tao, «Electrochemical performance enhancement of electrospun nanofiber cathode through impregnation method», *International Journal of Hydrogen Energy*, vol. 48, fasc. 91, pp. 35765–35770, nov. 2023, doi: 10.1016/j.ijhydene.2023.05.296.

[158] X. Liu, M. Cheng, Y. Zhao, e Y. Qiu, «Theoretical Studies on the Chemical Degradation and Proton Dissociation Property of PBI used in High-Temperature Polymer Electrolyte Membrane Fuel Cells», *J. Phys. Chem. B*, vol. 128, fasc. 25, pp. 6167–6177, giu. 2024, doi: 10.1021/acs.jpcb.4c00882.

[159] E. De Gregorio *et al.*, «Electrospun Polybenzimidazole Membranes: Fabrication and Fine-Tuning Through Physical and Statistical Approaches», *Polymers*, vol. 17, fasc. 12, p. 1594, giu. 2025, doi: 10.3390/polym17121594.

[160] A. N. Ebelegi, N. Ayawei, e D. Wankasi, «Interpretation of Adsorption Thermodynamics and Kinetics», *OJPC*, vol. 10, fasc. 03, pp. 166–182, 2020, doi: 10.4236/ojpc.2020.103010.

[161] D. Aili *et al.*, «Polybenzimidazole-Based High-Temperature Polymer Electrolyte Membrane Fuel Cells: New Insights and Recent Progress», *Electrochem. Energ. Rev.*, vol. 3, fasc. 4, pp. 793–845, dic. 2020, doi: 10.1007/s41918-020-00080-5.

[162] H. Tang *et al.*, «Fuel cells with an operational range of –20 °C to 200 °C enabled by phosphoric acid-doped intrinsically ultramicroporous membranes», *Nat Energy*, vol. 7, fasc. 2, pp. 153–162, gen. 2022, doi: 10.1038/s41560-021-00956-w.

[163] B. Wang *et al.*, «Phosphoric Acid-in-Clay Electrolyte Boosting Polybenzimidazole Membranes for High-Performance Fuel Cells», *Adv Funct Materials*, p. e18482, ott. 2025, doi: 10.1002/adfm.202518482.

[164] P. Kallem, N. Yanar, e H. Choi, «Nanofiber-Based Proton Exchange Membranes: Development of Aligned Electrospun Nanofibers for Polymer Electrolyte Fuel Cell Applications», *ACS Sustainable Chem. Eng.*, vol. 7, fasc. 2, pp. 1808–1825, gen. 2019, doi: 10.1021/acssuschemeng.8b03601.

ANNEX - A

SULFONATED POLY(2,6-DIMETHYL-1,4-PHENYLENE OXIDE) - sPPO

A.1 – FTIR/ATR Spectra

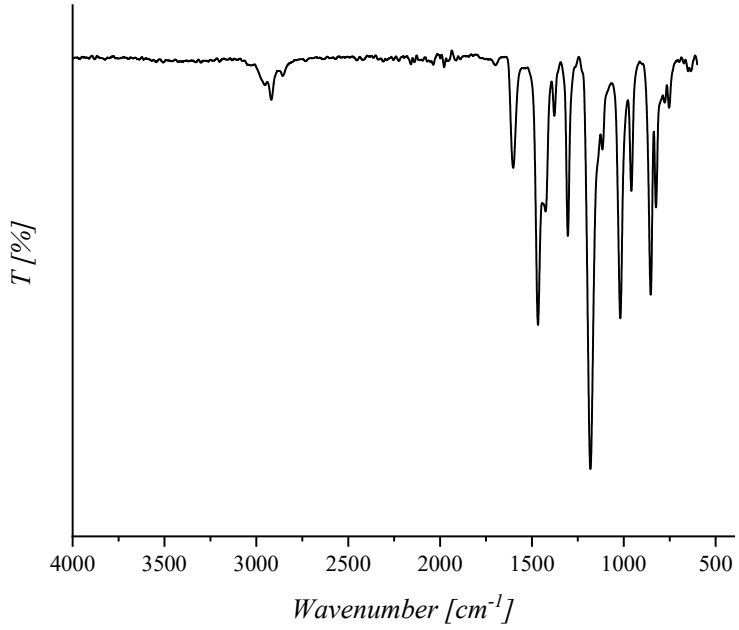

Figure A.1.1 – FTIR/ATR spectrum of the PPO neat sample recorded in transmittance in the range 4000-400 cm^{-1}.

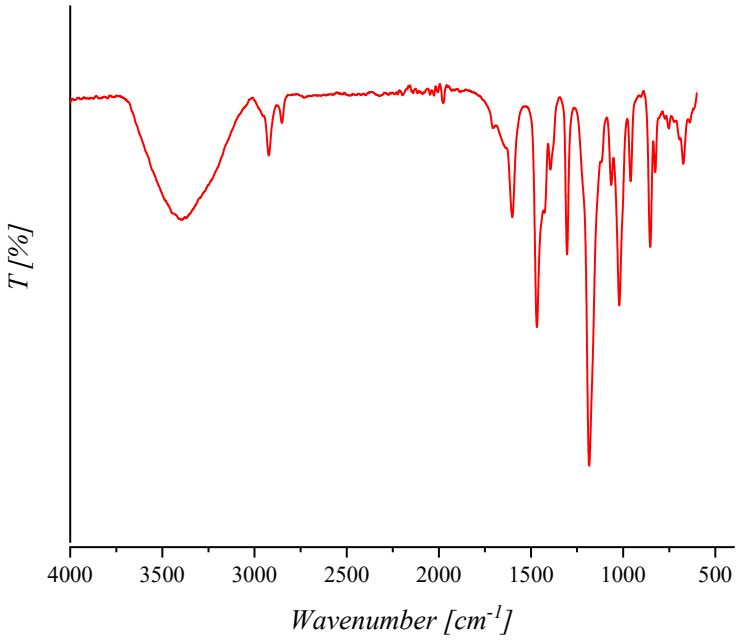

Figure A.1.2 – FTIR/ATR spectrum of the sPPO sample with a IEC ~ 1.3 meq g^{-1} recorded in transmittance in the range 4000-400 cm^{-1}.

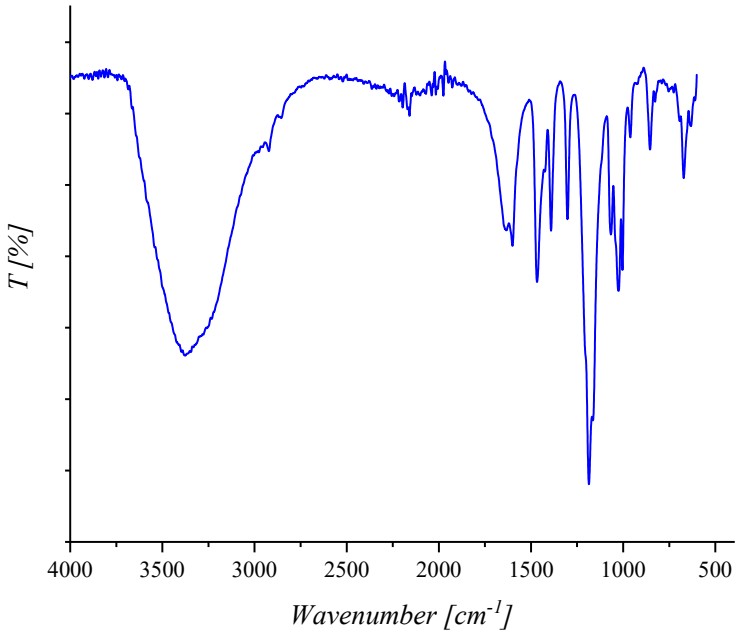

Figure A.1.3 – FTIR/ATR spectrum of the sPPO sample with a IEC ~ 2.0 meq g^{-1} recorded in transmittance in the range 4000-400 cm^{-1}.

A.2 – XRD Spectra

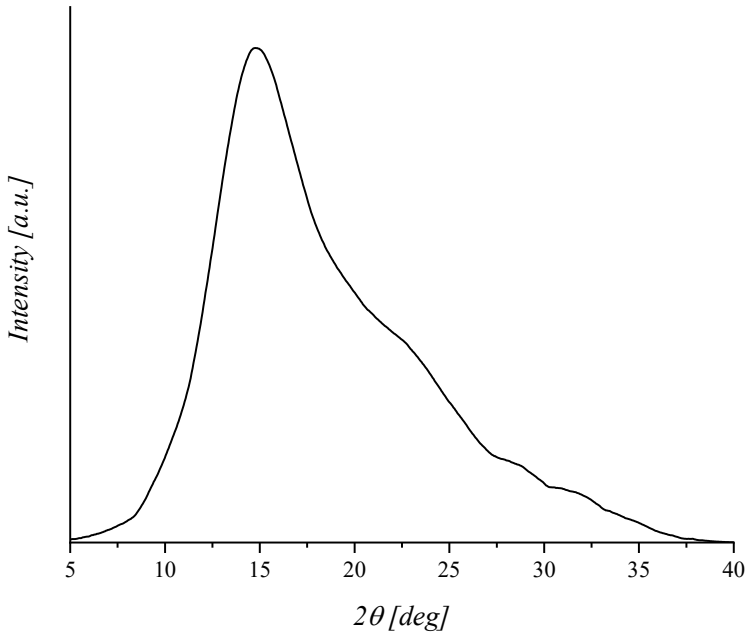

Figure A.2.1 – XRD spectrum of the PPO neat sample recorded in the range 5-40° 2θ (Bragg-Brentano, CuK_{α}).

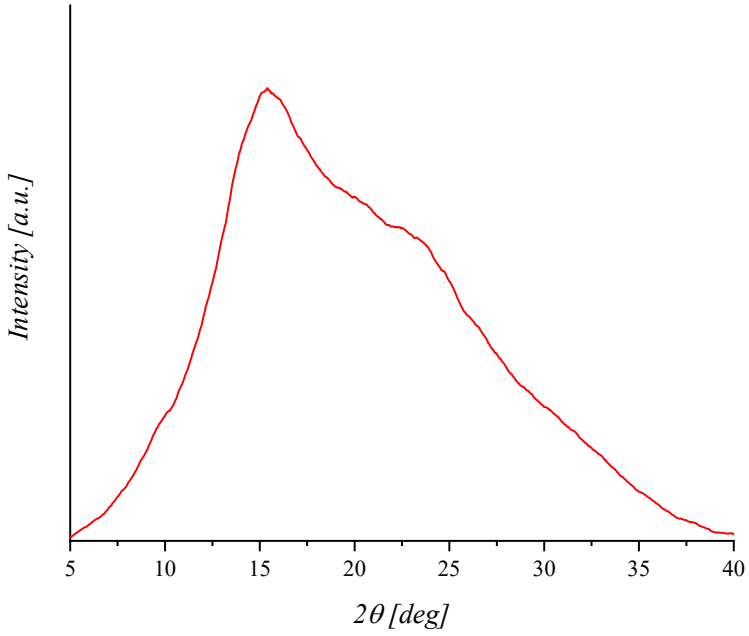

Figure A.2.2 – XRD spectrum of the sPPO sample recorded in the range 5-40° 2θ (Bragg-Brentano, CuK_{α}).

A.3 – Thermogravimetric Analysis: TGA

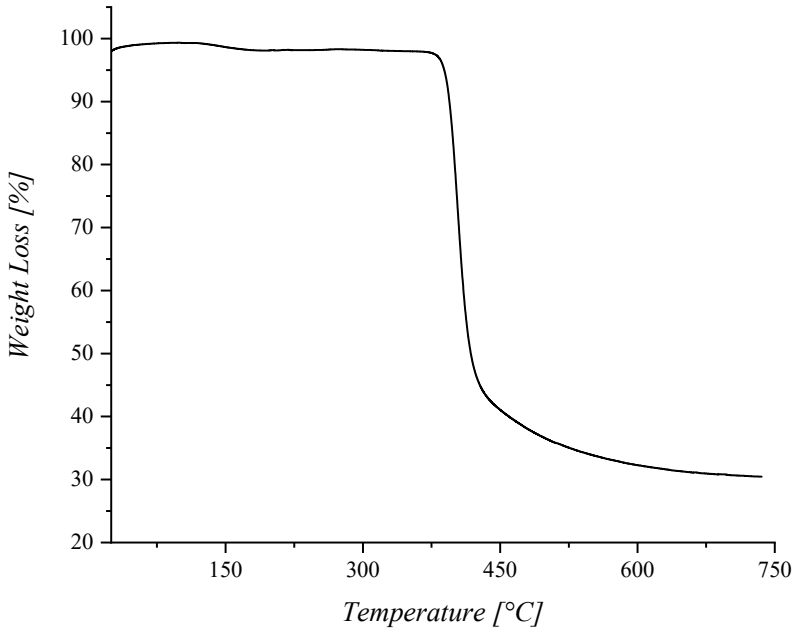

Figure A.3.1 – Thermogram of PPO neat sample showing weight loss as temperature changes. Scan rate= 10°C/min under N_2-flow from 25 to 750 °C.

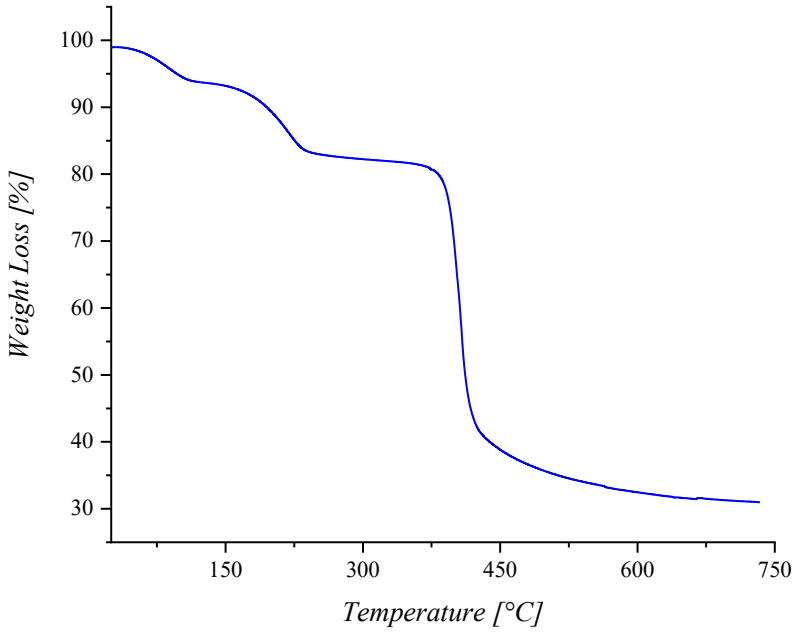

Figure A.3.2 – Thermogram of sPPO sample with a IEC ~ 2.0 meq g^{-1} showing weight loss as temperature changes. Scan rate= 10°C/min under N_2-flow from 25 to 750 °C.

A.4 – Electrochemical evaluation: LSV

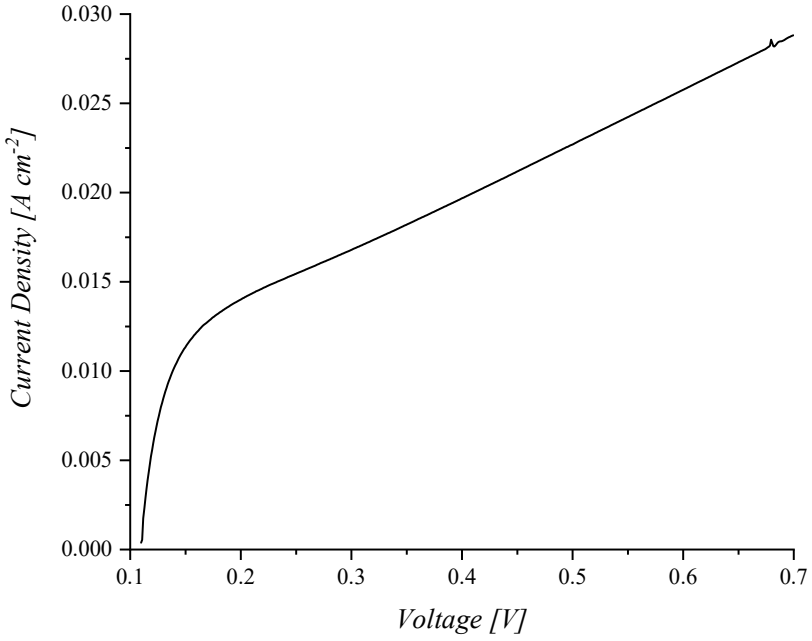

Figure A.4.1 – LSV curve of Nafion 212 sample for hydrogen crossover analysis in non-reactive gases (H_2/N_2). Scan rate= 1 mV s^{-1} from 0.1 to 0.7 V at T=80 °C e RH=90%.

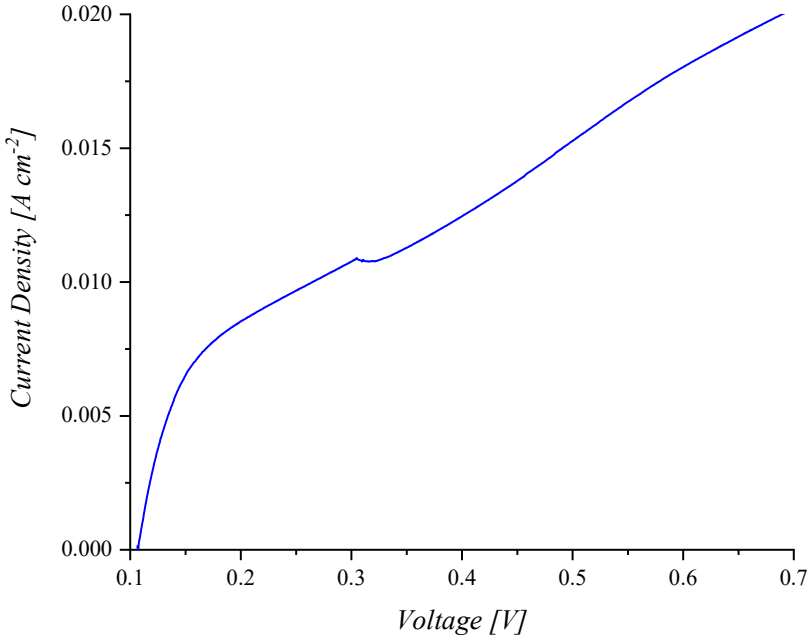

Figure A.4.2 – LSV curve of 25 µm sPPO sample with a IEC~ 0.69 meq g^{-1} for hydrogen crossover analysis in non-reactive gases (H_2/N_2). Scan rate= 1 mV s^{-1} from 0.1 to 0.7 V at T=80 °C e RH=90%.

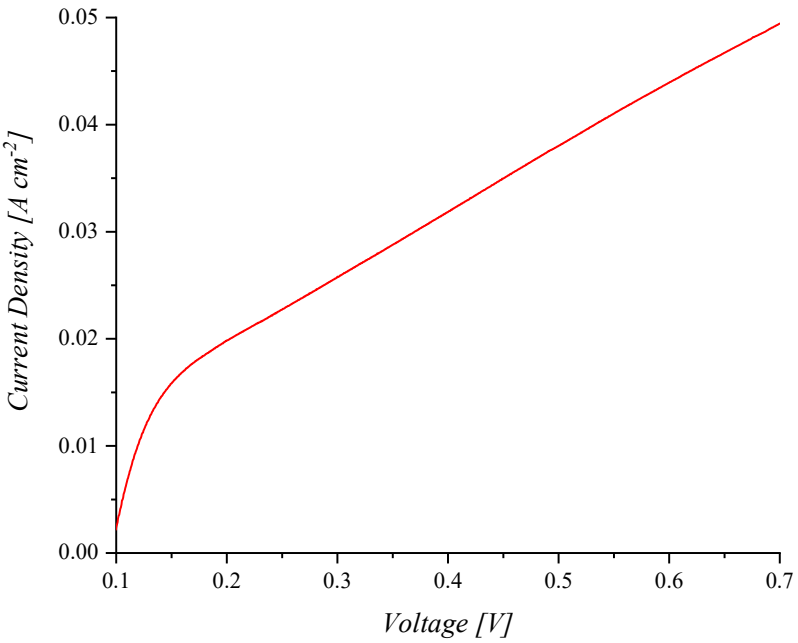

Figure A.4.3 – LSV curve of 25 µm sPPO sample with a IEC~ 1.3 meq g^{-1} for hydrogen crossover analysis in non-reactive gases (H_2/N_2). Scan rate= 1 mV s^{-1} from 0.1 to 0.7 V at T=80 °C e RH=90%.

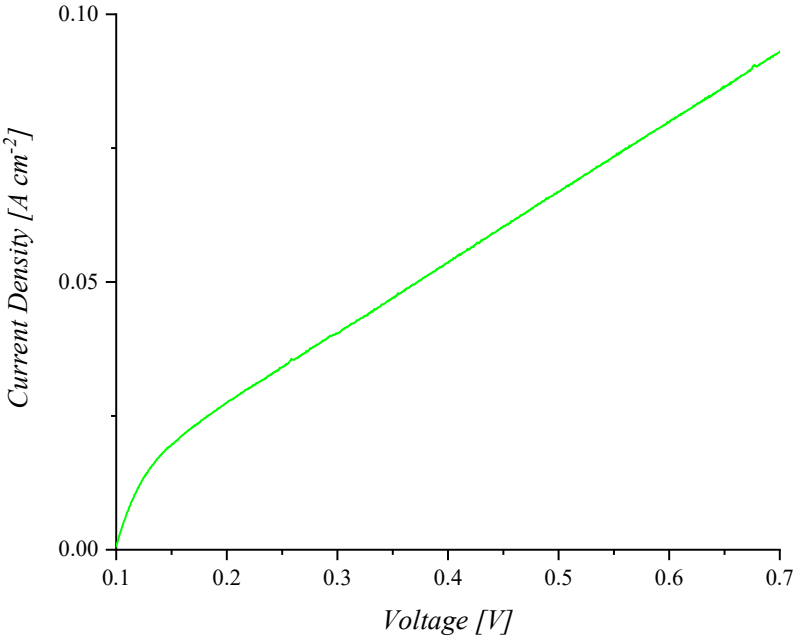

Figure A.4.4 – LSV curve of 25 µm sPPO sample with a IEC~ 2.0 meq g^{-1} for hydrogen crossover analysis in non-reactive gases (H_2/N_2). Scan rate= 1 mV s^{-1} from 0.1 to 0.7 V at T=80 °C e RH=90%.

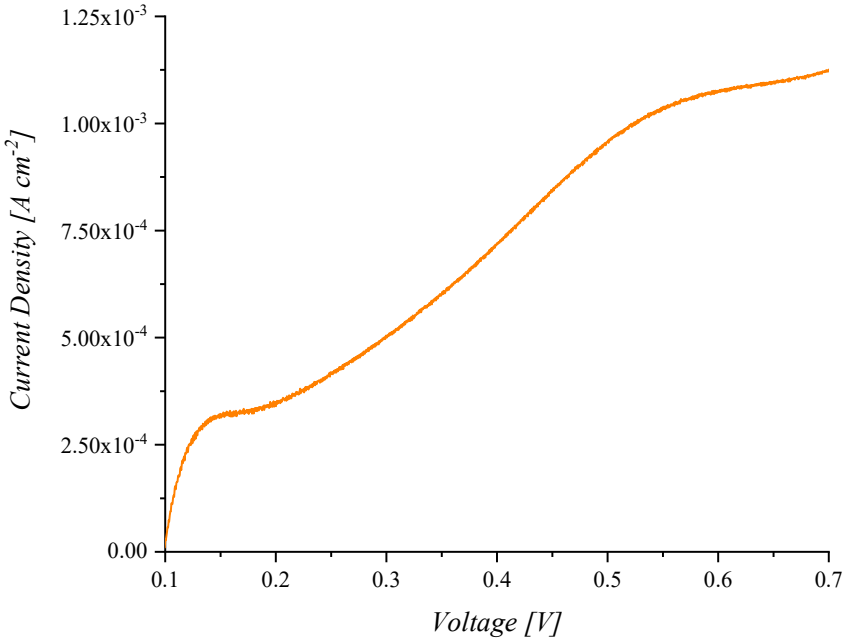

Figure A.4.5 – LSV curve of 50 µm sPPO sample with a IEC~ 2.1 meq g^{-1} for hydrogen crossover analysis in non-reactive gases (H_2/N_2). Scan rate= 1 mV s^{-1} from 0.1 to 0.7 V at T=80 °C e RH=90%.

A.5 – Electrochemical evaluation: Potentiostatic EIS (PEIS)

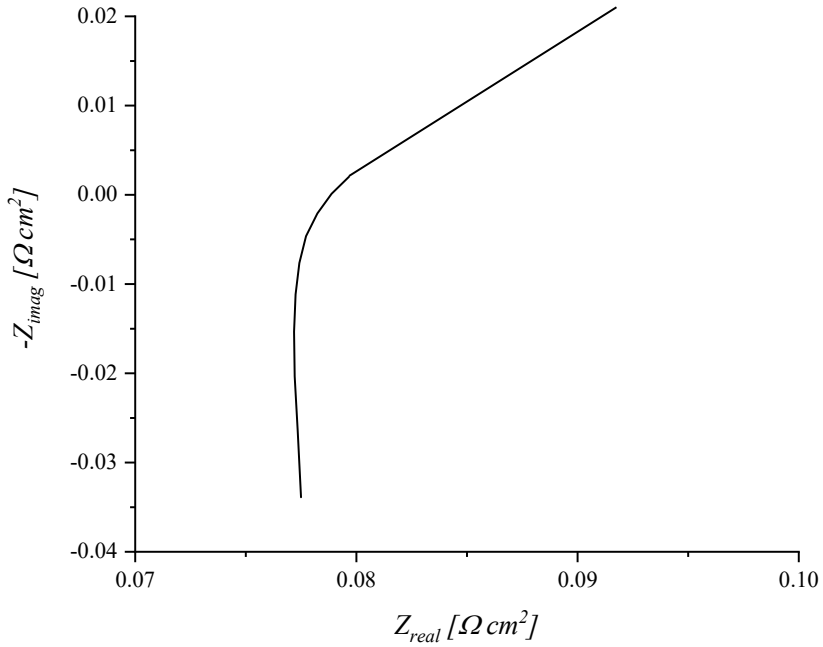

Figure A.5.1 – Nyquist plot of the Potentiostatic impedance (PEIS) of the Nafion 212 sample, recorded in non-reactive gases (H_2/N_2) in a frequency range from 100 kHz to 0.1 Hz at T=80 °C and RH=90%.

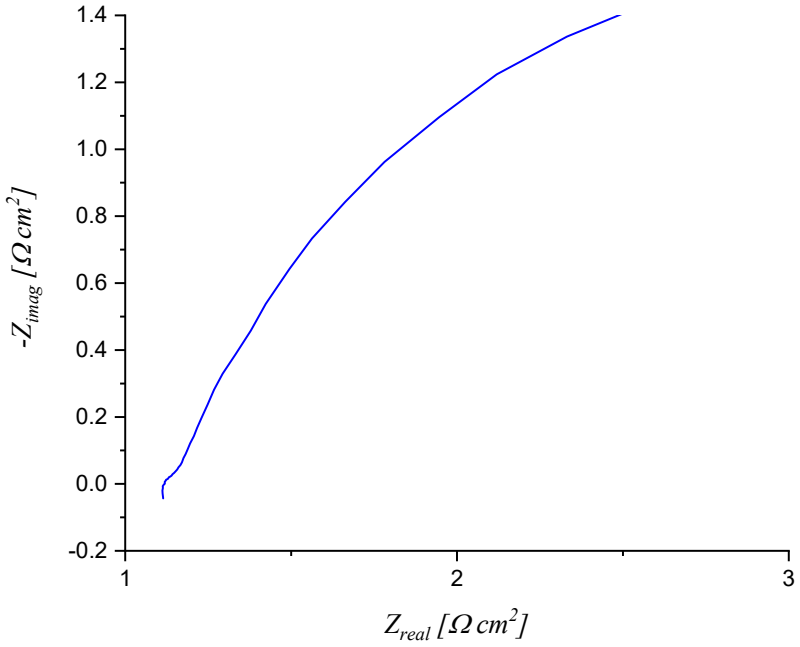

Figure A.5.2 – Nyquist plot of the Potentiostatic impedance (PEIS) of the 25 µm sPPO sample with a IEC~ 0.69 meq g^{-1}, recorded in non-reactive gases (H_2/N_2) in a frequency range from 100 kHz to 0.1 Hz at T=80 °C and RH=90%.

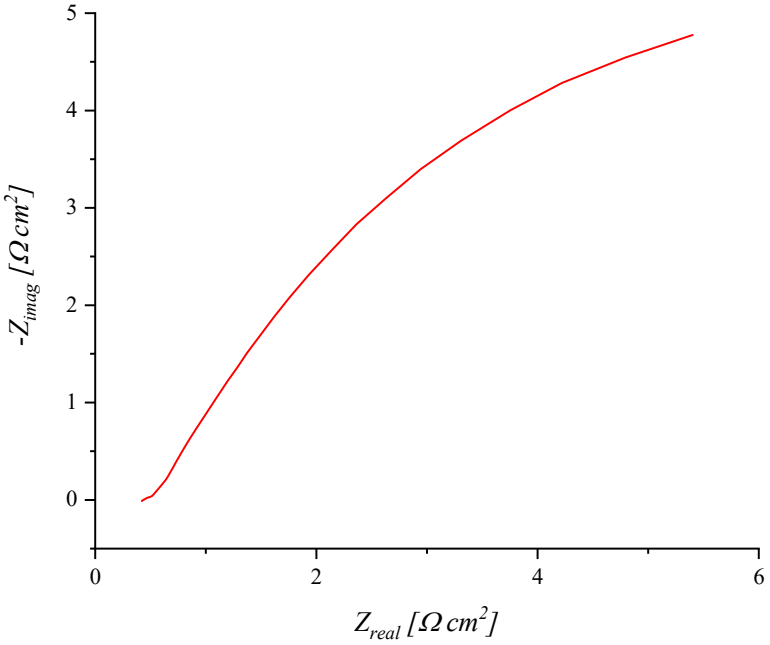

Figure A.5.3 – Nyquist plot of the Potentiostatic impedance (PEIS) of the 25 µm sPPO sample with a IEC~ 1.3 meq g^{-1}, recorded in non-reactive gases (H_2/N_2) in a frequency range from 100 kHz to 0.1 Hz at T=80 °C and RH=90%.

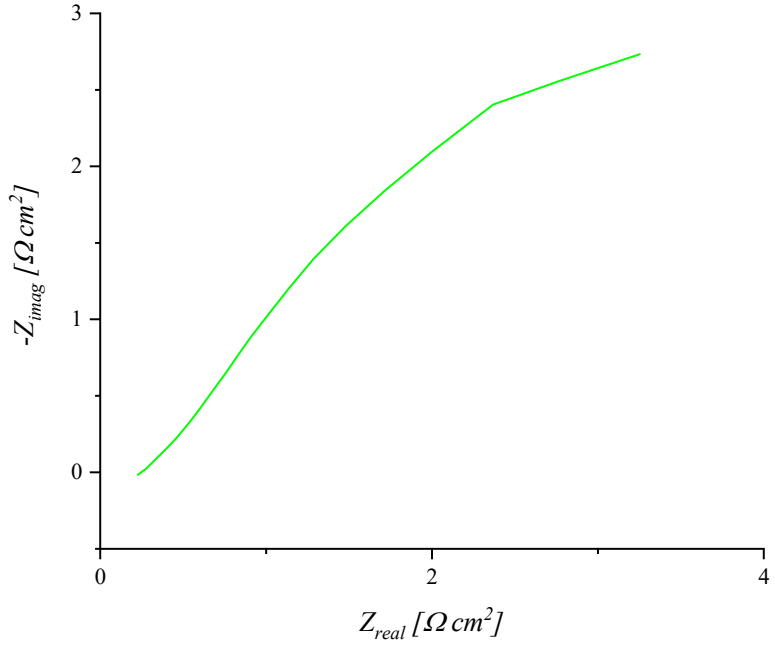

Figure A.5.4 – Nyquist plot of the Potentiostatic impedance (PEIS) of the 25 µm sPPO sample with a IEC~ 2.0 meq g^{-1}, recorded in non-reactive gases (H_2/N_2) in a frequency range from 100 kHz to 0.1 Hz at T=80 °C and RH=90%.

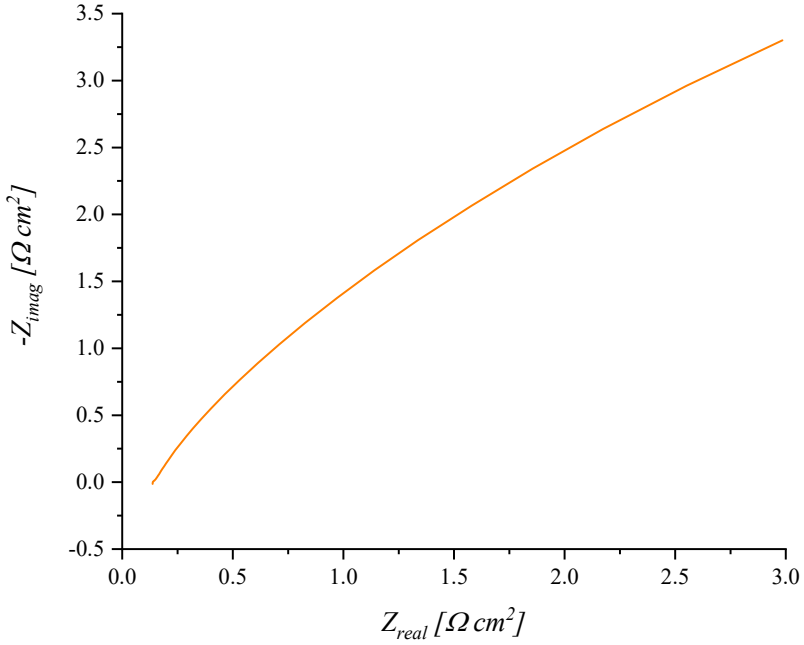

Figure A.5.5 – Nyquist plot of the Potentiostatic impedance (PEIS) of the 50 µm sPPO sample with a IEC~ 2.1 meq g^{-1}, recorded in non-reactive gases (H_2/N_2) in a frequency range from 100 kHz to 0.1 Hz at T=80 °C and RH=90%.

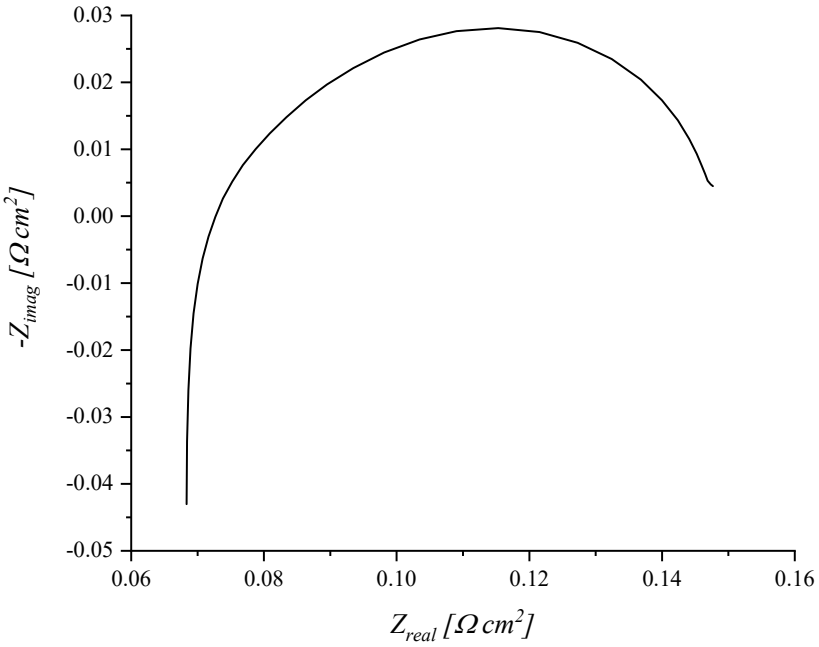

Figure A.5.6 – Nyquist plot of the Potentiostatic impedance (PEIS) of the Nafion 212 sample, recorded in reactive gases (H_2/O_2) in a frequency range from 100 kHz to 0.1 Hz at T=80 °C and RH=90%.

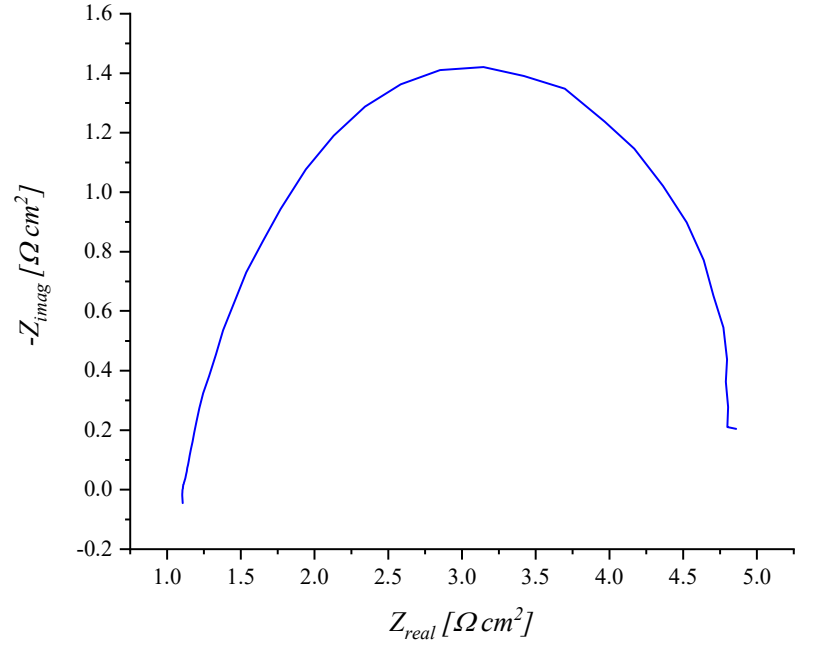

Figure A.5.7 – Nyquist plot of the Potentiostatic impedance (PEIS) of the 25 µm sPPO sample with a IEC~ 0.69 meq g^{-1}, recorded in reactive gases (H_2/O_2) in a frequency range from 100 kHz to 0.1 Hz at T=80 °C and RH=90%.

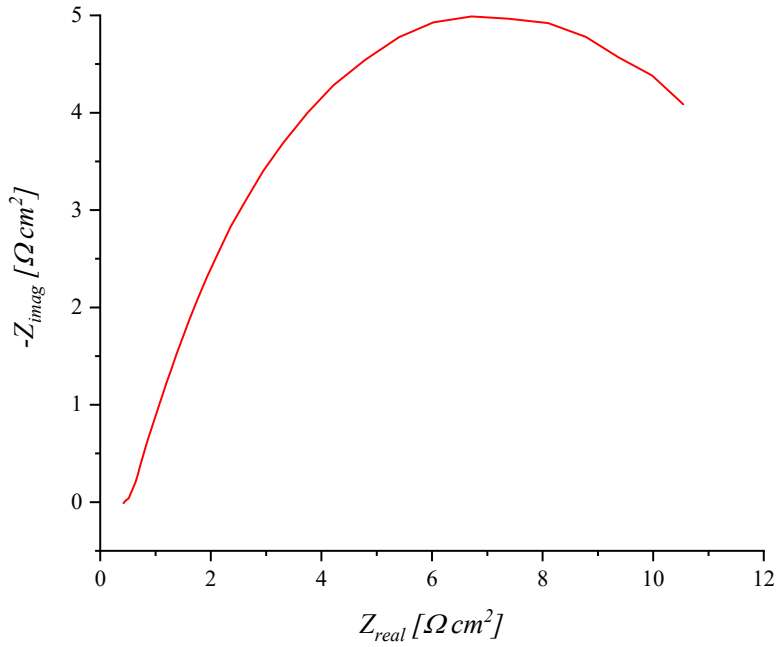

Figure A.5.8 – Nyquist plot of the Potentiostatic impedance (PEIS) of the 25 µm sPPO sample with a IEC~ 1.3 meq g^{-1}, recorded in reactive gases (H_2/O_2) in a frequency range from 100 kHz to 0.1 Hz at T=80 °C and RH=90%.

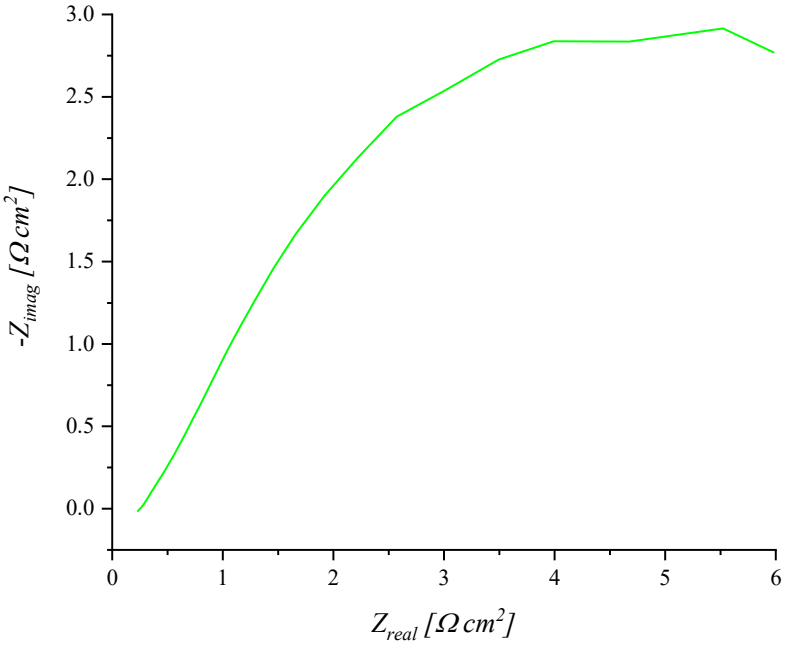

Figure A.5.9 – Nyquist plot of the Potentiostatic impedance (PEIS) of the 25 µm sPPO sample with a IEC~ 2.0 meq g^{-1}, recorded in reactive gases (H_2/O_2) in a frequency range from 100 kHz to 0.1 Hz at T=80 °C and RH=90%.

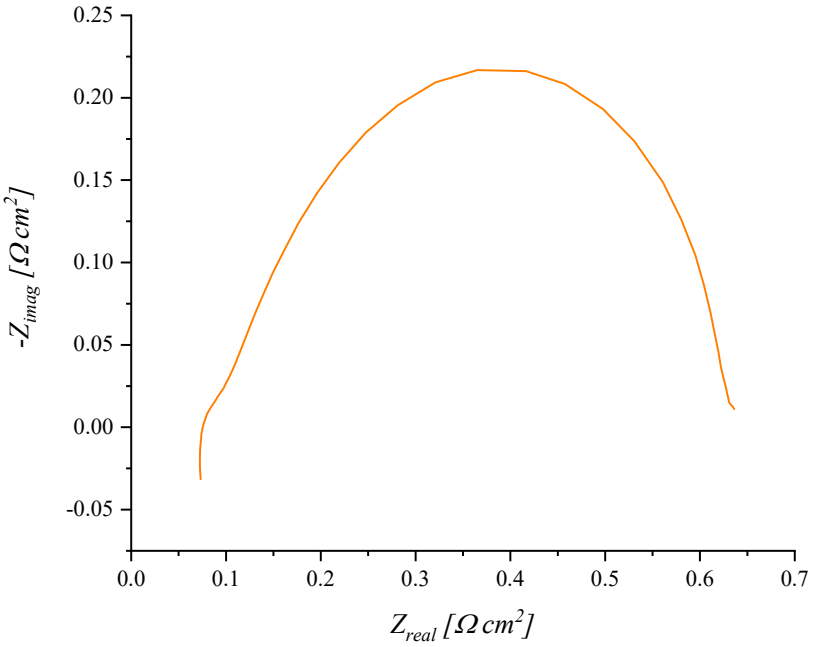

Figure A.5.10 – Nyquist plot of the Potentiostatic impedance (PEIS) of the 50 µm sPPO sample with a IEC~ 2.1 meq g^{-1}, recorded in reactive gases (H_2/O_2) in a frequency range from 100 kHz to 0.1 Hz at T=80 °C and RH=90%.

A.6 – Electrochemical evaluation: Polarization and Power Density Curves

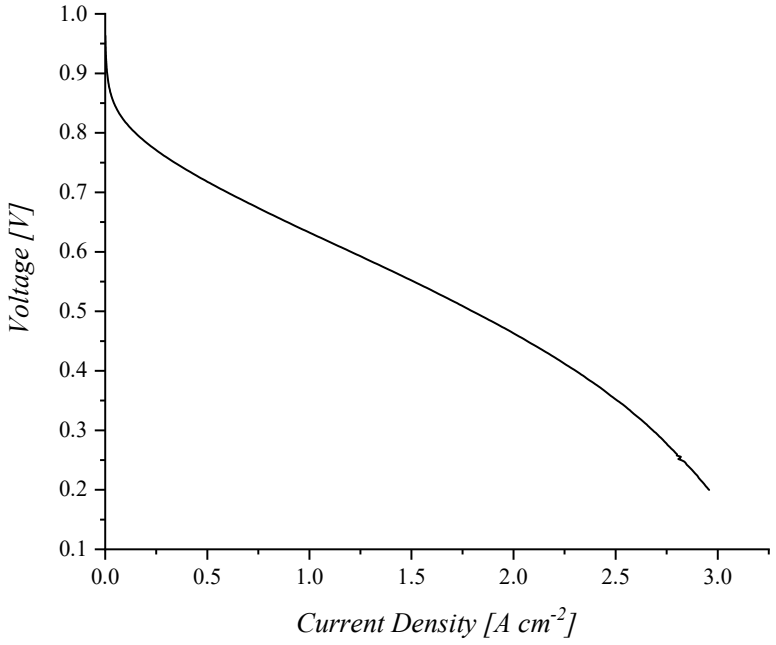

Figure A.6.1 – Polarization curve of the Nafion 212 sample, recorded in reactive gases (H_2/O_2) with a scan rate of 1 mV s^{-1}.

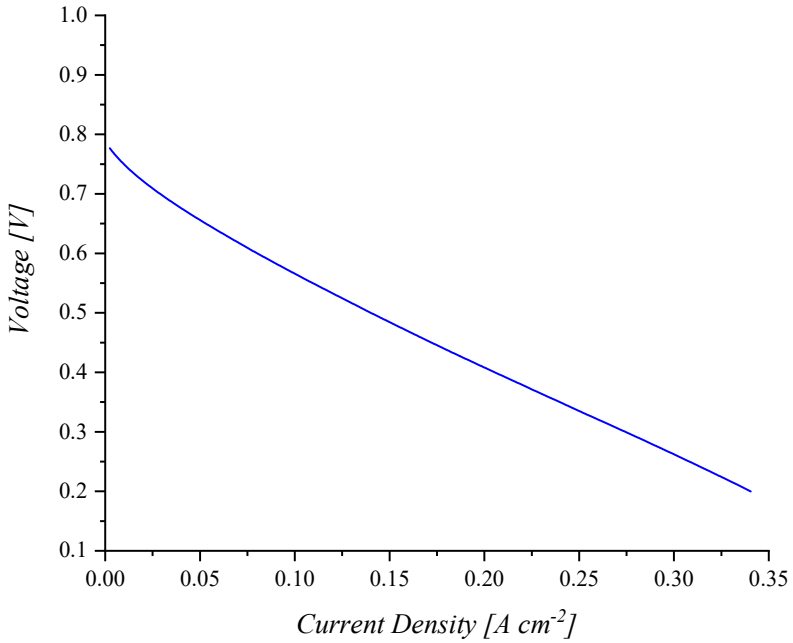

Figure A.6.2 – Polarization curve of the 25 µm sample with a IEC ~ 0.69 meq g^{-1}, recorded in reactive gases (H_2/O_2) with a scan rate of 1 mV s^{-1}.

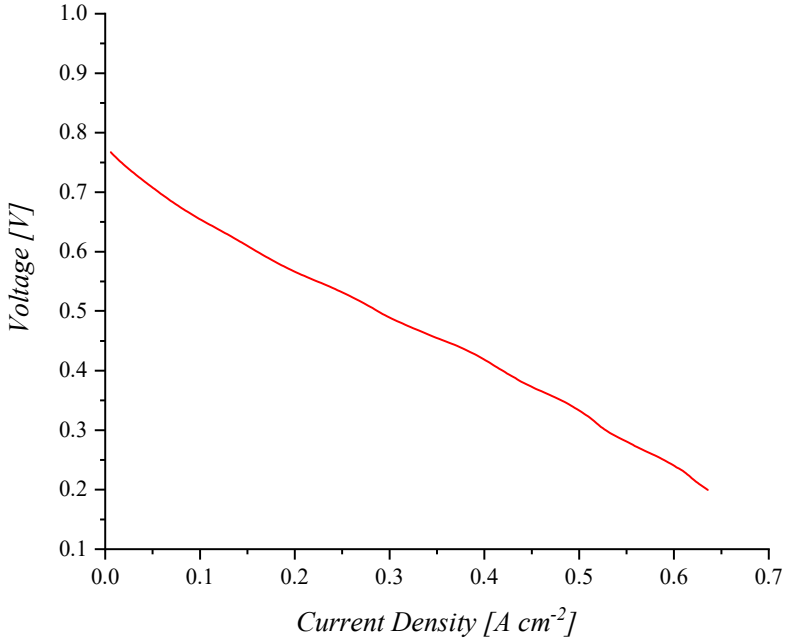

Figure A.6.3 – Polarization curve of the 25 µm sample with a IEC ~ 1.3 meq g^{-1}, recorded in reactive gases (H_2/O_2) with a scan rate of 1 mV s^{-1}.

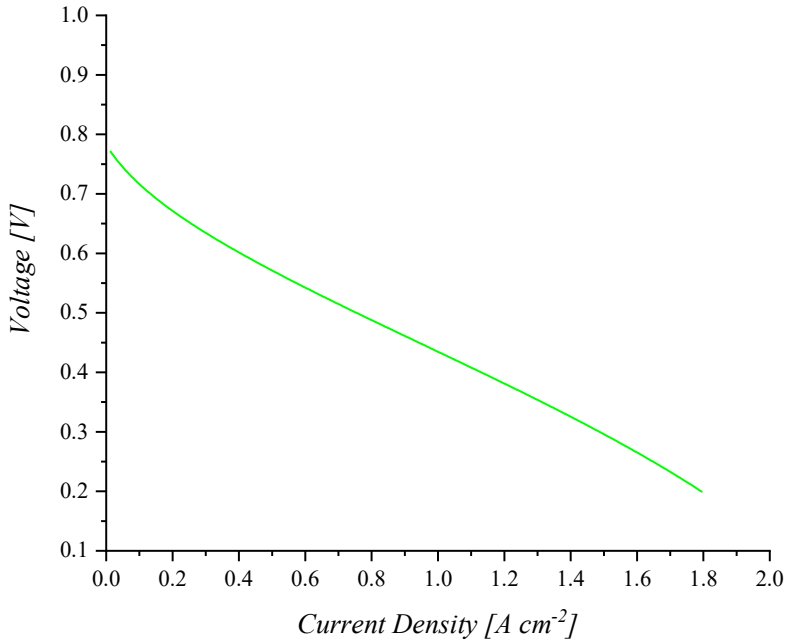

Figure A.6.4 – Polarization curve of the 25 µm sample with a IEC ~ 2.0 meq g^{-1}, recorded in reactive gases (H_2/O_2) with a scan rate of 1 mV s^{-1}.

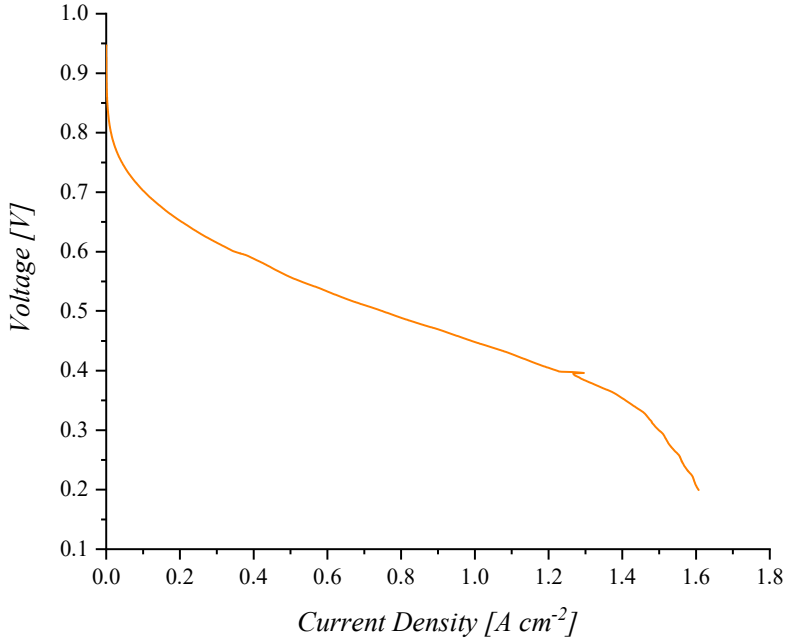

Figure A.6.5 – Polarization curve of the 50 µm sample with a IEC ~ 2.1 meq g^{-1}, recorded in reactive gases (H_2/O_2) with a scan rate of 1 mV s^{-1}.

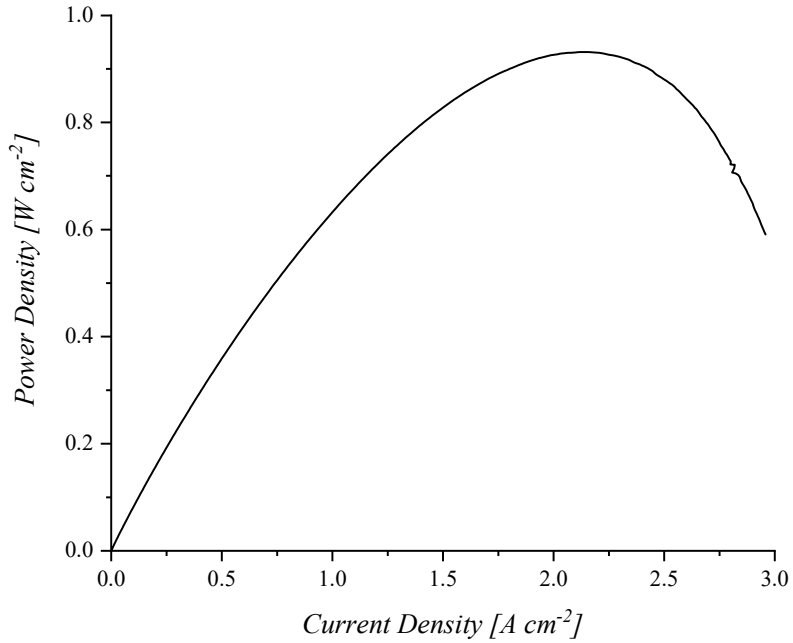

Figure A.6.6 – Power density curve of the Nafion 212 sample, recorded from the polarization curve in reactive gases (H_2/O_2) with a scan rate of 1 mV s^{-1}.

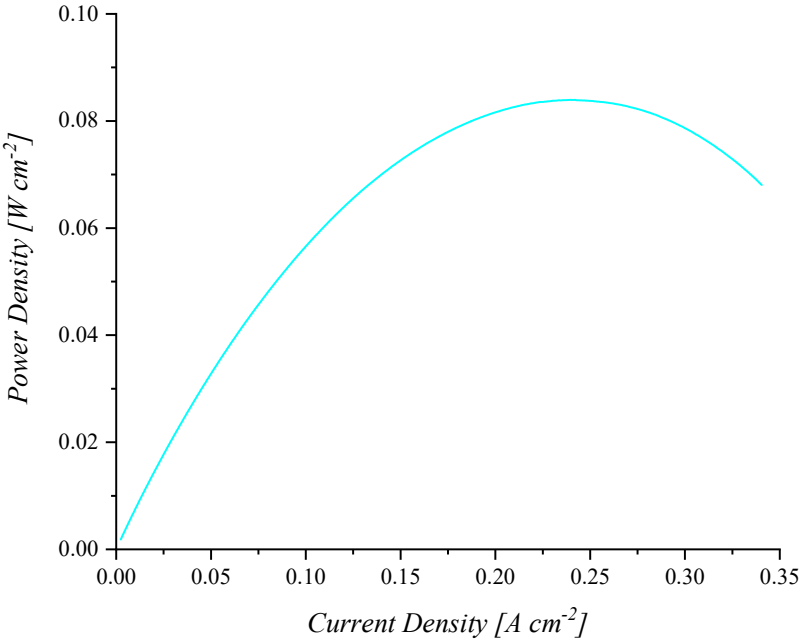

Figure A.6.7 – Power density curve of the 25 µm sample with a IEC ~ 0.69 meq g^{-1}, recorded from the polarization curve in reactive gases (H_2/O_2) with a scan rate of 1 mV s^{-1}.

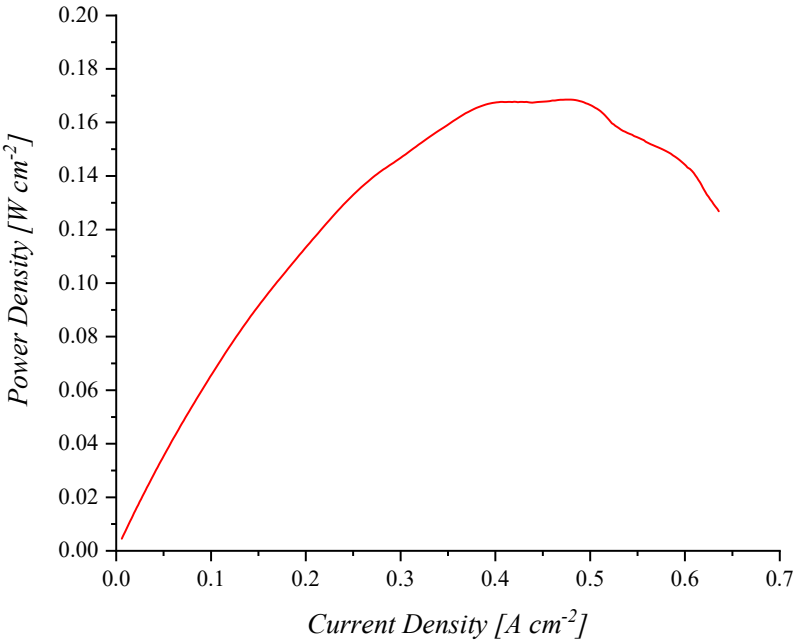

Figure A.6.8 – Power density curve of the 25 µm sample with a IEC ~ 1.3 meq g^{-1}, recorded from the polarization curve in reactive gases (H_2/O_2) with a scan rate of 1 mV s^{-1}.

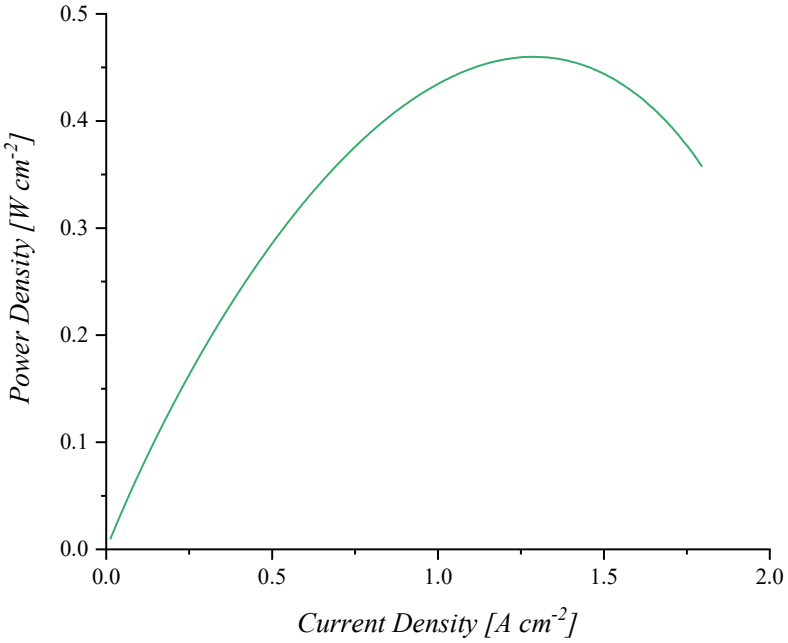

Figure A.6.9 – Power density curve of the 25 µm sample with a IEC ~ 2.0 meq g^{-1}, recorded from the polarization curve in reactive gases (H_2/O_2) with a scan rate of 1 mV s^{-1}.

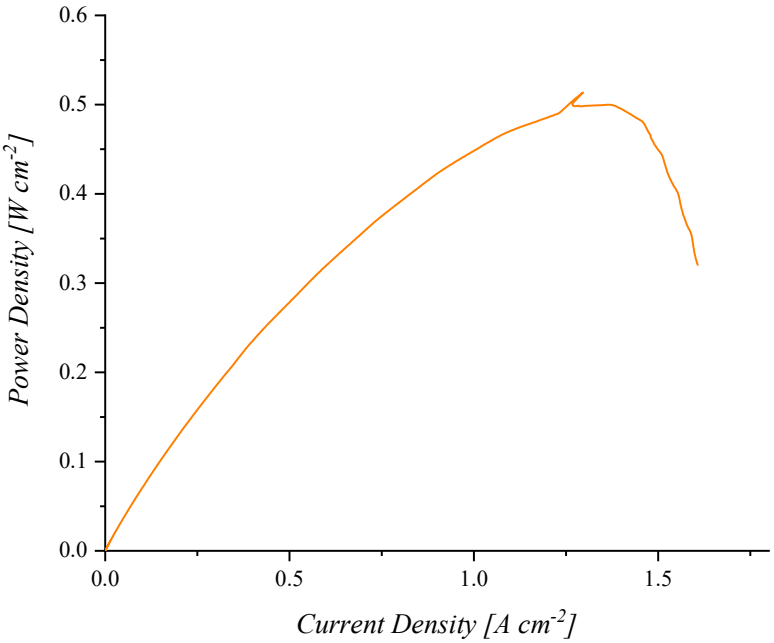

Figure A.6.10 – Power density curve of the 50 µm sample with a IEC ~ 2.1 meq g^{-1}, recorded from the polarization curve in reactive gases (H_2/O_2) with a scan rate of 1 mV s^{-1}.

ANNEX - B

POLY[2,2'-(m-PHENYLENE)-5,5'-BISBENZIMIDAZOLE] – PBI

B.1 – Morphology evaluation: Scanning Electron Microscopy (SEM)

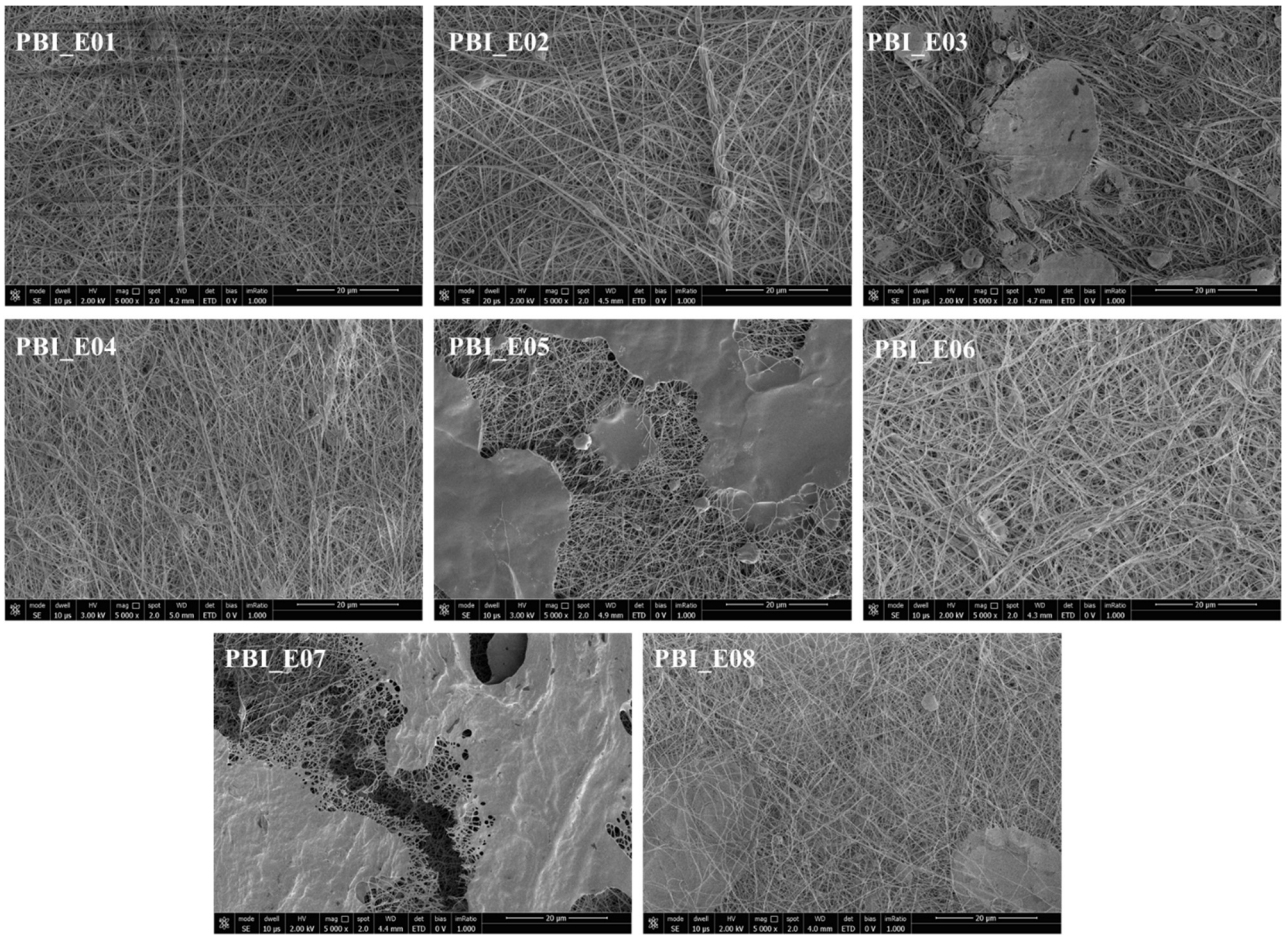

Figure B.1.1 – SEM micrographs of the electrospun *m*-PBI samples obtained from a 14% wt solution and a magnification of 5000x. The electrospinning conditions are shown in Chapter 5.

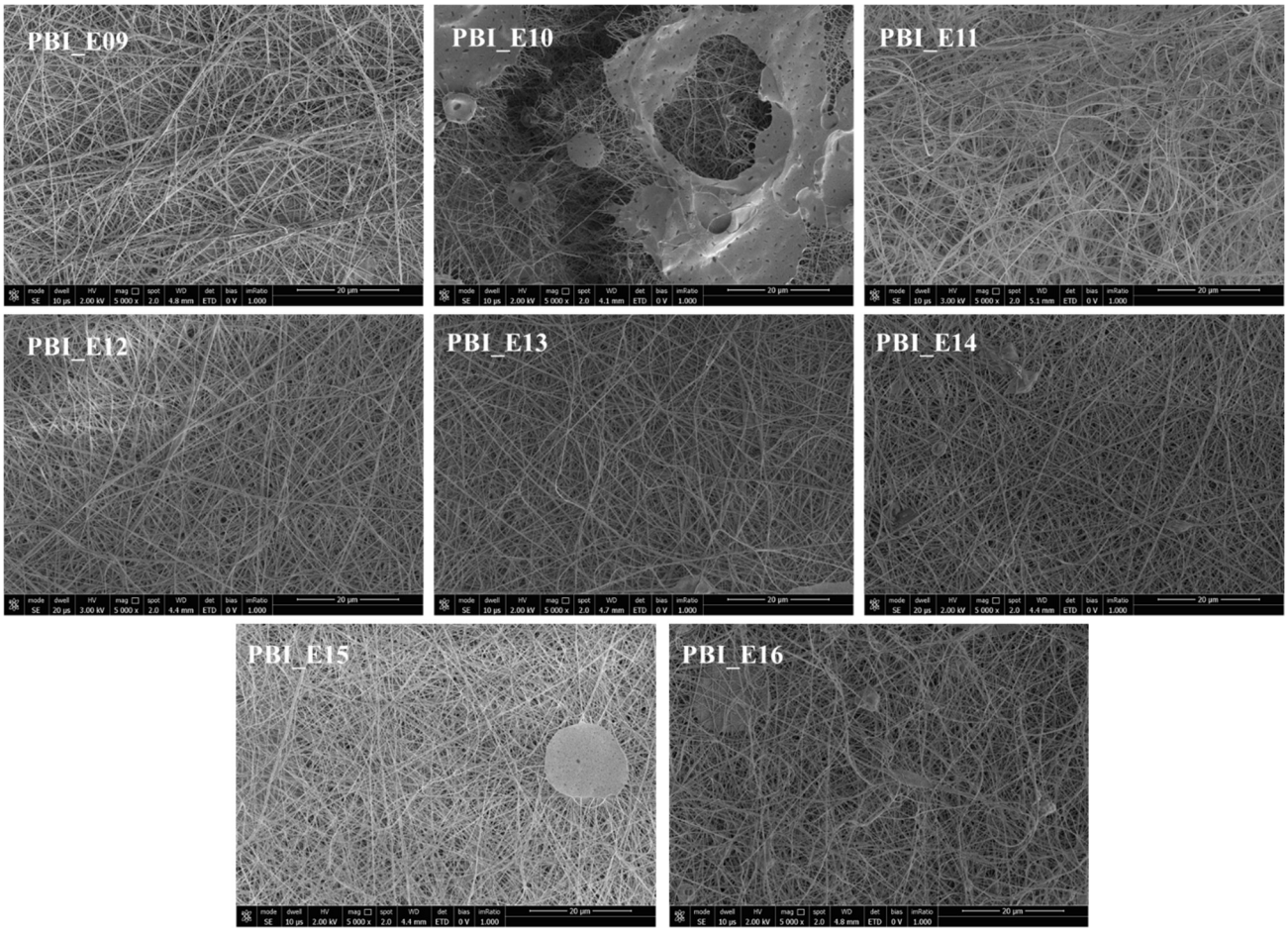

Figure B.1.2 – SEM micrographs of the electrospun *m*-PBI samples obtained from a 16% wt solution and a magnification of 5000x. The electrospinning conditions are shown in Chapter 5.

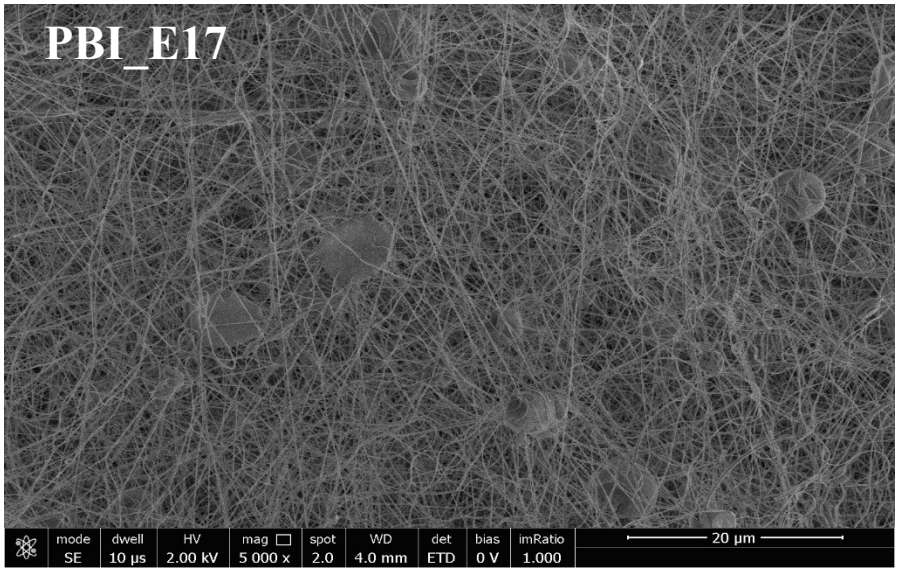

Figure B.1.3 – SEM micrographs of the electrospun *m*-PBI samples obtained from a 15% wt solution and a magnification of 5000x. The electrospinning conditions are shown in Chapter 5.

B.2 – Statistical evaluation: p-Value

Interaction	*p-Value*
X_4	0
X_3	0.001
$X_2X_3X_4$	0.001
X_2X_4	0.00225
X_2X_3	0.017
X_1X_2	0.0495
$X_1X_3X_4$	0.10575
X_1	0.11075
$X_1X_2X_3$	0.114667
X_3X_4	0.131
X_1X_3	0.133
X_4	0

Table B.2.1 – p-Value values for the Y_1 response, mean fiber diameter, recorded on the 17 electrospun *m*-PBI samples. Determination of p-value was performed using JMP software in step-wise mode with a significance limit set at 0.1.

Interaction	*p-Value*
X_4	0
X_3X_4	0
X_2	0.003333
X_1X_2	0.003333
$X_1X_2X_3$	0.003333
$X_1X_3X_4$	0.003333
X_2X_4	0.005667
$X_1X_2X_4$	0.006333
X_2X_3	0.042667
$X_2X_3X_4$	0.1035
X_1X_3	0.155

Table B.2.2 – p-Value values for the Y_2 response, mean fiber diameter standard deviation, recorded on the 17 electrospun *m*-PBI samples. Determination of p-value was performed using JMP software in step-wise mode with a significance limit set at 0.1.

Interaction	*p-Value*
X_2	0
X_3	0.002
X_1X_4	0.026
X_1	0.058333
$X_1X_2X_3$	0.074333
$X_2X_3X_4$	0.085333
$X_1X_2X_3$	0.113333
X_1X_3	0.147
$X_1X_3X_4$	0.182
X_3X_4	0.1855
X_1X_2	0.189333

Table B.2.3 – p-Value values for the Y_3 response, porosity, recorded on the 17 electrospun *m*-PBI samples. Determination of p-value was performed using JMP software in step-wise mode with a significance limit set at 0.1.

Interaction	*p-Value*
X_2X_3	0
X_3	0.000333
X_3X_4	0.000667
$X_1X_2X_4$	0.001333
X_1X_2	0.004
$X_1X_3X_4$	0.016
$X_2X_3X_4$	0.027667
X_1	0.034667
X_2X_4	0.044667
X_4	0.061333
$X_1X_2X_3$	0.147
X_1X_4	0.151

Table B.2.4 – p-Value values for the Y_4 response, air permeability, recorded on the 17 electrospun *m*-PBI samples. Determination of p-value was performed using JMP software in step-wise mode with a significance limit set at 0.1.

Interaction	*p-Value*
X_1X_3	0.001
X_1X_4	0.002
X_3X_4	0.006
X_2X_4	0.013
X_1	0.02
$X_2X_3X_4$	0.022667
X_3	0.025667
X_1X_2	0.028333
$X_1X_2X_3$	0.031667
X_4	0.036
$X_1X_2X_3$	0.095
X_2X_3	0.154

Table B.2.5– p-Value values for the Y_5 response, defects percentage, recorded on the 17 electrospun *m*-PBI samples. Determination of p-value was performed using JMP software in step-wise mode with a significance limit set at 0.1.

B.3 – Characterization of m-PBI Electrospun membranes: Mechanical properties

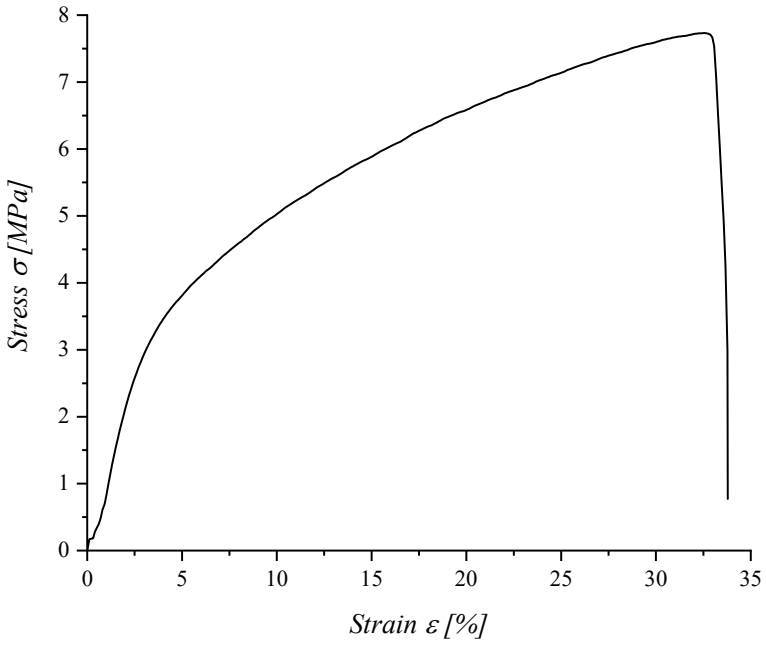

Figure B.3.1 – Stress-strain curve of *m*-PBI-based membrane obtained through solution casting.

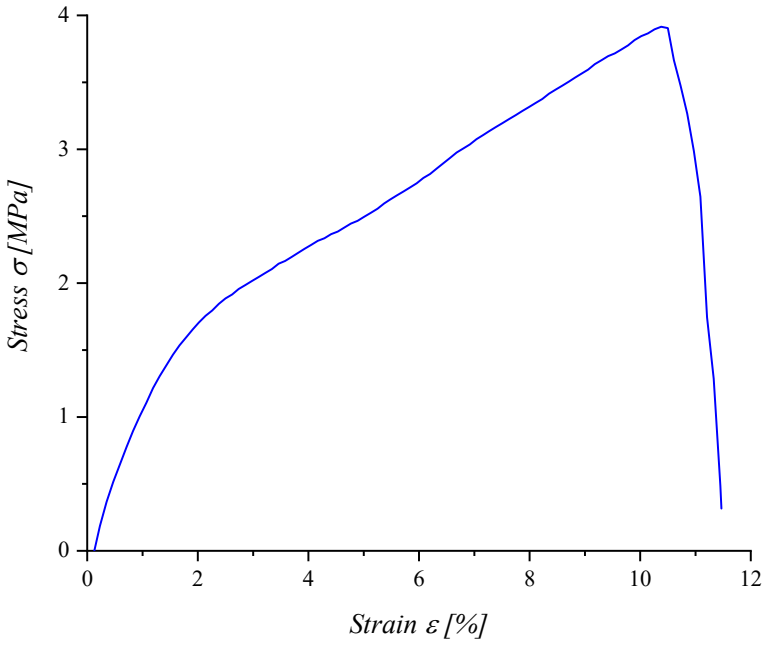

Figure B.3.2 – Stress-strain curve of *m*-PBI-based membrane obtained through electrospinning.

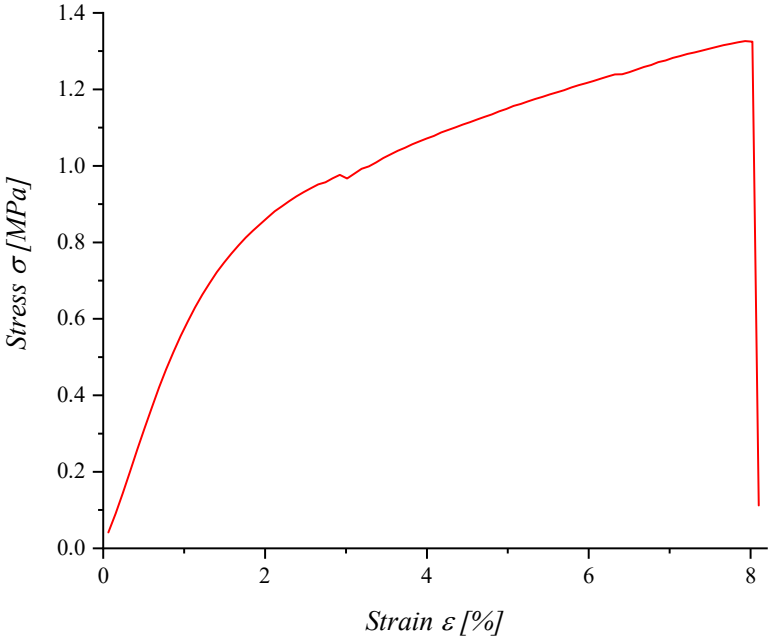

Figure B.3.3 – Stress-strain curve of *m*-PBI-based membrane obtained through electrospinning and doped with a 1M phosphoric acid solution.

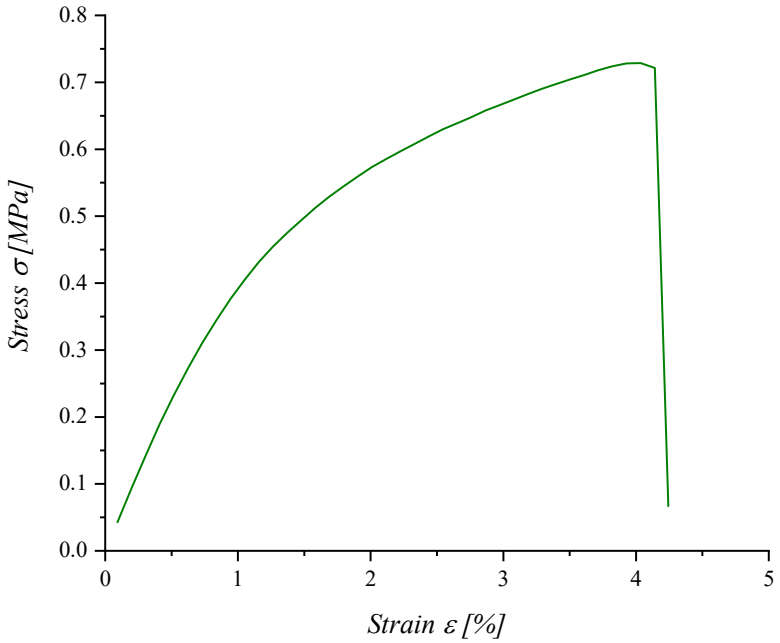

Figure B.3.4 – Stress-strain curve of *m*-PBI-based membrane obtained through electrospinning and doped with a 5M phosphoric acid solution.

B.4 – Kinetic and thermodynamic evaluation

Mathematical modelling

Table B.4.1 Pseudo-first-order

Parameter	Value ± C.I. 95 %	Correlation Matrix		Adj-R^2	SD
		A_0	Ea		
A_0	33.6 ± 2.5	1		0.8924	336.94
Ea	20934 ± 377	0.2518	1		

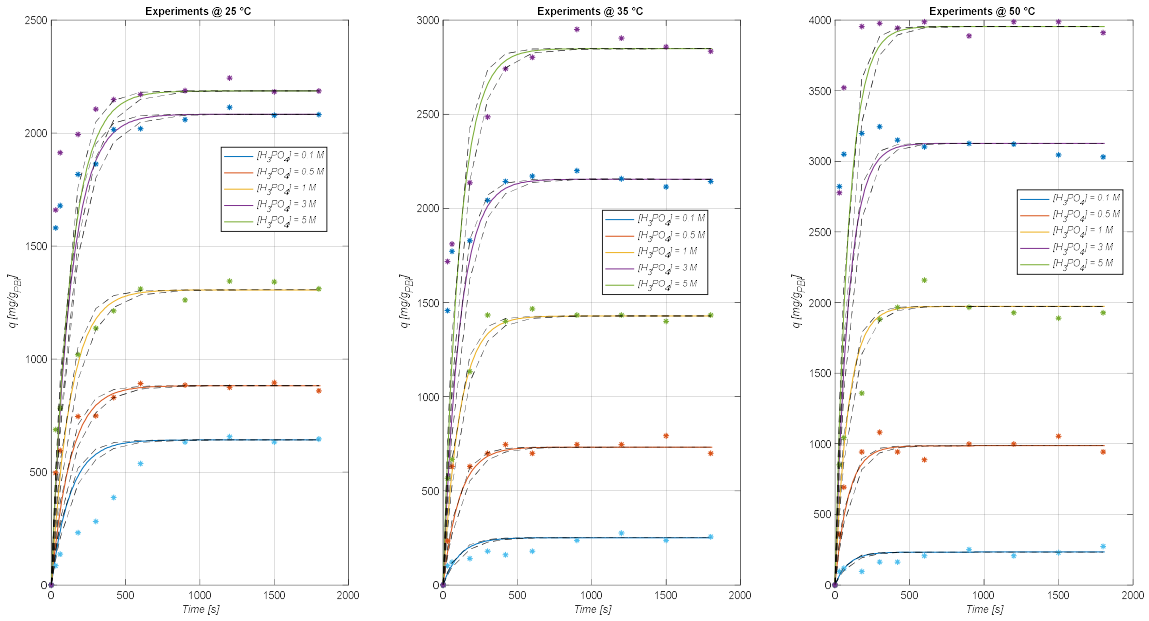

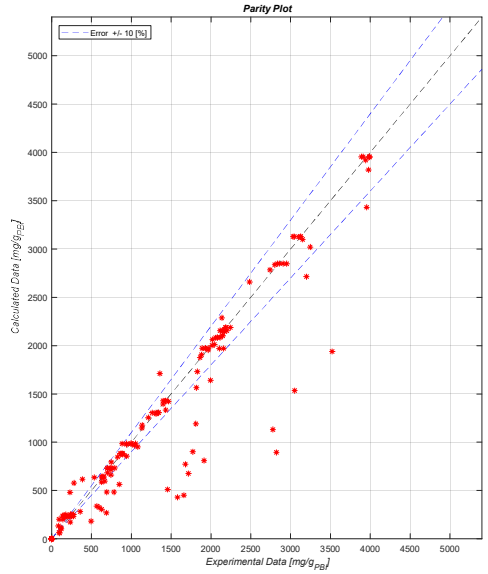

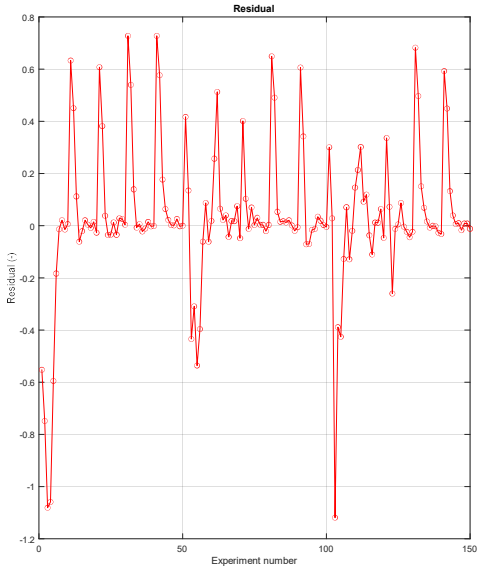

Table B.4.2. Pseudo-second-order

Parameter	Value ± C.I. 95 %	Correlation Matrix		Adj-R^2	SD
		A_0	Ea		
A_0	3997 ± 2.5	1		0.9722	183.88
Ea	20934 ± 377	0.1013	1		

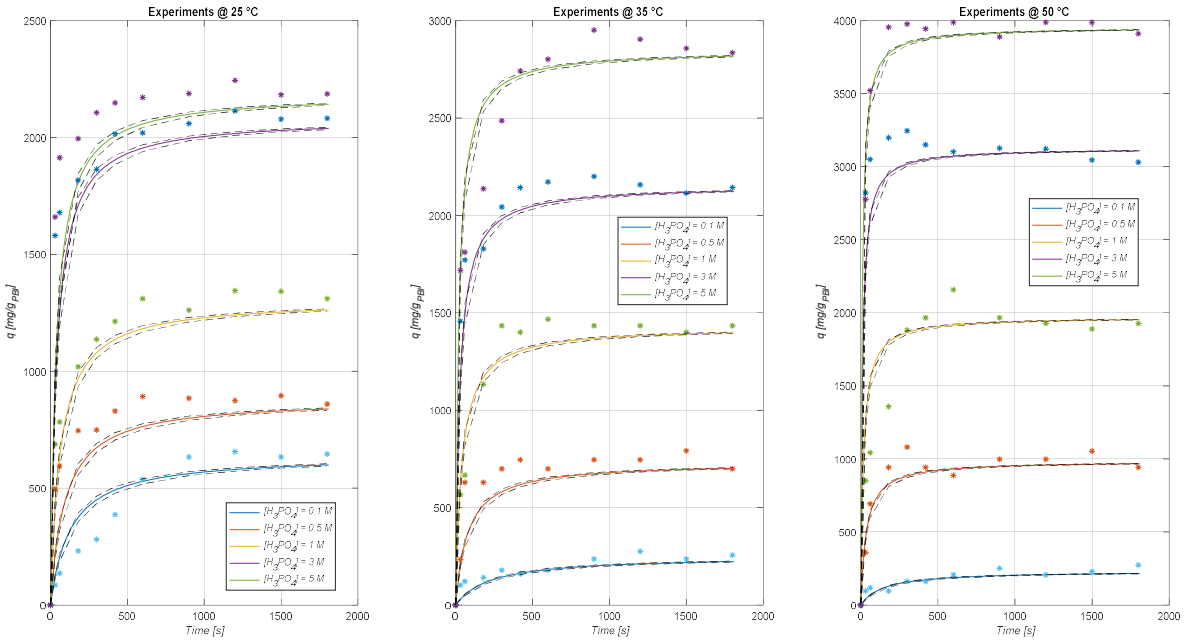

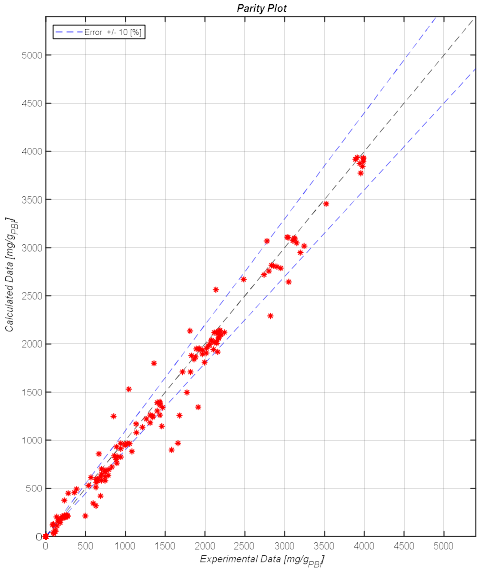

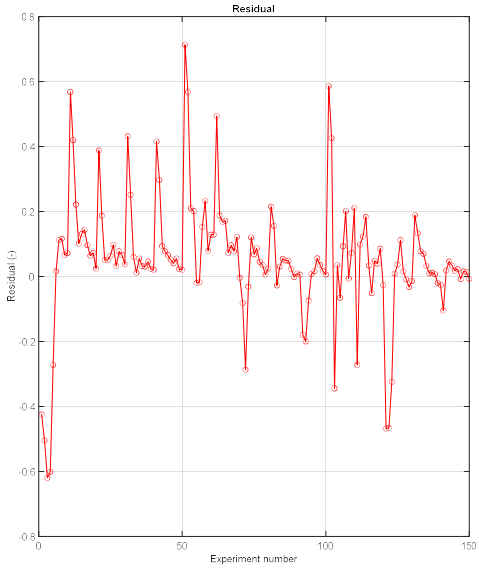

Adsorption Isotherms

The following isotherm models, along with the Liu isotherm, have been tested looking for the one which better fits the experimental data.

Table B.4.3. Langmuir equation $q = \frac{Q_{\max} K_L C_e}{1 + K_L C_e}$

	Parameters		
***T* (°C)**	***Q*max**	***K***	**Adj-R²**
25	0.027	1.16	0.9558
35	0.039	0.52	0.9917
50	0.060	0.46	0.9971

Table B.4.4. Freundlich equation $q = K_F C_e^{\frac{1}{n_F}}$

	Parameters		
***T* (°C)**	***k*F**	n	**Adj-R²**
25	0.013	2.75	0.9839
35	0.012	1.88	0.9890
50	0.018	1.79	0.9824

Table B.4.5. Sips equation $q = \frac{Q_{\max} K_S C_e^{\frac{1}{n_S}}}{1 + K_S C_e^{\frac{1}{n_S}}}$

	Parameters			
***T* (°C)**	***Q*max**	***K*s**	n	**Adj-R²**
25	0.0163	0.0433	1.34	0.8912
35	0.0188	0.0504	1.48	0.9154
50	0.0207	0.0550	1.50	0.9384

Water Uptake Evaluation

Sample	*Water Uptake [mol_{H2O} mol_{PBI}^{-1}]*
1	5.55552
2	6.12931
3	5.49189
4	5.79681
5	5.68962
6	5.70193
7	5.9803
8	5.70357
9	5.62541
10	6.10689
11	6.09367
12	6.05739
13	5.69423
14	5.50002
15	5.85151
16	5.73277
17	5.53106
18	5.92886

Table B.4.6 – Water Uptake evaluation for *m*-PBI membranes obtained through solution casting tecnique for 18 independent samples.

Sample	*Water Uptake [mol_{H2O} mol_{PBI}^{-1}]*
1	63.94683
2	62.74029
3	56.23226
4	69.91904
5	83.68088
6	69.79736
7	39.8686
8	56.12404
9	53.89961
10	60.5729
11	48.76632
12	54.75516
13	50.99074
14	54.75516
15	55.78182
16	54.75516
17	47.91077
18	59.71735

Table B.4.7 – Water Uptake evaluation for *m*-PBI membranes obtained through electrospinning tecnique for 18 independent samples.

Time [min]	*ADL [H_3PO_4] 0.1M*	*ADL [H_3PO_4] 0.5M*	*ADL [H_3PO_4] 1M*	*ADL [H_3PO_4] 3M*	*ADL [H_3PO_4] 5M*
1	5.66E-04	0.0053	0.03018	0.55503	0.10938
3	0.00396	0.00265	0.06036	0.37002	0.35002
5	0.00792	0.0053	0.07545	0.21347	0.39377
10	0.00905	0.01326	0.09054	0.42694	0.96255
15	0.00735	0.01591	0.1509	0.48387	0.74379
30	0.00905	0.0053	0.13581	0.55503	0.9188
60	0.00509	0.01856	0.12072	0.56926	1.33445
120	0.01018	0.01856	0.11318	0.74004	1.26882
240	0.00905	0.02386	0.12072	0.85389	1.42196
360	0.00962	0.04772	0.11318	0.89658	1.55321
420	0.00792	0.03712	0.11318	0.98197	1.59697
1350	0.01075	0.06628	0.11318	1.09582	1.3782
1440	0.01471	0.06628	0.10563	0.83966	1.3782
1560	0.01471	0.06097	0.11318	1.05313	1.59697
2880	0.01697	0.05567	0.10563	1.05313	1.3782

Table B.4.8 - Dynamic evaluation of ADL (Acid Doping Level) values obtained at different concentrations of H_3PO_4 on dense *m*-PBI membranes obtained through solution casting.

Time [min]	*ADL [H_3PO_4] 0.1M*	*ADL [H_3PO_4] 0.5M*	*ADL [H_3PO_4] 1M*	*ADL [H_3PO_4] 3M*	*ADL [H_3PO_4] 5M*
0.5	0.065787	1.257446	2.3477589	4.969857056	4.541198
1	0.122993	1.745669	2.647409	5.237629527	4.765936
3	0.752258	2.396633	3.3965344	5.70623135	5.889624
5	0.695052	2.288139	3.8460096	5.572345115	7.013312
7	1.267112	2.233892	4.0707472	6.107890056	6.938399
10	1.667553	2.505127	4.3703974	6.308719409	6.788574
15	1.667553	2.613621	4.0707472	6.174833174	6.788574
20	2.010789	2.396633	4.595135	6.57649188	7.013312
25	1.839171	2.505127	4.4453099	6.509548762	6.713662
30	1.896377	2.342386	4.3703974	6.107890056	6.563836

Table B.4.9 - Dynamic evaluation of ADL (Acid Doping Level) values obtained at different concentrations of H_3PO_4 on fibrous *m*-PBI membranes obtained through electrospinning.

Time [min]	*ADL [H_3PO_4] 0.1M*	*ADL [H_3PO_4] 0.5M*	*ADL [H_3PO_4] 1M*	*ADL [H_3PO_4] 3M*	*ADL [H_3PO_4] 5M*
0.5	0.321893	2.199502	1.782918	4.584647	5.405096
1	0.3824	1.979991	2.097551	5.573493	5.697778
3	0.442906	1.979991	3.565837	5.753283	6.722163
5	0.563919	2.199502	4.509735	6.742128	7.819719
7	0.503412	2.345843	5.873143	7.371394	8.624593
10	0.563919	2.199502	3.985347	6.832023	8.185571
15	0.745437	2.345843	3.565837	6.292653	9.283127
20	0.86645	1.614139	3.460959	7.730974	9.136786
25	0.745437	1.760479	4.404857	6.022968	8.990445
30	0.805944	1.467798	4.509735	6.742128	8.917275

Table B.4.10 - Dynamic evaluation of ADL (Acid Doping Level) values obtained at 35 °C and different concentrations of H_3PO_4 on fibrous *m*-PBI membranes obtained through electrospinning.

Time [min]	*ADL [H_3PO_4] 0.1M*	*ADL [H_3PO_4] 0.5M*	*ADL [H_3PO_4] 1M*	*ADL [H_3PO_4] 3M*	*ADL [H_3PO_4] 5M*
0.5	0.300649	1.129182	2.676798	10.13567	8.7363
1	0.370567	2.177957	3.281861	9.910929	9.505402
3	0.300649	2.964539	3.644898	10.06075	12.44197
5	0.510404	3.401529	4.976036	10.21058	12.51189
7	0.510404	2.964539	6.186162	9.910929	11.46312
10	0.650241	2.789743	6.791225	9.761103	11.60295
15	0.790078	3.139335	6.186162	9.836016	11.60295
20	0.650241	3.139335	6.065149	11.70883	14.12001
25	0.720159	3.314131	5.944137	11.78374	14.74928
30	0.859996	2.964539	6.065149	9.536366	14.8192

Table B.4.11 - Dynamic evaluation of ADL (Acid Doping Level) values obtained at 50 °C and different concentrations of H_3PO_4 on fibrous *m*-PBI membranes obtained through electrospinning.

B.5 – Structural evaluation: FTIR

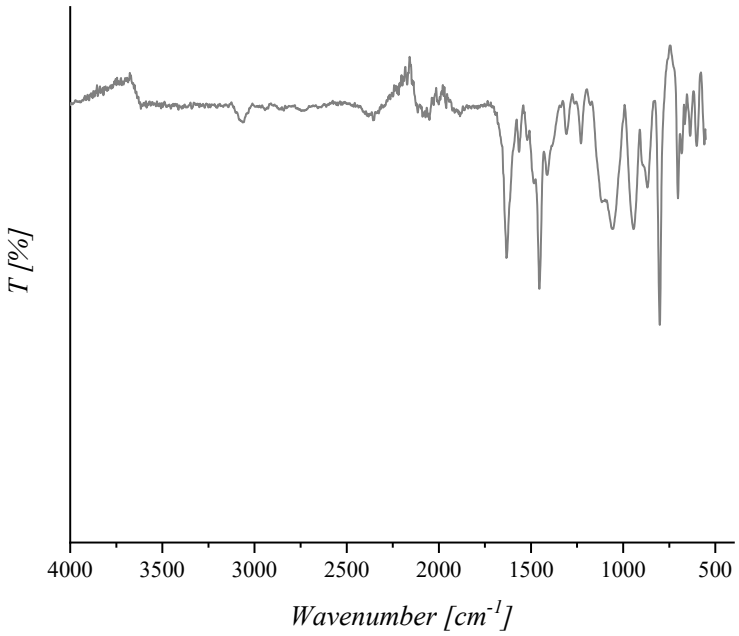

Figure B.5.1 – FTIR/ATR spectrum of the electrospun membrane of *m*-PBI recorded before acid impregnation treatment.

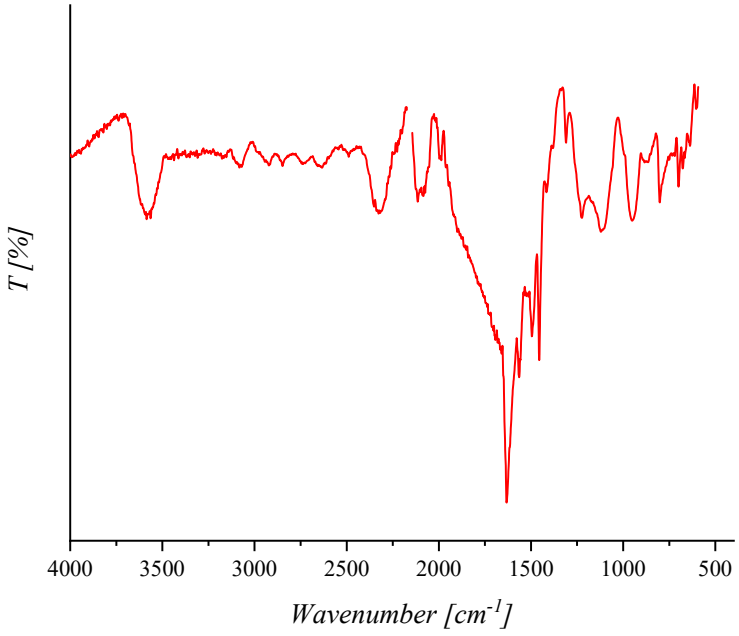

Figure B.5.2 – FTIR/ATR spectrum of the electrospun membrane of *m*-PBI recorded after the acid impregnation treatment with a 1M H_3PO_4 solution

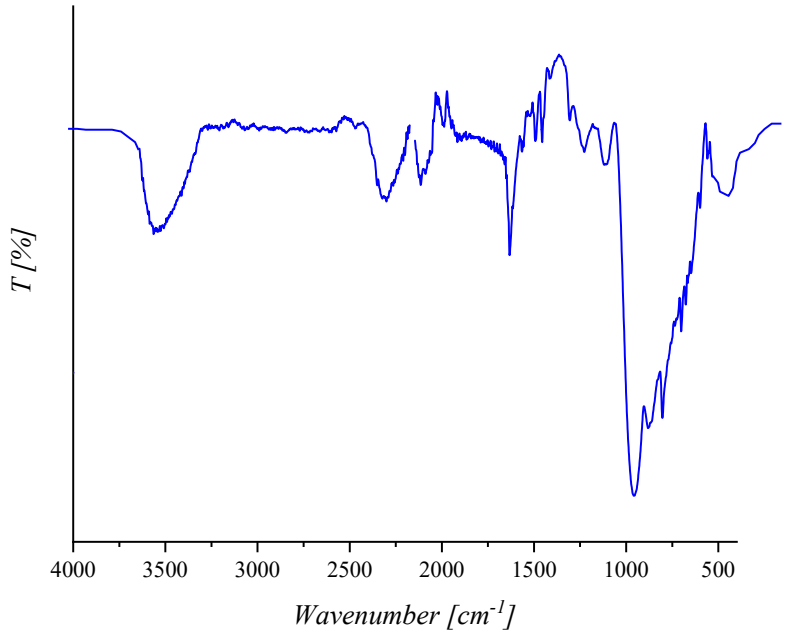

Figure B.5.3 – FTIR/ATR spectrum of the electrospun membrane of *m*-PBI recorded after the acid impregnation treatment with a 5M H_3PO_4 solution

B.6 – Electrochemical evaluation: Proton conductivity

Temperature [°C]	***Proton conductivity [mS cm^{-1}]***
50	76
100	87
150	91
180	93

Table B.6.1 – Proton conductivity values of *m*-PBI-based dense membranes obtained through solution casting technique as temperature changes.

Temperature [°C]	***Proton conductivity [mS cm^{-1}]***
50	82
100	98
150	132
180	130

Table B.6.2 – Proton conductivity values of *m*-PBI-based fibrous membranes obtained through electrospinning technique as temperature changes.

ANNEX - C

AMINATED POLY(2,6-DIMETHYL-1,4-PHENYLENE OXIDE) – aPPO

C.1 – Structural evaluation: FTIR and ^{1}H-NMR

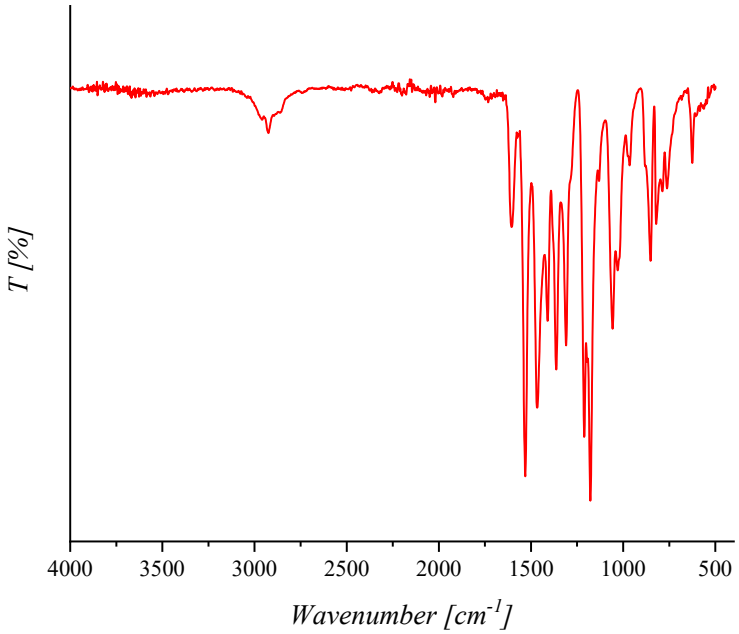

Figure C.1.1 – FTIR/ATR spectrum of the PPO-NO_2 precursor used for subsequent synthesis steps and obtained starting from a nitration of neat PPO using an acid mixture HNO_3/H_2SO_4 3:1 vol/vol.

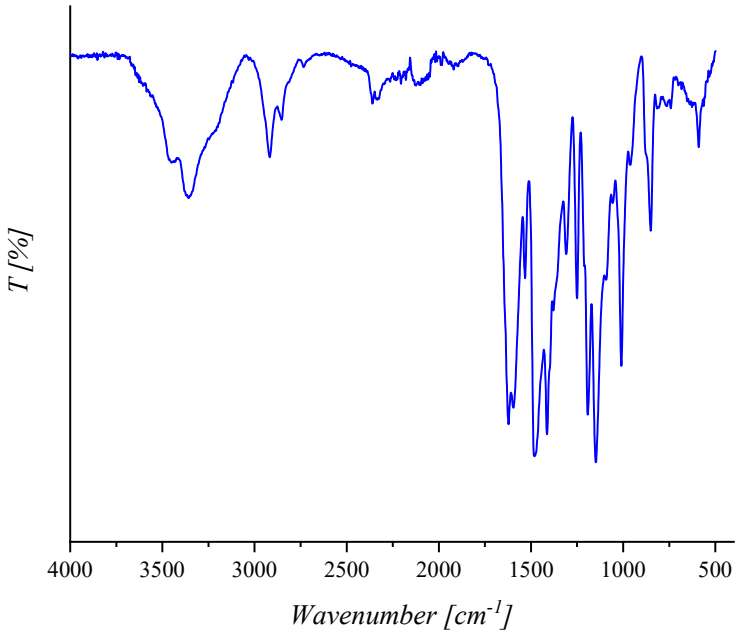

Figure C.1.2 – FTIR/ATR spectrum of the aPPO sample obtained following the PPO-NO_2 sample reduction process.

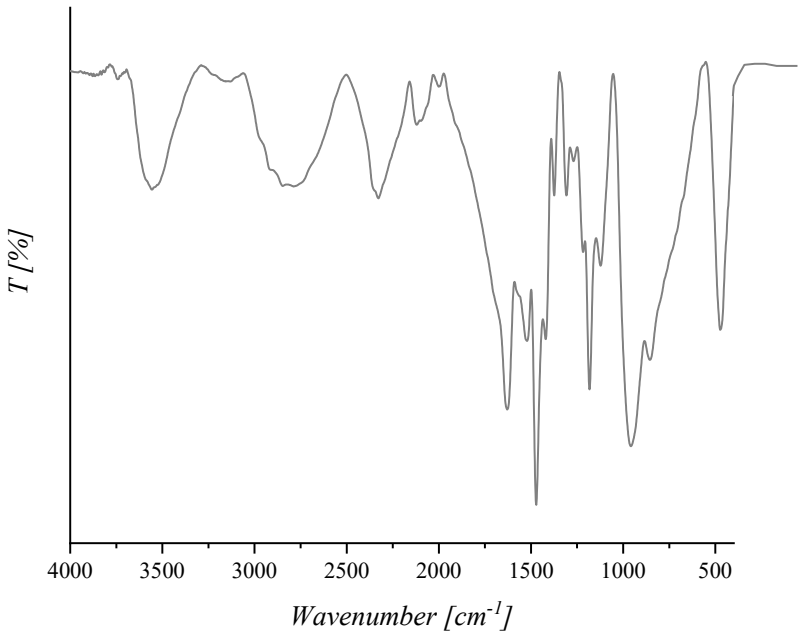

Figure C.1.3 – FTIR/ATR spectrum of the aPPO sample after the 85% wt. H_3PO_4 acid treatment for 2h.

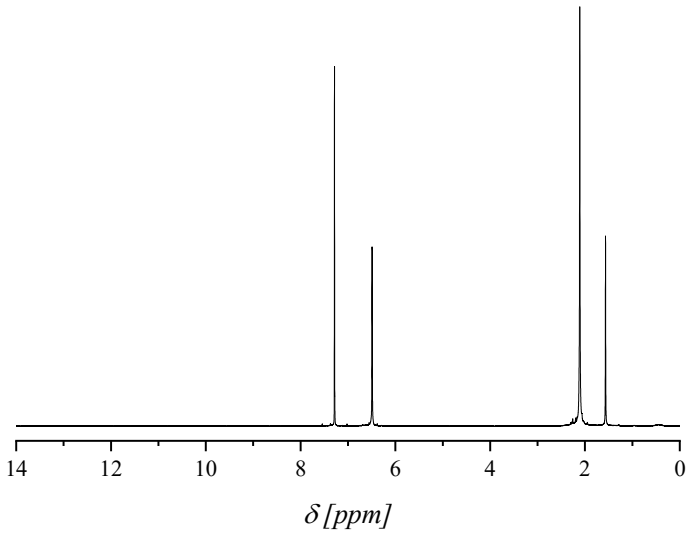

Figure C.1.4 – ^{1}H-NMR spectrum of PPO neat sample used as precursor for two-step amination, recorded by dissolving the polymer in $CDCl_3$.

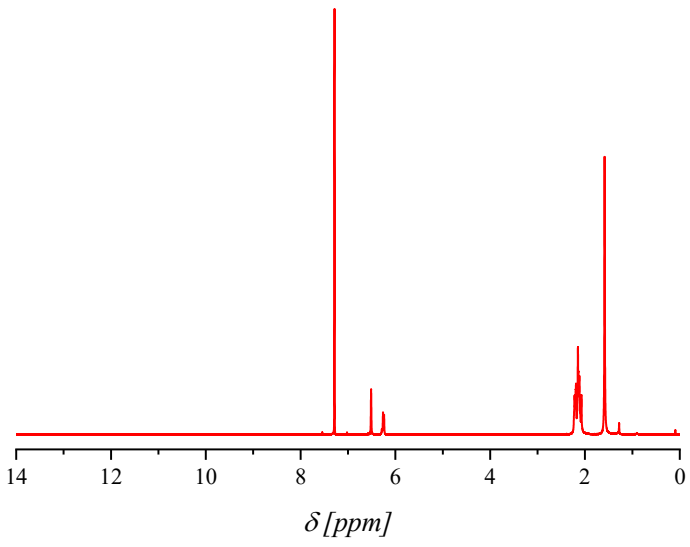

Figure C.1.5 – ^{1}H-NMR spectrum of PPO-NO_2 sample used as precursor for the amination reaction, recorded by dissolving the polymer in $CDCl_3$.

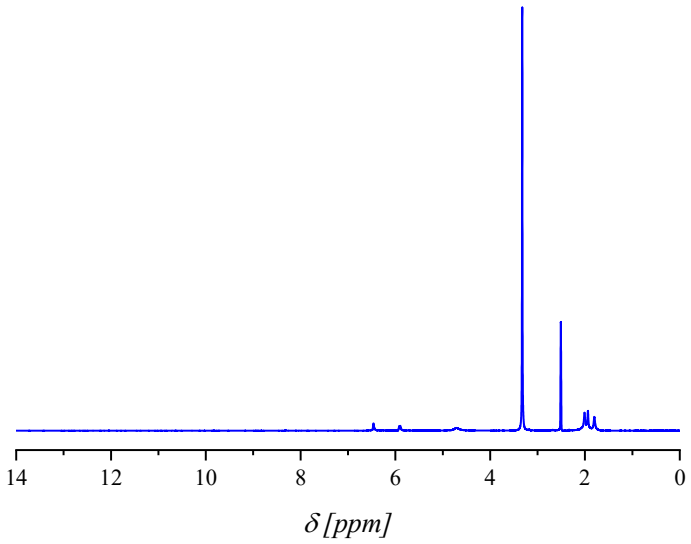

Figure C.1.6 – ^{1}H-NMR spectrum of aPPO-sample obtained from the amination reaction, recorded by dissolving the polymer in DMSO-d_6.

C.2 – Structural evaluation: XRD

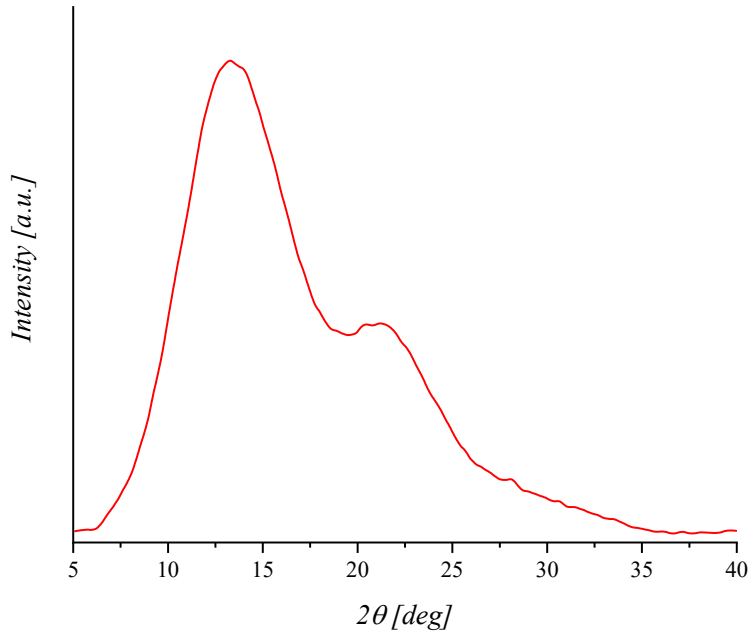

Figure C.2.1– XRD diffraction spectrum of the PPO-NO_2 sample recorded in the range of 5-40° 2θ using CuKα as the source.

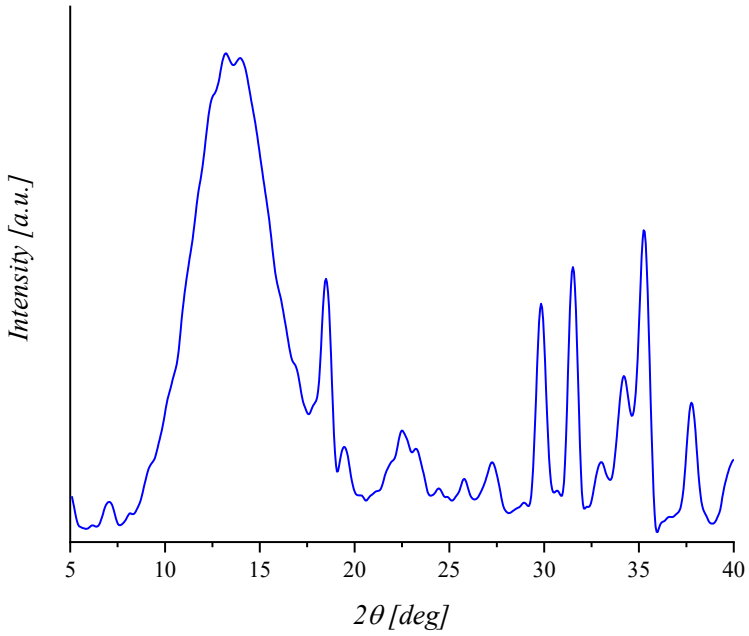

Figure C.2.2– XRD diffraction spectrum of the aPPO sample before the purification step, recorded in the range of 5-40° 2θ using CuKα as the source.

PUBLICATIONS

Emmanuel De Gregorio*, Giuseppina Roviello, Valentina Naticchioni, Viviana Cigolotti, Alfonso Pozio, Luis Alexander Hein, Carlo De Luca, Claudio Ferone, Antonio Rinaldi, Oreste Tarallo,* "Electrospun Polybenzimidazole Membranes: Fabrication and Fine-tuning through physical and statistical approaches". *Polymers,* 2025, 17(12), 1594. **10.3390/polym17121594.**

polymers

MDPI

Article

Electrospun Polybenzimidazole Membranes: Fabrication and Fine-Tuning Through Physical and Statistical Approaches

Emmanuel De Gregorio [1,2], Giuseppina Roviello [1], Valentina Naticchioni [2], Viviana Cigolotti [2], Alfonso Pozio [2], Luis Alexander Hein [3], Carlo De Luca [2,4], Claudio Ferone [1], Antonio Rinaldi [2,*] and Oreste Tarallo [4,*]

[1] Department of Engineering, University of Naples 'Parthenope', Centro Direzionale, Isola C4, 80143 Napoli, Italy; emmanuel.degregorio001@studenti.uniparthenope.it (E.D.G.); giuseppina.roviello@uniparthenope.it (G.R.); claudio.ferone@uniparthenope.it (C.F.)

[2] Department of Energy Technologies and Renewable Sources (TERIN), ENEA, Via Anguillarese 301, 00123 Rome, Italy; valentina.naticchioni@enea.it (V.N.); viviana.cigolotti@enea.it (V.C.); alfonso.pozio@enea.it (A.P.); carlo.deluca2@unina.it (C.D.L.)

[3] Nanofaber s.r.l., Via Anguillarese 301, 00123 Rome, Italy; luis.hein@nanofaber.com

[4] Department of Chemical Sciences, Università degli Studi di Napoli Federico II, Complesso Universitario di Monte Sant'Angelo, Via Cintia, 80126 Napoli, Italy

* Correspondence: antonio.rinaldi@enea.it (A.R.); oreste.tarallo@unina.it (O.T.)

Abstract: Polybenzimidazole (PBI), a high-performance polymer known for its exceptional thermal stability and chemical resistance, was processed by solution electrospinning to manufacture fibrous non-woven membranes. The process was repeated under different conditions by adjusting four main settings: the polymer solution concentration, the flow rate, the voltage applied between the needle and the collector, and the separating distance. To clarify the interplay between process parameters and material properties, a Design of Experiment (DOE) approach was used to systematically analyze the effects of said parameters on microstructural properties, including fiber diameter, porosity, and air permeability, pointing out that the increase in viscosity improves fiber uniformity, while optimizing the applied voltage and the needle–collector distance enhances jet stability and solvent evaporation, crucial for defect-free fibrous microstructures. Post-processing via calendering further refined the membrane texture and properties, for example by reducing porosity and air permeability without significantly altering the fibrous morphology, particularly at low lamination ratios. Thermal and mechanical evaluations highlighted that the obtained electrospun PBI membranes exhibited enhanced flexibility, but lower tensile strength compared to cast films due to the underlying open pore microstructure. This integrated approach—combining experimental characterization, DOE-guided optimization, and post-processing via calendering—provides a systematic framework for tailoring PBI membranes for specific applications, such as filtration, fuel cells, and molecular sieving. The findings highlight the potential of PBI-based electrospun membranes as versatile materials, offering high thermal stability, chemical resistance, and tunable properties, thereby establishing a foundation for further innovation in advanced polymeric membrane design and applications for energy and sustainability.

Keywords: polybenzimidazole membranes; electrospinning; Design of Experiment (DOE); analysis of variance (ANOVA)

Academic Editors: Chaocan Zhang and Lili Wu

Received: 8 May 2025
Revised: 29 May 2025
Accepted: 5 June 2025
Published: 6 June 2025

Citation: De Gregorio, E.; Roviello, G.; Naticchioni, V.; Cigolotti, V.; Pozio, A.; Hein, L.A.; De Luca, C.; Ferone, C.; Rinaldi, A.; Tarallo, O. Electrospun Polybenzimidazole Membranes: Fabrication and Fine-Tuning Through Physical and Statistical Approaches. *Polymers* **2025**, *17*, 1594. https://doi.org/10.3390/polym17121594

1. Introduction

Polybenzimidazoles represent a family of heterocyclic polymers characterized by a condensed aromatic structure and imidazole ring (Scheme 1), imparting them a basic character.

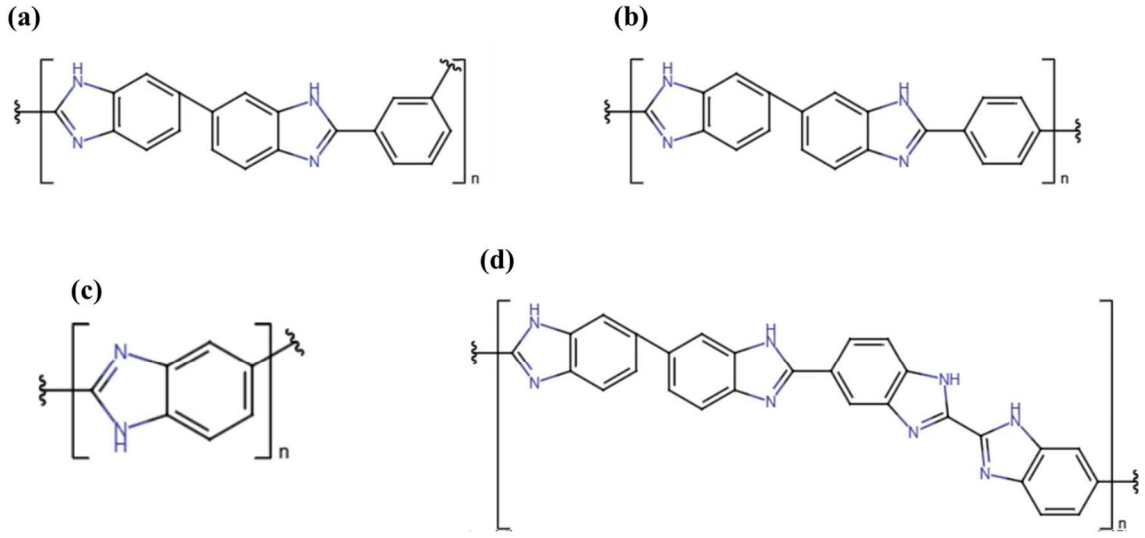

Scheme 1. Chemical structure of different polybenzimidazoles: (**a**) poly(2,2′-*m*-phenylene–5,5′-bibenzimidazole), (**b**) poly(2,2′-(*p*-phenylene)5,5′-bibenzimidazole), (**c**) poly(2,5-benzimidazole), and (**d**) isomeric-Poly(2,5-benzimidazole).

Among these, the acronym PBI typically refers to the only commercially available polybenzimidazole polymer: poly [2,2′-(*m*-phenylene)–5,5′-bibenzimidazole] (also indicated as *m*-PBI, Figure 1). PBI is a polymer with remarkable thermal, chemical and mechanical properties. It has a T_g of 425 °C and a decomposition temperature > 600 °C [1]. The synthesis reaction for this material was developed in the 1960s [2] and consists of a condensation polymerization process between 3,3′-diaminobenzidine and terephthalic acid (Figure 1). Generally, the PBI is insoluble or poorly soluble in almost all major organic solvents but, depending on the nature of the starting dicarboxylic acid (DCAs), it exhibits good solubility in high-boiling polar aprotic solvents such as N,N-dimethylacetamide (DMAc), dimethyl sulfoxide (DMSO) and N-methyl–2-pyrrolidone (NMP) [3]. Furthermore, the addition of heteroatoms in the polymer backbone (principally oxygen and nitrogen) significantly increases the solubility of PBI even in low-boiling and polar solvents [4] such as formic acid (FA) [5].

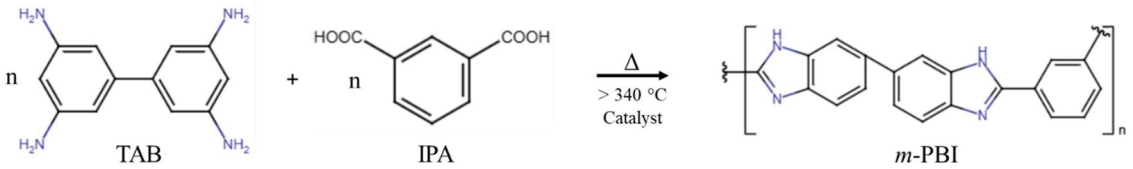

Figure 1. *m*-PBI synthesis route (TAB: tetraaminobiphenyl; IPA: isophthalic acid): the reaction is typically conducted in polyphosphoric acid (PPA), which acts both as a dehydrating agent and as a catalyst. The mixture is heated in stages—initially to approximately 200 °C to promote the formation of imidazole oligomers, and then to temperatures above 300 °C to complete cyclization and enable polymer chain growth.

Over the past decade, PBI has been widely studied and used due to its ability to interact with strong acids due to the presence of the nitrogen groups present in imidazole. For this reason, PBI membranes are generally 'doped', i.e., loaded with organic [6] and/or inorganic fillers [7] such as graphene oxide or silicon dioxide [8]. Due to its excellent chemical stability, mechanical strength, thermal stability, durability and low cost, PBI is used in the form of membranes for various purposes, especially at high temperatures and in aggressive environments. Furthermore, due to the close packing of the polymer chains deriving from the rigidity of the molecular structure and the strong hydrogen bonding between them, PBI membranes are characterized by very low gas permeability [9]. PBI can be used for different types of applications: (a) CO_2 capture, due to its basic structure that promotes interactions with Lewis acids, even under anhydrous conditions [10]; (b) high-temperature fuel cells (HTPEMFCs), thanks to the fact that the impregnation of PBI with phosphoric acid (PA) makes the material ductile and highly conductive, even at temperatures above 100 °C and thus in the absence of water [11]; (c) electrodialysis, thanks to the promising transport rates for HCl, H_2SO_4 and HNO_3 [12]; (d) osmosis, thanks to excellent chemical and mechanical stability even in harsh conditions [13].

Several techniques for manufacturing PBI membranes have been developed to date, such as blade casting and sol–gel [14]. Prominent among these is electrospinning, which is an advanced nanofiber production technique that can be used to produce polymeric membranes [15]. The main electrospinning advantage lies in the production of materials with a fibrous morphology, characterized by a high surface area-to-volume ratio and a reduced thickness (typically < 10 μm) [16]. In addition, physical parameters such as the porosity of the mat and average fiber diameter can be controlled depending on the characteristics of the capture or adsorption system and production requirements [17]. This morphology also results in improved mechanical properties of the material, as the fibrous structure with aligned and/or interconnected fibers provides high tensile strength and good flexibility, ensuring the integrity of the membrane during operation [18]. The formation of a fibrous matrix is strongly dependent on process parameters such as flow rate, ejector and collector voltages and needle–collector distance, but is also a function of the polymer–solvent pair and the environmental conditions of temperature and humidity [19].

As the electrospinning technique is rather complex and capable of generating a variety of porous structures, heuristic approaches based on statistical methods can be convenient and effective to optimize the microstructural parameters of the material such as porosity, gas permeability and the distribution of the mean diameter of the fiber affecting the impregnation capacity of the scaffold [20,21]. Statistical Design of Experiments (DOE) can be effectively used for this aim, to determine whether fine-tuning (input) process parameters allows the electrospinning process to produce (output) membranes that better suit a given application. On the other hand, the materials obtained by electrospinning can also be modified by post-processing physical treatments. One of these is calendering, representing a simple route for optimizing electrospun membranes by a thermo-mechanical treatment [22]. For example, this procedure allows fine-tuning of the morphological characteristics and porosity of membranes, crucial in sectors such as separation, filtration and adsorption.

This work aims to identify a robust set of process conditions for achieving PBI fibrous membranes using solution electrospinning and to illustrate the main effects and interactions of process parameters on the morphology of the resulting membrane. Furthermore, we discuss the possibility of fine-tuning the electrospinning process to produce PBI scaffolds for various engineering applications, ranging from filtration to batteries and/or fuel cell membranes.

2. Materials and Methods

2.1 Electrospinning of PBI and Design of Experiments

PBI solution (S26, PBI Product©, Charlotte, NC, USA, M_w = 28 kDa), with a viscosity of 2100 ± 200 Poise containing 26 %wt. of PBI in dimethylacetamide (DMAc, ≥99%, Sigma Aldrich, Burlington, MA, USA) and LiCl (4%wt.), was used for the preparation of electrospun membranes. Several PBI solutions have been prepared at different concentrations by dilution in further DMAc. The electrospun fibers were manufactured with a pilot-scale electrospinning station (Fluidnatek LE100, Bioinicia SL, Valencia, Spain) equipped with a stationary planar collector (x-y plane) measuring 40 cm × 40 cm (approximately A6 sheet format) and with an environmental chamber capable of controlling temperature with an accuracy of 1 degree and humidity with a maximum error of 5%. Initial trials at 15 %wt were run to find the environmental and process settings (Table 1) that yield a clear fibrous structure. Analysis showed that fiber shape depends strongly on temperature and humidity, and that stable flow appears only at high enough voltages and flow rates (see entry PBI_15_d, Table 1). Using these promising conditions as a starting point, we fixed temperature, humidity and collector voltage and set up a 2^k factorial design with k = 4. Spinning solutions at 14 and 16 %wt were also prepared to refine the process. Each solution was mixed in a vortex for 20 min and then stirred for 24 h at room temperature to ensure complete homogeneity. During electrospinning, we adjusted the flow rate and spinning area so every sample had a uniform thickness.

Table 1. Electrospinning parameters for PBI trial samples: temperature, relative humidity, ejector and collector voltages, needle–collector distance, and solution flow rate.

Sample	Temperature [°C]	Relative Humidity [%]	V Ejector [kV]	V Collector [kV]	Needle–Collector distance [mm]	Flow Rate [ml/h]
PBI_15_A	25	40	20	−20	125	5
PBI_15_B	35	25	20	−20	125	0.4
PBI_15_C	40	25	20	−20	125	1
PBI_15_D	45	20	20	−20	125	1

For each process parameter—polymer solution concentration, ejector voltage, flow rate, and needle–collector distance—two levels were chosen, yielding 17 experiments in total (see Table 2).

Table 2. Electrospinning conditions obtained by perturbing the initial trials set according to a 2^4 factorial scheme.

Sample	Flow Rate [mL/h]	V Ejector [kV]	Height [mm]	Concentration [%wt.]	Temperature [°C]	Humidity [%]	V Collector [kV]
PBI_E01	1	17	135	14	45	20	−20
PBI_E02	2	17	135	14	45	20	−20
PBI_E03	1	20	135	14	45	20	−20
PBI_E04	2	20	135	14	45	20	−20
PBI_E05	1	17	115	14	45	20	−20
PBI_E06	2	17	115	14	45	20	−20
PBI_E07	1	20	115	14	45	20	−20
PBI_E08	2	20	115	14	45	20	−20
PBI_E09	1	17	135	16	45	20	−20
PBI_E10	2	17	135	16	45	20	−20
PBI_E11	1	20	135	16	45	20	−20
PBI_E12	2	20	135	16	45	20	−20

Design of Experiment (DOE) is a systematic method to determine the relationship between factors affecting a process and the output of that process. Regression models play a crucial role in DOE analysis as they help quantify the effects of different factors and their interactions on the response variable. Linear regression models describe the dependence of each output variable (Y) on the process variables (X). The general form of the regression model is described by the following equation (Equation (1)) in the case of four regressors:

$$Y = \beta_0 + \beta_i X_i + \beta_{ij} X_i X_j + \beta_{ijk} X_i X_j X_k + \beta_{ijkm} X_i X_j X_k X_m \rightarrow (i, j, k, m = 1 \text{ to } 4) \quad (1)$$

The primary objective of this approach is to identify the optimal descriptive model using a limited number of parameters and experiments, which can be directly and reproducibly applied to produce materials with desired chemical–physical properties, in accordance with the employment application. The electrospinning process is strongly influenced by the operating conditions used (X_i), which in turn have a significant impact on the chemical–physical properties of the membranes obtained (Y_i). As described above, a 16 %wt. PBI solution in DMAc was prepared and kept stirring for 24 h at room conditions to ensure complete and homogeneous dissolution. Each membrane was obtained from a specific combination of X_i parameters, which were implemented to produce a combinatorial full-factorial 2^4 approach from Design of Experiment (DOE) that aimed to examine the influence of 4 process parameters shown in Table 3 on the microstructural properties of the membranes described in Table 4.

Table 3. Input factors (X_i) related to the electrospinning process of PBI solutions.

Parameter	Label	Unit	Low Level (–1)	High Level (+1)	Average Level (0)
Flow rate	X_1	mL/h	1	2	1.5
Ejector voltage	X_2	kV	17	20	18.5
Needle–collector distance	X_3	mm	115	135	125
PBI-solution concentration	X_4	%wt.	14	16	15

Table 4. Output responses (Y_i) relating to the microstructural properties of electrospun PBI membranes.

Parameter	Label	Unit
Mean Fibre Diameter (FD)	Y_1	nm
FD Dev. St.	Y_2	nm
Air Permeability	Y_3	cm/s
Porosity	Y_4	%
Beads	Y_5	%

The parameters shown in Table 2 are coded using '+1', '−1' and '0' to identify the highest, lowest and intermediate level of each factor: the model employs coded variables "X_j^*", derived from the natural variables through linear transformations, as described in the formula (Equation (2)) where "HIGH" and "LOW" correspond to the maximum and minimum ranges as indicated previously. To minimize the impact of uncontrolled ambient variables, the order of treatments in Table 2 was randomized during the experiment.

$$X_j^* = \frac{x_i - \bar{x}_i}{(x_{HIGH} - x_{LOW})/2} \quad \text{(j from 1 to 4)} \tag{2}$$

By using coded variables, it is possible to standardize the range and scale for each parameter, which simplifies the comparison of their individual effects on the outcome [23]. This approach also supports the creation of an orthogonal design, ensuring that each factor can be estimated independently without interference from the others [22]. As a result, these coded variables play a critical role in the regression model by enabling the straightforward and immediate identification of significant terms. *p*-values are then used to assess whether the influence of each coded variable or their interactions is statistically significant. Specifically, if a coded variable yields a *p*-value below a set threshold (such as 0.05 or 0.10), it indicates that the factor has a meaningful impact on the response. Conversely, higher *p*-values imply that the factor's effect might be negligible, warranting its removal from the model to streamline the analysis. By leveraging *p*-values to fine-tune the model, one can achieve a more parsimonious model that still effectively accounts for the variability in the response variable [21]. The ANOVA analysis for the subsequent models was carried out using JMP Pro software (version 17, SAS Institute, Cary, NC, USA) with a 10% significance level, thereby facilitating a clear distinction between significant and non-significant terms. To evaluate the quality of the experimental design derived from the ANOVA, the coefficient of determination (R^2) is employed as the primary indicator of fit quality, reflecting the proportion of variance explained by the model. However, because R^2 typically increases with the addition of more parameters, it is also essential to consider the adjusted R^2 (R^2_{adj}) (see Equation (3)).

$$R^2_{adj} = 1 - (1 - R^2)\frac{p}{n-p-1} \tag{3}$$

The value is consistently lower than R^2 and is determined by the ratio of the number of predictors (p) to the number of data points (n) [21].

2.1 Sample Characterization

2.2.1 Scanning Electron Microscopy (SEM) Evaluation: Morphological Characterization and Fiber Analysis

The morphology of the electrospun samples was examined using the Scanning Electron Microscopy technique. SEM analysis was carried out using a Nova Nanosem 450 (FEI, Austin, TX, USA) on the pristine PBI-based scaffolds, metallized with Pd/Au. The acceleration potential used for image acquisition is in the 2–5 kV range. The fiber diameter and the distribution of the beads were measured with ImageJ software (version 1.54, Rasband, W.S., Image J, U.S. Nation Institute of Health, Bethesda, MD, USA). The fiber diameter mean values (MFD) and root mean square errors (RMS) distributions were obtained by analyzing at least 50 random spots over at least three different micrographs for each sample (5000× magnification).

2.2.2 Porosity and Air Permeability

The porosity of the electrospun materials was determined gravimetrically on membranes with dimensions 2 × 2 cm² using the liquid displacement technique [24] in ethanol (Sigma Aldrich, 99% anhydrous), which was chosen because it permeates through the membrane without generating interactions or swelling. The percentage porosity ($\varepsilon_{\%}$) was calculated from the following equation (Equation (4)):

$$\varepsilon\% = \frac{(m_3 - m_4 - m_1)}{(m_2 - m_4)} \cdot 100 \tag{4}$$

where m_1 refers to the mass of the dry membrane as such, m_2 refers to the mass of a graduated flask containing ethanol, m_3 is the mass of the same system containing the PBI

membrane to which the excess ethanol due to the displaced excess volume caused by the presence of the membranes has been carefully removed, m_4 is the mass of the graduated system without the membrane. The determination of air permeability for PBI-based electrospun membranes was conducted using a Gurley densimeter (Model 4320, Troy, NY, USA). All electrospun samples were cut into 2 × 2 cm^2 to ensure the passage of a volume (V) of air equal to 100 cm^3 through the required active area (A) of 1.58 cm^2 at a time (t). Permeability (P) was calculated for each sample from Equation (5) and is expressed in cm/s:

$$P = \frac{V}{A \cdot t} \quad (5)$$

2.2.3 X-Ray Diffraction

The study of the PBI electrospun membrane structure was carried out through a Wide-Angle X-ray Diffraction (WAXD) technique using the Malvern Panalytical (Mal- vern, Worcestershire, UK) Empyrean multipurpose diffractometer using Cu Kα (λ = 1.5418 Å) by using a continuous scan of the diffraction angle 2θ from 5–40° with a scan rate of 0.05°/s.

2.2.4 Attenuated Total Reflectance Fourier-Transform Infrared Spectroscopy (ATR-FTIR)

The pristine electrospun PBI-based membrane was characterized through ATR-FTIR Spectroscopy. This analysis was performed using an Anton Paar (Rivoli, Italy) Lyza 7000. The scans were recorded using a diamond crystal cell through 36 scans at a resolution of 4 cm^{-1}. The sample was cut into 1 × 1 cm^2 by applying the required torque to keep in contact the membrane with the crystal.

2.2.5 Thermogravimetric Analysis (TGA)

The thermal degradation of PBI-based electrospun membranes was evaluated using the TA Instrument (Sesto San Giovanni, Italy)—SDT650. Approximately 8–10 mg of sample were placed in an alumina crucible and tested under a N_2 atmosphere (20 mL/min) with a heating rate of 10 °C/min up to a temperature of 800 °C.

2.2.6 Mechanical Tests

Mechanical properties were performed at room temperature by using the Instron (Norwood, MA, USA) 5566H1543 machine to determine the tensile strength, Young's modulus and the elongation at break according to standard ASTM D638 [25]. The dimensions of the testing samples were 100 mm × 10 mm, and the thickness of the samples was 100 μm. The deformation speed was adjusted to 10 times the initial gauge length (L_0) per minute, resulting in a strain rate of v = 10 min^{-1} for measuring the stress–strain curves and subsequently determining the tensile parameters up to failure. For the assessment of Young's moduli, the speed was set to 0.1×L_0 per minute, corresponding to v = 0.1 min^{-1}.

2.3 Calendering

The calendering process involves the use of heated rollers to compress and flatten the membranes, enhancing their mechanical properties and surface characteristics. The thickness of the as-spun polybenzimidazole membrane was first mapped on 50 different spots to identify an initial average thickness (IT) with a digital micrometer. Then, the material was placed between two (near incompressible compared to the electrospun membrane) Mylar supports and subjected to calendering using a Hot Roller Press Machine (model 200L, by TOB Machine, Xiamen City, Fujian Province, China). The distance between the two pressing rollers was set as a function of the initial thickness of the electrospun

membrane by defining a "lamination ratio" (LR), which represents the ratio between the initial membrane thickness and the nominal target value (FT). LR = 2 and 3 were applied to the as-spun membranes in order to verify the effect of the treatment on air permeation rate and porosity.

3.Results

3.1 Electrospinning Process: Morphological Study

The variation in electrospinning parameters is crucial due to their precise correlation with the chemical, physical, and morphological properties of the electrospun membrane. Specifically, the influence of different electrospinning parameters on the morphology of the samples was investigated by analyzing their surfaces using SEM microscopy. The micrographs shown in Figure 2 refer to preliminary electrospinning tests conducted on a 15%wt. PBI solution in DMAc. Moving from micrograph A to D, the effect of temperature and humidity in the electrospinning chamber on the final material morphology becomes evident, with the formation of interconnected fibers interspersed with dense regions. In particular, under standard room conditions (Figure 2, sample A), the whipping motion required to form fibers is not achieved. Instead, the sample exhibits a dense morphology interconnected with small fibrous spots and defects (beads) across its surface. This is likely due to the high flow rate, which reduces the charge density at the ejector, preventing the formation of a continuous polymer jet. It is well known that increasing the feed rate decreases the charge density, while higher charge density induces jet bending instabilities, leading to the formation of thinner fibers [26]. Additionally, a high feed rate hinders the complete evaporation of solvent molecules, resulting in the presence of beads. However, by modifying the temperature, and relative humidity, and reducing the flow rate (as detailed in Table 1), the development of a fibrous structure becomes more pronounced, as seen in micrograph B of Figure 2. Adjustments to temperature and humidity significantly improved the sample morphology, producing well-interconnected fibrous regions deposited on a dense matrix. Despite these improvements, the samples still display bead-like spots, as observed in conditions C and D (Figure 2C and D, respectively).

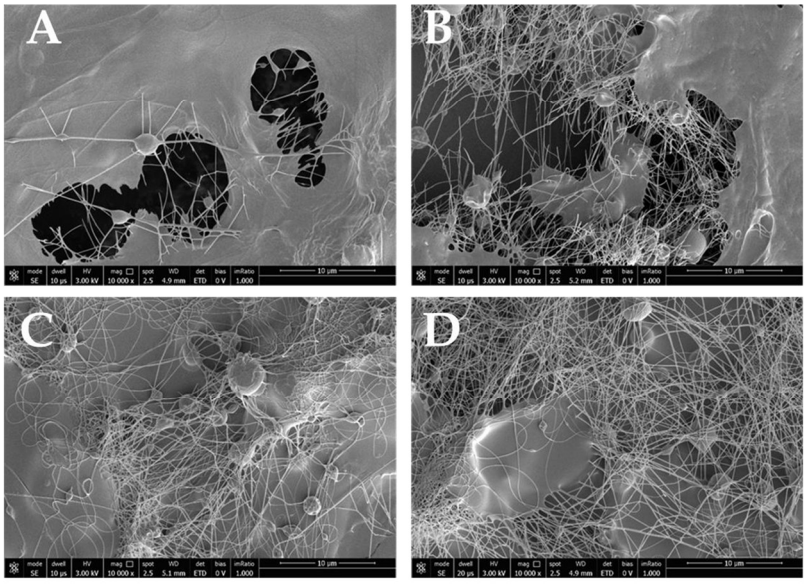

Figure 2. SEM micrographs at 10,000× magnification of preliminary sample mats produced using a 15 %wt PBI solution in DMAc. Sample obtained at 25°C and 40% RH (**A**), at 35°C and 25% RH (**B**), at 40°C and 25% RH (**C**), and at 45°C and 20% RH (**D**).

As expected, the SEM micrographs from the preliminary sample tests demonstrate that variations in electrospinning parameters are crucial in the formation of the fibrous structure. Consequently, electrospinning production run were conducted using a Design of Experiments (DOE) approach to systematically and efficiently plan experiments, enabling the correlation of experimental outcomes with specific electrospinning parameters. These parameters, selected from a range tested at a 15%wt. polymer solution concentration, included ejector voltage, needle–collector distance, and flow rate, as outlined in Table 1. Also in these cases, SEM micrographs were analyzed to evaluate the impact of each individual process parameter, aiming to establish a morphological correlation across the samples. In the following paragraphs, the morphology of selected samples obtained by this approach have been discussed.

3.1.1 Effects of Voltage and Collector Distance

The effects of voltage and collector distance were studied by the 14 %wt. samples characterization. Figure S1 shows SEM micrographs of the 14%wt. samples obtained at a flow rate of 1 mL/h but at different ejector voltages and different needle–collector distances (see Table 1 for experimental conditions). The pictures show a different situation: samples PBI_E01 and PBI_E05 were obtained at the same voltage (V = 17 kV) but at different needle–collector distances (135 and 115 mm, respectively). The micrographs suggest that the decrease in distance, at the same voltage and flow rate, does not guarantee the continuity of the polymer jet likely due to a repulsion phenomenon between the charged particles, as shown by the sample PBI_E05. In fact, on the other hand, by increasing the distance (e.g., PBI_E01), the sample structure appears quite different, with a well-defined and rather uniform morphology, which is much better than the PBI_E05 sample. This comparison highlights the high influence of the distance parameter in the electrospinning process of PBI that can modify all the properties of the resulting material.

In addition, also voltages and the flow rate show a high impact on the sample quality. For example, the excessive voltage (20 kV) in the PBI_E03 resulted in a sample with a not well-defined fibrous morphology that is full of defects. While high voltage promotes rapid solvent evaporation, the short distance might not provide sufficient time for complete evaporation. The combination of high voltage and low needle–collector distance did not allow the jet to solidify properly, resulting in a dense and non-uniform structure, as is evident in PBI_E07. In this last situation, it is clear that the polymer solution had no time to allow the solvent to evaporate completely, leading to wet fibers that during their solidification process, generated a densified microstructure, not fully fibrous. This supports the earlier statement that high applied voltages worsen the overall sample quality by degrading microstructural morphology and causing fiber coalescence.

Figure S2 shows the micrographs of the 14%wt. electrospun samples that were obtained at a constant flow rate of 2 mL/h but at different voltages and needle–collector distances. The increase in flow rate makes it possible to obtain materials characterized by an interconnected fibrous morphology with the presence of beads and small dense areas, randomly distributed. Only the PBI_E08 sample shows a different behavior: working at a shorter distance (115 mm) from the collector, it is more affected by the ejector voltage. The discovery of dense structures that were not electrospun correctly confirmed the previous claim. In particular, the electric field strength between the needle and the collector is greater with a shorter distance, which can lead to instability in the jet. Moreover, the shorter distance can lead to needle clogging, especially if the polymer solution is not properly atomized and stretched. The result is the formation of unspun in-desiderate dense structures, as described for the previous samples with the same structured materials.

3.1.2 Effects of Viscosity and Interactions with the Other Parameters

The increase in concentration (16 %wt.) resulted in a remarkable improvement in the final morphology of the samples. In particular, the polymeric solution has a higher viscosity than the materials synthesized and shown before (14 %wt.). It is already known that viscosity is a critical parameter in electrospinning because it can reduce the occurrence of bead defects in the fibers, producing smoother and more uniform samples [27]. In addition, higher viscosity helps stabilize the jet, reducing the chances of jet breakup and resulting in more consistent fiber diameters [28]. In particular, micrographs of the samples obtained at a constant flow rate of 1 mL/h can be seen in Figure S3. It is worth pointing out that both the voltages used, and the needle–collector distances allow the obtainment of homogeneous materials with good fibrous distribution. Sample PBI_E015, therefore, shows a large fibrous spot probably due to a sudden interruption of the flow during the electrospinning process that leads to a beads-like structure over the surface.

By increasing the flow rate (2 mL/h) it is possible to obtain materials with different morphology (Figure S4) and, at the same time, to understand the influence of the various process parameters. For example, the PBI_E10 sample shows a surface characterized by large, non-fibrous spots randomly interconnected by non-continuous fibers of irregular thickness. This can likely be attributed to the lower applied voltage, which allows for a larger needle–collector distance. The combination of low voltage and high distance results in significantly reduced electric field strength, which may cause difficulties in initiating and sustaining a stable jet stream. In support of this thesis, the PBI_E12 sample obtained at the same needle–collector distance but at a higher applied voltage shows a uniform and completely fibrous morphology, without any beads or narrow fibers defects as reported in Figure 3. The decrease in distance (115 mm) slightly affects the subsequent samples PBI_E014 and PBI_E016, which show a good fibrous surface but the presence of random beads and dense spots due to an incorrect ejection of the polymer solution.

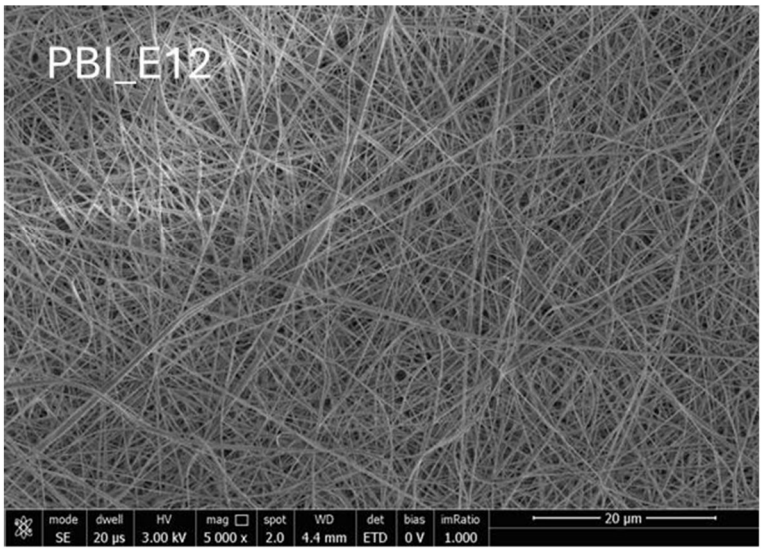

Figure 3. SEM micrograph of PBI_E12, produced from a 16 %wt PBI solution using a flow rate of 2 mL/h, 20 kV at the ejector, and a needle–collector distance of 135 mm. This sample was chosen as the best from the experimental campaign and was used for all subsequent chemical, physical, and mechanical characterizations.

The last sample analyzed in Figure S5, PBI_E17, was obtained under average electrospinning conditions in respect to the values used for all other samples, working with a

15%wt. solution. The material is characterized by the presence of fibers spaced with dense dots greater than 1 μm in diameter that cover the entire surface of the sample. The lower viscosity of the sample and the use of a relatively high flow rate do not allow the formation of a continuous and stable jet, able to guarantee the correct evaporation of the solvent during the time of flight and, therefore, the formation of the fibers. The DOE model can be improved by incorporating intermediate tests, which is an effective strategy to improve the quality and reliability of experimental results. It helps not only to validate and optimize the model but also to ensure that the conclusions drawn are robust and well founded.

3.2 Fiber Diameter Distribution, Porosity and Air Permeability

In electrospun membranes, the relationships between fiber diameter, porosity and air permeability are interdependent [27]. These properties are crucial for the performance of the membrane in various applications such as filtration, sensors, and tissue engineering. The increase in fiber diameter leads to a reduction in the space between the fibers, in turn leading to a decrease in the overall porosity and permeation properties of the membrane [16,27]. The average values of these parameters are reported in Table 5. Figure 4 shows how the increase in concentration of the PBI solution (from 14 %wt. to 16 %wt.) leads to a decrease in porosity (Figure 4a) and air permeability (Figure 4b) with an overall increase in fiber diameter. The increase in fiber diameter is accompanied by a decrease in porosity that indicates a balance between the viscoelastic forces of the polymer and the physical structure of the fiber; at higher concentrations, the solution becomes more viscous, which may affect the polymer's ability to "stretch" or "elongate" during the fiber formation process [29,30]. As expected, increasing the polymer concentration results in a higher viscosity of the electrospinning solution. This reduces the stretching of the jet under the electric field, producing fibers with larger diameters. Since the mass flow rate remains constant, fewer but thicker fibers are deposited. As a result, the total void volume (i.e., porosity) stays nearly unchanged: although the pores become slightly larger, they are fewer in number. This compensating effect maintains a similar overall porosity and air permeability, despite differences in fiber diameter and morphology.

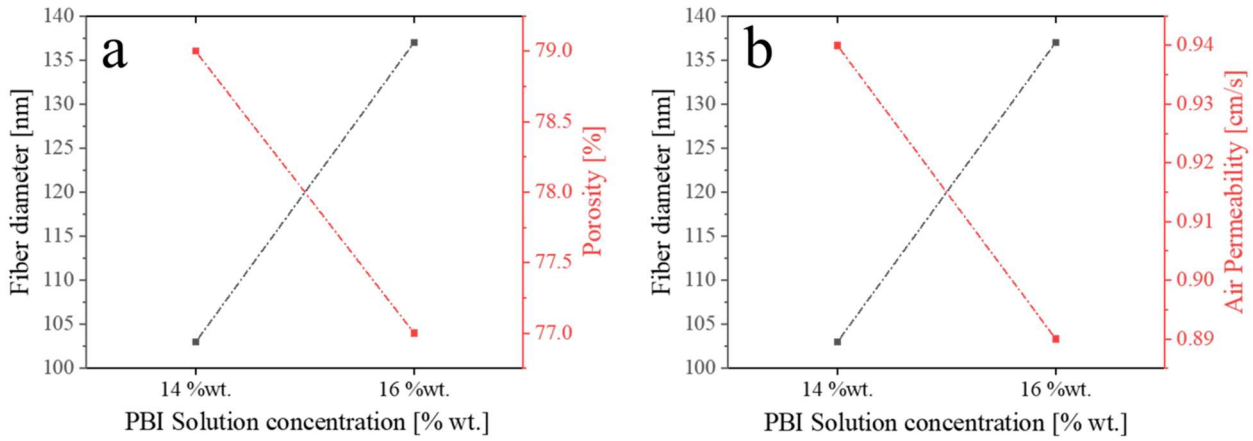

Figure 4. Variation in porosity (**a**) and air permeability (**b**) with the concentration of the PBI solution. Reported data points are obtained as the average of multiple measurements performed on each of the samples studied (see Table 5). Dashed lines are a guide for the eye.

Table 5. Average values of microstructural parameters due to increasing polymer solution concentration in PBI.

PBI Solution Concentration [%wt.]	Mean Fiber Diameter [nm]	Air Permeability [cm/s]	Porosity [%]
14	103 ± 25	0.9 ± 0.5	79 ± 5
16	137 ± 30	0.9 ± 0.4	77 ± 8

3.3 Structural Characterization: WAXD, TGA and ATR-FTIR

The PBI electrospun membrane exhibits, as expected, an essentially amorphous structure, as shown by the WAXD diffraction spectrum in Figure 5. In particular, the sample shows a diffuse amorphous halo centered approximately 2θ~20° with the absence of any sharp peaks, as occurs in the polybenzimidazole film obtained by solution casting [31,32].

FTIR spectra performed in ATR (Figure 6) display characteristic peaks related to aromatic C-H bending out-of-plane vibration (801 cm^{-1}) and stretching vibrations due to imidazole's C-N bond (1280 cm^{-1}). The peaks in the range 1442–1638 cm^{-1} refer to the stretching of the C=N and C=C bonds while the signal at approximately 3200 cm^{-1} is attributable to the OH bond due to moisture as the material is slightly hydrophilic. The N-H functional group related to imidazole is indicated in the peak at 3400 cm^{-1}.

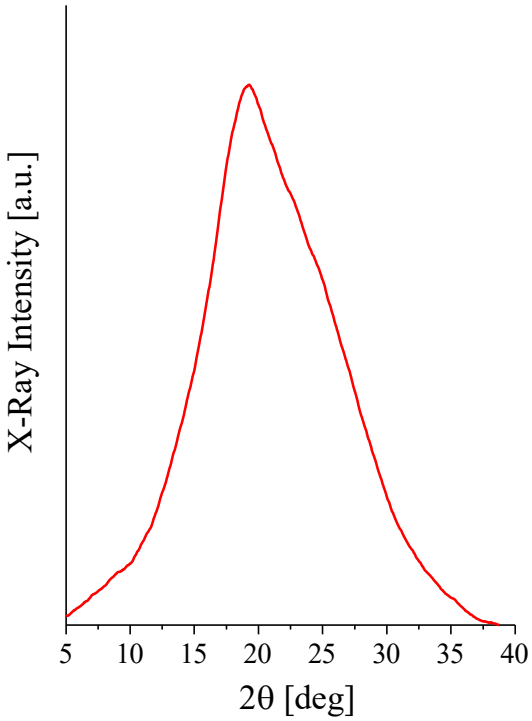

Figure 5. XRD pattern of PBI-based electrospun membrane. The pattern typically shows a broad diffraction peak, indicating a predominantly amorphous structure. This is consistent with the nature of electrospun polymer mats, where rapid solvent evaporation and fiber formation lead to less organized molecular packing. The presence of a broad peaks approximately 20–25° 2θ can be attributed to short-range ordering of the polymer chains [33].

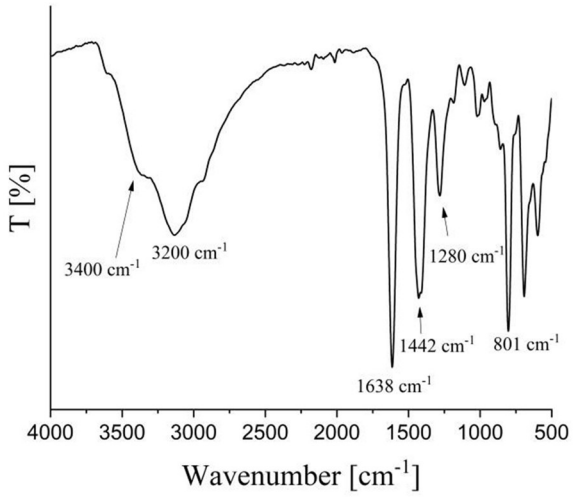

Figure 6. FTIR analysis of PBI electrospun membrane. Characteristic absorption bands are observed at approximately 3400 cm^{-1}, corresponding to N-H stretching vibrations, indicating the presence of imidazole groups. Peaks near 1640 cm^{-1} and 1440 cm^{-1} are assigned to C=N and C=C stretching vibrations within the benzimidazole rings. The absence of significant peaks related to solvent residues (approximately 1650–1690 cm^{-1} and corresponding to carbonyl (C=O) stretching vibration) confirms effective removal of solvents during electrospinning.

The thermogram in Figure 7 shows a 3-stage decomposition, typical for polybenzimidazoles [34]. The first weight loss (region I) of about 17 %wt. is associated with moisture and minor solvent residue, up to a temperature of about 130 °C. In the 150–450 °C range (region II), there is a further overall loss of 7 %wt. due to further solvent residues and deterioration of the N-H and N=C functional groups of the imidazole group of PBI. Finally, in the third stage of decomposition (region III), the polymer backbone is degraded up to a temperature of 800 °C with a residual of 40%.

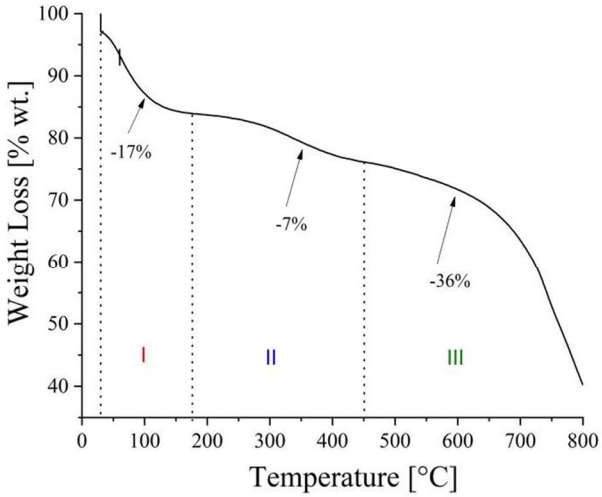

Figure 7. Thermogravimetric analysis of PBI-based electrospun membrane. A three-stage decomposition is apparent: region I, with a 17% weight loss, corresponds to moisture removal; region II, with an

additional 7% weight loss, is due to minor residual solvents and degradation of N-H and N=C functional groups; region III, with a 40% weight loss, reflects the breakdown of the polymer backbone.

3.4 Mechanical Test

From a mechanical point of view, the material shows a specific stress–strain curve (Figure 8). The PBI produced by the electrospun process exhibits unique mechanical properties due to the nanoscale fibrous structure. The curves describe a sufficiently ductile material with an initial linear stretch in which the membrane behaves elastically. The slope of this region is defined by Young's modulus which has a value of 100 ± 20 MPa that is quite low compared to the PBI casting membrane (Table 6). Likewise, the tensile strength is 4 ± 0.3 MPa which is a low value that indicates that this particular morphology strongly influences the mechanical behavior of PBI membranes leading to a decrease in stiffness. The elongation at break is also lower, 12 % ± 1, and this is surely due to the porous nature of the sample. It is well known that porous materials generally exhibit lower strength compared to their non-porous counterparts [31,35]. This is a result of pores acting as stress concentrators, resulting in localized high-stress areas that can lead to cracks and failure at lower loads. In addition, the presence of pores reduces the effective cross-sectional area that can carry a load, making the material less ductile. It is worth pointing out that the mechanical properties of PBI electrospun membranes are strongly dependent on their intrinsic morphology: fiber diameter and their spatial arrangement are fundamental parameters for the material mechanical improvement as they allow the applied load to be distributed along the alignment direction, improving load transfer between the fibers.

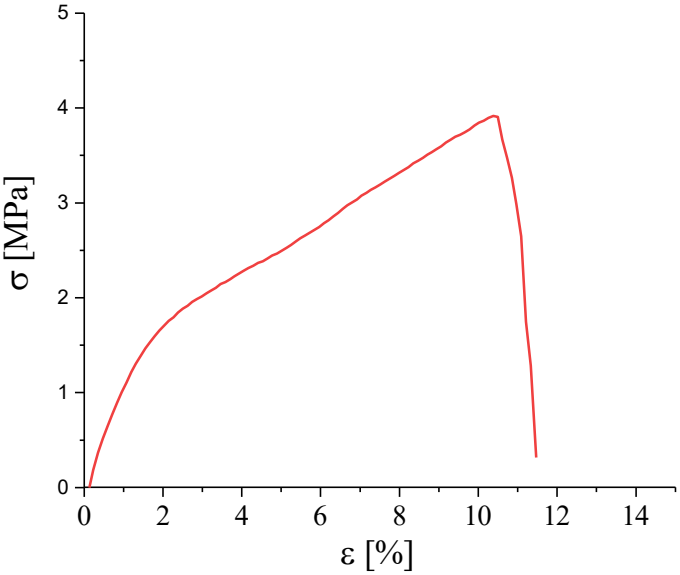

Figure 8. Stress–strain curves of PBI_E12 sample: the red curve is representative of an average value of the mechanical parameters.

Table 6. Mechanical properties of PBI by casting and electrospinning.

Sample	Young's Module [GPa]	Tensile Strength [MPa]	Elongation at Break [%]
PBI Cast Film	5.9 ± 1 [36]	120 ± 16 MPa [36]	10 ± 2 [32]
PBI_E12	0.1 ± 0.02	4 ± 0.3 MPa	10 ± 2

3.5 PBI-Based Electrospun Fine-Tuning

As previously mentioned, PBI is employed in a wide range of applications, from producing aerospace suits to capturing pollutants [37,38]. In this context, structural and morphological parameters such as material thickness and porosity play a crucial role, as they must be strategically tuned according to the intended application. To this end, we propose two complementary methodologies in the following sections. The first methodology involves the optimization of electrospinning parameters through a statistical approach based on ANOVA analysis. The second methodology focuses on the post-processing treatment of the electrospun membrane via calendering, primarily aimed to controlling porosity, gas permeability, and membrane thickness while preserving the characteristic fibrous structure of electrospun materials. The integration of these two approaches allows, in principle, the development of materials capable of meeting specific technical requirements, both in terms of mechanical strength and transport properties of gases and liquids.

3.5.1 ANOVA Model for Yi

As previously reported, each membrane was obtained through a unique combination of X_i factors characterized by different values, identified as 'levels' that are coded using '+1', '−1' and '0' to identify the highest, lowest and intermediate level of each factor (Table 7). To each interaction corresponds an experimental output Y_i, directly correlated to the X_i factors employing an analysis of variance (ANOVA).

Table 7. Coded factors (X_i) of the four electrospinning parameters and four output variables (Y_i) (* coded factors).

Sample	X_1	X_2 *	X_3 *	X_4 *	Y_1	Y_2	Y_3	Y_4	Y_5
	[-]	[-]	[-]	[-]	[nm]	[nm]	[cm/s]	[%]	[%]
PBI_E01	−1	−1	1	−1	132	30	1.20	76	1.06
PBI_E02	1	−1	1	−1	125	33	1.52	75	1.07
PBI_E03	−1	1	1	−1	100	25	0.75	83	22.2
PBI_E04	1	1	1	−1	102	25	0.91	82	6.56
PBI_E05	−1	−1	−1	−1	105	28	0.84	82	46.7
PBI_E06	1	−1	−1	−1	89	22	1.11	83	6.79
PBI_E07	−1	1	−1	−1	83	20	0.52	72	52.2
PBI_E08	1	1	−1	−1	89	20	0.68	76	8.23
PBI_E09	−1	−1	1	1	133	33	0.95	74	0
PBI_E10	1	−1	1	1	116	27	1.27	84	49.3
PBI_E11	−1	1	1	1	174	28	0.91	85	0
PBI_E12	1	1	1	1	156	26	0.79	85	0
PBI_E13	−1	−1	−1	1	143	35	1.16	70	14.6
PBI_E14	1	−1	−1	1	132	29	0.89	77	1.89
PBI_E15	−1	1	−1	1	114	28	0.59	76	13.7
PBI_E16	1	1	−1	1	130	40	0.55	68	3.99
PBI_E17	0	0	0	0	139	41	0.59	79	9.81

The best-proposed models for Y_1, Y_2, Y_3 and Y_4 are shown in Table 8 with the respective R^2 and R^2_{adj} values. As shown, the predicted values have a good correlation R^2 coefficient, also because the proposed models consider binary (e.g., X_1X_2) and ternary (e.g., $X_1X_2X_3$) interactions that render a deep improvement in the final model. Details on the statistic models, the calculated residuals and the influence of each interaction on Y_i responses can be found in the supporting information.

Table 8. Descriptive static models for the three analyzed outputs with the correlation parameters associated with each equation.

Output Variable	Model Equation	R^2	R^2_{adj}
Y_1	$Y_1 = 120.2 + 9.47\ X_3 + 16.9\ X_4 + 5.01\ X_2X_3 + 7.90\ X_2X_4 + 9.04\ X_2X_3X_4$	0.918	0.8687
Y_2	$Y_2 = 28.11 - 1.440\ X_2 + 2.653\ X_4 + 1.492\ X_1X_2 - 0.759\ X_2X_3 + 1.317\ X_2X_4 - 2.661\ X_3X_4 - 1.442\ X_1X_2X_3 + 1.257\ X_1X_2X_4 - 1.472\ X_1X_3X_4$	0.983	0.936
Y_3	$Y_3 = 0.9149 - 0.2031\ X_2 + 0.1231\ X_3 - 0.0644\ X_1X_4$	0.833	0.778
Y_4	$Y_4 = 78.11 + 0.831\ X_1 + 2.436\ X_3 - 0.692\ X_4 - 1.434\ X_1X_2 + 2.957\ X_2X_3 + 0.767\ X_2X_4 + 2.255\ X_3X_4 - 1.824\ X_1X_2X_4 + 1.035\ X_1X_3X_4 - 0.886\ X_2X_3X_4$	0.978	0.943
Y_5	$Y_5 = 14.01 - 4.54\ X_1 - 4.24\ X_3 - 3.83\ X_4 - 4.13\ X_1X_2 + 8.75\ X_1X_3 + 7.9\ X_1X_4 + 6.13\ X_3X_4 - 3.99\ X_1X_2X_3 - 4.39\ X_2X_3X_4$	0.954	0.876

A *p*-value analysis was conducted to assess the effect of the different factors and their interactions on four response variables (Y_1, Y_2, Y_3, Y_4, Y_5). The objective is to identify which factors have a statistically significant effect (*p*-value < 0.1) on each response variable and to construct regression models to describe these effects. Figure 9 shows the *p*-values of the different factors for the Y_i response variables, with a red line indicating the significance level set at 0.1. Factors whose bars are below the red line are considered statistically significant. Relative to the Y_1 and Y_2 responses, significant facts include the variables X_2, X_3 and X_4 and specific ternary interactions suggesting a combined influence on the output. The R^2 parameter is sufficiently high (see Table 3) and appropriately describes the microstructural behavior of the material. The *p*-value analysis suggests a strong significance of parameters such as the needle–collector distance (X_3), which influences the evaporation of the solvent and, thus, the formation of a continuous and regular fiber, and the concentration of the polymer solution (X_4), which clearly defines the viscosity f the solution and the thickness of the fiber itself.

Ejector voltage (X_2) and needle–collector distance (X_3) are highly significant for air permeability (Y_3), suggesting a significant effect on this response variable. This is a clear consequence of the electrospinning process, as the formation and distribution of fibers on the collector are dependent on the electrostatic action applied to the polymer solution, the needle tip and the velocity of the solvent evaporation, as described above.

Material porosity (Y_4) shows the greatest number of significant factors, including both single effects and multiple interactions, indicating that the variability of Y_4 is influenced by a combination of factors. It is important to emphasize that porosity, as well as the formation of the entirely fibrous material itself, is crucial for the use of polybenzimidazole-based membranes in various applications. Finally, the distribution of beads (Y_5) is influenced by the flow rate and needle–collector distance, which affect the evaporation and distribution of fibers across the sample surface and, thus, the formation of microstructural defects (beads) and dense areas. This statistical study intends to provide a rational approach to the production of electrospun materials by appropriately setting the electrospinning parameters to obtain functional and reproducible materials with controlled physical and mechanical characteristics.

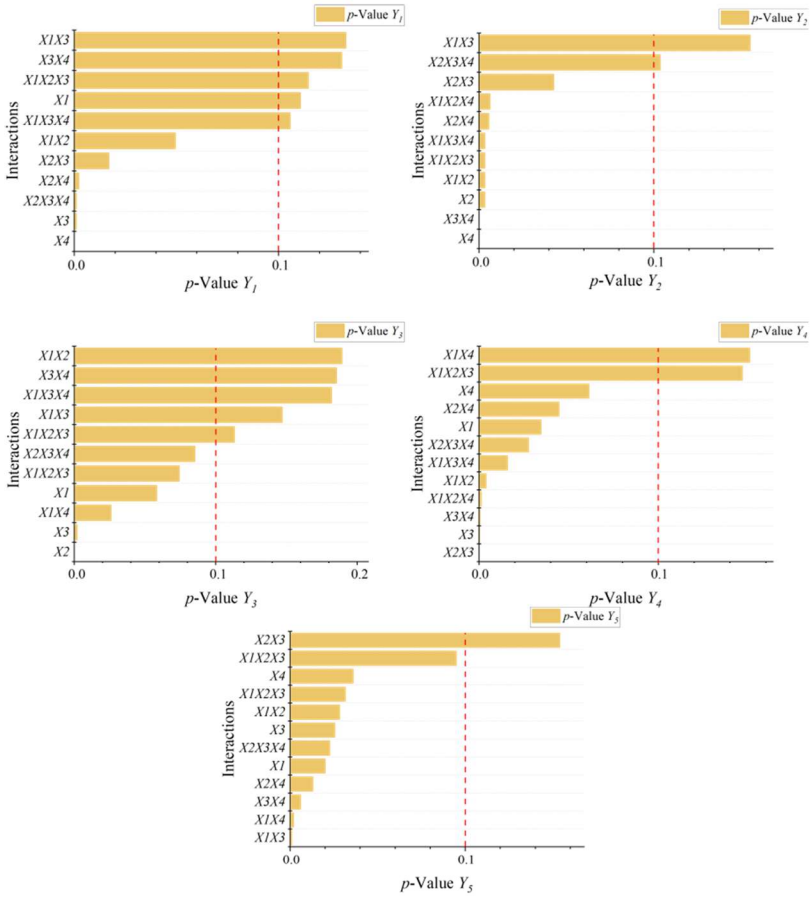

Figure 9. Bar diagram describing the *p*-values of each interaction for the studied outputs. The bars below the red lines are significant for the regression.

3.5.2 Calendering Process

Calendering resulted in extremely thin and homogeneous membranes (<25 μm) with significantly different permeation and porosity properties than the initial one. In particular, by increasing the rolling ratio and, thus, decreasing the distance between the rollers, the pressing process becomes extremely useful as it allows a reduction in air permeation rate and porosity by approximately 90% compared to the initial values (Figure 10). This is extremely relevant as the present work aims to produce and develop electrospun PBI membranes for various engineering applications through a special tuning of the morphological properties of the materials. Indeed, the reduction in porosity allows these materials to be used as true molecular sieves for gaseous effluents or enables the use of such membranes in electrochemical applications such as electrodialysis or fuel cells, processes in which low porosity prevents gaseous and/or liquid crossover phenomena.

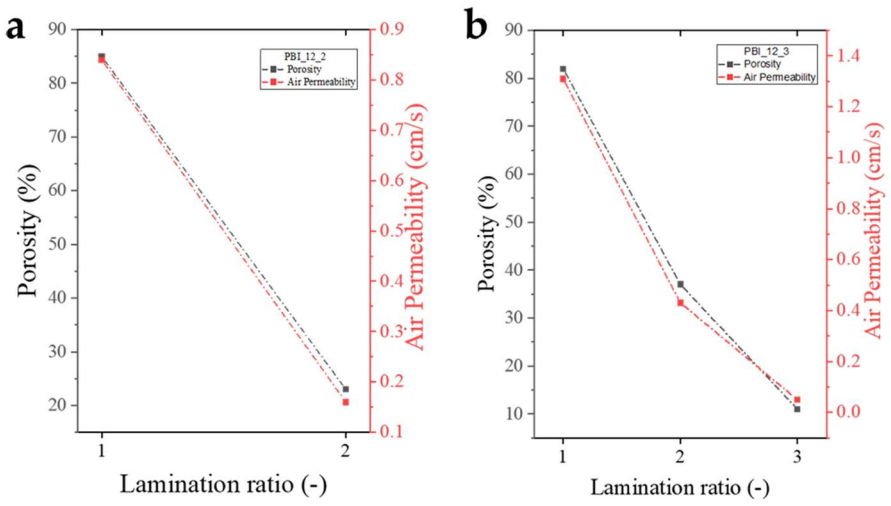

Figure 10. Effect of calendering process on air permeability and porosity of PBI-based electrospun membranes ((**a**), R = 2; (**b**), R = 3). Lines are only a guide for the eye.

It is important to point out that the calendering process does not significantly alter the fibrous morphology of the material, except for high lamination ratios: SEM analysis reveals the presence of distinct fibers on the material (Figure 11), which allows the high surface area and high adsorption capacity of the membrane to be exploited, a crucial point for the various applications. However, the increase in the lamination ratio makes it possible to observe spots in which a coalescence phenomenon is visible due to the mechanical action of pressing, which modifies the fibrous structure by altering its morphology, making the membrane, at least, close to one obtained, for example, by solvent casting. The analysis reported in this work has allowed the identification of an optimal lamination ratio that succeeds in guaranteeing the fibrous structure while maintaining the morphology as shown in Figure 11. It is worth highlighting that calendering is not only an effective post-processing technique for tuning the properties of electrospun PBI membranes but also serves as a valuable tool for further refining the physical and structural parameters of materials obtained through an ANOVA-based optimization of electrospinning conditions (see Section 2.1). This dual role enhances the ability to precisely tailor microstructural properties to meet specific application requirements.

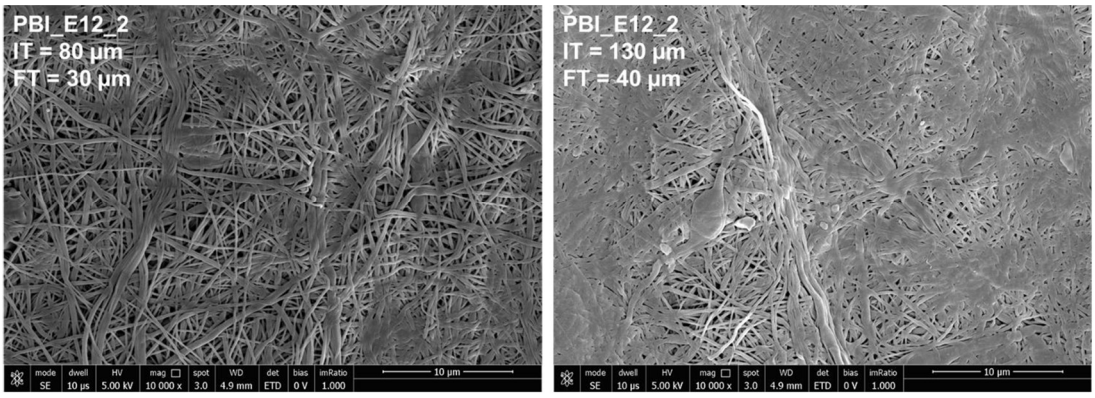

Figure 11. SEM micrographs of PBI-based electrospun membrane after calendering treatment using R = 2 (**left**) and R = 3 (**right**); IT = initial thickness; FT = final thickness.

4 Conclusions

The present work offers a comprehensive analysis of the electrospinning process for the production of polybenzimidazole-based membranes, highlighting the interplay between process parameters and the resulting material properties. This study demonstrates that the morphology, porosity, and functional performance of electrospun PBI membranes are significantly influenced by key factors such as polymer solution concentration, flow rate, ejector voltage, and needle–collector distance. Employing a Design of Experiment methodology, the relationships between these parameters were quantitatively established, enabling the development of statistically robust models to describe critical output variables, including fiber diameter, air permeability, porosity and surface defects. The results confirmed the importance of optimizing electrospinning conditions to achieve homogeneous fibrous structures. For instance, increasing the polymer solution concentration improved viscosity, which reduced the presence of bead defects and resulted in more uniform fibers. Similarly, precise control over the ejector voltage and needle–collector distance was found to be essential for maintaining jet stability and ensuring complete solvent evaporation, thereby facilitating the formation of continuous and defect-free fibers. Additionally, an ANOVA-based statistical approach and post-production methods, such as calendering, were suggested to fine-tune the morphological and microstructural properties of the electrospun membranes. In particular, it has been shown that, while preserving a fibrous structure, the calendering process effectively reduces porosity and air permeability, yielding thin, homogeneous membranes suitable for specialized applications such as energy storage or environmental remediation. To the best of our knowledge, this study is one of a handful of reports dealing with the production of PBI-based membranes made by electrospinning. Through a rational approach, the combination of statistical methods of Design of Experiments and calendering post-processing proved that it is possible to achieve a controlled modulation of processing parameters to fine-tune the physicomechanical properties of the resulting membrane material. This strategy enables the development of membranes with optimized characteristics, making them suitable for a wide range of high-performance applications.

Supplementary Materials: The following supporting information can be downloaded at: https://www.mdpi.com/article/10.3390/polym17121594/s1, Figure S1. SEM Micrographs of PBI electrospun membrane at 1 mL/h (14 %wt.): samples PBI_E01 and PBI_E05 were obtained at the same flow rate and 17 KV voltage at the ejector; PBI_E03 and PBI_E07 was obtained by varying the voltage (20 kV) and the distance.; Figure S2. SEM Micrographs of PBI electrospun membrane at 2 mL/h (14 %wt.): samples PBI_E02 and PBI_E06 were obtained at the same flow rate and 17 kV at the ejector and different needle-collector distance of 135 and 115 mm, respectively; PBI_E04 and PBI_E08 were obtained by varying the voltage at the same 20 kV at the ejector and different needle-collector distance (135-115 mm).; Figure S3. SEM Micrographs of PBI electrospun membrane at 1 mL/h (16 %wt.): samples PBI_E09 and PBI_E13 were obtained at the same flow rate and 17 kV at the ejector and a needle-collector distance of 135-115 mm, respectively; PBI_E11 and PBI_E15 were obtained by varying the voltage at the same values of 20 kV and different needle-collector distance (135-115 mm).; Figure S4. SEM Micrographs of PBI electrospun membrane at 2 mL/h (16 %wt.): samples PBI_E10 and PBI_E14 were obtained at the same flow rate and 17 kV at the ejector and a needle-collector distance of 135-115 mm, respectively; PBI_E12 and PBI_E16 were obtained by varying the voltage at the same values of 20 kV and different needle-collector distance (135-115 mm).; Figure S5. SEM micrograph of PBI electrospun membrane at 15 %wt. working in intermediate conditions (FR = 1.5 ml/h, Vej =18.5 kV, d = 125 mm, c = 15 %wt.).

Author Contributions: Conceptualization, G.R., A.R. and O.T.; methodology, G.R., A.P., A.R. and O.T.; formal analysis, V.N., L.A.H., C.D.L., A.R. and O.T.; investigation, E.D.G., V.N., L.A.H. and

C.D.L.; resources, G.R. and V.C.; data curation, V.N., V.C. and C.D.L.; writing—original draft, E.D.G., G.R., A.R. and O.T.; writing—review and editing, G.R., V.C., A.P., C.F. and A.R.; supervision, V.C. and O.T.; funding acquisition, G.R. and O.T. All authors have read and agreed to the published version of the manuscript.

Funding: O.T. gratefully acknowledges the ENEA Italian National Agency for New Technologies, Energy and Sustainable Economic Development for funding (PNRR POR H2 WP3.1 LA3.1.1). G.R. and O.T. gratefully acknowledge Ministero dell'Università e della Ricerca (PRIN 2022 Prot. 2022SBYXNE, ENCRYPT CUP MASTER I53D23001860006, CUP E53D23003660006).

Institutional Review Board Statement: Not applicable

Data Availability Statement: The original contributions presented in this study are included in this article/Supplementary Materials. Further inquiries can be directed to the corresponding authors.

Conflicts of Interest: Author Luis Alexander Hein was employed by the company Nanofaber Srl. The remaining authors declare that this research was conducted in the absence of any commercial or financial relationships that could be construed as a potential conflict of interest.

***Emmanuel De Gregorio**, Tommaso Cogliano, Giuseppina Roviello, Valentina Naticchioni, Claudio Ferone, Giulia Monteleone, Oreste Tarallo,* "Adsorption of Phosphoric Acid on Electrospun PBI Membranes: A Thermodynamic and Kinetic Insight". *ACS Applied Energy Materials, 202*6. **https://doi.org/10.1021/acsaem.5c03104.**

ACS APPLIED ENERGY MATERIALS

www.acsaem.org
Article

Adsorption of Phosphoric Acid on Electrospun PBI Membranes: A Thermodynamic and Kinetic Insight

Emmanuel De Gregorio, Tommaso Cogliano, Giuseppina Roviello, Valentina Naticchioni,* Claudio Ferone, Giulia Monteleone, and Oreste Tarallo*

Cite This: https://doi.org/10.1021/acsaem.5c03104

ABSTRACT: This study presents, for the first time, a comprehensive investigation of phosphoric acid impregnation in electrospun poly[2,2′-(*m*-phenylene)-5,5′-bibenzimidazole] (*m*-PBI) membranes and a comparison with the dense counterpart. The kinetics and thermodynamics of acid adsorption were systematically explored by varying concentration, temperature, and contact time. To this aim, a tailored experimental protocol was developed to dynamically quantify the amount of adsorbed acid and to prevent acid leaching phenomena. Electrospun membranes were found to reach Acid Doping Levels (ADL) as high as 12.9 mol H_3PO_4/mol PBI within only 10 min, far exceeding the typical maximum of 2.3 mol acid/mol polymer observed in conventional cast membranes after 24 h of immersion. A postdoping washing step with methanol used to distinguish between "free" (loosely held) phosphoric acid and "bound" (chemically or strongly hydrogen-bonded) acid showed that electrospun membranes retained a significant amount of bound acid compared to cast membranes, highlighting their superior stability. Adsorption isotherms were effectively described using Liu's model, which allowed the extraction of equilibrium constants and thermodynamic parameters, indicating an endothermic adsorption mechanism. Kinetic analysis based on a reactive adsorption model yielded a reaction order of 1.91 and an activation energy of 26.6 kJ/mol. In addition, preliminary in-plane proton conductivity measurements under anhydrous conditions showed promising electrochemical performances for the acid-doped electrospun membranes, with conductivities up to 132 mS/cm at 150 °C, significantly higher than those of cast membranes (91 mS/cm). These results demonstrate a direct correlation between fibrous morphology, adsorption mechanisms, and functional properties of the membranes for next-generation fuel cell applications.

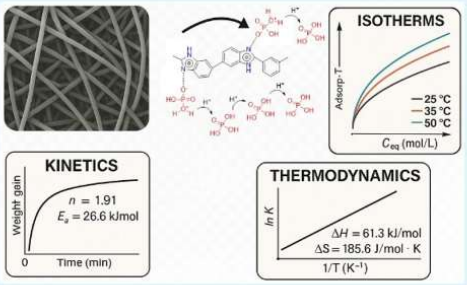

KEYWORDS: *polybenzimidazole, high-temperature proton exchange membrane, electrospinning, phosphoric acid adsorption, kinetic modeling, thermodynamic evaluation*

1. INTRODUCTION

Over the past decades, the development of polymer membranes for fuel cells has gained increasing attention due to the need for sustainable and efficient energy technologies.[1] Among high-temperature materials (T > 150 °C), poly[2,2′-(*m*-phenylene)-5,5′-bibenzimidazole] (*m*-PBI, Figure 1) stands out for its thermal and chemical stability.[1−4] A common strategy for preparing PBI membranes as solid electrolytes to be used in High-Temperature Proton Exchange Membrane Fuel Cells (HT-PEMFCs) is by doping them with strong inorganic acids, which binds strongly to the imidazole groups.[5,6] These acids induce distinct effects on the polymer, influencing its plasticity, mechanical stability, and proton exchange capacity.[7] Among these, the highest proton conductivity values have been reported for PBI membranes doped with inorganic acids in the following order: H_2SO_4 > H_3PO_4 > $HClO_4$ > HNO_3 > HCl.[8] Despite its superior conductivity, sulfuric acid requires high water content for optimal performance,[9] necessitating continuous humidification above 50%, which hinders its use in high-temperature applications, a distinguishing feature of PBI-based membranes. Consequently, phosphoric acid has become the most commonly used acid for functionalizing PBI, offering a balance of high conductivity and thermal stability, even at temperatures exceeding 100 °C. Phosphoric acid impregnation takes advantage of PBI's strong hydrophilicity and of its microporous amorphous regions, where loosely packed rigid chains create subnanometer voids that promote acid uptake and retention, enhancing proton conductivity and stability.[10] In these

Received: October 7, 2025
Revised: December 9, 2025
Accepted: December 22, 2025

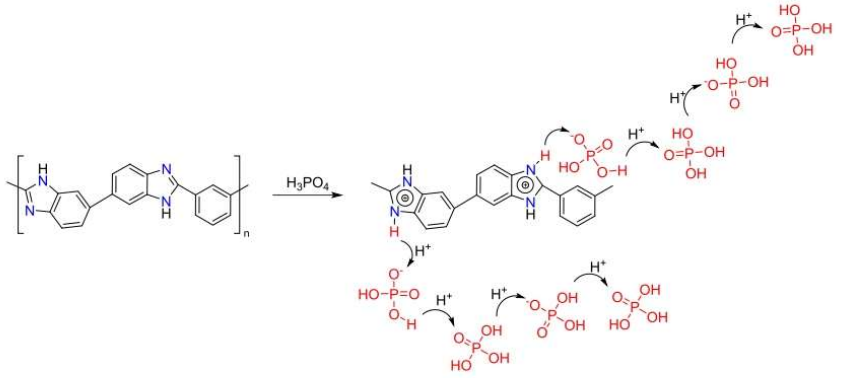

Figure 1. Schematic representation of the proton conducting mechanism in phosphoric acid doped *m*-PBI.[12]

systems, proton conduction occurs mainly through a combination of the Grotthuss mechanism (i.e., proton hopping between imidazole N−H groups and acid species) and the vehicle mechanism where phosphoric acid molecules act as carriers to shuttle protons, as reported in Figure 1.[11,12]

Commercial PBI membranes are usually obtained by casting a solution in aprotic solvents such as *N*,*N*-dimethylacetamide (DMAc), followed by immersion in H_3PO_4. This slow process often gives membranes with uneven acid distribution, since uptake occurs by diffusion through amorphous regions.[13] Moreover, this impregnation process leads to significant changes not only in the polymer's proton transport properties but also in its structure[10] and mechanical properties, by increasing the elasticity of the membrane through the plasticizing effect of the acid, although excessive doping levels can negatively impact mechanical robustness.[3,14] An advanced method for preparing phosphoric acid-doped PBI membranes is the polyphosphoric acid (PPA)-based process.[15] This technique synthesizes PBI directly in PPA, acting as a solvent and dehydrating agent. The resulting material is then subjected to controlled hydrolysis, transforming the residual PPA into H_3PO_4, which remains embedded in the polymer matrix.[16] This process allows fine control over polymerization reaction, producing membranes with a high homogeneity in acid distribution, resulting in membranes with superior chemical stability and proton conductivity. Owing to these advantages, the PPA method has been widely implemented for large-scale membrane production.[17] Alongside the PPA process, which yields dense and homogeneous PBI membranes, it is also important to explore alternative fabrication routes such as electrospinning. This technique produces nano- to microscale fibrous structures[18] with high surface area and tunable porosity,[19] features that can greatly accelerate acid impregnation and allow finer control of membrane morphology. Such control is relevant for optimizing proton transport[20] mechanical behavior,[21] and the overall doping kinetics. In this context, electrospinning provides a complementary approach to both solution casting and PPA-based synthesis,[22] enabling membrane architectures that are more accessible to H_3PO_4 and better suited for achieving high and rapid doping levels. Electrospun PBI membranes have been shown to exhibit faster acid uptake, higher attainable ADL values, and enhanced proton conductivity compared to dense cast films,[23] due to their open fiber network and improved formation of continuous proton-conducting pathways.[24,25]

This study investigates phosphoric acid impregnation of electrospun PBI membranes by analyzing the effects of acid concentration, temperature, and exposure time, and compares the results with conventional cast PBI membranes. This comparative analysis offers new insights into the kinetics of the acid impregnation process, supported by computational modeling utilizing various kinetic models. To the best of our knowledge, this approach has not yet been applied to this class of materials, and it can provide useful insights into the use of such materials.

2. MATERIALS AND METHODS

2.1. Preparation of Electrospun Membranes

Electrospun polymer mats were fabricated using a commercial poly[2,2′-(*m*-phenylene)-5,5′-bibenzimidazole] (*m*-PBI) solution (S26, PBI Performance Products©, Charlotte, USA), characterized by a viscosity of 2100 ± 200 Poise and containing 26 wt % *m*-PBI in N,N-dimethylacetamide (DMAc Merck KGaA, Darmstadt, Germany) with 1.5 wt % lithium chloride (LiCl, Merck KGaA, Darmstadt, Germany). After a preliminary optimization study to find the best electrospinning conditions,[26] the optimal formulation was identified as a 16 wt % *m*-PBI solution in DMAc and the electrospinning process was carried out by applying a voltage of +20 kV to the needle and −20 kV to the collector, with a tip-to-collector distance of 135 mm and a feed rate of 2 mL/h by using a pilot-scale electrospinning station (Fluidnatek LE100, Bioinicia SL, Valencia, Spain). SEM analysis confirmed that the resulting fibrous mats exhibited a uniform morphology with an average fiber diameter of 156 ± 5 nm, free from defects such as beads or ribbon-like structures, making them suitable for kinetic adsorption studies.

2.2. Preparation of Solution Cast Membranes

To enable comparative analysis, dense *m*-PBI membranes were prepared via solvent casting using the same S26 solution, diluted to 16 wt % by the addition of extra DMAc. The solution was cast into Petri dishes and thermally treated in a nitrogen-purged oven at 150 °C for 5 h to facilitate solvent evaporation. The resulting membranes were peeled off, thoroughly washed in boiling deionized water for 24 h to remove residual LiCl and DMAc and subsequently cut into 2 × 2 cm^2 specimens for further processing by dipping in commercial H_3PO_4 (85% wt., Merck KGaA, Darmstadt, Germany).

2.3. Water Uptake and Phosphoric Acid Impregnation

Soon after their fabrication, both dense and electrospun membranes were repeatedly washed in deionized water to remove any remaining LiCl and solvent residues that could otherwise interfere with later

https://doi.org/10.1021/acsaem.5c03104
ACS Appl. Energy Mater. XXXX, XXX, XXX−XXX

characterization and impregnation steps. The samples were then dried under vacuum at 120 °C for 24 h and weighed to determine their dry mass (W_{dry}), serving as a reference for subsequent analyses. At first, acid impregnation treatments were carried out according to standard protocols used for commercial membranes,[1] with the samples immersed in a 85 wt % phosphoric acid solution. Under these conditions, the dense membranes showed excellent chemical resistance and retained their structural integrity. In contrast, the electrospun membranes dissolved almost immediately, in some cases within less than a minute of exposure. This behavior is attributed to their intrinsically high porosity and very large specific surface area, which promote rapid acid penetration and greatly accelerate polymer chain solvation and disruption of interchain hydrogen bonding, ultimately leading to loss of mechanical integrity of the fibrous network. For this reason, in the present work, the doping treatment was carried out using moderate H_3PO_4 concentrations (0.1−5 M), which allow a controlled and reproducible acid uptake while preserving the structural continuity of the membrane. This choice represents a practical compromise between achieving sufficient protonation of the imidazole groups and maintaining the robustness of the polymer architecture. Importantly, this limitation concerns only the membrane preparation stage: during HT-PEMFC operation, the phosphoric acid is confined within the polymer matrix and the membrane is not exposed to free concentrated acid. Therefore, while the use of 85 wt % H_3PO_4 is not applicable during doping, this does not restrict the practical applicability of the electrospun membranes under real operating conditions. In this work, a modified procedure for determining the Acid Doping Level (ADL) was developed to account for the exceptionally high water uptake (WU) of electrospun PBI membranes, for which repeated thermal drying cycles may be detrimental. In contrast to the conventional equilibrium method—where the sample is fully dried between measurements—the dynamic protocol used here avoids oven drying to preserve the delicate microstructure of the fibrous mats. Because the membrane retains a significant amount of water at each time point, WU must be explicitly included in the ADL equation to separate the contribution of absorbed water from that of phosphoric acid in the total measured mass. This correction is essential to avoid overestimating the acid content, particularly in highly porous membranes where water uptake is substantial. After each interval, the sample was removed from the acid bath, gently drained and blotted to eliminate only the external liquid film, and then weighed until the mass stabilized, ensuring that only absorbed species contributed to the measurement. Incorporating WU into the calculation therefore provides a more accurate and physically meaningful determination of ADL under dynamic conditions while preventing microstructural damage associated with repeated heating. The reliability of this modified method was confirmed by performing each measurement in triplicate at every time point, yielding fully reproducible data across all samples.

Water uptake (WU) was evaluated as a preliminary indicator of membrane absorptive capacity. Membranes (50 ± 10 μm thickness, 80 ± 5% porosity) were washed in boiling water for 24 h, dried at 150 °C for 24 h, weighed (W_{dry}), and then immersed in deionized water. At predetermined intervals, samples were removed, surface-blotted, and reweighed (W_{wet}). Water uptake was then calculated using eq 1:

$$\mathrm{WU} = \frac{(W_{wet} - W_{dry})}{W_{dry}} \times 100 \tag{1}$$

For acid uptake, the same procedure was followed using phosphoric acid solutions ([H_3PO_4] = 0.1−5.0 M). After removal from the acid bath, each membrane was handled with PTFE tweezers and placed on a PTFE support to remove only the superficial liquid film. The surface was then gently blotted with filter paper for a few seconds on both sides to take off residual droplets, avoiding any applied pressure that could induce acid loss from the porous network. The sample was then transferred to the balance and weighed repeatedly until reaching a stable mass. This handling step prevents acid leaching and ensures that only nonretained, surface acid is removed while preserving the acid absorbed within the polymer matrix. The acid doping level (ADL) was monitored at regular intervals and calculated from the weight change (m_{tot}) relative to the dry mass (m_{dry}), normalized to WU, as given in eq 2:

$$\mathrm{ADL} = \frac{\mathrm{mol}_{H3PO4}}{\mathrm{mol\ PBI}} = \left[\frac{m_{tot} - m_{dry}(1 + \mathrm{WU})}{98}\right] \Big/ \left(\frac{m_{dry}}{308}\right) \tag{2}$$

where 98 g/mol is the molar mass of phosphoric acid and 308 g/mol is the molar mass of the PBI repeating unit.

To determine the equilibrium ADL, membranes were dried at 150 °C for 24 h after impregnation, and final weights were recorded. Each experiment was repeated in triplicate, with results reported as mean values and error bars representing the 95% confidence interval (eq 3):

$$\bar{x} = \frac{1}{n}\sum_{i=1}^{n} x_i \pm 1.96\left(\frac{\sigma}{\sqrt{n}}\right) \sigma = \sqrt{\frac{1}{n}\sum_{i=1}^{n}(x_i - \bar{x})^2} \tag{3}$$

The impregnation procedure for dense membranes was optimized using the same methodological framework as that applied to electrospun membranes to ensure consistency. All adsorption experiments were conducted under static conditions, minimizing external diffusion effects and isolating the intrinsic absorption kinetics of the membranes.

2.4. Morphological Characterization and Structural Analysis

The morphological features of the membranes before and after acid impregnation were analyzed via scanning electron microscopy (SEM, Nova NanoSEM 450 FEI, Austin, TX, USA). Samples were gold-coated to enhance conductivity and image clarity. Morphological changes induced by H_3PO_4 impregnation at varying concentrations were evaluated, with particular attention given to microstructural integrity and fiber morphology. Additionally, ATR-FTIR spectroscopy was employed to investigate chemical interactions between PBI and phosphoric acid. Spectra were collected for untreated membranes and samples doped with 1 and 5 M H_3PO_4, using a diamond crystal ATR cell (Anton Paar Lyza 7000, Anton Paar GmbH, Graz, Austria) and 36 scans per sample at a resolution of 4 cm^{-1}. This analysis enabled the identification of functional group modifications associated with acid impregnation.

2.5. Phosphoric Acid Adsorption Kinetics on PBI Membranes

The kinetics of H_3PO_4 adsorption on PBI membranes were modeled using reaction-based kinetic frameworks, commonly derived from chemical reaction theory. These models describe the overall adsorption process without explicitly accounting for mass transfer or diffusion phenomena. Although this assumption simplifies the system, such models remain widely applied in the literature[27] due to their practicality and the valuable insights they offer into adsorption dynamics, reflecting the specific interest in the interaction between PBI membranes and H_3PO_4 molecules. The primary objective of applying these kinetic models was to quantify the solute uptake rate, which directly determines the residence time required to achieve equilibrium. This information is particularly useful for estimating the minimum contact time needed for adsorption completion, rather than for deriving mechanistic insights or designing large-scale adsorption columns.

The adsorption process was described by a generalized rate equation in the form of an ordinary differential equation (ODE), expressed as (eq 4):

$$\frac{dq}{dt} = k(q_e - q)^n \tag{4}$$

where q and q_e represent the amount over time and at the equilibrium of adsorbed acid per amount of polymer matrix (mol/g_{pm}), k is the kinetic constant, and n is the total reaction order. The temperature dependence is considered through the kinetic constant, which was written according to the Arrhenius equation (eq 5):

https://doi.org/10.1021/acsaem.5c03104
ACS Appl. Energy Mater. XXXX, XXX, XXX−XXX

$$k = A_0 \exp\left(\frac{-E_a}{RT}\right) \quad (5)$$

where A_o is the pre-exponential factor, E_a is the activation energy (kJ/mol), R is the universal gas constant, and T is the absolute temperature (K). Three kinetic models were evaluated: pseudo-first-order (n = 1), pseudo-second-order (n = 2), and a generalized power-law model with variable n. For the first two models, only A_o and E_a were estimated, as the reaction order was fixed. In contrast, the power-law model included A_o, E_a, and n as fitting parameters to identify the best representation of the experimental data. Model fitting and parameter estimation were performed in MATLAB (MathWorks, Inc., R2025a Version). The ODE system was numerically solved using MATLAB's "*ode23s*" solver. Parameter optimization was carried out by minimizing the objective function (eq 6) using the "*lsqnonlin*" routine, which employs the Levenberg−Marquardt algorithm for nonlinear least-squares fitting. Confidence intervals for the estimated parameters were calculated using the "*nlparci*" function.

$$O(\beta) = \sum_{i=1}^{N} (x_i - \hat{x}_i)^2 \quad (6)$$

2.6. Methanol Test

In order to distinguish between "free" (loosely held, F) and "bound" (chemically or strongly hydrogen-bonded to imidazole sites, B) phosphoric acid, a postdoping washing step with methanol was carried out using a procedure reported elsewhere.[1] Dried membranes were first weighed and then immersed for 30 min in H_3PO_4 solution at different concentrations (1, 3, 5 M). At the end of the acid treatment, the samples were blotted and placed in a vacuum oven at 110 °C overnight to remove residual water and then weighed to determine the initial ADL value (ADL_0). The samples were then immersed in anhydrous methanol (≥99.8%, Sigma-Aldrich), at a mass-to-volume ratio of 1:3000 for 24 h. This ratio is twice that used by Li et al.[1] for conventionally cast PBI membranes, and was selected here to account for the much lower density and higher porosity of the electrospun membranes. Finally, the samples were recovered, dried in a vacuum oven at 60 °C and repeatedly weighed to calculate the post-treatment ADL (ADL_{post}). Methanol extracts the free or excess phosphoric acid but leaves behind the fraction that is chemically bound to PBI. The fraction of acid retained stably bound to the PBI structure was calculated according to eq 7:

$$B = \frac{ADL_{post}}{ADL_0} \quad (7)$$

2.7. In-Plane Proton Conductivity

The in-plane proton conductivity of PBI-based membranes obtained through casting and electrospinning techniques was measured under anhydrous conditions at different temperatures, using a Scribner 740 Membrane Test System station (Scribner Associates Inc., Southern Pines, NC, USA) equipped with a Solartron Analytical Potentiostat/Galvanostat (AMETEK, Farnborough, UK). The cell consists of two parallel platinum electrodes separated by a fixed distance (L) of 0.425 cm. All measurements were conducted used anhydrous conditions using dry nitrogen (N_2) as both purge and measurement gas, bypassing the humidification line through a dedicated dry-gas circuit. Prior to each measurement, the membrane was equilibrated at the testing temperature for 4 h under a continuous flow of dry N_2 (100 sccm) ensuring complete removal of residual moisture. For measurements conducted at lower temperatures (50−100 °C), the purge time was extended to 5 h to further minimize humidity effects inside the chamber, while at temperatures above 140 °C proton transport is intrinsically anhydrous. All membranes tested are characterized by a thickness (T) of 50 ± 5 μm and an ADL ∼ 11 in order to obtain a rational and reproducible comparison, with a useful sample width (W) of 1 cm. Measurements were conducted through a linear voltage sweep from −0.1 to 0.1 V with a scan rate of 10 mV/s. A current−voltage (I−V) curve was recorded for each sample, from which the ohmic resistance (R) could be derived as the slope of the linear region of these curves. The in-plane proton conductivity (σ_{IP}) was calculated using eq 8:

$$\sigma_{IP} = \frac{L}{R \times W \times T} \quad (8)$$

Each proton conductivity measurement was performed on five independent I−V curves for each sample and for each temperature, in order to reduce the influence of any experimental variations while ensuring the reproducibility of the measurements.

3. RESULTS AND DISCUSSION

3.1. Water Uptake Evaluation

Water Uptake (WU) is a key parameter to describe the ability of *m*-PBI-based membranes to retain polar species and represents the first step in understanding their interaction with phosphoric acid. In this work, WU was determined following the protocol described in Section 2.3 by immersing the samples in deionized water and collecting them at regular intervals. The measured weight gain was converted to moles of water relative to the moles of *m*-PBI in the dry membrane, providing a normalized value independent of sample mass or thickness and thus reducing the effects of morphological variability.

Figure 2 shows the average WU values for *m*-PBI membranes obtained by solution casting and electrospinning,

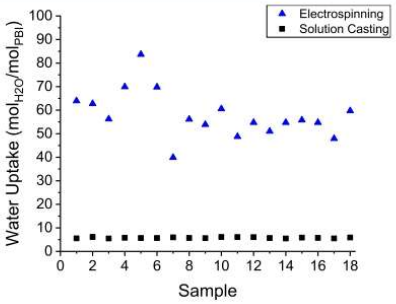

Figure 2. Water Uptake (WU) normalized to the moles of *m*-PBI for dense (black squares) and electrospun (blue triangles) membranes after 30 min of immersion in deionized water at room temperature. Values are based on 18 different samples.

calculated from a total of 18 independent samples. For cast membranes, the average WU is 5.6 ± 0.3 mol_{H2O}/mol_{PBI}, showing an excellent reproducibility across tests and in full agreement literature values.[1,4] Fibrous membranes, on the other hand, display a markedly different behavior, with an average of 60 ± 4 mol_{H2O}/mol_{PBI}, about ten times higher than the dense counterpart. The comparison between the two types of membranes highlights the decisive role of morphology in water absorption capacity. Dense membranes, with their compact and poorly porous structure, restrict water access to the polymer matrix, confining absorption mainly to the bulk material. By contrast, fibrous membranes benefit from their porous network and interconnected fibers, which trap water both in the pores and along the outer surface. This microstructure enhances retention through multiple mechanisms, confirming that porous morphology is a crucial factor in modulating the impregnation capacity of PBI membranes and in interpreting Acid Doping Level (ADL) values. Interestingly,

https://doi.org/10.1021/acsaem.5c03104
ACS Appl. Energy Mater. XXXX, XXX, XXX−XXX

it is worth pointing out that, despite the large difference in WU values, the method showed high reproducibility in both cases. Some variability was observed, especially in fibrous samples, but this does not indicate unreliability of the method. Instead, it reflects the natural microstructural heterogeneity of porous materials, where fiber diameter distribution and pore interconnection can vary slightly from sample to sample.

The analysis of water retention is also useful for correlating experimental results with phosphoric acid concentration. As shown in Figure 3, dense membranes display nearly constant

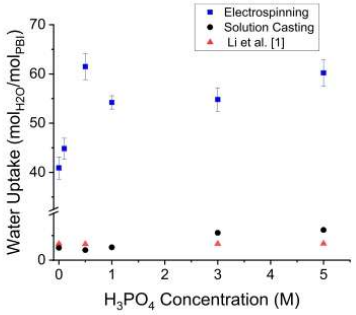

Figure 3. Water Uptake (WU) of PBI membranes after doping with phosphoric acid solutions of different concentrations for 30 min: electrospun mats (blue squares) and dense membranes prepared by solution casting (black circles). Literature data from ref 1 (red triangles) are included for comparison.

WU values (~5 mol_{H_2O}/mol_{PBI}) regardless of H_3PO_4 concentration. This indicates that the compact structure of dense membranes strongly limits water retention, suggesting the presence of a threshold beyond which the material is no longer influenced by additional water molecules. This trend is consistent with previous reports for dense membranes, such as those by Li et al.[1] Fibrous materials, on the other hand, behave differently, showing a more complex response. While their WU values remain higher overall, they are clearly affected by the acid concentration. At low concentrations, WU reaches 40−45 mol_{H2O}/mol_{PBI}, increasing further to 60−62 mol_{H2O}/mol_{PBI} at 0.5 M. A slight decrease occurs at 1 M, followed by a renewed increase and stabilization at higher concentrations (3−5 M). This nonmonotonic behavior reflects the balance between two competing effects. At low acid concentrations, protonation of the imidazole sites enhances hydrophilicity and promotes water retention, resulting in higher WU. However, when the acid concentration reaches ~1 M and above, H_3PO_4 begins to compete with water for the same hydrogen-bonding sites, progressively replacing water as the dominant solvating species. Consequently, the acid uptake continues to increase, while the amount of water retained in the membrane does not increase proportionally and instead shows a slight decrease.

3.2. Adsorption of H_3PO_4: Solution-Cast Membranes

Phosphoric acid adsorption tests on solution-cast membranes provide a direct measurement of the Acid Doping Level (ADL), defined as the moles of phosphoric acid retained per mole of *m*-PBI. When considered together with the water uptake (WU), this parameter becomes particularly informative. Indeed, normalizing ADL with respect to WU does not simply indicate the total amount of acid absorbed; rather, it highlights the fraction of acid that directly interacts with the polymer, excluding the contribution of acid dissolved in the bulk water phase. In this way, the analysis assesses the intrinsic affinity of the membrane system for phosphoric acid, independent of the purely volumetric effect of imbibition. The acid impregnation protocol developed in this work made it possible to quantify the amount, and therefore the moles, of H_3PO_4 retained in dense *m*-PBI membranes as a function of time. From this, time-dependent ADL curves were constructed, describing the evolution of the adsorption process. As detailed above, the doping level at each time point was determined from the mass change of the membranes, normalized by WU, while the equilibrium ADL was obtained after a postimpregnation 24-h heat treatment, which removed water and thus isolated the fraction of acid truly bound to the polymer matrix. The experimental conditions and corresponding Acid Doping Level (ADL) values at equilibrium are summarized in Table 1.

Table 1. Experimental Conditions Used for the Phosphoric Acid Impregnation and Corresponding Equilibrium ADL Values for Solution-Cast Membranes

Experiment	H_3PO_4 (mol/L)	Temperature (°C)	ADL ($mol_{H_3PO_4}/mol_{PBI}$)
1	0.1	25	0.75 ± 0.03
2	0.5	25	1.03± 0.02
3	1	25	1.23± 0.04
4	3	25	1.82± 0.06
5	5	25	2.30± 0.03

The obtained results are in good agreement with previous studies on solution-cast PBI membranes.[1,17] Specifically, Li et al.[1] reported equilibrium ADL values of approximately 1, 2, 2.5, and 3 for phosphoric acid concentrations of 0.5, 1, 3, and 5 mol/L, respectively, closely matching the values observed in this work (see Table 1). Figure 4 shows the impregnation behavior of phosphoric acid in dense membranes obtained through solution casting, with the adsorbed amount *q* expressed as milligrams of H_3PO_4 per gram of *m*-PBI membrane. Figure 4a illustrates the impregnation kinetics in 0.1−5 M phosphoric acid solutions. In all cases, impregnation is fast during the first few hours, then the increase in *q* gradually slows until it reaches a *plateau*, indicating an equilibrium condition. The amount of acid retained strongly depends on the acid concentration, increasing with higher molarity (Figure 4b). This behavior can be explained by acid−base interactions between the imidazole groups of PBI and phosphoric species, leading to progressive protonation of the basic sites and, consequently, greater incorporation of acid molecules within the membrane matrix. Notably, in all cases, equilibrium was reached after 24 h of exposure, regardless of acid concentration. This slow adsorption behavior is attributed to the dense, cohesive morphology of solution-cast membranes, which exhibit low porosity (see Figure 9a). Consequently, the diffusion of phosphoric acid into the polymer matrix is hindered, resulting in extended equilibration times. As a result, the overall acid uptake remains relatively low, underscoring the limitations of this method in achieving high doping levels within practical timeframes on dense membranes prepared by solution casting. As a final remark, it is worth noticing that from a kinetic and modeling standpoint, the slow and almost monotonous evolution of the uptake profile—lacking an initial linear regime typically associated

https://doi.org/10.1021/acsaem.5c03104
ACS Appl. Energy Mater. XXXX, XXX, XXX−XXX

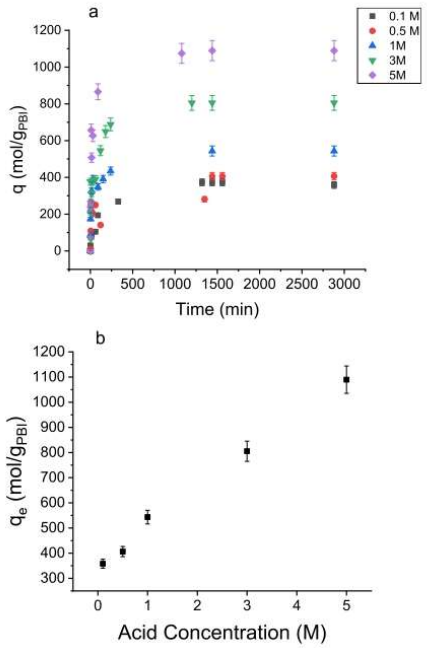

Figure 4. Adsorbed amount of phosphoric acid (q, mol H_3PO_4 per g PBI) as a function of time at different acid concentrations (a), and equilibrium values q_e as a function of acid concentration (b).

with surface-controlled adsorption(see Figure 4a)—prevents the reliable extraction of kinetic constants. In particular, it is not possible to clearly distinguish between pseudo-first-order (PFO), pseudo-second-order (PSO), or n-th order kinetic models. In this case, since the overall process is dominated by diffusion, applying surface-reaction-based models would yield kinetic parameters of ambiguous interpretation and limited physical significance. In dense PBI films, the time evolution of acid uptake show a smooth and gradual increase toward equilibrium, indicating that the overall kinetics are dominated by slow intraphase diffusion of phosphoric acid within the polymer matrix, rather than by a surface protonation step at the polymer-acid interface. This behavior is consistent with the compact morphology and limited porosity of the cast membrane, which restrict mass transport and make bulk diffusion the rate-determining step of the process.

3.3. Adsorption of H_3PO_4: Electrospun Membranes

The kinetic behavior of m-PBI membranes obtained by electrospinning is markedly different from that of membranes prepared by solution casting. The morphological change, characterized by a network of nanometer-scale fibers woven into a three-dimensional network, has a direct and substantial impact on the kinetics of acid impregnation. At 25 °C, the dynamic analysis of phosphoric acid uptake per unit mass of m-PBI, shown in Figure 5a as a function of H_3PO_4 concentration, reveals a highly distinctive trend. The curves display an extremely fast initial stage, in which the membrane rapidly captures a large fraction of the acid, followed by a quick attainment of equilibrium. A striking feature is that equilibrium is reached within just a few minutes for all the studied concentrations—by contrast, solution-cast films, as discussed above, require almost 24 h to approach equilibrium. From an interpretative point of view, the process could be divided into two stages:

i) a first stage, where acid molecules are quickly adsorbed by surface sites that are immediately accessible;

ii) a second stage, governed by intrafiber diffusion, where progressive polymer plasticization controls the acid–polymer interaction until a plateau is reached.

The combination of high porosity and plasticization explains both the speed of the kinetics and the high doping values achieved, confirming the crucial role of fibrous microstructure in the impregnation capability of the membranes. To highlight the advantage of the fibrous morphology, Figure 5b compares equilibrium ADL values as a function of H_3PO_4 concentration for both dense and electrospun membranes. As expected, ADL systematically increases more for electrospun membranes than for their dense counterparts. This behavior arises from the greater accessibility of imidazole sites, which reduces diffusion limitations and allows acid molecules to reach them quickly. Furthermore, normalizing by water uptake (WU) shows that,

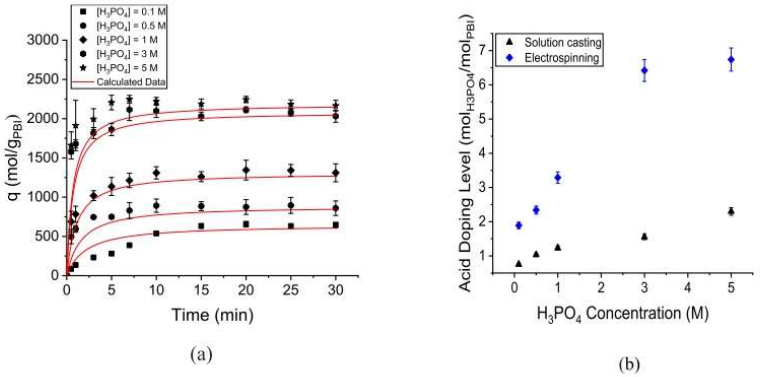

Figure 5. Adsorption of phosphoric acid on electrospun m-PBI membranes at 25 °C: (a) dynamic uptake of phosphoric acid per unit mass of membrane at different acid concentrations; (b) comparison of ADL values at equilibrium between solution-cast and electrospun membranes.

https://doi.org/10.1021/acsaem.5c03104
ACS Appl. Energy Mater. XXXX, XXX, XXX−XXX

for the same retained water, the ADL/WU ratio is more favorable in fibrous membranes. This effect is due to the confinement of acid within the pores and the higher local density of accessible basic sites, which promote the formation of acidic interfiber domains. From a practical perspective, this means that under identical time and temperature conditions, electrospun membranes always achieve higher final ADL after impregnation, and this improvement translates into better proton conductivity and lower ohmic resistance, from an applicative point of view. These results reinforce the conclusion that the observed behavior is not due to microstructural variability among samples but is an intrinsic feature of the electrospun morphology. This robustness is essential for practical applications, as it ensures that the extracted kinetic parameters can reliably support large-scale impregnation protocols.

All kinetic tests were also repeated at higher temperatures (35 and 50 °C) under the same H_3PO_4 concentration conditions as shown in Table 1, both to validate the model and to estimate energy parameters using the Arrhenius equation. Equilibrium measurements at these higher temperatures (Figure 6a,b) show that the degree of acid doping increases with temperature, confirming the endothermic nature of the process. The imbibition of phosphoric acid is favored by greater thermal energy, which helps loosen the intermolecular bonds within the polymer chains and enables the formation of new interactions with the acid. Figure 6c reports the equilibrium adsorption capacity (q_e) as a function of acid concentration at the three different temperatures. In all cases, q_e increases with concentration, but the effect of temperature is decisive: at the same concentration, q_e is always higher at higher temperatures. This indicates that increasing temperature enhances both diffusion and acid−polymer interactions, thereby improving the overall adsorption capacity.

Kinetic modeling was carried out using power-law differential reaction models applied to equilibrium data. Three models were tested: pseudo-first-order (PFO, $n = 1$), pseudo-second-order (PSO, $n = 2$), and n-order kinetics. The comparison showed that the first-order model fails to capture the initial transient, underestimating the rate of acid uptake in the early stages. The second-order model provides a much better fit, accurately describing both the initial linear increase and the later slowdown toward equilibrium. However, the best agreement was obtained with an n-order law, yielding an exponent of about $n = 1.91 \pm 0.03$. Although the apparent reaction order is close to 2, suggesting the possible involvement of more than one interacting species in the rate-limiting step, this value cannot be straightforwardly assigned a priori to a specific molecular mechanism[27] between phosphoric acid species and imidazole groups, rather than evidence of a single well-defined bimolecular elementary step. Numerical results are reported in Table 2.

This conclusion is important not only mathematically ($R^2_{adj} = 0.977$), but also physically, as it indicates a process governed by cooperative and complex mechanisms. The availability of active sites, intrafiber diffusion, and polymer plasticization act together, producing an interaction rate with an almost quadratic dependence on concentration. In addition, the model allowed for the estimation of kinetic and energetic parameters with strong statistical robustness. The activation energy (E_a) was found to have intermediate values, between those typical of physisorption and chemisorption, consistent with the hybrid nature of this interaction.

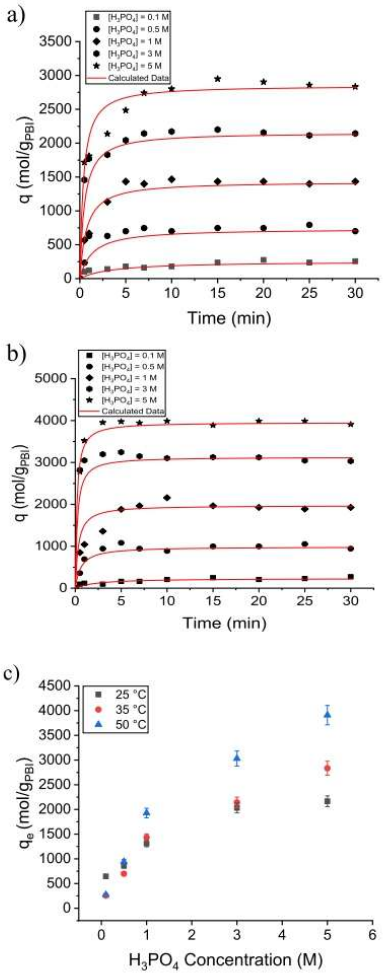

Figure 6. Adsorption kinetics at 35 °C (a) and 50 °C (b) for electrospun membranes, and equilibrium adsorption capacity (q_e) as a function of H_3PO_4 concentration (c) at different temperatures (25, 35, 50 °C). Experimental data are shown as scatter points; calculated fits are represented by red lines.

Table 2. Estimated Kinetic Parameters for the Interaction between H_3PO_4 and Electrospun *M*-PBI Membranes at 25 °C, Obtained by Nonlinear Regression of an *N*-Order Differential Model. A_0= [$L^{0.91}$ $mol^{-0.91}$ s^{-1}]; E_a = [J mol^{-1}]; N = [−]

		Correlation Matrix			
Parameter	Value ± C.I. 95%	A_0	E_a	n	Adj-R^2
A_0	0.85 ± 0.02	1			0.9770
E_a	26597 ± 605	−0.4440	1		
n	1.91 ± 0.03	−0.6329	0.8437	1	

The correlation analysis of kinetic parameters further supports the existence of a complex adsorption mechanism, influenced by both energetic and structural factors. A moderate

https://doi.org/10.1021/acsaem.5c03104
ACS Appl. Energy Mater. XXXX, XXX, XXX−XXX

negative correlation between the pre-exponential factor (A_0) and activation energy (E_a, −0.4440) suggests an enthalpy–entropy compensation effect. This indicates that increased molecular mobility may offset higher energetic demands. A strong positive correlation between reaction order (n) and E_a (0.8437) implies that adsorption becomes more energy demanding as its dependence on acid concentration increases, possibly due to multispecies interactions or site saturation effects. The negative correlation between A_0 and n (−0.6329) suggests that effective collision frequency decreases as reaction order rises, likely due to steric or diffusion constraints in the porous medium.

Overall, the estimated kinetic parameters point to a complex adsorption mechanism, with a possible rate-limiting step influenced by both acid concentration and membrane microstructure. To validate and quantitatively describe the proposed hybrid adsorption mechanism, advanced spectroscopic and gravimetric techniques could be employed in future work. Solid-state NMR is particularly powerful: ^{1}H and ^{15}N SS-NMR measurements can distinguish between protons directly bound to imidazole sites (N–H^{+}), reflecting true PBI protonation, and those participating in the broader hydrogen-bonding network (O–H···O, O–H···N) within the phosphoric acid clusters. Analysis of chemical shifts and ^{1}H–^{15}N or ^{1}H–^{31}P heteronuclear correlations would allow quantification of the relative populations of these two environments, providing a direct measure of the effective protonation degree. Complementary techniques such as Quartz Crystal Microbalance with Dissipation monitoring (QCM-D) could track mass uptake and viscoelastic changes during acid sorption, helping to separate polymer protonation from the formation of hydrogen-bonded acid–water networks. FTIR or Raman spectroscopy—especially using temperature-dependent measurements—may further resolve the evolution of specific vibrational bands associated with protonated imidazole groups and P–O–H interactions. Together, these methods would significantly refine the mechanistic picture and will be explored in a dedicated future study. All the tested kinetic models, together with their fitting curves, are reported in the Supporting Information.

3.3.1. Thermodynamic Description. Dynamic analysis and stability tests in methanol (described in section 3.6) showed that only part of the acid content is truly relevant for membrane performance, as it corresponds to the fraction of acid stably interacting with imidazole sites. To fully describe the acid–membrane interaction, a thermodynamic approach is essential, as it clarifies the mechanisms of interaction between acid and polymer across different concentrations and temperatures. To quantitatively describe equilibrium behavior at different temperatures, several isothermal models were tested, including Langmuir, Freundlich, Sips, and Liu. The first three, though widely used in the literature, showed significant deviations from the experimental data, especially at high phosphoric acid concentrations. The Langmuir model, based on the assumption of equivalent adsorption sites and monolayer coverage, is too restrictive for porous matrices with the complex microstructure of electrospun membranes. The Freundlich model accounts for heterogeneity but does not predict a saturation limit, while the Sips model provides a compromise but introduces uncertainties in fitting parameters. The Liu model, an extension of Langmuir's equation with an empirical exponent (n_L) to account for deviations from ideal monolayer adsorption, provided the best fit to the data. The Liu isotherm is expressed as (eq 9):

$$q = \frac{Q_{max}(KC_e)^{n_L}}{1 + (KC_e)^{n_L}} \tag{9}$$

where q is the adsorbed acid at equilibrium (mol/g), Q_{max} is the theoretical maximum adsorption capacity (mol/g), K is the affinity constant (L/mol), C_e is the equilibrium concentration of phosphoric acid (mol/L), and n_L is a dimensionless and empirical parameter describing site heterogeneity. This model assumes a heterogeneous distribution of adsorption energies and a finite sorption capacity (Q_{max}). Unlike Langmuir and Freundlich, the Liu model does not rely on the monolayer or infinite adsorption assumptions.

Figure 7 shows the experimental isotherms together with Liu model fits at 25, 35, and 50 °C. With increasing temperature,

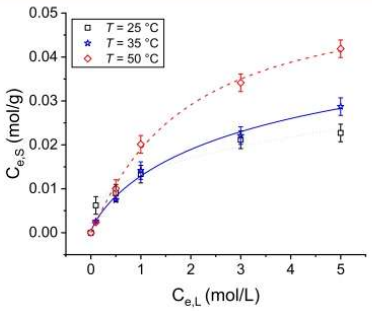

Figure 7. Adsorption isotherms of phosphoric acid (scatter symbols) and Liu model fits (lines) at 25 °C (black), 35 °C (blue), and 50 °C (red) for electrospun PBI membranes.

adsorption capacity rises at the same initial concentration, and the isotherm plateaus shift toward higher values. The upward shift of the curves confirms an endothermic process, where higher temperatures enhance the interaction between PBI functional groups and phosphoric acid.

The Liu parameters estimated at the three temperatures are summarized in Table 3. The equilibrium constant K increases with temperature, indicating a stronger affinity between the membrane and the acid. The Q_{max} parameter remains nearly constant (0.05–0.06 mol/g), confirming a stable maximum doping capacity. Interestingly, the exponent n_L evolves from low values (0.495 at 25 °C) to values slightly above 1 at 50 °C. The increase in n_L from ∼0.5 at 25 °C to values close to (and slightly above) 1 at higher temperature reflects a marked evolution in the acid adsorption behavior. At low temperature, $n_L < 1$ indicates an energetically heterogeneous population of adsorption sites, where acid uptake is dominated by a limited number of high-affinity imidazole environments. As the temperature increases, polymer segmental mobility and local plasticization enhance the accessibility and uniformity of binding sites, leading to $n_L \approx 1$. Values slightly above unity suggest the onset of cooperative adsorption, where the presence of already-adsorbed acid facilitates further uptake locally. In practical terms, doping at higher temperature yields a more homogeneous acid distribution and more continuous proton-conducting pathways, which is beneficial for conductivity. However, this increased uniformity is associated with greater plasticization and may therefore reduce the elastic

https://doi.org/10.1021/acsaem.5c03104
ACS Appl. Energy Mater. XXXX, XXX, XXX–XXX

Table 3. Liu Isotherm Parameters at 25, 35, and 50 °C, with Adsorption Enthalpy and Entropy Estimated from van't Hoff Linearization

	Liu Parameters				Thermodynamic	
T (°C)	K (L/mol)	Q_{max} (mol/g)	n_L (−)	Adj-R^2	ΔS (J/mol K^{-1})	ΔH(J/mol)
25	0.079 ± 0.006	0.060 ± 0.001	0.495 ± 0.004	0.9975	185.58	61337
35	0.24 ± 0.03	0.05 ± 0.01	0.8 ± 0.2	0.9917		
50	0.6 ± 0.2	0.055 ± 0.007	1.1 ± 0.2	0.9962		

modulus, an aspect that should be considered with respect to long-term membrane stability under HT-PEM operation. Linearization of the van't Hoff equation (Figure 8) allowed the calculation of the adsorption enthalpy (ΔH) and entropy (ΔS).

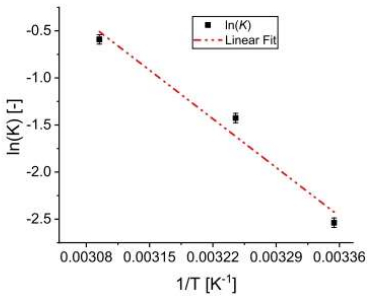

Figure 8. Linearized van't Hoff plot for the estimation of ΔH and ΔS, obtained from the Liu isotherm equilibrium constant (K) at 25, 35, and 50 °C.

The positive enthalpy confirms the endothermic nature of the process, while its magnitude suggests interactions stronger than simple physisorption. The endothermic nature of the H_3PO_4 adsorption process, apparently in contrast with the typically exothermic character of acid−base reactions, can be rationalized by considering the overall thermodynamic balance of the phenomena occurring during impregnation. In addition to the exothermic protonation of the imidazole groups of PBI, the process involves several endothermic contributions, namely the disruption of the interchain hydrogen-bond network, the partial dehydration and reorganization of the phosphoric acid species, and the conformational rearrangement of the polymer matrix to accommodate the acid molecules. These structural and solvation changes require an overall energy input that outweighs the local heat released by the acid−base neutralization step, resulting in a net endothermic adsorption process. This supports the interpretation of a weak but cooperative chemisorption mechanism, involving the formation of stable hydrogen-bond networks within the polymer matrix. Moreover, the strong positive entropy reflects the increase in disorder accompanying the process: as acid penetrates the fibrous structure, polymer chains reorganize, increasing the overall configurational freedom of the system.

Overall, doping is a thermodynamically favorable process, becoming increasingly spontaneous at higher temperatures. This further confirms that electrospun membranes are excellent candidates for HT-PEM applications, where doping stability must be ensured under high-temperature operating conditions. Results from all tested isotherm models (Langmuir, Freundlich, and Sips), together with fit parameters and determination coefficients, are reported in the Supporting Information. From a kinetic point of view, the affinity constant K increases with temperature, confirming a greater tendency of phosphoric acid to adsorb onto the membrane at higher temperatures. From the data fit, similar values of Q_{max} are estimated from the three independent fits. In addition, an Adj-R^2 greater than 0.99 is obtained in all cases, which indicates a fairly consistent range, suggesting that the adopted isotherm model describes the experimental data. Finally, as mentioned above, the parameter n_L indicates a process that becomes progressively more uniform with equivalent sites at higher temperatures. Finally, a reasonable estimation of the thermodynamic parameters of the process, namely enthalpy and entropy, was obtained from the equilibrium data. However, a comparison with other studies is not possible because, to the best of the authors' knowledge, no similar investigations on the thermodynamics of H_3PO_4 adsorption on electrospun PBI membranes have been reported in the literature. The thermodynamic parameters shown in Table 3 allow important considerations to be made about the mechanism of interaction between PBI and phosphoric acid molecules. The positive enthalpy value (ΔH) indicates that adsorption is clearly an endothermic process: the diffusion of the acid into the polymer matrix therefore requires energy to break the polymer's intra- and interchain interactions. Heat enhances the swelling and plasticization of the fibrous network, making the interaction sites accessible. The entropic contribution (ΔS) is strongly positive, suggesting, as could be expected, that adsorption does not lead to a rigidly ordered system, but to increased structural disorder. The presence of phosphoric acid induces plasticization phenomena, as well as generating mobile ionic species ($H_2PO_4^-$ and HPO_4^{2-}) which, while remaining associated with the polymer matrix, retain a certain mobility, contributing to a marked increase in the number of states accessible to the system. Overall, the high entropic gain makes the process favored at higher temperatures, consistent with the increase in ADL values observed experimentally. The process, therefore, is not governed by acid−base interaction alone but by a more complex structural reorganization of the polymer matrix, which facilitates the dynamic incorporation of the acid. This analysis could also allow some considerations on the nature of the process, in terms of physisorption or chemisorption. Actually, the enthalpy value determined is intermediate if compared to typical values observed for physisorption (<40 kJ/mol) and chemisorption (>80 kJ/mol), suggesting a mixed mechanism. The high entropic contribution and the pronounced plasticization of the polymer matrix indicate a significant contribution of physisorption, but, at the same time, relatively high enthalpy values suggest the presence of "stronger" interactions, compatible with a contribution of chemisorption. Overall, the interaction between H_3PO_4 molecules and PBI fibers could be described as a hybrid process in which specific bonds and dynamic interactions coexist. However, the exact nature and relative weight of the different components remain to be

https://doi.org/10.1021/acsaem.5c03104
ACS Appl. Energy Mater. XXXX, XXX, XXX−XXX

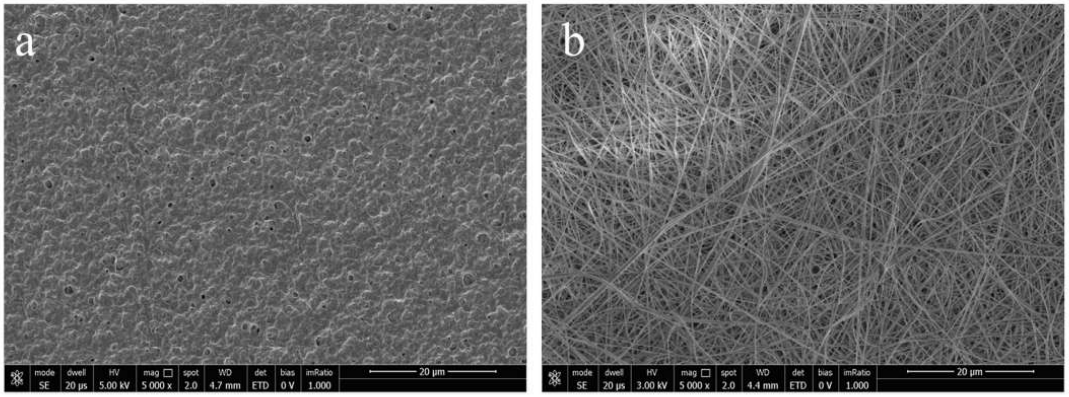

Figure 9. SEM micrographs at 5000× magnification of undoped cast (a) and electrospun (b) PBI membranes.

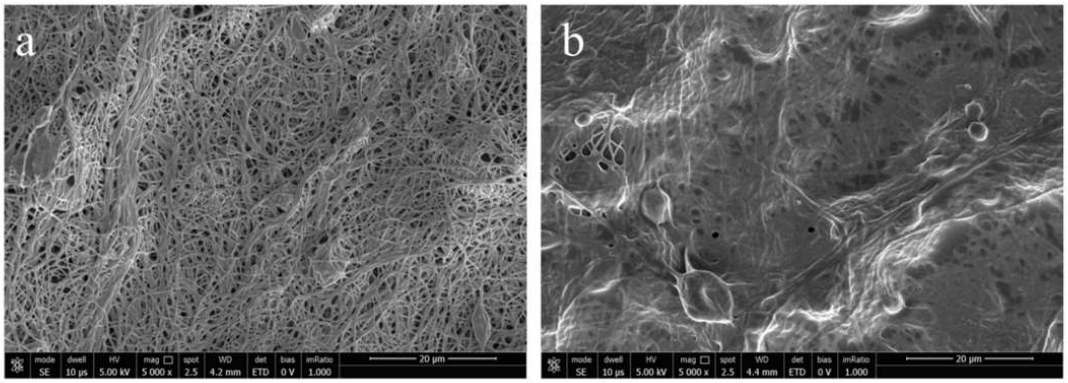

Figure 10. SEM micrographs at 5000× magnifications of *m*-PBI electrospun membranes after acid treatment for 30 min: (a) H_3PO_4 1M, (b) H_3PO_4 5M.

elucidated and could be the subject of more focused and in-depth future studies.

3.4. Microstructural Evaluation

To understand the effects of phosphoric acid treatment on the structure of PBI membranes, a morphological analysis was conducted using scanning electron microscopy (SEM). This technique enabled the observation of the material's surface microstructure, highlighting the changes induced by the doping process. In particular, dense and fibrous membrane samples were compared before and after impregnation at different H_3PO_4 concentrations, to assess variations in material continuity, fiber diameter, and the integrity of the polymer network. The observations obtained provide critical insights for interpreting the differences in adsorption kinetics and doping levels across the different membrane types, serving as a fundamental support for the kinetic analysis. The SEM image of the neat dense PBI membrane (Figure 9a) reveals a compact, continuous film with a smooth surface and no significant porosity or discernible fibrous features. This uniform structure is typical of solvent-cast membranes and results in low permeability and limited specific surface area due to the absence of internal voids. In contrast, the SEM micrograph of the neat (undoped) electrospun PBI membrane (Figure 9b) displays a highly porous, three-dimensional network of thin, interconnected fibers. This morphology is characteristic of electrospun materials and originates from the rapid solidification of a polymer jet subjected to a high-voltage electric field during fabrication. The resulting fibrous architecture significantly enhances the membrane's porosity, specific surface area, and permeability.

Following impregnation with 1 M H_3PO_4 for 30 min (Figure 10a), the electrospun membrane undergoes moderate but noticeable morphological changes. While the fibrous network remains largely intact, a slight increase in average fiber diameter and partial adhesion between adjacent fibers are observed. These changes indicate that phosphoric acid has penetrated the fibers, inducing swelling due to polymer chain plasticization. In some regions, coalescence of adjacent fibers occurs, evidenced by permanent contact points or "welded" junctions where polymer softening has facilitated fusion during treatment. However, the relatively low concentration of acid limits the total amount of absorbed liquid (and the extent of polymer protonation), resulting in a mild reduction in porosity. Nonetheless, the overall structure remains largely preserved: most fibers are still distinguishable, and a substantial fraction of interfiber voids persists. This suggests that 1 M H_3PO_4 is

https://doi.org/10.1021/acsaem.5c03104
ACS Appl. Energy Mater. XXXX, XXX, XXX−XXX

sufficient to induce doping and partial morphological rearrangement without compromising the fibrous architecture.

In contrast, treatment with 5 M H_3PO_4 for 30 min (Figure 10b) results in pronounced morphological transformation. The SEM image reveals significant fiber swelling and extensive fusion between adjacent fibers, which now appear as thickened, indistinct bundles or continuous plates. The clear outlines of individual fibers are largely lost, indicating that the polymer has undergone partial flow or reorganization during acid exposure. This leads to a marked densification of the membrane, with the structure increasingly resembling a compact film rather than a fibrous mat. Consequently, the interfiber porosity is dramatically reduced: many of the original voids are eliminated, and those that remain are notably smaller. This progressive coalescence of fibers with increasing acid concentration demonstrates a concentration-dependent transition from a porous to a dense morphology. Importantly, this acid-induced structural evolution has significant implications for membrane performance in fuel cell applications. The densification and reduced porosity resulting from high-concentration acid treatment could effectively minimize gas crossover, making the membranes promising candidates for proton exchange membrane fuel cells. However, it should also be noted that this densification is expected to affect the mechanical behavior of the membrane. Similar effects have been reported for both solution-cast PBI films and PBI-based composite membranes, where high acid uptake and increased chain plasticization lead to a reduction in elastic modulus and creep resistance under HT-PEM operating conditions.[28] Although a full mechanical analysis is beyond the scope of the present work, the balance between improved gas-barrier performance and possible mechanical trade-offs should be considered when evaluating the membrane for practical fuel-cell applications. This aspect will be addressed in future studies.

3.5. FTIR-ATR Spectroscopic Evaluation

To complement the morphological analysis, a spectroscopic investigation of the interactions between phosphoric acid and the polymer matrix was carried out using the FTIR-ATR technique. The analysis was performed on samples doped at two representative acid concentrations and compared to the neat material, to highlight the progressive protonation of the polymer and the presence of adsorbed phosphate species. The resulting spectra provide a qualitative understanding of the acid−polymer interactions at the molecular level and are essential for interpreting the thermodynamic and kinetic mechanisms discussed above. Moreover, the analysis confirms the effective presence of phosphate species within the membrane structure. Figure 11 presents the spectra of electrospun PBI membranes treated with 1 and 5 M H_3PO_4 for 30 min, compared to the undoped (neat) electrospun PBI sample. New absorption bands are observed in the region of 954−962 cm^{-1}, corresponding to the symmetric stretching vibrations of P−O bonds, indicating the presence of phosphate species either adsorbed on the surface or chemically bound to the polymer matrix.[29] Additionally, a prominent signal appears around 1110 cm^{-1}, attributed to P═O stretching, further confirming the incorporation of phosphoric acid within the membrane. Significant spectral changes are also detected in the 2350−2400 cm^{-1} range, where new bands emerge that are absent in the neat membrane.[29] These are associated with protonation of the imidazole rings in the PBI backbone, providing direct evidence of acid−base interactions between

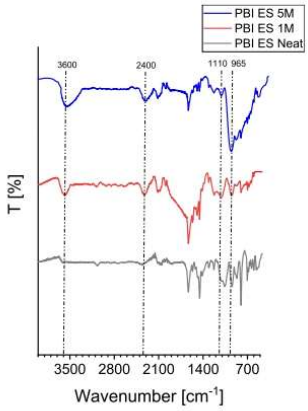

Figure 11. FTIR-ATR spectra of electrospun PBI membranes: neat (black line), doped with 1 M (red line), and 5 M (blue line) H_3PO_4.

H_3PO_4 and the polymer's nitrogen-containing functional groups. The intensity of these bands increases with acid concentration, suggesting a progressive and structurally relevant protonation process, which can alter the electronic distribution and rigidity of the polymer chains. Finally, the region between 3500 and 3850 cm^{-1} exhibits a broad, intense band attributed to O−H stretching vibrations. However, this region arises from overlapping contributions associated with both the O−H stretching of phosphoric acid species and the N−H···O−H hydrogen-bonded complexes formed between H_3PO_4 and the imidazole groups of PBI.[30] Due to this spectral overlap, deconvolution of this region does not allow unambiguous separation of the different hydrogen-bonding environments. Instead, further insight into the acid−polymer interaction can be drawn from the 1110 cm^{-1} band, which is characteristic of the H_2PO^{4-} species and indicates the establishment of acid−base and hydrogen-bonding[30] interactions within the polymer matrix. The increase in intensity and width of these bands with rising H_3PO_4 concentration is indicative of enhanced doping efficiency and higher adsorbate uptake, correlating with the morphological changes discussed earlier.

These spectroscopic observations confirm that the interaction between H_3PO_4 and the PBI matrix is not limited to simple physisorption but involves stronger acid−base interactions. In particular, the protonation of the imidazole rings indicates the formation of specific and relatively stable bonds, consistent with a partial chemisorption contribution, supporting what has already been described in the previous paragraphs.

3.6. Acid Doping Stability: Methanol Test Results

To better understand the nature of acid doping and to preliminarily distinguish between physiosorbed and chemisorbed contributions, electrospun membranes impregnated with phosphoric acid were subjected to selective treatment in methanol (MeOH), as described in Section 2.6.[1] Because of its protic and polar properties, methanol can effectively remove H_3PO_4 molecules that are not strongly bound, leaving behind only the fraction of acid firmly attached to imidazole sites or stabilized through cooperative hydrogen bonding. By comparing the acid doping level (ADL) values before and after the

https://doi.org/10.1021/acsaem.5c03104
ACS Appl. Energy Mater. XXXX, XXX, XXX−XXX

Table 4. Methanol Test Results on Electrospun *M*-PBI Membranes: Initial and Post-Treatment ADL, Fraction of Bound Acid (B), and Free Acid (F)

Acid Concentration [mol/L]	Starting ADL [−]	Post-MetOH ADL [−]	Bound acid fraction (B)	Free acid fraction (F)
1	2.3 ± 0.1	1.14 ± 0.08	0.50 ± 0.04	0.49 ± 0.04
3	6.2 ± 0.2	3.1 ± 0.2	0.50 ± 0.04	0.49 ± 0.04
5	8.1 ± 0.4	4.6 ± 0.1	0.57 ± 0.03	0.43 ± 0.03

methanol test, it is possible to separate the fraction of bound acid (B, resistant to methanol) from the free acid (F, removed by methanol), which is likely located in the pore bulk. Table 4 reports the results obtained at 25 °C for three representative concentrations (1, 3, and 5 M).

The results in Table 4 show that electrospun *m*-PBI membranes retain a significant fraction of acid after methanol treatment, demonstrating strong interactions with the polymer matrix. Even at 1 M, a residual ADL of 1.14 is observed, and this increases to values above 4 at higher concentrations. Thus, increasing the acid concentration not only raises the absolute uptake but also strengthens the interaction between H_3PO_4 and imidazole sites, reducing the fraction of easily extractable free acid. The fibrous morphology of electrospun membranes enhances the accessibility of active sites and promotes a more homogeneous distribution of acid, which explains the higher bound fraction (B). The comparison with dense films obtained by solution casting is striking. Li et al.[1] reported that dense PBI membranes retain an ADL of about 2 after methanol washing, in line with stoichiometric expectations, with the excess acid entirely removed as free acid. In contrast, electrospun membranes preserve a much larger fraction of phosphoric acid even after washing, indicating that the fibrous structure enables stable and cooperative interactions. These findings are consistent with the kinetic analysis discussed earlier. The observed reaction order close to two and the moderate activation energy ($E_a \approx 26.6$ kJ mol^{-1}) suggest a hybrid mechanism: not purely physisorption, but also not limited to acid−base interactions. Instead, the process involves strong acid−base interactions combined with an extended network of cooperative hydrogen bonds. The ability of electrospun membranes to stably retain phosphoric acid beyond the stoichiometric ratio of imidazole sites represents a major advantage for their application as proton exchange membranes in high-temperature fuel cells (HT-PEMFCs). A higher bound acid fraction improves long-term proton conductivity while reducing the risks of premature degradation caused by free acid migration to the catalyst layer, which can accelerate membrane aging. All data relating to changes in mass and volumes of MetOH used are reported in Tables S6, S7, and S8 in the Supporting Info.

3.7. Proton Conductivity

Preliminary proton conductivity data were collected to probe the correlation between the morphological features of the membranes, the acid adsorption mechanisms and their final functional properties. As shown in Figure 12, markedly different conductivities between electrospun (PBI_ES) and solution casting (PBI_Cast) PBI membranes, with the same thickness and doping level (ADL ∼ 11), were recorded. In particular, PBI_ES membranes show significantly higher values than their dense counterparts with an operational maximum at around 150 °C.

At 50 °C, the two membranes show comparable conductivity values, but as the temperature increases, there is a progressive increase in the relative difference in conductivity,

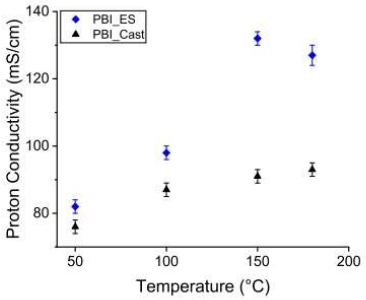

Figure 12. Proton conductivity tests performed under anhydrous conditions for electrospun (PBI_ES, blue rhombi) and cast (PBI_Cast, black triangles) PBI membranes at different temperatures.

which becomes particularly evident at 150 °C, where the PBI_ES membrane reaches a proton conductivity as much as 132 mS/cm where, under identical conditions, the solution-cast PBI membrane exhibits an in-plane proton conductivity of 91 mS/cm, confirming the substantial advantage imparted by the nanofibrous morphology. Therefore, this value is significantly higher than those recorded for the solution-cast PBI membranes reported under comparable conditions,[31] and is on par with advanced PBI-based composite membranes (e.g., PBI with inorganic/ionically conductive fillers) designed to enhance anhydrous transport.[32] These better performances could be attributed to the fibrous morphology of the PBI_ES membrane: SEM micrographs showed that the membrane obtained by electrospinning is highly porous and continuous, which allows the phosphoric acid to diffuse rapidly and homogeneously within the mat. On the contrary, the more compact morphology of cast films severely limits the accessibility of proton sites, leading to a more inhomogeneous acid distribution. Morphology, therefore, has a strong influence on the distribution of acid sites and, in particular, the strong interconnection between fibers ensured the formation of proton pathways[33] in the PBI_ES material rather than the dense counterpart (PBI_Cast). In addition, it is worth pointing out that the increase in conductivity as the temperature increases improves the ion mobility of the acid species in the polymer matrix, showing better ionic conductivity across the membrane thickness. Proton conductivity was evaluated in the in-plane configuration, as the predominant fiber alignment within the electrospun mat promotes lateral proton transport along continuous pathways; in this context, the in-plane value can be considered an upper limit of the material's conductivity, while through-plane measurements, expected to yield lower values due to interfiber discontinuities, will be addressed in future studies.

In conclusion, the comparison shows that the superiority of electrospun does not depend solely on the level of acid-doping that could be achieved (ADL) but also, and above all, on the way in which its morphology affects the capacity for

https://doi.org/10.1021/acsaem.5c03104
ACS Appl. Energy Mater. XXXX, XXX, XXX−XXX

continuous and efficient ion transport. This characteristic makes electrospun PBI membranes particularly promising for applications in anhydrous and high-temperature conditions, as is the case in HT-PEMFC systems, where high proton conductivity in anhydrous conditions is a prerequisite for durable and reliable performance.

4. CONCLUSIONS

This work provides the first comprehensive characterization of phosphoric acid adsorption on electrospun *m*-PBI membranes, highlighting their distinct advantages over conventional dense films. Through systematic kinetic and thermodynamic analysis, we demonstrate that the fibrous morphology of electrospun membranes enables rapid and efficient acid uptake, reaching unprecedented doping levels in a fraction of the time required by dense counterparts. Using a newly developed protocol, we accurately quantified dynamically adsorbed acid, revealing that electrospun membranes can achieve acid doping levels (ADL) as high as 12.9 mol H_3PO_4/mol PBI in under 5 min. In contrast, dense membranes reach a maximum ADL of only 2.3 mol H_3PO_4/mol PBI, requiring more than 24 h to reach equilibrium. Methanol-washing tests show that electrospun membranes retain a larger bound-acid fraction, whereas dense films lose most free acid and settle near stoichiometric values—evidence that fibrous morphology improves acid retention. Kinetic modeling described the adsorption process with a universal reaction law, yielding an apparent reaction order of 1.91 and an activation energy of 26.6 kJ/mol. Thermodynamic analysis confirmed an endothermic adsorption mechanism, with an enthalpy change of 61.3 kJ/mol and a positive entropy change of 185.6 J/mol·K, indicating increased adsorption affinity at higher temperatures. Equilibrium data were well described by the Liu isotherm model, which showed temperature-dependent increases in the affinity constant and a theoretical maximum adsorption capacity (Q_{max}) between 0.055 and 0.060 mol/g. Thermodynamic interpretation suggests a mixed adsorption process, characterized by the coexistence of physical interactions and stable acid−base bonds with imidazole groups. In support of these interpretations, SEM and FTIR analyses conducted pre- and postdoping provided direct evidence of structural and chemical changes induced by the acid treatment. Finally, the evaluation of proton conductivity under anhydrous conditions showed significantly higher values for electrospun membranes than for cast films, over the entire temperature range analyzed. This behavior confirms that fibrous morphology not only facilitates fast and homogeneous adsorption but also results in a continuous and efficient proton transport network. To the best of our knowledge, this is the first comprehensive study to explore the kinetic, thermodynamic, equilibrium and electrochemical aspects of H_3PO_4 adsorption on electrospun PBI membranes. These findings confirm the superior acid doping performance of electrospun membranes and highlight their potential as advanced electrolyte materials for high-temperature proton exchange membrane fuel cells, contributing to improved efficiency and faster activation times. This work also provides a solid foundation for future studies focused on optimizing membrane design and surface chemistry for next-generation fuel cell technologies.

■ ASSOCIATED CONTENT

Data Availability Statement

The data supporting this article have been included as part of the Supporting Information.

Supporting Information

The Supporting Information is available free of charge at https://pubs.acs.org/doi/10.1021/acsaem.5c03104.

Details on adsorption isotherms, mathematical modeling of kinetics, and methanol test results (PDF)

■ AUTHOR INFORMATION

Corresponding Authors

Oreste Tarallo − *Department of Chemical Sciences, Università Degli Studi di Napoli Federico II, Napoli 80126, Italy;* orcid.org/0000-0001-5952-523X; Email: oreste.tarallo@unina.it

Valentina Naticchioni − *Department of Energy Technologies and Renewable Sources, ENEA, Roma 00123, Italy;* Email: valentina.naticchioni@enea.it

Authors

Emmanuel De Gregorio − *Department of Engineering, University of Naples 'Parthenope', Napoli 80143, Italy; Department of Energy Technologies and Renewable Sources, ENEA, Roma 00123, Italy*

Tommaso Cogliano − *Department of Engineering, University of Naples 'Parthenope', Napoli 80143, Italy; Department of Energy Technologies and Renewable Sources, ENEA, Roma 00123, Italy; Laboratory of Industrial Chemistry and Reaction Engineering (TKR), Åbo Akademi, Åbo/Turku FI-20500, Finland;* orcid.org/0000-0001-6225-6157

Giuseppina Roviello − *Department of Engineering, University of Naples 'Parthenope', Napoli 80143, Italy*

Claudio Ferone − *Department of Engineering, University of Naples 'Parthenope', Napoli 80143, Italy*

Giulia Monteleone − *Department of Energy Technologies and Renewable Sources, ENEA, Roma 00123, Italy*

Complete contact information is available at: https://pubs.acs.org/10.1021/acsaem.5c03104

Notes

The authors declare no competing financial interest.

■ ACKNOWLEDGMENTS

Authors acknowledge Dr. Antonio Rinaldi and Dr. Luis Alexander Hein (NANOFABER srl, Via Anguillarese 301, 00123, C.R. ENEA Casaccia Ed. 58, Roma) for experimental support in the preparation of electrospun mats. O.T. and V.N. gratefully acknowledge ENEA, the Italian National Agency for New Technologies, Energy and Sustainable Economic Development, for funding (PNRR POR H2 WP3.1 LA3.1.1). This research was funded by the European Union - NextGenerationEU from the Italian Ministry of Environment and Energy Security, POR H2 AdP MEES/ENEA with involvement of CNR and RSE, PNRR - Mission 2, Component 2, Investment 3.5 "Ricerca e sviluppo sull'idrogeno", CUP: I83C22001170006.

■ ABBREVIATIONS

A0 $[mol^{-0.91}\ L^{0.91}\ s^{-1}]$ Pre-exponential factor

C_e [mol/L]	Equilibrium concentration
E_a [J/mol]	Activation energy
K[L/mol]^{nL}	Affinity constant
n [-]	Reaction order
n_L [-]	Liu's heterogeneity parameter
q [mol/g_{PBI}]	Adsorbed acid amount over time per amount of PBI polymer
q_e [mol/g_{PBI}]	Adsorbed acid amount at the equilibrium per amount of PBI polymer
Q_{max} [mol/g_{PBI}]	Theoretical maximum adsorption capacity
T [K]	Temperature
ΔS [J/mol K^{-1}]	Adsorption reaction entropy
ΔH [J/mol]	Adsorption reaction enthalpy

REFERENCES

(1) Li, Q.; He, R.; Jensen, J. O.; Bjerrum, N. J. PBI-Based Polymer Membranes for High Temperature Fuel Cells − Preparation, Characterization and Fuel Cell Demonstration. *Fuel Cells* **2004**, *4* (3), 147−159.

(2) Giffin, G. A.; Galbiati, S.; Walter, M.; Aniol, K.; Ellwein, C.; Kerres, J.; Zeis, R. Interplay between Structure and Properties in Acid-Base Blend PBI-Based Membranes for HT-PEM Fuel Cells. *J. Membr. Sci.* **2017**, *535*, 122−131.

(3) Lobato, J.; Cañizares, P.; Rodrigo, M. A.; Linares, J. J. PBI-Based Polymer Electrolyte Membranes Fuel Cells. *Electrochim. Acta* **2007**, *52* (12), 3910−3920.

(4) Wang, K. Y.; Weber, M.; Chung, T.-S. Polybenzimidazoles (PBIs) and State-of-the-Art PBI Hollow Fiber Membranes for Water, Organic Solvent and Gas Separations: A Review. *J. Mater. Chem. A* **2022**, *10* (16), 8687−8718.

(5) Lin, J.; Korte, C. PBI-type Polymers and Acidic Proton Conducting Ionic Liquids − Conductivity and Molecular Interactions. *Fuel Cells* **2020**, *20* (4), 461−468.

(6) Lin, J.; Willbold, S.; Zinkevich, T.; Indris, S.; Korte, C. Ionic (Proton) Transport and Molecular Interaction of Ionic Liquid−PBI Blends for the Use as Electrolyte Membranes. *J. Mol. Liq.* **2021**, *342*, 116964.

(7) Abdi, Z. G.; Chen, J.; Chiu, T.; Yang, H.; Yu, H. Synthesis of Ionic Polybenzimidazoles with Broad Ion Exchange Capacity Range for Anion Exchange Membrane Fuel Cell Application. *J. Polym. Sci.* **2021**, *59* (18), 2069−2081.

(8) Chendake, Y. J.; Kharul, U. K. Transport of Inorganic Acids through Polybenzimidazole (PBI) Based Membranes by Chemo-Dialysis. *Desalin. Water Treat* **2012**, *38* (1−3), 96−103.

(9) Schoeman, H.; Krieg, H. M.; Kruger, A. J.; Chromik, A.; Krajinovic, K.; Kerres, J. H2SO4 Stability of PBI-Blend Membranes for SO2 Electrolysis. *Int. J. Hydrogen Energy* **2012**, *37* (1), 603−614.

(10) Perry, A. K.; More, K. L.; Payzant, E. A.; Meisner, R. A.; Sumpter, B. G.; Benicewicz, B. C. A Comparative Study of Phosphoric Acid-doped *m* -PBI Membranes. *J. Polym. Sci. B Polym. Phys.* **2014**, *52* (1), 26−35.

(11) Asensio, J. A.; Sánchez, E. M.; Gómez-Romero, P. Proton-Conducting Membranes Based on Benzimidazole Polymers for High-Temperature PEM Fuel Cells. A Chemical Quest. *Chem. Soc. Rev.* **2010**, *39* (8), 3210.

(12) Javed, A.; Palafox Gonzalez, P.; Thangadurai, V. A Critical Review of Electrolytes for Advanced Low- and High-Temperature Polymer Electrolyte Membrane Fuel Cells. *ACS Appl. Mater. Interfaces* **2023**, *15* (25), 29674−29699.

(13) Mamlouk, M.; Scott, K. Phosphoric Acid-Doped Electrodes for a PBI Polymer Membrane Fuel Cell. *Int. J. Energy Res.* **2011**, *35* (6), 507−519.

(14) Dai, Q.; Xing, F.; Liu, X.; Shi, D.; Deng, C.; Zhao, Z.; Li, X. High-Performance PBI Membranes for Flow Batteries: From the Transport Mechanism to the Pilot Plant. *Energy Environ. Sci.* **2022**, *15* (4), 1594−1600.

(15) Fishel, K.; Qian, G.; Benicewicz, B. C. PBI Membranes Via the PPA Process, In *High Temperature Polymer Electrolyte Membrane Fuel Cells*, Li, Q.; Aili, D.; Hjuler, H. A.; Jensen, J. O., Eds. Springer International Publishing: Cham, 2016; pp. 217−238. .

(16) Murdock, L. A.; Benicewicz, B. C. Preparation of Dense Polybenzimidazole Films without Organic Solvents. *Macromolecules* **2023**, *56* (7), 2729−2735.

(17) Liu, Z.; Tsou, Y.-M.; Calundann, G.; De Castro, E. New Process for High Temperature Polybenzimidazole Membrane Production and Its Impact on the Membrane and the Membrane Electrode Assembly. *J. Power Sources* **2011**, *196* (3), 1055−1060.

(18) Chen, J.; Rong, F.; Xie, Y. F. Microstructures and Sensor Applications of Highly Ordered Electrospun Nanofibers: A Review. *Materials* **2023**, *16* (9), 3310.

(19) Shi, S.; Si, Y.; Han, Y.; Wu, T.; Iqbal, M. I.; Fei, B.; Li, R. K. Y.; Hu, J.; Qu, J. Recent Progress in Protective Membranes Fabricated via Electrospinning: Advanced Materials, Biomimetic Structures, and Functional Applications. *Adv. Mater.* **2022**, *34* (17), 2107938.

(20) Wang, J.; You, C.; Xu, Y.; Xie, T.; Wang, Y. Research Advances in Electrospun Nanofiber Membranes for Non-Invasive Medical Applications. *Micromachines* **2024**, *15* (10), 1226.

(21) Wang, Y.; Zhai, W.; Li, J.; Liu, H.; Li, C.; Li, J. Friction Behavior of Biodegradable Electrospun Polyester Nanofibrous Membranes. *Tribol. Int.* **2023**, *188*, 108891.

(22) Matsumoto, H.; Tanioka, A. Functionality in Electrospun Nanofibrous Membranes Based on Fiber's Size, Surface Area, and Molecular Orientation. *Membranes* **2011**, *1* (3), 249−264.

(23) Wu, S.; Qin, X.; Li, M. The Structure and Properties of Cellulose Acetate Materials: A Comparative Study on Electrospun Membranes and Casted Films. *J. Ind. Tex.* **2014**, *44* (1), 85−98.

(24) Hu, W.; Zhang, P.; Zhao, L.; Tao, Z. Electrochemical Performance Enhancement of Electrospun Nanofiber Cathode through Impregnation Method. *Int. J. Hydrog. Energy* **2023**, *48* (91), 35765−35770.

(25) Liu, X.; Cheng, M.; Zhao, Y.; Qiu, Y. Theoretical Studies on the Chemical Degradation and Proton Dissociation Property of PBI Used in High-Temperature Polymer Electrolyte Membrane Fuel Cells. *J. Phys. Chem. B* **2024**, *128* (25), 6167−6177.

(26) De Gregorio, E.; Roviello, G.; Naticchioni, V.; Cigolotti, V.; Pozio, A.; Hein, L. A.; De Luca, C.; Ferone, C.; Rinaldi, A.; Tarallo, O. Electrospun Polybenzimidazole Membranes: Fabrication and Fine-Tuning Through Physical and Statistical Approaches. *Polymers* **2025**, *17* (12), 1594.

(27) Ebelegi, A. N.; Ayawei, N.; Wankasi, D. Interpretation of Adsorption Thermodynamics and Kinetics. *OJPC* **2020**, *10* (3), 166−182.

(28) Aili, D.; Henkensmeier, D.; Martin, S.; Singh, B.; Hu, Y.; Jensen, J. O.; Cleemann, L. N.; Li, Q. Polybenzimidazole-Based High-Temperature Polymer Electrolyte Membrane Fuel Cells: New Insights and Recent Progress. *Electrochem. Energy Rev.* **2020**, *3* (4), 793−845.

(29) Zeis, R. Materials and Characterization Techniques for High-Temperature Polymer Electrolyte Membrane Fuel Cells. *Beilstein J. Nanotechnol.* **2015**, *6*, 68−83.

(30) Glipa, X.; Bonnet, B.; Mula, B.; Jones, D. J.; Rozière, J. Investigation of the Conduction Properties of Phosphoric and Sulfuric Acid Doped Polybenzimidazole. *J. Mater. Chem.* **1999**, *9* (12), 3045−3049.

(31) Tang, H.; Geng, K.; Wu, L.; Liu, J.; Chen, Z.; You, W.; Yan, F.; Guiver, M. D.; Li, N. Fuel Cells with an Operational Range of − 20 to 200 °C Enabled by Phosphoric Acid-Doped Intrinsically Ultramicroporous Membranes. *Nat. Energy* **2022**, *7* (2), 153−162.

(32) Wang, B.; Ling, Z.; Liu, Q.; Fu, X.; Zhang, R.; Hu, S.; Zhao, F.; Li, X.; Bao, X.; Li, N.; Yang, J. Phosphoric Acid-in-Clay Electrolyte Boosting Polybenzimidazole Membranes for High-Performance Fuel Cells. *Adv. Funct. Mater.* **2025**, No. e18482.

(33) Kallem, P.; Yanar, N.; Choi, H. Nanofiber-Based Proton Exchange Membranes: Development of Aligned Electrospun Nano-

https://doi.org/10.1021/acsaem.5c03104
ACS Appl. Energy Mater. XXXX, XXX, XXX−XXX

RINGRAZIAMENTI

Non è semplice trovare le parole giuste per descrivere tutto ciò che questo percorso mi ha donato. È stato qualcosa di inaspettato, ma che fin dal primo momento mi ha completamente catturato. Dedico questo lavoro ai momenti difficili, alla disperazione più profonda e alla consapevolezza di essere riuscito, nel mio piccolo, a portare avanti un progetto che considero un grande traguardo, uno dei motivi principali che mi spinge, ogni giorno, a dare il meglio di me stesso.

Un ringraziamento speciale va alla mia famiglia, il vero motore di ogni cosa. Grazie per il vostro sostegno costante e per i tentativi, spesso vani, di capire cosa combinassi ogni giorno in laboratorio. Grazie per essere sempre presenti, per essere la spina dorsale della mia vita e per donarmi, con l'esempio e il coraggio, la forza di affrontare ogni ostacolo. Vi dedico questo piccolo traguardo e tutto ciò che di bello arriverà.

Ai miei suoceri, per l'accoglienza, l'affetto e la vicinanza che non mi avete mai fatto mancare. Una seconda famiglia, in ogni senso.

Un sincero e profondo ringraziamento alla Prof.ssa Giuseppina Roviello: molto più di un tutor, un'amica leale, sempre pronta ad ascoltarmi e a offrirmi consigli in ogni situazione. Grazie per aver creduto in me e per avermi dato l'opportunità di vivere questa magnifica esperienza di crescita personale e professionale. Grazie per le innumerevoli chiacchierate, per la sua gentilezza, per la sua intraprendenza e per la sua capacità di riuscire sempre a trovare del buono in ogni cosa. Grazie semplicemente per essere ciò che è: caparbia, tenace e sensibile.

Al Prof. Oreste Tarallo, che ha saputo assecondare e valorizzare ogni mio pensiero "stravagante" ed "esotico". Ricordo con chiarezza ogni nostro scambio di idee, dai quali ho imparato che la perseveranza e la capacità di uscire dagli schemi spesso conducono ai risultati migliori.

Un ringraziamento sentito anche al Prof. Claudio Ferone e al Prof. Raffaele Cioffi, sempre disponibili e straordinariamente aperti a ogni tipo di discussione, dalla scienza alla birra che, in fondo, è pur sempre chimica.

Nulla di tutto ciò sarebbe stato possibile senza l'aiuto del Prof. Elio Jannelli. La ringrazio per aver creduto nel mio lavoro e, soprattutto, per avermi insegnato che credere non significa accettare, ma interrogare, approfondire, mettere alla prova ogni idea. La sua curiosità autentica e la sua attenzione

ai dettagli mi hanno mostrato cosa significhi davvero fare ricerca: non accontentarsi mai delle risposte facili.

Grazie di cuore a tutto il team ENEA, alla Dott.ssa Viviana Cigolotti, alla Dott.ssa Valentina Naticchioni e al Dr. Alfonso Pozio. Mi avete fatto sentire davvero a casa, e questo, per me, ha significato moltissimo. Sono orgoglioso di aver condiviso con voi questo percorso.

Ovviamente questo traguardo non sarebbe stato lo stesso senza la presenza di Michele, Alessio, Carlo, Ciro, Peppe, Gigio, Luca, Domenico e di tutti coloro che ho avuto la fortuna di incontrare lungo il cammino.
Siete molto più che semplici colleghi o amici: vi considero dei veri fratelli acquisiti. Grazie per le mille risate, per i caffè condivisi e, semplicemente, per esserci sempre stati. Avete migliorato la mia vita, forse senza accorgervene, rendendo ogni giorno un'esperienza più leggera e piena di allegria.

Un ringraziamento speciale va a una persona altrettanto speciale: nonno Gigi, il Pistolero di Sant'Antonio Abate. Più di un semplice nonno, un padre e un amico vero. Non dimenticherò mai le tue prime parole, quando cercavo, un po' impacciato, di spiegarti l'inizio di questo percorso:

"*Devi fare tutto ciò che ti sta bene. Se tu sei contento, allora prendi questa strada*."

Io quella strada l'ho presa, l'ho percorsa e oggi sono arrivato fin qui. Ti dico grazie, non solo per quel consiglio, ma per l'esempio che mi hai dato: anche nelle difficoltà della vita, hai sempre affrontato tutto con un sorriso. Mi hai lasciato così all'improvviso che non metabolizzerò mai la tua assenza. Un pezzo del mio cuore è andato via con te ma resta, vivido, il ricordo del tuo sorriso, delle tue battute e del tuo modo di essere: umile, divertente e amorevole. Io e te abbiamo ancora un punto in sospeso..un bel piatto di spaghetti che tanto amavi e che io dovevo cucinarti. Quanto darei per rivivere quei momenti. Ti dedico questo piccolo traguardo nella speranza di poter riascoltare, un giorno, le tue barzellette e il tuo fantastico motto: Amabile? Sempre!

Adesso che siete arrivati tutti fin qua, arriva la parte più bella. Maria, luce dei miei occhi, non sai quanto bene mi fai. Grazie per essere stata sempre presente, notte e giorno, nei momenti bui e in quelli più difficili.

Platone disse: "*L'amore è il desiderio di possedere per sempre il bene*."

E io, quel bene, l'ho trovato in te. Se oggi arrivo qui con il sorriso, con la forza di non mollare e con la serenità di chi sa dove sta andando, è perché ci sei tu. Hai creduto in me anche quando io non ci riuscivo, hai raccolto i pezzi delle mie giornate storte e li hai rimessi insieme con la tua pazienza, con

la tua ironia, con la tua dolcezza disarmante. Hai dato un senso a ogni mia fatica, trasformando il caos in calma, la stanchezza in sollievo, la paura in coraggio. Ogni volta che ho pensato di non farcela, bastava guardarti per ricordarmi perché valeva la pena continuare.

Tu sei casa. Se questo lavoro è un traguardo, tu sei il motivo per cui l'ho potuto raggiungere. Non so cosa ci riserverà il futuro, ma so che qualunque cosa verrà, voglio affrontarla con te, perché con te tutto è più vero, più semplice, più mio, più nostro. Grazie per avermi amato anche nei giorni in cui non lo meritavo. Grazie per avermi aspettato, sostenuto, spronato e ammorbidito.

E grazie, soprattutto, per essere tu: la mia costante, il mio equilibrio, il mio amore per sempre.

Un abbraccio forte a tutti voi lassù. Spero siate orgogliosi di me.